ABSTRACT

CUSTOM ENGINEERED NANOMATERIALS FOR ENERGETICS AND ENERGY APPLICATIONS

by
Ani Abraham

Recent interest in reactive material has shifted to more custom formulations targeting specific applications. In this work, preparation and characterization of nanomaterials used for several energetics and energy applications are addressed.

The main challenge of this effort is to design and prepare nanomaterials which have significant improvements associated with combustion dynamics, reaction rates, sensitivity, biocidal effectiveness, moisture stability, and are environmentally safer over the existing energetics. Nanomaterials that are used to defeat stockpiles of chemical and biological weapons, modify ionosphere properties for transmission of optical and radio signals, and for energy storage are prepared under room or cryogenic temperatures via mechanical milling.

This offers a scalable and versatile method for modifying or creating nanostructured composite materials. Additionally, nano-composite films used for on-chip energetics are prepared using electrochemical etching via solutions containing hydrofluoric acid, ethanol and hydrogen peroxide. Lastly, a less sensitive bimetal nano-powder for replacement of commonly used nano-sized aluminum is prepared by electro-exploded wires of pure metals.

Morphology and phase compositions of nanomaterials are characterized by scanning electron microscopy (SEM), transmission electron microscopy (TEM), and X-ray diffraction (XRD). Thermal analysis is performed using thermo-gravimetry (TG),

differential scanning calorimetry (DSC), and bomb calorimetry. TG results indicate the stability of the biocidal content as well as the individual decomposition and oxidation reactions involving the nanomaterials. DSC results are used to quantify the thermal energy storage capabilities and material performance upon cycling for energy storage materials. Bomb calorimetry results establish the energy density of nano-composite films and furthermore, agrees with thermodynamic equilibrium calculations for on-chip energetics.

Ignition temperatures of several nanomaterials are determined at heating rates of 10^3 to 10^5 K/s using a heated filament experiment. In a separate ignition experiment, the electrostatic discharge (ESD) ignition stimulus is used to characterize minimum ignition energy and cloud combustion characteristics. Aerosol combustion inside a constant volume explosion vessel is used to determine the combustion performance. Additionally, single particle combustion times as a function of particle size are quantified using products of hydrocarbon flame as the oxidative environment. Propagation velocities of the combustion event are also measured under air, nitrogen and vacuum environments using a high-speed video camera for several nanomaterials.

Nanomaterials prepared for bioagent defeat application in comparison to pure Al or Mg metals have substantially reduced ignition temperatures and longer combustion times. Their stability and effectiveness to inactivate bioagents are also substantially improved.

For on-chip energetics, moisture-stable and perchlorate-free compositions of nano-composite films are prepared; however, slower propagation rates compared to previous composite systems are seen.

The efficiency and overall charge of the refractory metal, samarium (Sm), in the starting composition is substantially improved by increasing the reactive interface surface area, via mechanical milling, within the nano-energetic material used as the heat source for Sm evaporation. Altering the interface chemistry of nano-energetic materials helps to achieve high reaction rates and consequently, high combustion temperatures to ionize Sm metal while inhibiting undesired reaction between Sm and the components of the nano-energetic material.

Lastly, the Al-Ni bimetal nano-powders prepared with doped amount of nickel could be used as replacement for aluminum nano-powders. It is observed that the bimetal powder is oxidizing slower than n-Al, leading to its greater stability during handling and storage. Furthermore, the bimetal powder is less ESD-ignition sensitive than n-Al with similar combustion temperatures.

CUSTOM ENGINEERED NANOMATERIALS FOR ENERGETICS AND ENERGY APPLICATIONS

by
Ani Abraham

A Dissertation
Submitted to the Faculty of
New Jersey Institute of Technology
in Partial Fulfillment of the Requirements for the Degree of
Doctor of Philosophy in Chemical Engineering

Otto H. York Department of
Chemical, Biological, and Pharmaceutical Engineering

May 2016

APPROVAL PAGE

CUSTOM ENGINEERED NANOMATERIALS FOR ENERGETICS AND ENERGY APPLICATIONS

Ani Abraham

Dr. Edward L. Dreizin, Dissertation Advisor Date
Professor and Associate Chair of Chemical, Biological, and Pharmaceutical Engineering, NJIT

Dr. Rajesh N. Dave, Committee Member Date
Distinguished Professor of Chemical, Biological, and Pharmaceutical Engineering, NJIT

Dr. Mirko Schoenitz, Committee Member Date
Associate Research Professor of Chemical, Biological, and Pharmaceutical Engineering, NJIT

Dr. Sagnik Basuray, Committee Member Date
Assistant Professor of Chemical, Biological, and Pharmaceutical Engineering, NJIT

Dr. Christopher J. Morris, Committee Member Date
Team Leader, U.S. Army Research Laboratory, Adelphi, MD

BIOGRAPHICAL SKETCH

Author: Ani Abraham

Degree: Doctor of Philosophy

Date: May 2016

Undergraduate and Graduate Education:

- Doctor of Philosophy in Chemical Engineering,
  New Jersey Institute of Technology, Newark, NJ, 2016

- Bachelor of Science in Chemical Engineering,
  University of Florida, Gainesville, FL, 2010

Major: Chemical Engineering

Publications:

A. Abraham, H. Nie, M. Schoenitz, A. B. Vorozhtsov, M. Lerner, A. Pervikov, N. Rodkevich, E. L. Dreizin, Bimetal Al-Ni nano-powders for energetic formulations, Journal of Physical Chemistry C (2016). Submitted.

N. Rodkevich, M. Lerner, A.B. Vorozhtsov, H. Nie, A. Abraham, M. Schoenitz, E. L. Dreizin, Oxidation of nano-sized aluminum powders, Thermochimica Acta (2016). Submitted.

A. Abraham, Z. Zhong, R. Liu, S.A. Grinshpun, M. Yermakov, R. Indugula, M. Schoenitz, E.L. Dreizin, Preparation, ignition and combustion of Mg·S reactive nanocomposites, Combustion Science and Technology (2016). Submitted.

A. Abraham, N.A. MacDonald, E.L. Dreizin, Reactive materials for evaporating samarium, Propellants, Explosives, Pyrotechnics (2016). Accepted.

S. Wang, A. Abraham, Z. Zhong, M. Schoenitz, E.L. Dreizin, Ignition and combustion of boron-based Al·B·I_2 and Mg·B·I_2 composites, Chemical Engineering Journal 293 (2016) 112-117.

A. Abraham, M. Schoenitz, E.L. Dreizin, Energy storage materials with oxide-encapsulated inclusions of low melting metal, Acta Materialia 107 (2016) 254-260.

A. Abraham, N.W. Piekiel, C.J. Morris, E.L. Dreizin, Combustion of energetic porous silicon composites containing different oxidizers, Propellants, Explosives, Pyrotechnics 41 (2016) 179-188.

A. Abraham, J. Obamedo, M. Schoenitz, E.L. Dreizin, Effect of composition on properties of reactive Al·B·I2 powders prepared by mechanical milling, Journal of Physics and Chemistry of Solids 83 (2015) 1-7.

A. Abraham, S. Zhang, Y. Aly, M. Schoenitz, E.L. Dreizin, Aluminum-iodoform composite reactive material, Advanced Engineering Materials 16 (2014) 909-917.

Conference Proceedings:

A. Abraham, N.W. Piekiel, C.R. Knick, C.J. Morris, E. Dreizin, Quantification of oxidizer systems for porous silicon combustion, MRS Online Proceedings Library 1758 (2015).

Presentations:

A. Abraham, Z. Zhong, R. Liu, M. Schoenitz, E.L. Dreizin, Preparation, ignition and combustion of metal-sulfur nanocomposite thermites with biocidal properties, AIChE Annual Meeting Salt Lake City, UT, November 2015.

A. Abraham, M. Schoenitz, E.L. Dreizin, Energy storage materials with nano-encapsulated inclusions of an easy to melt metal, AIChE Annual Meeting Salt Lake City, UT, November 2015.

A. Abraham, Z. Zhong, R. Liu, M. Schoenitz, E.L. Dreizin, Preparation, ignition and combustion of Mg·S reactive nanocomposites, DTRA Technical Review Springfield, VA, July 2015.

A. Abraham, N.W. Piekiel, C.R. Knick, C.J. Morris, E. Dreizin, Quantification of oxidizer systems for porous silicon, 2014 MRS Fall Meeting & Exhibit Boston, MA, December 2014.

A. Abraham, J. Obamedo, M. Schoenitz, E.L. Dreizin, Effect of composition on properties of reactive Al·B·I_2 powders prepared by mechanical milling. AIAA Region I Young Professional, Student, and Education Conference Laurel, MD, November 2014.

A. Abraham, J. Obamedo, M. Schoenitz, E.L. Dreizin, Effect of composition on properties of reactive Al·B·I_2 powders prepared by mechanical milling. AIChE Annual Meeting Atlanta, GA, November 2014.

A. Abraham, J. Obamedo, M. Schoenitz, E.L. Dreizin, Effect of composition on properties of reactive $Al{\cdot}B{\cdot}I_2$ powders prepared by mechanical milling, DTRA Technical Review Springfield, VA, July 2014.

A. Abraham, M. Schoenitz, E.L. Dreizin, Metal-based reactive materials with biocidal reaction products, AIAA Region I Young Professional, Student, and Education Conference Laurel, MD, November 2013.

A. Abraham, M. Schoenitz, E.L. Dreizin, Metal-based reactive materials with biocidal reaction products, AIChE Annual Meeting San Francisco, CA, November 2013.

A. Abraham, M. Schoenitz, E.L. Dreizin, Metal-based reactive materials with biocidal reaction products, SHS 2013 XII International Symposium South Padre Island, TX, October 2013.

A. Abraham, M. Schoenitz, E.L. Dreizin, Metal-based reactive materials with biocidal reaction products, DTRA Technical Review Springfield, VA, July 2013.

To my parents:
Jaisamma John (Mommy) and Abraham Joseph (Daddy)
Thank you for everything! Your unconditional love and support kept me going.

Padmavathy Subramanian (Amma) & Ananth Subramanian (Appa) (July 26th, 1943 – January 9th, 2016)
For always being there for me.

To my sisters, brothers-in-law, & niece:
Dhanya, Tani, Arun, Raman (March 24th, 1983 – May 15th, 2006), & Isa
For bringing countless amounts of joy and enjoyment to my life!

Lastly to my wife: Dr. Sangeeta Abraham
You always believed in me and we finally made it happen!

ACKNOWLEDGMENT

Completing my Ph.D. would not have been possible if it was not for the great support group around me. I have many people to thank for making this journey worthwhile.

I would like to express my deepest gratitude to my advisor, Dr. Edward Dreizin. I thank him for providing me with this great opportunity to work in his research group. His guidance, expertise, intelligence and support has allowed me to learn, grow and accomplish a great deal. As an advisor, I could not have asked for anyone better than Dr. Dreizin as he understood my true potential and guided me to think towards the bigger picture and provided me with great direction in achieving my research goals. His mentorship, and optimistic outlook toward research and life has truly inspired me to put my best effort towards everything.

I want to express my gratitude to my co-advisor, Dr. Mirko Schoenitz and his brilliant mind. I thank him for providing me with valuable advice, and assistance towards my research. I have learned various skills from him and it has been an honor to have worked with him. I also want to thank other members of my committee, Dr. Rajesh Dave, and Dr. Sagnik Basuray, for their insights and constructive criticisms toward my research.

Dr. Christopher Morris, also a committee member, and Dr. Nicholas Piekiel deserves a special note of praise for giving me the opportunity to intern at U.S. Army Research Laboratory as a graduate student. They have played a pivotal role in my graduate life as fantastic mentors for my professional career. I thank them as well as other members of Dr. Morris's research group: Wayne Churaman, Cory Knick, David M. Lunking, and Brian Isaacson, for playing an important role in my studies.

I would also like to recognize the former research staff and current as well as graduated students in Dr. Dreizin's laboratory: Dr. Alexandre Ermoline, Dr. Shasha Zhang, Dr. Yasmine Aly, Dr. Priya Santhanam, Dr. Shashank Vummidi, Dr. Rayon Williams, Dr. Stefano Mercati, Vern Hoffmann, Hongqi Nie, John Obamedo, Amy Corcoran, Song Wang, Ian Monk, Kerri-Lee Chintersingh, Xinhang Liu, Ziyue Zhong, Ruodong Liu, Daniel Hasting, and Oleg Lagoviyer. Learning and working with everyone has been a great pleasure and I thank everyone for all of the great memories we have together.

I am grateful to our collaborator, Dr. Sergey Grinshpun's group, for readily testing and providing valuable insight on the performance of our materials.

I must express my acknowledgement to my sponsors, Defense Threat Reduction Agency (DTRA) and Air Force Research Laboratory for the financial support.

I acknowledge my family and friends for their unconditional love and support. To my parents, who have worked so hard in their lives to provide me with a great education, I hope I have made them proud. To my parents-in-law for welcoming me into their home and encouraging me with their best wishes as well as to my sisters, brothers-in-law and my niece for bringing joy and enjoyment during this journey.

Most importantly, I would like to thank my wife, Dr. Sangeeta Abraham. Her encouragement and belief were the stepping stones for me to choose this path. I could not have achieved everything without her support and love. I am grateful to have her by my side each and every day!

TABLE OF CONTENTS

TABLE OF CONTENTS
(Continued)

TABLE OF CONTENTS
(Continued)

Chapter **Page**

TABLE OF CONTENTS
(Continued)

Chapter **Page**

TABLE OF CONTENTS
(Continued)

Chapter **Page**

TABLE OF CONTENTS
(Continued)

Chapter **Page**

LIST OF TABLES

LIST OF FIGURES

LIST OF FIGURES
(Continued)

Figure **Page**

LIST OF FIGURES
(Continued)

Figure **Page**

LIST OF FIGURES
(Continued)

Figure **Page**

LIST OF FIGURES
(Continued)

Figure **Page**

LIST OF FIGURES
(Continued)

Figure **Page**

LIST OF FIGURES
(Continued)

Figure **Page**

CHAPTER 1

INTRODUCTION

In past decades, research of next generation reactive materials shared a common focus of improving ignition and combustion characteristics of metal-based powders, used as fuel additives in propellants, explosives, and pyrotechnics [1-9]. Recently, there has emerged a substantial interest in more custom engineered reactive materials formulated to target specific applications, some of which included modified fuels and/or oxidizers for bioagent defeat [10-16], on-chip energetics [17-29] for microelectromechanical systems (MEMS), and heaters for evaporation of refractory metals to modify ionosphere [30-37]. Additionally, there is interest in desensitizing nano-powders by additives and coating technology [38-42]. Lastly, use of reactive powders of metals, alloys, and metal-based composites for applications involving energy generation and harvesting has also been of interest recently [43-47].

1.1 Energetics for Biological Weapon Defeat

Reactive materials developed as components of advanced munitions, aimed to eliminate or inactivate stockpiles of biological weapons [48, 49], has primarily focused on fuels and oxidizers modified by added halogens (i.e., iodine), although additives including other materials with known biocidal properties were also investigated. Generally, these can be classified into three main groups: metal-based fuels [12, 16, 50, 51], oxidizers [52], and thermites (metal fuel and oxidizer compositions) with at least one component producing biocidal combustion products [10, 11, 14, 15]. Although various processing and preparation techniques can be used, mechanical milling [53, 54] was shown to be a

versatile and scalable method to prepare stable metal-iodine composite reactive powders, which generate biocidal combustion products [12, 13, 16, 50, 51]. Upon ignition, iodinated gas species must be readily generated inactivating in situ aerosolized spores and bacteria and thus preventing their escape and contamination of the surrounding areas. Prior to ignition, iodine or other components capable of generating biocidal gases, typically containing a halogen, should be stabilized in the reactive material so that it can be stored and processed along with other components of energetic systems [55, 56]. The halogen-holding materials should burn with a strong heat release to warrant their use in energetic formulations.

Several metal-based reactive materials are developed using mechanical milling at both liquid nitrogen and room temperatures. We characterized their stability, ignition and combustion performance to identify the most effective powders for spore inactivation. Although most of the prepared materials contained halogens as the biocidal component, we also explored a sulfur containing material, which may have potential biocidal benefits.

1.2 On-chip Energetics

Porous silicon (PS) is the primary fuel in on-chip energetics, which undergoes highly exothermic reactions with various oxidizers. One consistent result from the earlier studies is that sodium perchlorate ($NaClO_4$) performed very well as an oxidizer in terms of the qualitative measures used, including optical emission and acoustic intensities. Since then, several groups [22-29] have carried out extensive studies of the PS/$NaClO_4$ system, quantitatively validating its high reaction rates with high energy release and tunability [57-60]. The high performance of PS/$NaClO_4$ system compared to others is due in part to the high solubility of $NaClO_4$ in alcohols [28]; e.g., in methanol, where it exceeds 400 $g \cdot l^{-1}$

solvent at 25°C [61]. The higher solubility increases oxidizer filling of the pores when the solvent evaporates [62]. Although the PS/$NaClO_4$ energetic materials perform well, the high solubility of $NaClO_4$ in both alcohols and water also correlates with its high hygroscopicity, making it difficult to use in many practical situations. Furthermore, perchlorates may present environmental and health hazards due to the long-term stability of the chlorate ion and its tendency to mimic iodide ions in biological processes [63, 64].

Therefore, exploring alternative oxidizers with potential benefits of increased moisture stability and/or perchlorate-free composition is of interest. The primary focus is on the combustion of on-chip PS with solid oxidizers including sulfur and several nitrates.

1.3 Energetics for Modification of Ionosphere

Ejection of clouds of readily ionized metal atoms can be used to modify ionosphere to study and alter its properties important for transmission of optical and radio signals [30]. Conventional propellants or explosives used as a heat source to readily release and ionize metals, such as lithium [31, 32], barium [33-35], and, most recently, samarium [36, 37], are problematic because of the rapid reaction of evaporated metal with combustion products released simultaneously. A more custom engineered energetic materials are necessary to minimize the oxidation or chemical bonding of samarium with combustion products; thus, improving upon the current efficiencies [37] and maximizing the ionization of the entire charge of samarium in the starting formulation.

In this study, an approach for generation of samarium clouds is explored using metal-based reactive materials prepared by arrested reactive milling (ARM) [1], producing high combustion temperatures and forming relatively stable, inert condensed products. Conventional blending or mixing starting components with samarium discussed by

previous researchers [37] is purposefully avoided in this study to diminish any reaction of samarium with other components of reactive materials. A reactive material is initially prepared by Arrested Reactive Milling (ARM), containing components capable of highly exothermic reaction mixed on the scale of ca. 100 nm inside micron-sized fully dense powder particles. This material is then blended with samarium powder, utilizing a short milling step. Several borides, carbides, and sulfides, as well as thermite systems are prepared and tested as reactive materials to determine the best suited material for generation of clouds of evaporated samarium.

1.4 Nanomaterials for Energy Applications

Recently, reactive powders of metals, alloys, and metal-based composites have shown potential usefulness for energy applications [43-47]. Additionally, metal-based materials can serve as energy storage materials (ESM) with high thermal conductivity and high strength [65]. However, the containment of metal that melts upon heating (serving as an energy storage medium) in repetitive heating cycles is difficult, and therefore, bulk containers are often used [66], limiting the type of structures that can be manufactured using the ESM. In one proposed solution to overcome the structural difficulties, recently it was reported [67] that an easy to melt metal, Bi, can be incorporated into matrices of Ag metal, which does not form intermetallics with Bi. However, during repetitive thermal cycling, migration and coalescence of Bi is expected. In another study [68], nano-sized Bi particles were embedded in a polyimide resin matrix to prevent coalescence; but thermal conductivity would be jeopardized.

Similarly, it is possible to prepare composite materials with low-melting point metal dispersed in a metal or ceramic matrix with high melting point. However, to prevent

structural weakness and rapid deterioration from melt-freeze cycles, the low-melting point metal inclusions must be encapsulated inside a thermally stable matrix. Such a material is developed, prepared, and characterized in this work, exploiting a reactive nano-thermite as a precursor.

Using mechanical milling, a nanocomposite thermite is prepared. It is then slowly annealed to initiate a controllable redox reaction to yield an ESM composite. The composite after completion of the redox reaction contains nano-scale inclusions or layers of low-melting point metal surrounded by protective metal oxide. Such ESM structures have high thermal conductivity and strength in addition to being stable in time. Furthermore, these are not easily destroyed by repeated melting and solidification of the encapsulated inclusions, a desired characteristic for EMS.

1.5 Bimetal Nano-powders for Advanced Energetics

Research in new nano-energetic systems, including metal nano-powders, nano-thermites, and intermetallics are emerging [69-71] due to the increased availability of aluminum nano-powders from manufacturing processes matured over the past two decades [72-74]. Aluminum nano-powders remain to be the most widely used fuel additives to propellants, explosives, and pyrotechnics due to their ability to improve combustion efficiencies and detonation properties with its large available reactive surface area [75-77]. Consequently, the large surface area achieved from using nano-powders results in increased sensitivity to electrostatic discharge (ESD) ignition stimulus compared to micron-sized powders [78, 79]. Additionally, aging of aluminum powders causing deterioration of reactive properties has been a concern for nano-energetic materials and n-Al, in particular [80, 81].

Desensitizing energetic materials using non-metal additives [38-40] and organic coatings is effective [41, 42]; but often not viable due to the adverse effects on combustion dynamics and energy density. Therefore, preparing new nano-powders which are less sensitive to ESD ignition and aging while preserving energy density and high reactive surface remains a challenge. In this study, bimetal aluminum-nickel (Al-Ni) nano-powders are prepared via electro-exploded wires [72, 73] as a potential replacement for Al nano-powders. Ignition and ESD sensitivity are characterized experimentally. Furthermore, a detailed oxidation model developed for micron and nano-sized aluminum powders [82-84] are adapted for Al-Ni nano-powders and compared directly with the kinetics and aging process for aluminum nano-powders prepared using the same technique.

CHAPTER 2

ALUMINUM-IODOFORM COMPOSITE REACTIVE MATERIAL

2.1 Abstract

Mechanically alloyed aluminum-iodoform composites were prepared with iodine concentration of 20 wt. %. Ball milling at both room temperature and liquid nitrogen temperature was explored. Material characterization by electron microscopy and x-ray diffraction showed no difference between samples milled at different temperatures. However, samples prepared at room temperature aged rapidly. Thermo-gravimetric measurements quantifying release of iodine upon heating confirmed that cryogenic milling was necessary to stabilize iodoform in the Al-matrix. Iodine was released upon heating in four distinct stages. The oxidation of the prepared materials was also studied using thermo-gravimetric analysis and two main oxidation steps were detected. The ignition temperatures were determined for powders coated onto a metal filament heated electrically at 10^3 – 10^4 K/min. The ignition temperatures of the prepared materials were noticeably lower compared to the $Al{\cdot}I_2$ composite prepared using a similar cryo-milling approach. The combustion characteristics determined using constant volume explosions of aerosolized powders were found to be similar to those of $Al{\cdot}I_2$ composite. The maximum pressure and rate of pressure rise observed in the latter experiments were greater than for pure aluminum powders with comparable particle sizes.

2.2 Introduction

There is substantial interest in reactive materials with biocidal combustion products capable of eliminating or inactivating aerosolized microorganisms [10-15]. Research has

primarily addressed fuels and oxidizers modified by added halogens, although additives including other materials with known biocidal properties were also investigated. Some of the specific materials prepared and tested include silver oxides, iodine oxides, and thermite systems with silver iodates [10, 14, 85, 86].

Generally, it is possible to classify different reactive materials capable of producing biocidal combustion products in three main groups:

- Fuels, such as aluminum based powders; [12, 50, 51]
- Oxidizers, such as iodine oxides or iodate-based compositions; [52]
- Energetic formulations, such as thermites containing both fuel and oxidizer, with at least one of the components producing biocidal products [10, 11, 14, 15].

For either fuels or oxidizers to be used as drop-in replacements in the current energetic formulations, they should be compatible with the other formulation components and sufficiently stable to endure conventional processing routine [55, 56]. Use of the reactive materials comprising both fuel and oxidizer may require a complete redesign of energetic formulations. In any case, stability, compatibility with common binders, and insensitivity to ignition, e.g., by spark, are critical practical characteristics required of new reactive materials.

Both silver oxide and iodine oxides are expected to yield large quantities of biocidal combustion products; however they are moisture sensitive and relatively hard to handle. In initial experiments with silver oxide, the desired elemental silver, known to be a biocide, was not produced during combustion [10]. Most of the currently tested thermite compositions include moisture-sensitive oxides and nano-powders, such as nano-Al, known to be very sensitive to spark ignition [79, 87, 88].

Conversely, metal-halogen powders prepared by mechanical alloying with high energy densities, comparable to pure aluminum, are relatively stable and insensitive, and produce effective biocidal combustion products [12, 16, 50, 89]. Previous work investigated mechanically alloyed composites, $Al{\cdot}I_2$ [12, 16, 50] and $Al{\cdot}B{\cdot}I_2$ [90], prepared by ball milling elemental iodine respectively with aluminum and with blended aluminum/boron powders. Although these materials were shown to be effective in inactivating aerosolized microorganisms [13, 90, 91], elemental iodine used for their preparation is relatively unstable and quite volatile under ambient conditions with vapor pressure of 0.041 kPa at 298 K [92]. This work, therefore, is aimed to prepare stable aluminum-based iodine-containing powders without use of elemental iodine as a starting material. In particular, iodoform, CHI_3, which is a more stable iodine carrier with vapor pressure of 0.005 kPa at 298 K [93], is explored. In addition to iodine, iodoform contains carbon and hydrogen, which are both known to be effective fuels and may result in an improvement of energetic characteristics of the mechanically alloyed powders.

Iodoform is widely used in medicine as an antiseptic and antimicrobial agent. It is much less volatile and more stable at ambient conditions compared to elemental iodine. The sublimation of iodoform begins around 80 °C and the melting is reported to occur around 120 °C [94]. When exposed to higher temperatures, iodoform starts to decompose around 160 °C, and major decomposition products include double-ionized iodine, iodine radical, and oxidation products of CHI_3 or iodine (e.g. HIO_3) [94]. While Al-based composites using elemental iodine are best milled at liquid nitrogen temperature, so that iodine is solidified, this requirement may be less stringent for iodoform, and both room

temperature and cryo-milling options can be explored for preparation of aluminum-based, iodine containing powders.

2.3 Experimental

The starting material were aluminum powder, -325 mesh size (<45 μm), 99.5% pure, from Atlantic Equipment Engineers, and iodoform powder, purchased from Alfa Aesar, 99% pure.

2.3.1 Ball-Milling Equipment and Parameters

Two different ball-mills were used to prepare mechanically alloyed powders at room temperature and at the temperature of liquid nitrogen (-196 °C). A model 01HD attritor mill by Union Process with the vial cooled by liquid nitrogen, and a shaker mill (SPEX Certiprep, 8000 series) with the vial cooled by an air jet at room temperature were used to prepare composite samples A and B, respectively. The starting materials, Al and CHI_3, were mixed to obtain a material composition with a mass ratio of Al/I = 80/20 for both samples, to be directly comparable with the $Al{\cdot}I_2$ composites investigated earlier [13]. Both materials were milled using 3/8”-diameter case-hardened carbon steel balls.

Sample A prepared by cryogenic milling produced a 50-g batch of powder. It was prepared in a 750 mL stationary stainless steel milling vial placed inside an insulated cooling jacket, through which liquid nitrogen was circulated at approximately 2 CFM (0.94 L/s). The ball to powder mass ratio was 36. An impeller rotated at 400 rpm and the milling time was 24 hours. Additional information regarding the cryogenic milling process in the attritor mill is provided elsewhere [16].

Sample B synthesized by milling at room temperature was prepared in two 50-mL flat-ended steel vials simultaneously. Each vial contained 5 g of powder. Ball to powder mass ratio was 10. The vials were loaded and sealed inside an argon-filled glovebox. The milling time was 8 hours.

Milling parameters are summarized in Table 2.1.

Table 2.1 Milling Parameters Used for Preparing Samples A and B

Sample ID	Milling Media	Milling Time (hrs)	Batch Size (g)	BPR	Milling Condition
A	Attritor Mill	24	50	36	cryogenic
B	Shaker Mill	8	5	10	ambient

2.3.2 Characterization Techniques and Instrumentation

Back-scattered scanning electron microscopy (SEM) images were used to characterize the morphologies of both samples. Particle size distribution (PSD) of each sample was measured with low-angle laser light scattering using a Beckman-Coulter LS230 Particle Counter. A PANalytical Empyrean diffractometer was used for X-ray diffraction (XRD) to determine phase composition for each sample. The XRD powder diffractometer was operated at 45 kV and 40 mA using unfiltered Cu K_α radiation (λ=1.5438Å).

The stability of iodoform encapsulation into the Al-matrix and the release of iodine upon heating were investigated using thermo-gravimetric (TG) analysis. Under argon gas, TG traces for iodine release were obtained using a Netzsch Simultaneous Thermal Analyzer STA409 PG with a TG sample holder. A small piece of zirconium foil was placed in the furnace below the sample holder as an oxygen getter to eliminate any oxidation involving residual or trace oxygen. The furnace was purged with argon at 50 mL/min. The sample mass for each experiment varied in the range of 19 – 23 mg.

Oxidation of the prepared powders was studied using a TA Instruments model Q5000IR thermo-gravimetric analyzer. The powder was loaded into an alumina crucible with a sample mass of 2 – 4 mg. The balance was purged with argon at 10 mL/min and the furnace was purged with oxygen at 25 mL/min.

Ignition of the milled powder was characterized in air using a heated filament experiment described in detail elsewhere [95, 96]. A slurry with milled material and hexane was made to prepare a thin, 1-cm long coating on a 4.5 cm long, 0.5 mm diameter nickel-chromium alloy heating wire. The coated wire was heated by a DC current. Varied applied voltage and adjustable resistors connected in series with the wire were used to vary the heating rates in the range of 1000 – 10,000 K/s. The temperature of the filament was measured using a high-speed infrared pyrometer (DP1581 by Omega Engineering, Inc.) focused on an uncoated filament surface adjacent to the powder coating. The emission from the powder coating was visualized using a high speed video camera (MotionPro 500 by Redlake), operated at 500 fps. Prior to ignition, the coating surface was darker than that of the heated filament. The ignition instant was registered when the powder became brighter than the heated filament.

Combustion studies were conducted using a constant volume explosion (CVE) experiment [2, 70]. A spherical vessel of 9.2 L was used. The vessel was initially evacuated and the aerosolized powder was introduced into the vessel using an air blast delivered from a pressurized reservoir. The pre-ignition pressure in the vessel was close to 1 atm. After a 0.3-s delay necessary to minimize the turbulence, the powder cloud was ignited by an electrically heated tungsten wire placed at the center of the vessel. The pressure inside the vessel was recorded as function of time using a pressure transducer by

Schaevitz Sensors. The ratio of the maximum pressure to the initial pressure, P_{max}/P_{ini}, and maximum rate of pressure rise, $(dP/dt)_{max}$, were identified to characterize the energy released during the experiment and the rate of combustion, respectively. The CVE experiment was conducted with a fuel-rich system at a constant powder load of 4.65 g of the composite Al·CHI_3 powder. Assuming that the only combustion products are Al_2O_3, I_2O_5, CO_2, and H_2O, this powder load corresponds to an equivalence ratio of about 1.45. Present results can be directly compared to earlier experiments using the same experimental setup and pure aluminum powders, for which the same mass load was used to achieve reproducible ignition [12].

2.4 Results

2.4.1 Particle Sizes, Morphology, and Stability

After milling, both samples were recovered under argon; portions of the powders were loaded in clear glass bottles and stored under ambient condition. The glass bottles were closed but not sealed; thus, the powder was slowly exposed to air as well as the humidity present in the air-conditioned laboratory air. A noticeable difference in color due to aging was seen in sample B within two weeks of storage. Originally gray colored sample B changed to yellowish-gray, indicating release of iodine and its presence on the surface of the powder. The remainder of sample B that was stored under argon did not show any discoloration. No discoloration was observed for sample A stored in room air. These initial observations show that the cryogenic milling conditions help stabilize the iodoform in the Al-matrix.

SEM images of the samples A and B (cf. Table 2.1) are shown in Figure 2.1. The milled powders contain equiaxial particles with many fines (particles less than 10 μm.) Qualitatively, it appears that sample B includes more coarse particles compared to sample A. The images were produced using backscattered electrons; thus, they were sensitive to the phase contrast between elements with different atomic weights. For both samples, particle surfaces appear to be homogeneous and phase contrast is not detectable despite a large difference in the atomic weight of iodine and aluminum, which was expected to result in substantially brighter surfaces rich with iodoform. The uniform surface brightness indicates a homogeneous distribution of iodoform in the prepared composite powders.

The particle size distribution (PSD) and respective volume mean particle sizes for both samples A and B are presented in Figure 2.2. The average particle sizes are 14.1 μm and 26.0 μm for samples A and B, respectively. It is observed, therefore, that the milling at cryogenic temperatures (sample A) helps achieving finer particle sizes. It appears that for both samples the size distributions are bimodal; for sample A the second peak is relatively well resolved whereas for sample B it appears as a shoulder at the coarse-particle side of the distribution curve.

The XRD patterns for both samples are shown in Figure 2.3, where all the observed intensity peaks represent pure aluminum. There are no clear differences between the XRD patterns for both samples.

Surface area of sample A was measured to be 4.50 m^2/g, using Brunauer, Emmett and Teller (BET) method with MONOSORB® surface area analyzer manufactured by Quantachrome Corp. The high surface area may be the result of particles having well

developed rugged surface with small crevices observed from the image in Figure 2.1. The measurements were not performed for sample B which was difficult to handle in open air.

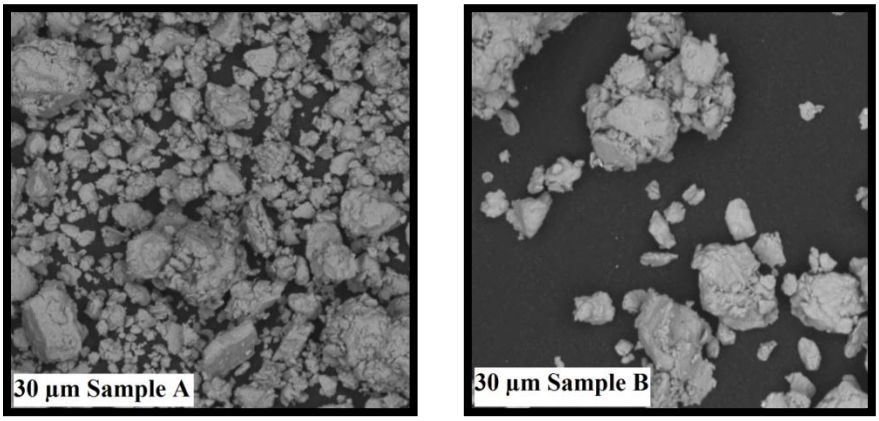

Figure 2.1 SEM images of sample A and sample B.

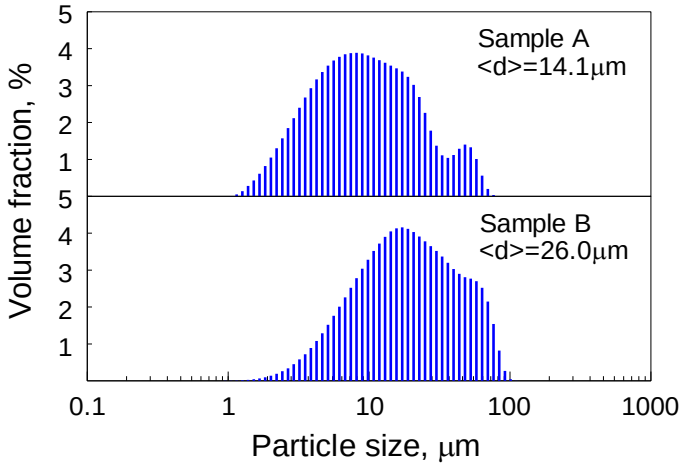

Figure 2.2 Particle size distribution of milled sample A and sample B.

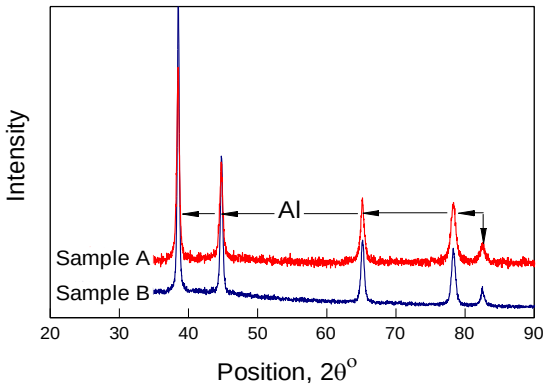

Figure 2.3 XRD patterns of sample A and sample B.

2.4.2 Iodine Release

For sample A, heating rates were varied from 2 to 20 K/min and experiments were carried out to the maximum temperature of 1400 °C. Derivatives of the TG traces, dm/dT, were used to identify individual stages of iodine release occurring during the temperature ramp. Both TG traces and their derivatives are shown in Figure 2.4. For reference, a single TG trace recorded at 10 K/min is also shown for $Al{\cdot}I_2$ [12]. Qualitatively, iodine release for the prepared Al-iodoform powder is similar to that observed for $Al{\cdot}I_2$.

The minima of the derivatives of TG traces show peaks in the rates of mass loss. There were four distinguishable peaks, and, respectively, four iodine release stages could be identified for sample A at heating rates of 10 K/min and above. The derivative peaks for stages I, II and IV show a shift towards higher temperatures with increasing heating rates, while the peak for stage III remains at an effectively constant temperature. At heating rates of 2 and 5 K/min, stages III and IV overlap, and only at higher heating rates does the peak for stage IV shift sufficiently to distinguish it from the stage III peak.

For sample B, because of its poor stability, a TG trace was recorded only at one heating rate of 20 K/min, as illustrated in Figure 2.5. Based on the TG derivative trace, two iodine release stages could be distinguished.

The iodine release stages for samples A and B could be compared to each other semi-quantitatively considering TG traces recorded at 20 K/min for both samples. This comparison is presented Table 2.2. Note that stages I and II are not the same for samples A and B, based on their respective temperature ranges. Stage II for sample B can roughly be related to stages III and IV for sample A.

For sample A, the iodine release at low-temperature stages I and II is quite small. Most of iodine is released in the vicinity of the aluminum melting point. Conversely, sample B shows a significant amount of sample mass loss (14.7%) during its low-temperature stage I.

These results show that the iodoform is much better stabilized inside the Al-matrix for sample A compared to sample B. This is consistent with the qualitative observation of discoloration/aging for sample B.

Because of poor stability of sample B, it was not characterized further.

Table 2.2 Iodine Release Stages at 20 K/min for Sample A and B

Sample ID		stage I	stage II	stage III	stage IV
A	Temp Range (°C)	104 - 301	407 – 513	543 - 693	693 – 786
	Δ Total Mass (%)	-2.4	-5.4	-12.1	-18.1
B	Temp Range (°C)	80 - 456	566 – 781		
	Δ Total Mass (%)	-14.7	-20.1		

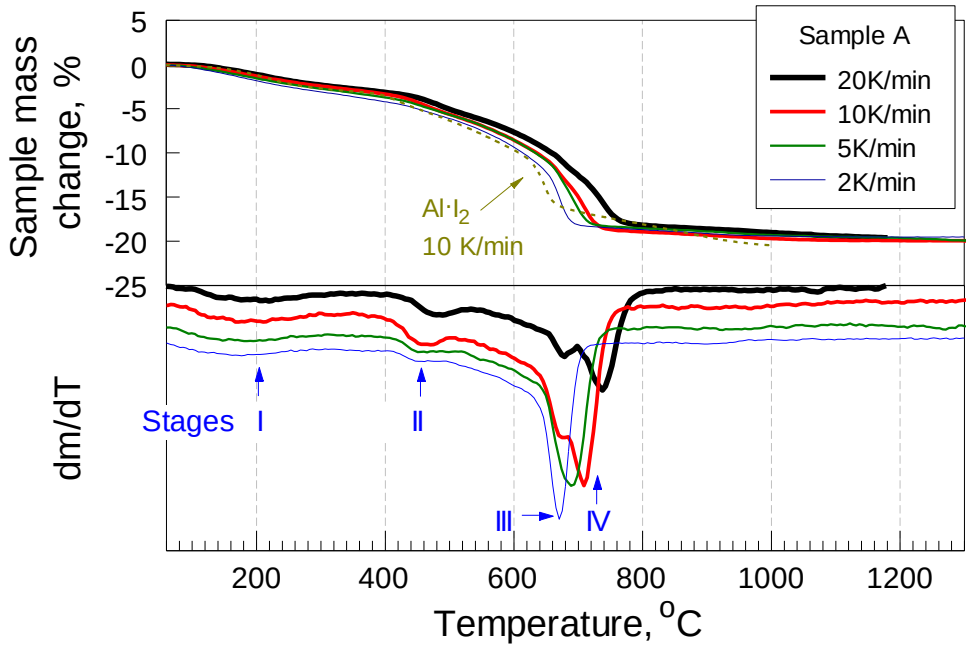

Figure 2.4 Mass change and derivative traces for sample A in heated in argon at various heating rates.

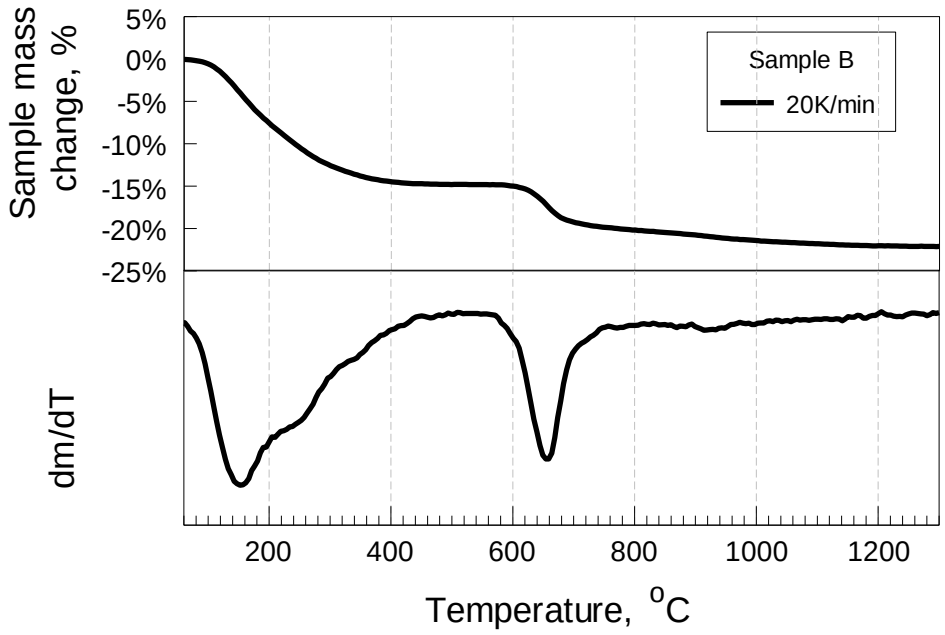

Figure 2.5 Mass change and derivative traces for sample B heated in argon at 20 K/min.

2.4.3 Oxidation

The oxidation of sample A was studied using heating rates from 2 to 20 K/min and the results are presented in Figure 2.6. Once again, for reference, a TG trace for oxidation of $Al{\cdot}I_2$ heated at 10 K/min is shown [12]. Qualitatively, oxidation behavior of sample A is similar to that of $Al{\cdot}I_2$. However, sample A oxidizes somewhat faster than $Al{\cdot}I_2$; also, a small stepwise mass increase is clearly observed for sample A when Al melts while it is less noticeable for $Al{\cdot}I_2$.

The TG traces for the Al-iodoform composite (sample A) show initial mass loss at low temperatures corresponding to release of iodine before two sharp oxidation steps are observed. As expected for thermally activated processes, higher heating rates result in a shift of the oxidation steps to higher temperatures.

The magnitude of the first oxidation step appears to be smaller for lower heating rates, compared to the higher heating rate experiments. The overall mass gain (and thus,

the oxidation degree) remains quite consistent when the material is heated to 1000 °C at different heating rates.

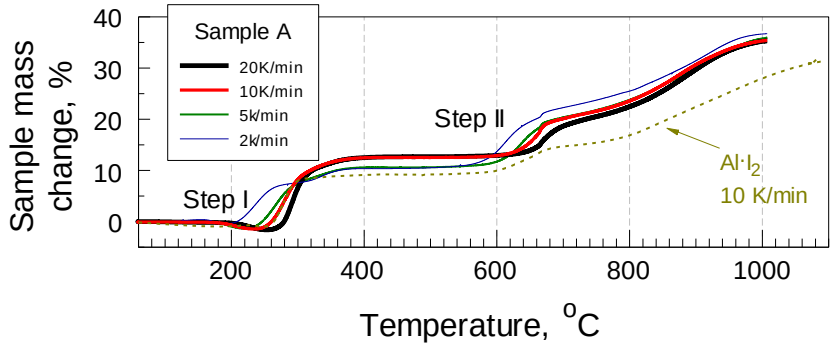

Figure 2.6 Oxidation of sample A at various heating rates.

2.4.4 Ignition

Figure 2.7 shows the measured ignition temperatures for sample A as a function of the heating rate. The data are scattered in a relatively narrow range of temperatures. A very weak trend of increasing temperatures at greater heating rates may be observed.

For comparison, ignition temperatures of Al·I_2 powder are also shown in Figure 2.7. It is apparent that Al-iodoform ignites at substantially lower temperatures than Al·I_2.

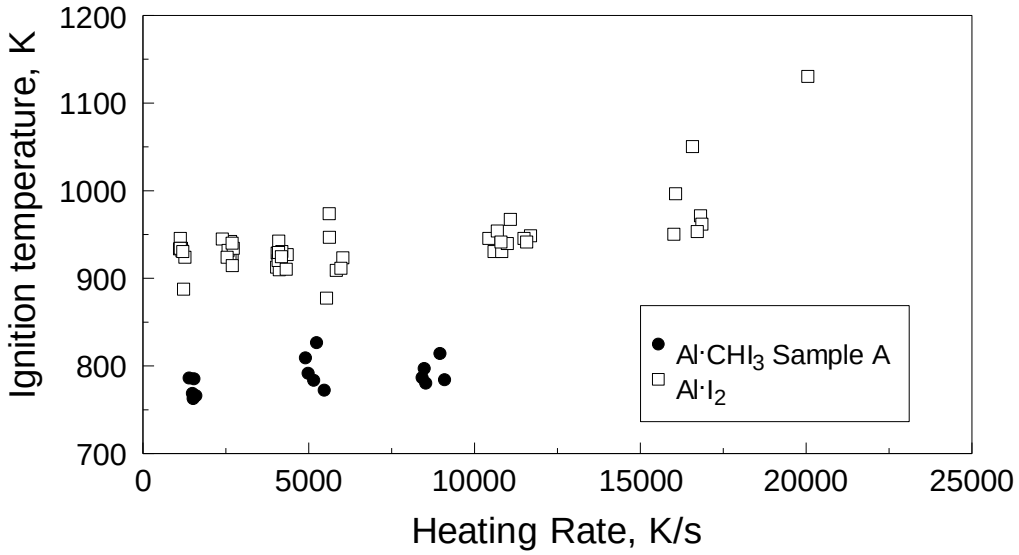

Figure 2.7 Ignition temperature of sample A and Al·I_2 composite [12] at different heating rates in air.

2.4.5 Reaction Kinetics

Temperatures marking positions of individual stages of iodine release (minima in the TG derivative traces), oxidation steps, and ignition temperatures are shown in a Kissinger plot [97] in Figure 2.8. The vertical axis shows $\ln(T^2/\beta)$, where β is the heating rate and T is the specific event temperature; the horizontal axis is the reciprocal temperature, 1/T. Iodine release stages I and II do not correlate with the first oxidation step. In contrast, the iodine release stages III and IV correlate with the second oxidation step occurring near the Al melting point.

Comparing events observed in low-heating rate TG experiments with ignition, it becomes apparent that ignition is well correlated with the iodine release stage II. Extrapolation of the kinetic trend for the first oxidation step into high heating rates also points to the temperature range close to that observed for ignition; however, the effect of heating rate on oxidation during stage I appears to be noticeably stronger than that observed for ignition temperatures.

Activation energies, ΔE, of individual iodine release stages and oxidation steps are directly proportional to the slopes of the linear-regression line that can be obtained from the Kissinger plot shown in Figure 2.8. No activation energy value is shown for the iodine release stage III, which appears to directly correlate with the Al melting. The activation energies are presented and compared to those for $Al{\cdot}I_2$ in Table 2.3. Although TG traces for both $Al{\cdot}CHI_3$ and $Al{\cdot}I_2$ look qualitatively similar to each other, a difference in activation energies for both individual iodine release stages and oxidation steps is observed. Activation energies of iodine release are generally lower for $Al{\cdot}CHI_3$. If the decomposition rate is limited by diffusion, then this lower activation barrier suggests lower diffusion

resistance in the case of the iodoform composite, possibly due to particle disintegration and therefore, increased creation of new surface during decomposition.

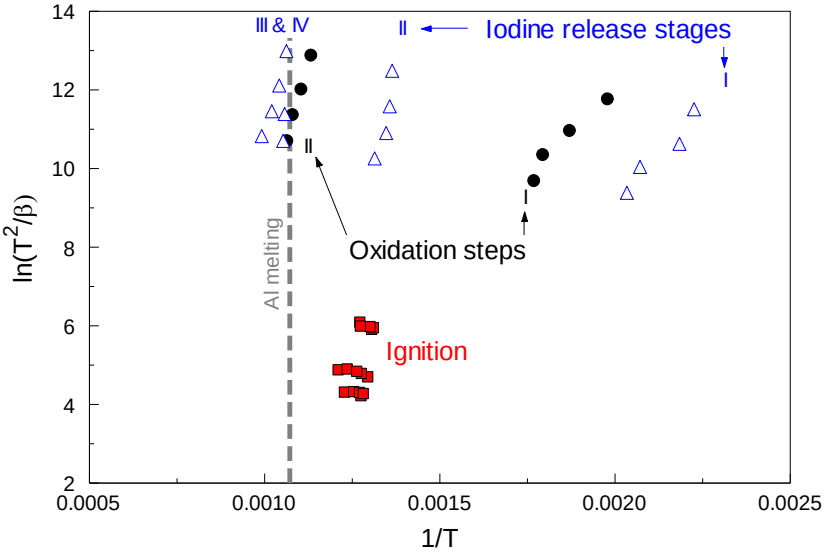

Figure 2.8 Kissinger plot of sample A with ignition temperatures (squares), iodine release stages (triangles), and oxidation steps (circles) measured at different heating rates. Al melting point (dashed line) is also shown.

For oxidation, the activation energies for the first step are similar for both Al·I_2 and Al·CHI_3. For the second step, activation energy for Al·CHI_3 is lower.

Table 2.3 Activation Energies, ΔE (kJ/mol), for Al·CHI_3 and Al·I_2 for Various Kinetic Mechanisms

	Iodine release			Oxidation	
	stage I	stage II[a]	stage IV[a]	step I	step II
Al·CHI_3	80±15	330±110	250±30	76±12	260±15
Al·I_2	130±10	530±100	530±90	65±6	380±39

[a] In reference [12], the iodine release stages corresponding to stages II and IV for Al·I_2 are referred to as "additional" and stage II, respectively.

2.4.6 Aerosol Combustion

Sample A ignited readily inside the explosion vessel; an example of characteristic pressure traces is shown in Figure 2.9. A summary of results is given in Figure 2.10. The results include the average ratios of maximum explosion pressure, P_{max}, to the initial pressure, P_{ini}

and the average maximum rate of pressure rise, $(dP/dt)_{max}$ for sample A compared to those for $Al{\cdot}I_2$ and several reference aluminum powders with volume-based average particle sizes varied from 9.0 to 15.1 μm. From earlier work [2, 70, 98], P_{max}/P_{ini} and $(dP/dt)_{max}$ are known to be proportional to the flame temperature and combustion rate, respectively. In comparison to the reference aluminum powder, sample A has higher values of both P_{max}/P_{ini} and $(dP/dt)_{max}$. Combustion characteristics for the prepared $Al{\cdot}CHI_3$ composite are similar to those observed for $Al{\cdot}I_2$ [12].

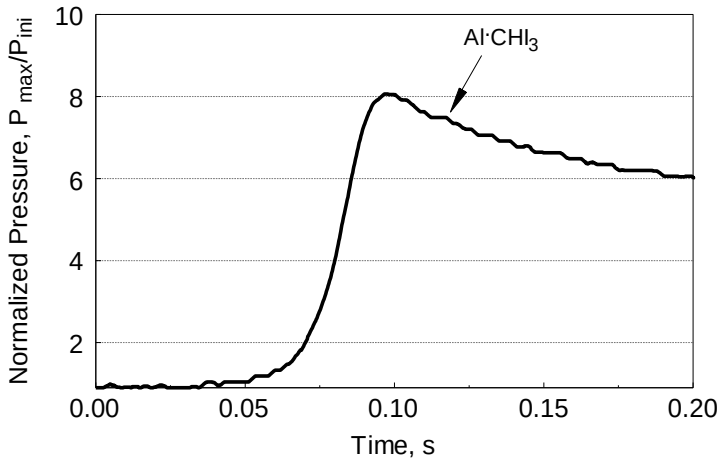

Figure 2.9 A characteristic pressure trace recorded in CVE experiments with the prepared $Al{\cdot}CHI_3$ composite powder burning in air (sample A).

Because the prepared powder is substantially different from pure aluminum, a more useful assessment of its combustion effectiveness compared to aluminum may be obtained considering results of respective thermodynamic equilibrium calculations. The calculations were performed using NASA CEA code[99]. Constant volume combustion was considered for two cases: aluminum/air and aluminum/iodoform/air. The calculations were performed for different powder mass loads and accounting for the experimental chamber volume. The maximum powder mass used in calculations corresponded to the experimental load. Smaller powder loads were considered to account for situations that are

likely to occur in experiments: some of the powder may not be effectively aerosolized and remain in the reservoir even after the air blast; in addition, some of the aerosolized powder could be deposited onto the explosion chamber walls before ignition. Previous experience suggests that the correction of the powder mass may be as large as 20% [100].

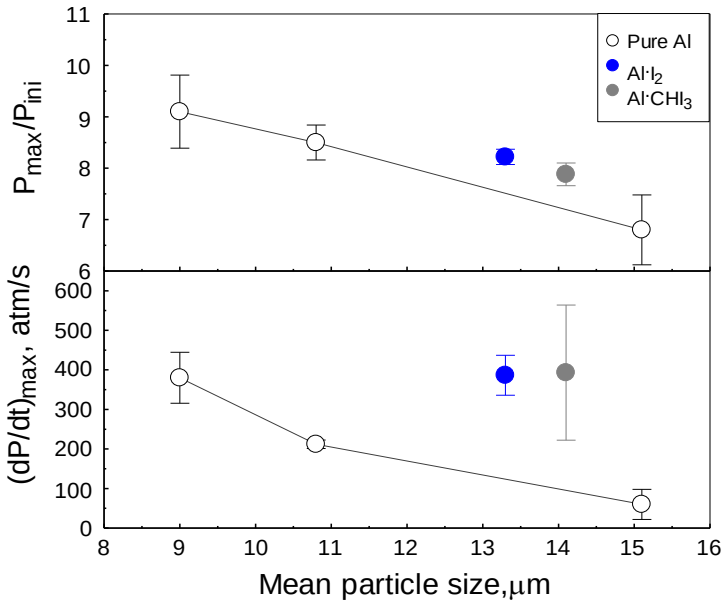

Figure 2.10 Comparison of CVE experiment results, maximum pressure and rate of pressure rise, for pure aluminum, $Al{\cdot}I_2$, and the prepared $Al{\cdot}CHI_3$ composite powder (sample A).

The results in terms of for P_{max}/P_{ini} and T_{max} are shown in Figure 2.11.

The flame temperature for the aluminum/air mixture peaks at about 3 g mass load. For the iodoform-containing mixture, the peak temperature is observed at a greater powder load, close to 3.75 g, whereas the mass of aluminum as a component in the aluminum-iodoform powder remains close to 3 g. The peak temperature for the iodoform-containing mixture is somewhat lower than for the pure aluminum combustion.

Generally, the calculated pressure ratios, P_{max}/P_{ini}, tend to increase with increasing powder mass for both fuels. The trend is stronger for the iodoform-containing mixture. The pressure is clearly affected by both calculated temperatures and product species and

for the experimental powder load, 4.65 g, the equilibrium pressure is expected to be higher for the iodoform-containing powder. However, this situation reverses for lower powder loads, which can be more relevant for the experimental conditions, when powder losses may occur during dispersion and on the vessel walls.

Because the range of powder mass loads shown in Figure 2.11 is likely greater than possible variation in the sample mass in experiments due to all possible losses, one observes that the range of pressure changes, is less than 5% for the iodoform-containing mixture and even narrower than that for the aluminum/air system. Thus, combustion efficiency of different mixtures can be relatively well assessed by direct comparison of their measured pressure ratios.

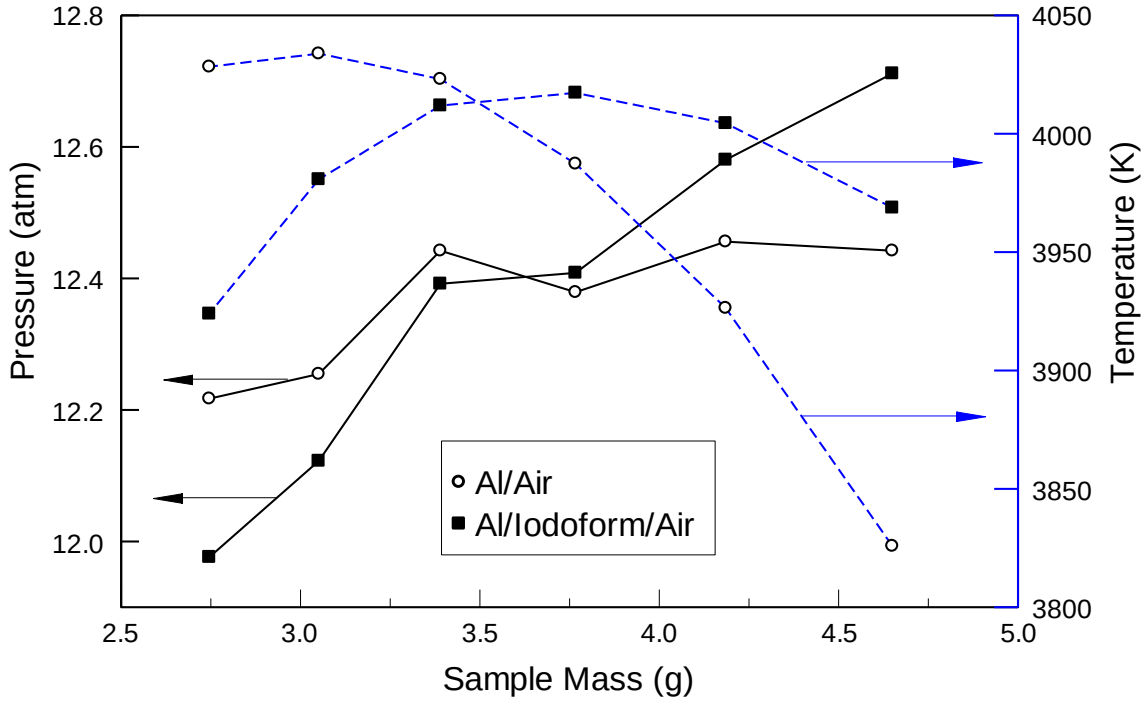

Figure 2.11 CEA pressure and temperature at various theoretical sample masses.

2.5 Discussion

2.5.1 Iodine Release, Oxidation and Ignition

Samples A and B, prepared using cryo-milling and room temperature milling, respectively, illustrate the importance of milling temperature for achieving a stable composite. Although iodoform itself is relatively stable at room temperature, the stability of the Al·CHI_3 composite is substantially improved by cryo-milling (cf. Figure 2.4 and Figure 2.5). A relative measure of material stability (see also APPENDIX A), *S*, introduced for Al·I_2 composite[12] is used to compare the stability of Al·CHI_3 to Al·I_2 and Al·B·I_2. The parameter *S* was defined as the percentage of weight loss at temperatures exceeding 400 °C (673 K). The values of S are 83% for both Al·CHI_3 (sample A) and Al·I_2 whereas for Al·B·I_2, it is 85%. Thus, both Al·CHI_3 and Al·I_2 prepared by cryo-milling are similar in stability to each other, and slightly less stable compared to Al·B·I_2.

A direct comparison of TG traces for sample A and Al·I_2 shows the iodine release stages for the cryo-milling prepared Al·CHI_3 are similar to those for Al·I_2. Individual iodine release stages observed in the TG traces can be attributed to different ways the iodoform may be bound inside the Al-matrix. Similar to that of Al·I_2 composite[50], the loosely bound iodoform is released from the Al-matrix during stages I and II, corresponding to the decomposition of iodoform and dissociation of AlI_3, respectively. Although pure AlI_3 boils off completely around 400 °C,[16] the decomposition TG trace of sample A at the heating rate of 20 K/min shows the iodine release stage II spanning over the temperature range of 407 – 513 °C. Due to the encapsulation of AlI_3 in the Al matrix, its effective boiling point may be shifting to higher temperatures because most of the AlI_3 molecules may not be readily available at the sample surface to be removed. In stages III

and IV, a significant amount of iodine is released around the aluminum melting point, 660 °C, indicating that iodine was confined within the aluminum crystal lattice or its defects, which are destroyed during melting. A comparison of TG traces for sample A and for $Al{\cdot}I_2$ shows that the mass of iodine stabilized in the Al-matrix is the same for both composites.

Qualitatively, both iodine release and oxidation processes are similar to those for $Al{\cdot}I_2$; however, there are differences in specific details and apparent activation energies for individual iodine release stages and oxidation steps. The lower activation energies for all iodine release stages suggest an easier release of iodine upon heating, when it is introduced by milling aluminum with iodoform. At the same time, the main sequence identified in reference [12] and including sequential release of iodine from phases behaving as elemental iodine and as decomposing AlI_3 remains valid.

The oxidation steps for $Al{\cdot}I_2$ and $Al{\cdot}CHI_3$ are very similar to each other. However, the activation energy for the second oxidations step is noticeably lower for $Al{\cdot}CHI_3$. This might be explained by release of hydrocarbon species, resulting in a stronger disruption of the powder particle surface and thus assisting in formation of fresh surface prone to rapid oxidation.

It is important to realize that because of the difference in activation energies of different oxidation steps and iodine release stages, the order of events might be reversed at high heating rates, typical of ignition. At low heating rates, oxidation step 1 for $Al{\cdot}CHI_3$ occurs before the iodine release stage II. At high heating rates, this could no longer be the case. A linear extrapolation of the kinetic trends (Figure 2.8) over a broad range of heating rates is likely invalid, and a more detailed modeling, taking into account heat transfer

processes specific for each ignition configuration, is necessary to assign which of the two processes is more likely triggering ignition of the prepared $Al{\cdot}CHI_3$ powders.

In the case of $Al{\cdot}I_2$ composite, the ignition occurs at the aluminum melting point where iodine release is substantial. Although the iodine release near the aluminum melting point remains substantial for the prepared $Al{\cdot}CHI_3$ powders, they ignite at much lower temperatures. It is suggested that the ignition temperature is reduced because of the presence of hydrogen and carbon in the prepared $Al{\cdot}CHI_3$ composite powder. At the iodine release stage II for $Al{\cdot}CHI_3$, it is possible for volatile species other than iodine, e.g., hydrocarbon molecules, to escape and oxidize, if the heating occurs in an oxidizing atmosphere. The ignition may thus be accelerated by an added heat release in the direct vicinity of the powder surface. The oxidation of the released hydrocarbon would also occur in the TG experiments; however, the process would unlikely affect the sample mass measurement – and thus, the recorded TG traces. The oxidation products are gases, e.g. CO_2, CO, OH and/or H_2O, which would be vented away from the sample and thus would not affect the heterogeneous surface reactions on its surface.

2.5.2 Combustion

The combustion dynamics of $Al{\cdot}CHI_3$ is very similar to that of $Al{\cdot}I_2$ [12], therefore, one would expect similar release of iodine-containing biocidal products during combustion. From the CVE experimental results shown in Figure 2.10, the $Al{\cdot}CHI_3$ composite is shown to be more energetic over comparable size pure Al powder in terms of both maximum pressure and rate of pressure rise. The improved combustion characteristics are attractive for practical applications in advanced energetics.

The overall combustion scenario of the prepared $Al{\cdot}CHI_3$ composite powder may be affected by both its ignition and combustion characteristics. In case of a powder dispersed in a fire ball generated by a high explosive, a reduced ignition temperature would imply that the prepared particles may ignite while being exposed only to the combustion products of the high explosive, well before they can be mixed with the surrounding environment. This may be advantageous for coupling their combustion energy to sustain the propagating shock wave. However, this will also mean that much of the halogenated combustion products will be released within the fire ball, where they will not effectively interact with any viable bio-aerosol (see APPENDIX B).

2.6 Conclusions

Cryo-milling is necessary to achieve a stable $Al{\cdot}CHI_3$ composite with the same mass of iodine stabilized as for $Al{\cdot}I_2$ into the Al-matrix. The addition of hydrocarbon e.g., C and H atoms, can alter the ignition and combustion of the $Al{\cdot}CHI_3$ composite. The iodoform is bound to the Al-matrix in three different forms and during thermal decomposition, at least three different stages of iodine release are observed. The initial oxidation step occurs at a temperature higher than the first stage of iodine release; it does not correlate directly with any of the iodine release stages. The ignition of $Al{\cdot}CHI_3$ composite occurs at a lower temperature than that of $Al{\cdot}I_2$. Based on a Kissinger plot, the kinetics trends for both first oxidation step and second stage of iodine release can be extrapolated to high heating rate at the temperature range, at which ignition is observed. A relatively weak effect of heating rate on the ignition temperature suggests its better correlation with the stage II of iodine release. A relatively low ignition temperature may be associated with release and instant

oxidation of volatile species other than iodine, e.g., hydrocarbon molecules. The combustion dynamics of $Al{\cdot}CHI_3$ composite is similar to that of $Al{\cdot}I_2$ composite. Furthermore, the maximum pressure and pressure rise observed in the constant volume explosion show an improvement compared to the pure Al.

CHAPTER 3

ALUMINUM-BASED REACTIVE MATERIALS WITH INCREASED BIOCIDAL CONTENT

3.1 Abstract

$Al{\cdot}TiI_4$ and $Al{\cdot}NbCl_5$ reactive materials with and without surface modification were prepared using mechanical alloying at liquid nitrogen temperatures. These composites were specifically engineered to stabilize high concentrations of halogens (two to three times more than the previously prepared $Al{\cdot}I_2$, $Al{\cdot}B{\cdot}I_2$ and $Al{\cdot}CHI_3$) in the overall composition, capable of releasing halogenated products during ignition and combustion to inactivate bioaerosol. Fresh composites without surface modification were susceptible to rapid oxidation upon exposure to air. Coating surface with Teflon® allowed mitigating this effect, and further stabilizing the halogens in the Al-matrix. Stability of materials was studied using thermo-gravimetry, where the most stable material was Teflon®-coated powder of $Al{\cdot}NbCl_5$. This powder was characterized by electron microscopy and low-angle laser light scattering to determine particle size distribution. Additionally, powder aging effects were determined by x-ray diffraction. Mostly, all of the chlorine release from the fresh coated powder of $Al{\cdot}NbCl_5$ was observed above 400 °C. Although the samples aged in ambient air showed early release of chlorine under 400 °C, its ignition temperatures, determined from powders coated onto a metal filament heated electrically at $10^3 – 10^5$ K/min, were not altered when compared to freshly coated powder. The ignition temperatures of the prepared materials were noticeably lower than for the pure Al and comparable to the $Al{\cdot}I_2$ composite prepared using a similar cryo-milling approach. Particle

combustion tested inside the products of a hydrocarbon laminar flame, showed that the Teflon® coated powder of $Al{\cdot}NbCl_5$ burns longer than pure Al at the same particle size.

3.2 Introduction

Reactive materials with biocidal combustion products capable of inactivating aerosolized microorganisms have been developed recently [12, 13, 50, 51, 90, 101]. The focus was on additives to conventional energetic formulations involving halogens, known to have strong biocidal properties. Materials developed can be classified into three main groups: metal-based fuels, oxidizers, and thermites (metal fuel and oxidizer compositions) with at least one component producing biocidal combustion products. In addition to generating the desired combustion products, reactive material components must be stable and compatible with common binders to endure conventional processing routine. Furthermore, insensitivity to spark, impact, friction, and other common ignition stimuli is also desired for material handling.

Our work has focused on incorporating halogens or halogen containing compounds in aluminum. Powders containing up to 20 wt. % of iodine with compositions of $Al{\cdot}I_2$ [12], $Al{\cdot}B{\cdot}I_2$ [90], and $Al{\cdot}CHI_3$ [101] have been developed and tested. In this study, efforts are aimed at developing new metal-based components with substantially increased halogen content.

The main challenge is to stabilize the halogen in a reactive metal matrix, so that the material can be handled and formulated as a regular metal fuel, e.g., aluminum powder, commonly added in energetic formulations. The approach taken in this study is based on mechanical alloying (or ball milling) starting metal powder and a halogen-containing material to produce a stable composite powder. Previous work showed that cryo-milling

was necessary to stabilize iodine in aluminum matrix. Milling at room temperature could be used to stabilize iodine in a binary Al-B composite. However, the amount of iodine that could be stabilized could not exceed 20 wt. %. Thus, new material compositions need to be explored to produce materials with greater halogen concentrations.

3.3 Approach

To select most promising halogen-containing starting components, properties of different metal halides were surveyed ranking them based on the maximum enthalpy, ΔH, required to convert the halide into the most stable metal oxide and oxidized halogen. This enthalpy is taken per mole of halogen. The results are shown in Figure 3.1 where the estimated reaction enthalpy is plotted vs. weight % of the respective halide that should be added to aluminum in order to prepare a reactive material with 40 wt. % of halogen. The 40 wt. % benchmark doubling the previously achieved content of iodine in the Al-based powders ($Al{\cdot}I_2$, $Al{\cdot}B{\cdot}I_2$, and $Al{\cdot}CHI_3$) serves as a target halogen content for the new reactive materials. In Figure 3.1, the most desired compositions would have the greatest negative reaction enthalpy and the lowest wt. % of metal halide (allowing their encapsulation into aluminum matrix); thus, they would be represented by symbols located at the lower left portions of the plots, shown separately for chlorine, bromine and iodine. It is clear that the iodine-containing materials are most favorable energetically. Among all materials considered, only a few could be selected taking into account their toxicity, stability, and cost. In particular, 44 wt. % of TiI_4, equaling to two times more iodine compared to previous materials, was selected for initial experiments with Al. In addition, a chlorine-containing starting material with 26 wt. % of $NbCl_5$, equaling to three times more halogens per mole basis compared to previous materials, was selected to evaluate the effect

of chlorine as a biocidal fuel additive when prepared as composite with Al. Due to the interest in stabilizing these metal-halides in the aluminum matrix, composite particles may need to be coated with Teflon®.

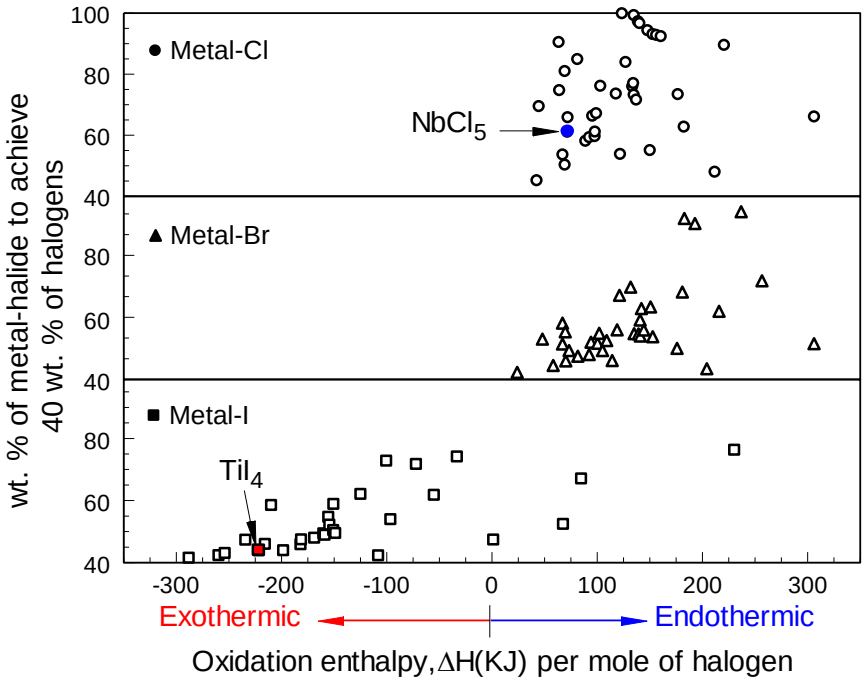

Figure 3.1 Survey of metal-halide oxidation enthalpies.

3.4 Experimental

Cryogenic milling technique, at the temperature of liquid nitrogen (-196 °C), was used to prepare mechanically alloyed powders of Al·TiI_4 and Al·$NbCl_5$. A model 01HD attritor mill by Union process with the vial cooled by liquid nitrogen, was used to prepare the composites. Materials were milled using 3/8"-diameter case-hardened carbon steel balls. Samples prepared by cryogenic milling produced a 50-g batch of powder. It was prepared in a 750 mL stationary stainless steel milling vial placed inside an insulated cooling jacket, through which liquid nitrogen was circulated at approximately 2 CFM (0.94 L/s). The ball to powder mass ratio was 36. An impeller rotated at 400 rpm for a milling time of 24 hours.

The starting materials were mixed to obtain a material composition with two times (44 wt. % TiI_4 with Al) more iodine for $Al{\cdot}TiI_4$ and with three times (26 wt. % of $NbCl_5$ with Al) more chlorine halogens for $Al{\cdot}NbCl_5$, compared to previous $Al{\cdot}I_2$ [12], $Al{\cdot}B{\cdot}I_2$ [90], and $Al{\cdot}CHI_3$ [101] composites. Additionally, using a shaker mill (SPEX Certiprep, 8000 series) with the vial cooled by an air jet at room temperature, the powders of $Al{\cdot}TiI_4$ and $Al{\cdot}NbCl_5$ were coated with 5 wt. % of Teflon®.

Back-scattered scanning electron microscopy (SEM) images were used to characterize the powder morphologies, shapes and sizes. Particle size distribution (PSD) was measured with low-angle laser light scattering using a Beckman-Coulter LS230 Particle Counter. A PANalytical Empyrean diffractometer was used for X-ray diffraction (XRD) to determine phase composition for each sample. The XRD powder diffractometer was operated at 45 kV and 40 mA using unfiltered Cu K_α radiation (λ=1.5438Å).

The stability of halogens encapsulation into the Al-matrix and the release of these halogens upon heating were investigated using thermo-gravimetric (TG) analysis. The samples were heated under argon to 1000 ºC using a TA Instruments model Q5000IR thermo-gravimetric analyzer. Sample masses ranging from 10 to 25 mg were loaded into the instrument in an alumina crucible. Both, the balance and furnace were purged with 100 mL/min of argon at 30 ºC for at least 500 min before starting the experiment. High gas flow rates and long flushing times were used to purge oxygen from the furnace, since it cannot be evacuated. During the actual measurements, gas flow rates were reduced to 20 and 50 mL/min for the balance and furnace, respectively. Mass loss as a function of temperature was determined at a fixed heating rate of 10 K/min for all powders.

Ignition of the most stable powders was characterized in air using a heated filament experiment described in detail elsewhere [95, 96]. A slurry with milled material and hexane was made to prepare a thin, 1-cm long coating on a 4.5 cm long, 0.5 mm diameter nickel-chromium alloy heating wire. The coated wire was heated by a DC current. Varied applied voltage and adjustable resistors connected in series with the wire were used to vary the heating rates in the range of 10^3 – 10^5 K/s. The temperature of the filament was measured using a high-speed infrared pyrometer (DP1581 by Omega Engineering, Inc.) focused on an uncoated filament surface adjacent to the powder coating. The emission from the powder coating was visualized using a high speed video camera (MotionPro 500 by Redlake), operated at 500 fps. Prior to ignition, the coating surface was darker than that of the heated filament. The ignition instant was registered when the powder became brighter than the heated filament.

Particle combustion of the most stable powders was conducted in an oxidizer comprising combustion products of hydrocarbon fuel, which is an environment similar to that encountered by metal particles burning in propellants and explosives. A detailed description of the pre-mixed air-acetylene laminar flame and the experimental set-up describing the particle feeding are described elsewhere [102-104]. Briefly, the powders were introduced into the premixed air-acetylene laminar flame using a custom screw feeder, where a thin layer of powder was deposited into threads of a stainless steel, ¾”-diameter screw with 16 threads per inch. The screw placed inside a cylindrical enclosure was attached to a DC-motor, allowing it to rotate in counter clock-wise direction. As the screw rotated, particles were fed into the hydrocarbon laminar flame by a focused nitrogen jet blowing across a tread of the screw, which was coated with the powder. The

powder feed rate was determined by the rotation speed of the screw. The particles ignited and combusted inside the hot flame products, where the optical emission from the burning particles were recorded using an array of three filtered photomultiplier tubes (PMTs). Assuming that larger particles burn longer, the measured statistical distribution of particle burn times was correlated with the PSD measured with low-angle laser light scattering.

3.5 Results and Discussion

3.5.1 Iodine Release and Stability of Al·TiI_4

The measured iodine release as a function of temperature for all of the powders prepared using Al·TiI_4 are presented in Figure 3.2. It was observed that the uncoated powder was hard to handle because it was pyrophoric and reacted immediately when exposed to air. In Figure 3.2, this oxidation effect is observed, causing the initial mass increase at the beginning of the TG trace, where the temperature was held constant while the TG was purged (see Section 3.4). The Teflon® coated samples do not show this behavior in the TG trace.

A relative measure of material stability (see also APPENDIX A), *S*, introduced for Al·I_2 composite [12] is used to compare the stability of all prepared powders. The parameter *S* was defined as the percentage of weight loss at temperatures exceeding 400 °C (673 K). The values of *S* are 34% and 68% for uncoated and coated powders of Al·TiI_4, respectively. Although, coating the powders helped to mitigate the rapid oxidation and improve the stability, it is still not comparable to the previously prepared powders of Al·I_2, Al·B·I_2, and Al·CHI_3. Due to instability, powders of Al·TiI_4 were not further characterized.

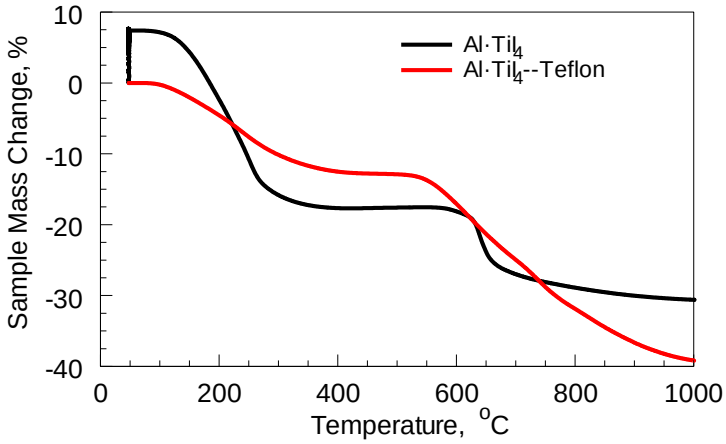

Figure 3.2 TG traces of uncoated and coated powders of Al·TiI_4.

3.5.2 Chlorine Release and Stability of Al·$NbCl_5$

In Figure 3.3, both uncoated and coated powders of Al·$NbCl_5$ were measured for the chlorine release as a function of temperature. In addition, same samples of both uncoated and coated powders of Al·$NbCl_5$ were aged in ambient air for two weeks and tested again for their chlorine release. Fresh uncoated powders were vulnerable to air oxidation, observed from the initial mass increase at the beginning of the TG trace in Figure 3.3(A). Similar to Al·TiI_4 powders, coated powders improved chlorine encapsulation and mitigated the rapid oxidation. These fresh powders showed that most of the chlorine was released at high temperatures after 400 °C with the value of stability, *S*, being 85% and 94% for uncoated and coated powders, respectively. The aged powders show that storage in ambient air caused part of the chlorine to be released early at low temperatures below 400 °C. The values of *S* were 48% and 64% for the aged uncoated and coated powders, respectively. From this analysis, it was evident that substantial amount of chlorine was released from all powders; but stability was compromised for powders stored in ambient air. The most stable powder of Al·$NbCl_5$, coated with Teflon®. It was used for further ignition and combustion experiments.

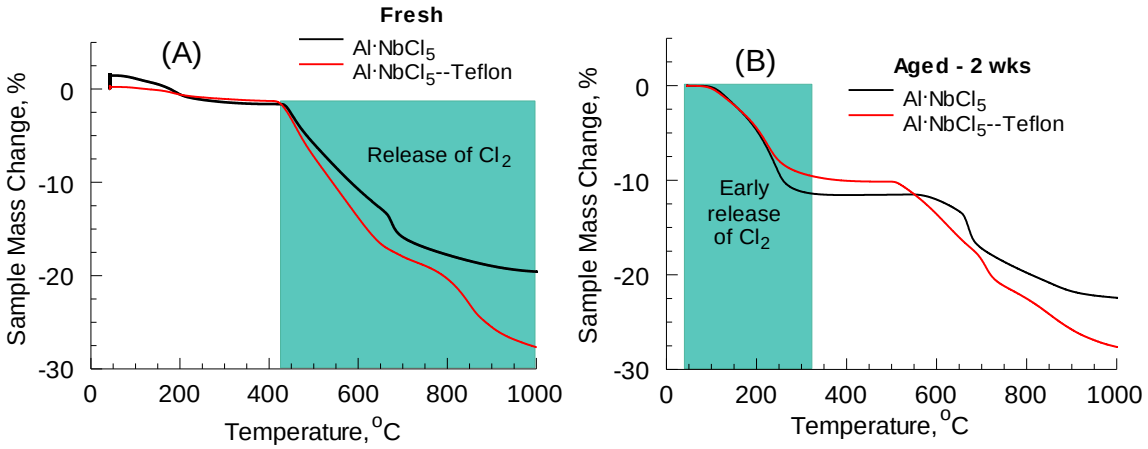

Figure 3.3 (A) TG traces of fresh uncoated and coated powder of Al·$NbCl_5$ and (B) 2 weeks aged uncoated and coated powder of Al·$NbCl_5$.

3.5.3 Particle Size, Morphology, and Phase Composition

SEM images of both uncoated and coated powders of Al·$NbCl_5$ are shown in Figure 3.4. Powders consist of equiaxial particles with many fines, (particles < 5 µm). These images produced using backscattered electrons are sensitive to the phase contrast between elements containing different atomic masses. Thus, niobium and chlorine should appear brighter than aluminum. However, the particle surfaces exhibit a rather uniform brightness, indicating that components are mixed on a scale finer than the resolution of the images. The coated powder (Figure 3.4(B)) surface looked smoother than the uncoated powder (Figure 3.4(A)), an indication that the coating was indeed applied.

Particle size distributions for coated powder of Al·$NbCl_5$ are shown in Figure 3.5. A narrow size distribution with a mean particle size of 6.7 µm is seen for this sample. The phase composition results from XRD are shown in Figure 3.6, where the freshly coated powder of Al·$NbCl_5$ shows mostly crystalline Al peaks. In contrast, the aged coated powder of Al·$NbCl_5$ shows both crystalline Al peaks and meta-stable oxide, $NbO_{1.64}$,

peaks. This result is consistent with the difference in the TG traces for fresh and aged coated powders.

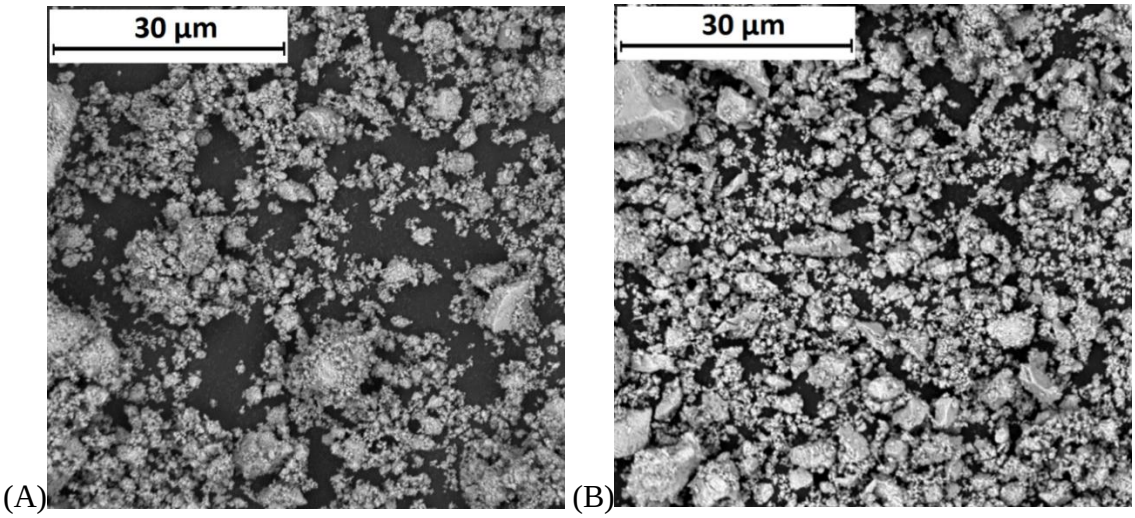

Figure 3.4 SEM images of fresh (A) uncoated and (B) coated powder of Al·$NbCl_5$.

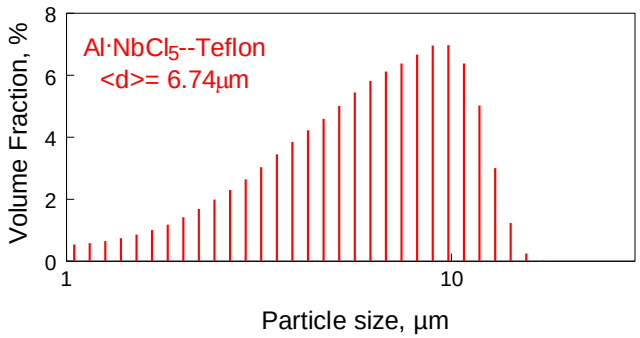

Figure 3.5 Particle size distribution of fresh coated powder of Al·$NbCl_5$.

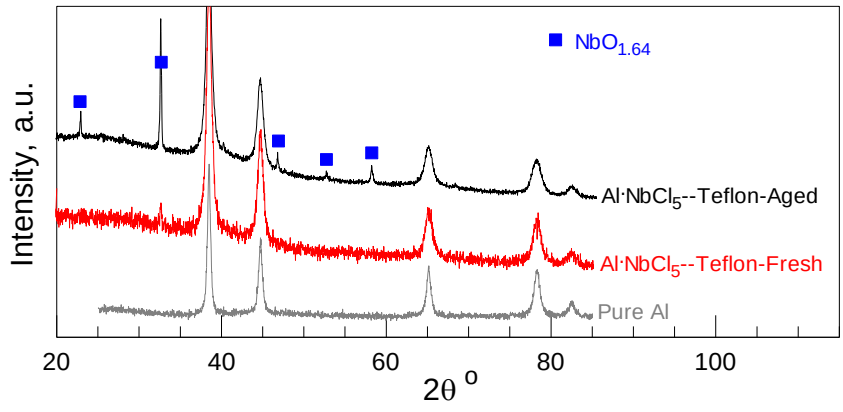

Figure 3.6 XRD pattern of fresh and aged coated powders of Al·$NbCl_5$.

3.5.4 Ignition

Ignition temperatures as a function of heating rate for both fresh and aged Teflon® coated powders of Al·$NbCl_5$ samples are shown in Figure 3.7, where both appear to ignite at similar temperatures. Although the data are scattered in a relatively narrow range of temperatures, a weak trend of increasing temperatures at greater heating rates may be observed. Additionally, these powders are also compared to several reference powders in Figure 3.7. It is seen that the ignition temperatures are close to that of the Al·I_2 powders.

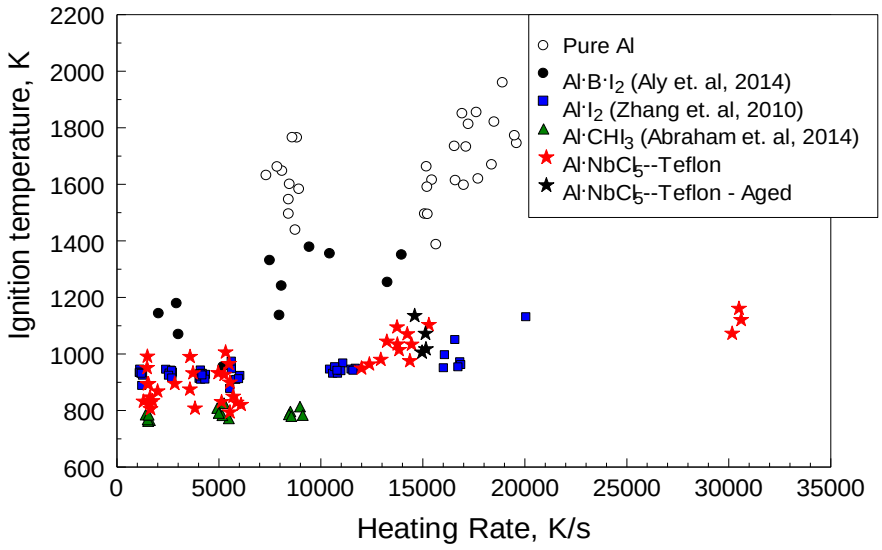

Figure 3.7 Ignition temperatures of both fresh and aged Teflon® coated powders of Al·$NbCl_5$ are compared to several reference powders.

3.5.5 Particle Combustion in a Laminar Flame

The emission pluses collected using the three filtered PMTs were processed using a rigorous data processing presented technique described elsewhere [104]. The distribution of burn times processed from the duration of the emission was correlated with the PSD, to show the average burn time for the respective particle size bin. This correlation of burn times as a function of particle size is presented for the Teflon® coated powder of Al·$NbCl_5$ in Figure 3.8, where it is compared to the pure Al. The results indicate that the Al·$NbCl_5$

powders burn slower than the pure Al. The images of the ignited particle streaks are also shown in Figure 3.8 for both Al·$NbCl_5$ and pure Al. In comparison, the burning particle streaks of Al·$NbCl_5$ are longer than for pure Al. Particles also tend to ignite lower in the flame, indicating a reduced ignition temperature. The effectiveness towards bioaerosol inactivation is presented in APPENDIX B.

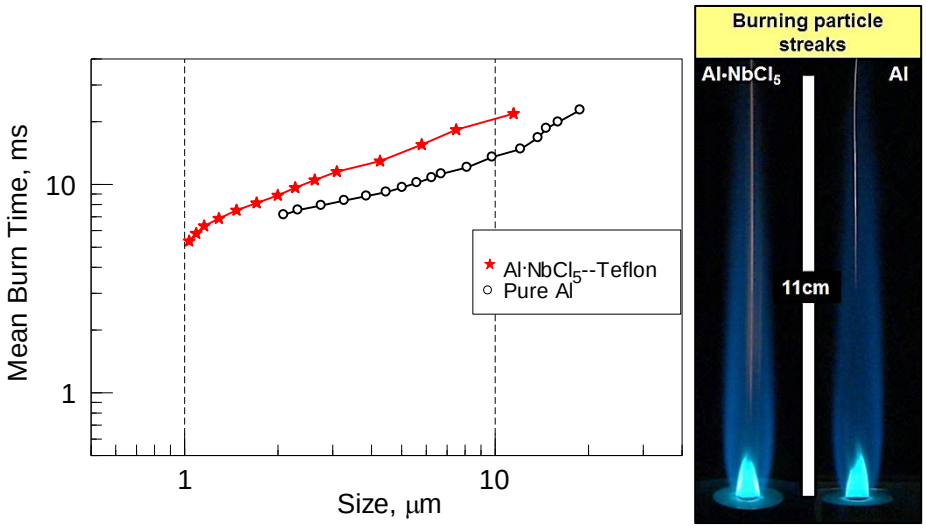

Figure 3.8 Combustion times as a function of particle size and burning particle streak of fresh coated powder of Al·$NbCl_5$ compared to pure Al.

3.6 Conclusions

Al-based composites with substantially increased concentration of halogens were prepared. It is not feasible to prepare stable composite materials containing 40 wt. % of iodine, doubling the halogen content using the same components as in the previously prepared materials. A more stable surface modified composite of Al·$NbCl_5$ was successfully prepared with tripling the amount of halogens with chlorine, compared to previous systems. From thermal analysis, it was observed that freshly Teflon® coated powder of Al·$NbCl_5$ was very stable, releasing most of the chlorine after 400 °C. Some aging effects were observed for the powders kept under ambient air; however, it did not

alter the ignition temperatures when compared to fresh powders. Ignition temperatures were comparable to those for $Al \cdot I_2$ and lower than for pure Al. Combustion times, however, were longer than for pure Al.

CHAPTER 4

EFFECT OF COMPOSITION ON PROPERTIES OF REACTIVE Al·B·I_2 POWDERS PREPARED BY MECHANICAL MILLING

4.1 Abstract

Metal-based fuels producing halogen-containing combustion products are being developed to enable rapid inactivation of harmful aerosolized spores and bacteria. Ternary reactive materials containing aluminum, boron, and iodine were prepared by mechanical milling with systematically varied Al:B ratio. The aluminum mass fraction varied from 0 to 70 %, and most materials included 20 wt. % of iodine. Prepared powders were inspected by electron microscopy; particle size distributions were measured using low angle laser light scattering. Stability of materials was studied using thermo-gravimetry and differential scanning calorimetry. As-prepared as well as pre-heated and quenched samples were analyzed using x-ray diffraction. Iodine was released upon heating in several stages. Low-temperature iodine release was relatively small. It overlapped with decomposition of $B(OH)_3$ releasing water. The most significant amounts of iodine were released when the samples were heated to 400 – 500 ºC, when AlB_2 formed. Both AlB_2 formation and iodine release were further accelerated by melting of aluminum. For the boron-rich samples, in which boron remained after all aluminum was used to form AlB_2, an additional, high-temperature iodine release stage was observed near 900 ºC. The results show that both boron and aluminum are capable of stabilizing substantial quantities of iodine in the metal matrix. The iodine is released at temperatures much greater than its boiling point. The mechanism by which iodine is retained in boron and aluminum remains unclear.

4.2 Introduction

Mechanical milling is a versatile and scalable technique used for processing and preparation of a wide range of advanced materials [53, 54]. These include metal-based mechanically alloyed or composite reactive powders used as fuel additives in propellants, explosives, and pyrotechnics [1-9]. Recently, mechanical milling was used to prepare metal-iodine composite reactive powders, which generate biocidal combustion products [12, 13, 50, 51]. Such materials are desired as components of advanced munitions aimed to eliminate or inactivate stockpiles of biological weapons [48, 49]. Upon ignition, iodinated gas species must be readily generated inactivating in situ aerosolized spores and bacteria and thus preventing their escape and contamination of the surrounding areas. Prior to ignition, iodine or other components capable of generating biocidal gases, typically containing a halogen, should be stabilized in the reactive material so that it can be stored and processed along with other components of energetic systems [55, 56]. The halogen-holding materials should burn with a strong heat release to warrant their use in energetic formulations. The capability to stabilize up to 20 wt. % of iodine in aluminum-based powders prepared by ball milling was shown in references [12, 13, 50, 51]; however, the mechanism by which the iodine was stabilized remains unclear. Materials containing comparable amounts of iodine were prepared using pure aluminum ball milled with iodine [105] and with iodoform [101], and using a blend of aluminum and boron (Al:B mass ratio = 6) milled with iodine [90]. All prepared composites were observed to be effective in producing biocidal combustion products and inactivating bio-agents [13, 90, 91], while exhibiting markedly different ignition and combustion characteristics. Specifically, particles of the $Al{\cdot}B{\cdot}I_2$ composite had the highest ignition

temperatures and longest combustion times, but their combustion products were somewhat more effective in inactivating bioaerosol [90]. Additionally, the prepared $Al{\cdot}B{\cdot}I_2$ was slightly more stable than other materials, i.e., iodine loss was observed upon heating to higher temperatures compared to other composites. Unlike $Al{\cdot}I_2$, requiring 24 hours of cryomilling, $Al{\cdot}B{\cdot}I_2$ was prepared at room temperature using relatively short milling times [90].

In this effort, both material stability and kinetics of iodine release are investigated as a function of Al:B ratio in the ternary, mechanically alloyed $Al{\cdot}B{\cdot}I_2$ composites containing 20 wt. % of iodine. It is of interest to clarify roles of both aluminum and boron in stabilizing iodine in the composite powders. A practical goal of this work is to develop a composition that is capable of simultaneously releasing both substantial energy and iodine upon ignition, while remaining stable at lower temperatures.

4.3 Materials and Experimental Methods

Starting materials used to prepare $Al{\cdot}B{\cdot}I_2$ composites were elemental aluminum powder, -325 mesh (<45 μm), 99.5% pure, from Atlantic Equipment Engineers, and amorphous boron powder (<1 μm), 93-96% pure, from SB Boron. In selected experiments, 99% pure, -325 mesh boron (mixture of amorphous and crystalline) from Alfa Aesar was used. Iodine chips (approximately 1–5 mm in size), 99% pure, from Sigma Aldrich were added to the initial powder load. In one experiment, the starting material mixture only consisted of amorphous boron and elemental iodine.

4.3.1 Ball-Milling Equipment and Parameters

All samples, except for one as discussed below, were prepared using a shaker mill (SPEX Certiprep, 8000 series) with two 50 mL flat-ended steel vials cooled by room-temperature air jets. All materials were milled with a fixed ball to powder mass ratio (BPR) of 10 using 3/8"-diameter case-hardened carbon steel balls. Each vial contained 5 g of powder. The vials were loaded and sealed inside an argon-filled glovebox. An exploratory milling study, in which multiple material and milling parameters were varied, was followed by further experiments with more promising material compositions. The Al:B mass ratios ranged from 0 to 7. Table 4.1 shows the compositions and milling times representing all prepared samples. The iodine content was fixed at 10 wt. % for samples 1 and 2. It was increased to 20 wt. % for samples 3A to 9.

Table 4.1 Composition of Al·B·I_2 Composites Prepared

Sample ID	Mass Ratio Al:B:I_2	Mass Ratio Al:B	Mole Ratio Al:B	Boron purity (%)	Milling Time (hrs)
1	0:90:10	0.00	0.00	95	4
2	10:80:10	0.13	0.05	95	4
3A	10:70:20	0.14	0.06	95	4
3B	10:70:20	0.14	0.06	95	8
4	15:65:20	0.23	0.09	95	4
5	30:50:20	0.60	0.24	95	4
6	40:40:20	1.00	0.40	95	4
7	50:30:20	1.67	0.67	95	4
8	60:20:20	3.00	1.20	95	4
9	70:10:20	7.00	2.80	95	4
10*	26:44:30	0.60	0.24	95	14
11	0:90:10	0.00	0.00	99	4
12	30:50:20	0.60	0.24	99	4
13	40:40:20	1.00	0.40	99	4

*Prepared in the attritor mill chilled by liquid nitrogen

Sample 10 with a higher iodine content of 30 wt. % was prepared using a model 01HD attritor mill by Union process with the vial cooled by liquid nitrogen at -196 °C. 50

g of powder was loaded into a 750 mL stationary stainless steel milling vial. The vial was placed inside an insulated cooling jacket, which was flushed with liquid nitrogen while gaseous nitrogen was flushed through the milling vial at about 2 CFM (0.94 L/s) to prevent oxidation during the milling process. Ball-milling was conducted for 14 hrs using 3/8"-diameter case-hardened carbon steel balls at a BPR of 36. Additional details regarding the preparation of mechanically alloyed powders at cryogenic milling conditions in the attritor mill are provided elsewhere [16].

Finally, as discussed below, samples 11-13 are analogs of samples 1, 5, and 6 prepared using higher purity boron as a starting material.

After milling, all samples were recovered and stored under argon in glass bottles in a glovebox.

4.3.2 Characterization Techniques and Instrumentation

The amount of iodine captured and retained inside the mechanically alloyed materials as a function of temperature was determined using thermo-gravimetric (TG) analysis. The samples were heated under argon to 1000 ºC using a TA Instruments model Q5000IR thermo-gravimetric analyzer. Sample masses ranging from 7 to 18 mg were loaded into the instrument in an alumina crucible. Both, the balance and furnace were purged with 100 mL/min of argon at 30 ºC for at least 500 min before starting the experiment. High gas flow rates and long flushing times were used to purge oxygen from the furnace, since it cannot be evacuated. During the actual measurements gas flow rates were reduced to 20 and 50 mL/min for the balance and furnace, respectively.

Mass loss as a function of temperature was determined at a fixed heating rate of 10 K/min for all powders. Powders exhibiting most of their mass loss at higher temperatures, and thus capable of better stabilizing iodine in the metal matrix, were characterized further.

Release of iodine upon heating was confirmed using mass spectrometry; however, quantitative mass-spectrometric measurements were difficult because iodine readily contaminated the instrument.

The morphologies of the stable powders were characterized using a Philips Phenom tabletop scanning electron microscope (SEM) with a back-scattered electron detector, showing the phase contrast between aluminum, boron, and iodine. Particle size distributions (PSD) were measured by low-angle laser light scattering using a Beckman-Coulter LS230 Particle Counter.

Phase compositions of the milled stable powders were determined by X-ray diffraction (XRD) using PANalytical Empyrean diffractometer operated at 45 kV and 40 mA using unfiltered Cu K_α radiation (λ=1.5438 Å). A spinning-stage sample holder was used for all XRD measurements at scan angles ranging from 5 to 90°. Furthermore, XRD measurements were performed for samples heated to and quenched at specific temperatures.

4.4 Results

TG traces for the heated samples showed mass loss stages occurring at different temperatures. A relative measure of the material stability, *S*, had been introduced previously for $Al{\cdot}I_2$ composite [105]. It was defined as the mass lost above 400 °C (673 K)

relative to the total mass loss starting at room temperature. For convenience, this quantitative measure is also used in the present study.

4.4.1 Exploratory Milling Study

An exploratory study was conducted by changing the Al:B ratio, overall iodine content, and milling time. It also included a cryo-milling experiment. TG traces were used to assess the stability, *S*, of the prepared samples. Figure 4.1 shows TG traces and their derivatives (DTG) for samples 1 – 3B (cf. Table 4.1), and for the cryo-milled sample 10. For clarity, traces for different samples are shifted vertically relative to one another. Different stages of mass loss are labeled in the DTG plot. All mass loss stages occurring before 400 ºC are grouped into stage I, with sub-stages I^a, I^b, and I^c.

The first sub-stage, I^a is observed for all samples, including sample 1 prepared without aluminum, although its magnitude is reduced when aluminum is present. Not shown in Figure 4.1, the starting, 93-96% pure boron also shows a 5-6% mass loss at the same temperature. It could, therefore, be associated with a boron impurity rather than iodine loss. XRD patterns for both starting boron and sample 1, not shown here, indicate the presence of hydroxide, $B(OH)_3$, suggesting that this low-temperature mass loss stage can be assigned to the decomposition of $B(OH)_3$. In samples mechanically alloyed with aluminum, it is likely that most of the boron hydroxide was partially reduced, and a more stable aluminum hydroxide formed instead, although it might not have been sufficiently crystalline to be detectable by XRD. This reaction would be expected because in commercial preparation of amorphous boron, metals such as Mg, Al, Fe, Ca, Na, Li are known to be reducing agents [106]. The dehydration of aluminum hydroxide was not

detected in the TG traces of sample 2, suggesting that it may be later decomposed to Al_2O_3 and H_2 resulting in a very small and hard to detect weight loss.

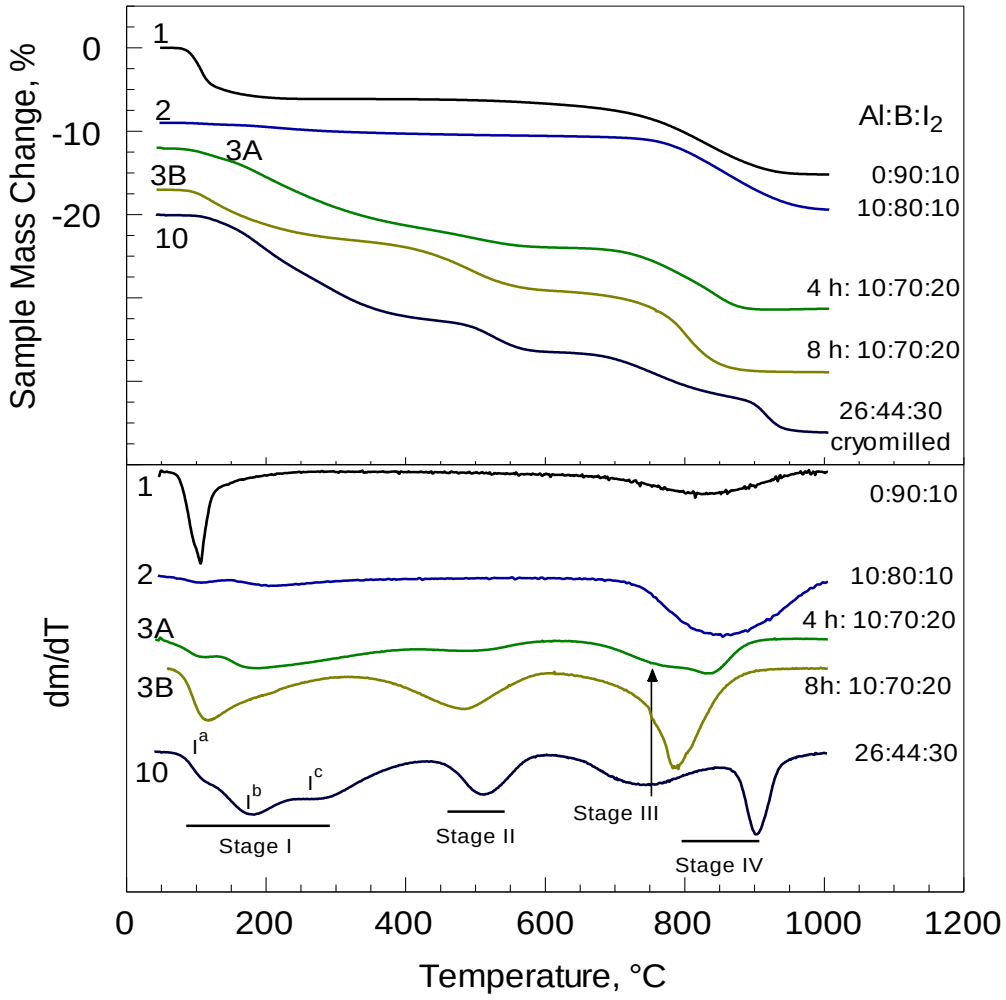

Figure 4.1 TG traces and their derivatives for initial exploratory experiments with 95% purity amorphous boron. Sample IDs are 1, 2, 3A, 3B, and 10 (cf. Table 4.1). Both TG and DTG traces are offset for clarity; the scale is valid for sample 1.

To verify the effect of impurity on the low-temperature mass loss, a high purity boron powder (99%) was used to prepare and characterize several reference samples (11 – 13 in Table 4.1). Respective TG traces are shown in Figure 4.2. The mass loss for sub-stage I^a is reduced to less than 1% for sample 11 with just boron and iodine, but increases to ~3 to 4% for samples 12 and 13, containing aluminum. Thus, sub-stage I^a is

likely to correlate with the decomposition of boron hydroxide for samples without aluminum. In the presence of aluminum, sub-stage I^a is most likely a coupled effect of dehydration of boron and iodine sublimation. The sublimation of iodine in the same temperature range was previously observed for binary $Al{\cdot}I_2$ materials [16].

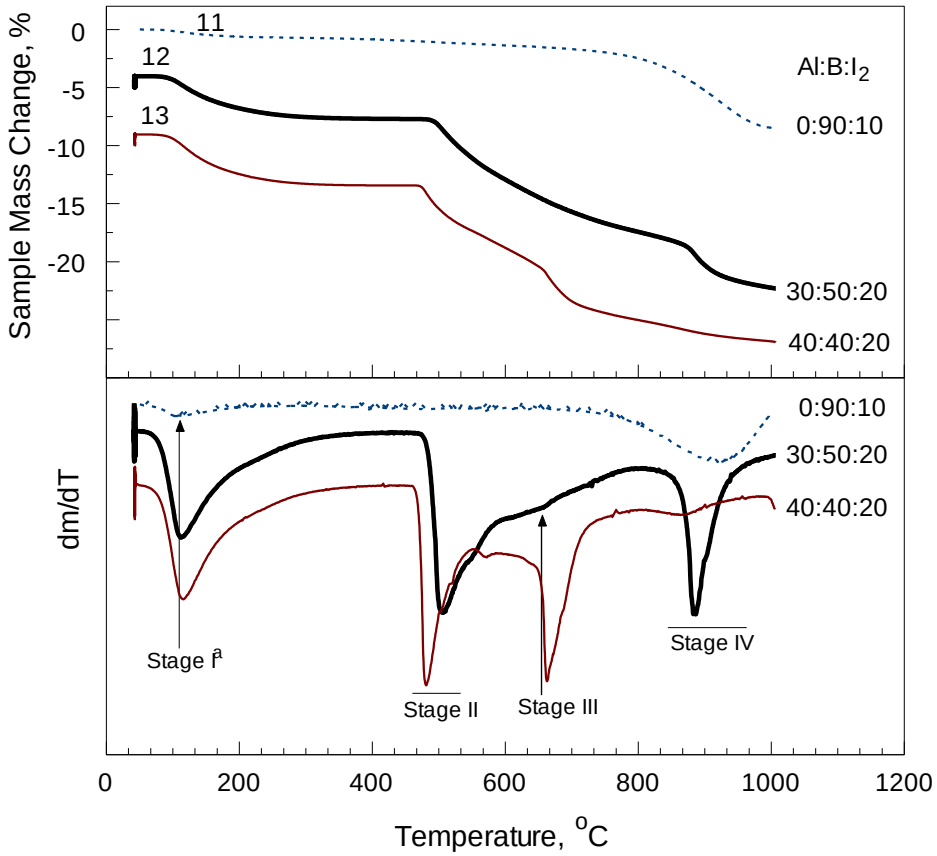

Figure 4.2 TG traces and their derivatives for initial exploratory experiments with high-purity (99%) boron. Sample IDs are 11– 13 (cf. Table 4.1). Both TG and DTG traces are offset for clarity; the scale is valid for sample 11.

It was observed that the materials prepared with high-purity boron (samples 12 and 13) were harder to handle because they reacted immediately when exposed to air, generating visible fumes. This suggests that any increased reactivity, e.g., surface oxidation, releases weakly bound iodine, and that it is, therefore, more practical to work with less pure boron that is not as susceptible to rapid surface reactions. This oxidation

effect also caused the initial mass increase seen at the beginning of the TG traces in Figure 4.2, where the temperature was held constant while the TG was purged (see Section 4.3.2). As a result, the stability parameter *S* as defined above is biased for these high-purity materials.

Sub-stage I^b correlates well with the boiling point of elemental iodine (182.3 ºC, [107]). In some materials (2, 3B, see Figure 4.1), the dm/dt peak is above 200 °C, and therefore correlates better with the decomposition of BI_3 (208 ºC, [108]). Regardless of the true nature of this peak, it is more or less clearly observed for all samples containing Al represented in Figure 4.1.

Sub-stage I^c is only developed for the sample prepared by cryo-milling (sample 10). Stage II is relatively strong for the cryomilled sample and for sample 3B prepared using an extended milling time. It becomes sharper and stronger with increasing aluminum concentration (see Figure 4.2 and Figure 4.3).

Cryo-milling (sample 10, in Figure 4.1) did not result in marked enhancement of the material stability *S* as defined above. Comparing TG traces for samples 3A (4 h) and 3B (8 h), it can be noted that a longer milling time also does not appear to result in an improved stability.

In Figure 4.1, stage III near the melting point of Al is only detected clearly in sample 10 prepared by cryomilling and with a greater aluminum concentration compared to samples 1 – 3B. Stage III becomes more pronounced for the samples with greater concentrations of aluminum (see Figure 4.2 and Figure 4.3 below).

Stage IV, occurring above the aluminum melting point is shifted for different samples. It is observed for all boron-containing materials, while it was not detected earlier for binary Al·I_2 materials [16].

4.4.2 Stable Al·B·I_2 Composites

Milling of ternary Al·B·I_2 composites with 20 wt. % iodine was continued to determine the Al:B ratio with optimal stability *S*. TG traces and their derivatives are shown in Figure 4.3 and Figure 4.4.

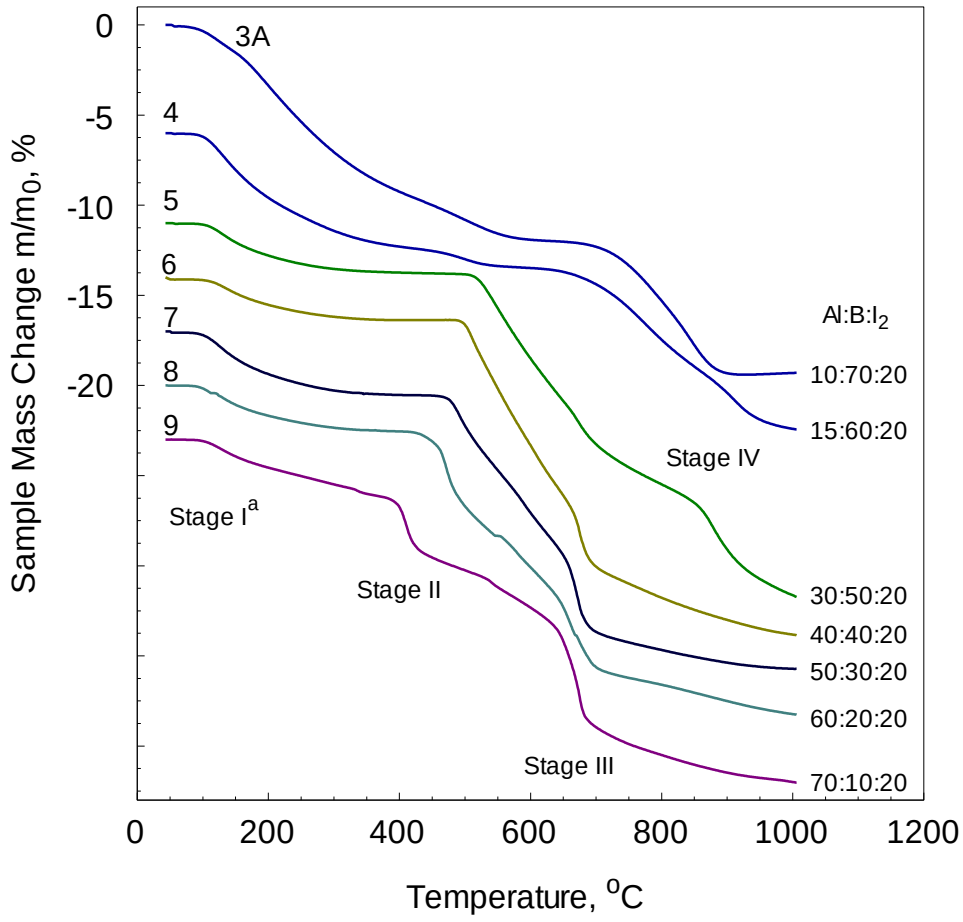

Figure 4.3 TG traces for Al·B·I_2 composites with 20 wt. % I_2 and Al ranging from 10 to 70 wt. % (samples 3A, 4 - 9, cf. Table 4.1). The vertical scale applies to sample 3A, the other traces are offset for clarity.

Samples 3A and 4 (10 and 15 wt. % Al, respectively) characteristically show a different shape compared to all other samples with 30 wt. % Al and above. The low-temperature mass loss is stronger, stage II is very weak, stage III is not observed, and stage IV is observed as a double step, poorly resolved for sample 3A and distinct for sample 4.

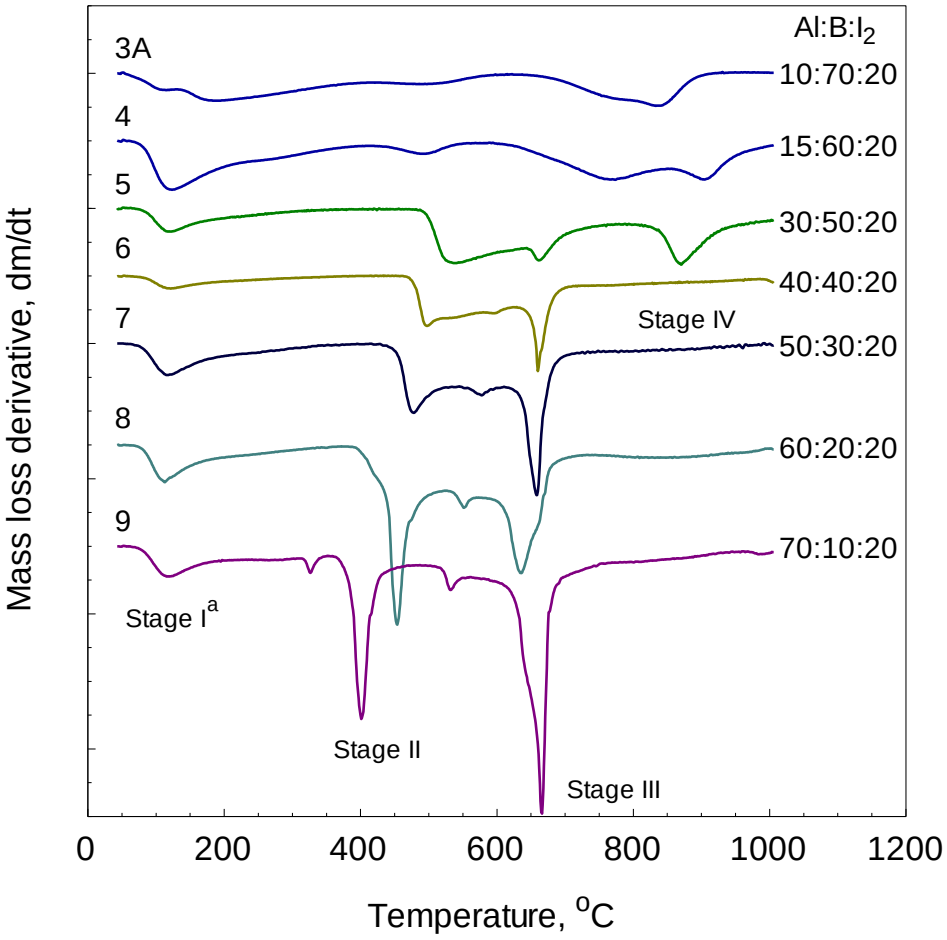

Figure 4.4 Derivatives of TG traces for Al·B·I_2 composites with 20 wt. % I_2 and Al ranging from 10 to 70 wt. % (samples 3A, 4 – 9, cf. Table 4.1). The curves are offset vertically for clarity.

At 30 wt. % Al and above, all curves have a similar shape with several observable trends: Stage I^a near 115 ºC occurs for all samples. Stage Ic is not observed. The onset of mass loss stage II is clearly defined only at Al concentrations of 30 wt. % and above; it

becomes sharper and shifts to lower temperatures with increasing aluminum concentration. A small mass loss step at 324 °C, distinct only in the dm/dt signal in Figure 4.4, precedes stage II for the most aluminum-rich material, sample 9. This coincides with the decomposition of AlI_3 previously reported for $Al{\cdot}I_2$ composites materials [16]. Following stage II, a smaller mass loss step is observed clearly for higher Al concentrations. It becomes less distinct and shifts to higher temperatures for lower Al concentrations. Stage III mass loss near the Al melting point is observed for samples with aluminum concentration of 30 wt. % and higher, while stage IV becomes undetectable above 30 wt. % Al. Stage III appears to be a composite step with two sub-stages at higher Al concentrations. The higher-temperature step dominates in samples 5, 6, 7, and 9, while in sample 8 with 60 wt. % Al the lower-temperature step is stronger.

In order to follow the stability, *S*, over time, sample 6 (40 wt. % Al, 20 wt. % I_2) was selected as a representative material with an Al/B ratio close to that of AlB_2, and subjected to aging at room temperature in both argon and air environments. The corresponding TG traces are shown in Figure 4.5. The material stored in argon (in glovebox) shows a reduced low-temperature mass loss compared to the fresh material. At higher temperature, the aged sample behaves similar to the fresh material. Conversely, the material stored in air shows an increased mass loss at lower temperatures, and an additional mass loss stage near 900 °C.

A plot of stability, *S*, as a function of the aluminum concentration for different $Al{\cdot}B{\cdot}I_2$ composites containing 20 wt. % of iodine is shown in Figure 4.6. Circles show data for the freshly milled samples. The time between sample recovery and TG measurement varied from few hours to one day. Squares show the results for the more stable samples

stored under argon for one month. For sample 7, a data point (triangle) is also shown for a measurement taken 1 week after the sample was prepared and stored under argon. A difference in stability for the fresh samples 7 and 8 is likely explained by the difference in time between their preparation and the TG measurement. Both samples were prepared simultaneously; however, TG traces were measured for sample 7 immediately after it was recovered, whereas sample 8 was analyzed the next day.

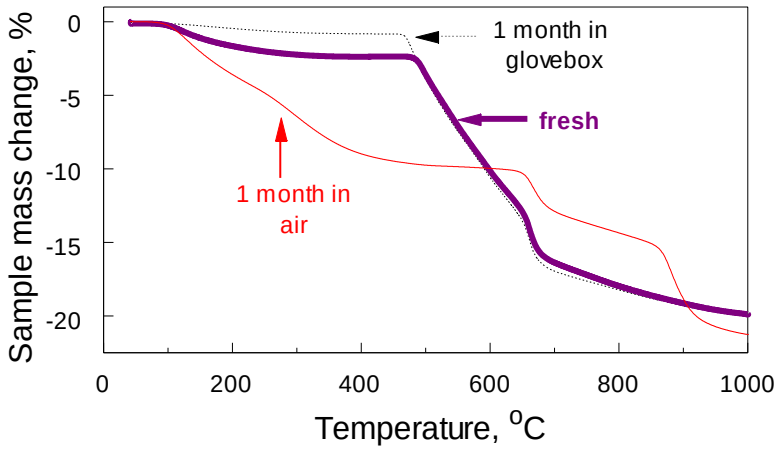

Figure 4.5 TG traces showing the effect of aging on sample 6 (40 wt. % Al, 20 wt. % I_2).

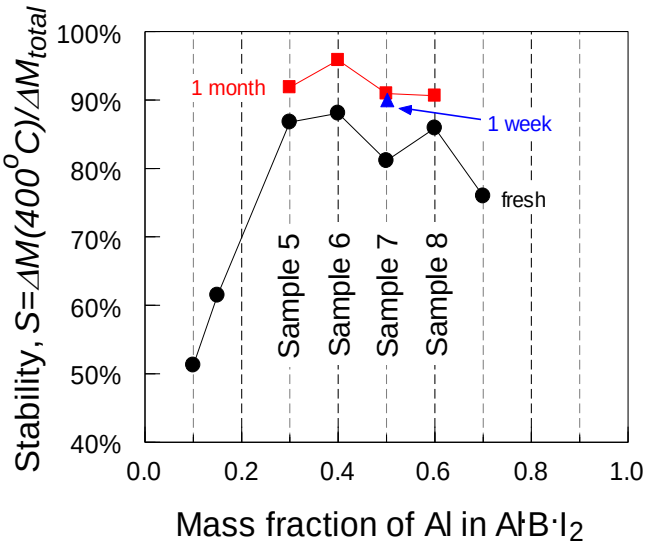

Figure 4.6 Stability of Al·B·I_2 composites with 20 wt. % of iodine. Data are shown for freshly milled samples and samples aged in the glovebox.

Based on the results presented in Figure 4.3 – Figure 4.6, samples 5 and 6 were recognized as the most stable (see also APPENDIX A), showing the highest absolute values of *S* and higher onset temperatures for the high-temperature mass loss stages. Therefore, their structure, morphology, and phase evolution during heating were analyzed further. Additionally, the sample 6 effectiveness to inactivate bioaerosol spores were tested and presented in APPENDIX B.

4.4.3 Particle Shape, Size, and Morphology

SEM images for samples 5 and 6 with 30 and 40 wt. % Al, respectively, are shown in Figure 4.7. Powders consist of equiaxial particles with many fines, (particles < 5 μm). These images produced using backscattered electrons are sensitive to the phase contrast between elements containing different atomic masses. Thus, iodine and boron should appear brighter and darker than aluminum, respectively. However, the particle surfaces exhibit a rather uniform brightness, indicating that components are mixed on a scale finer than the resolution of the images.

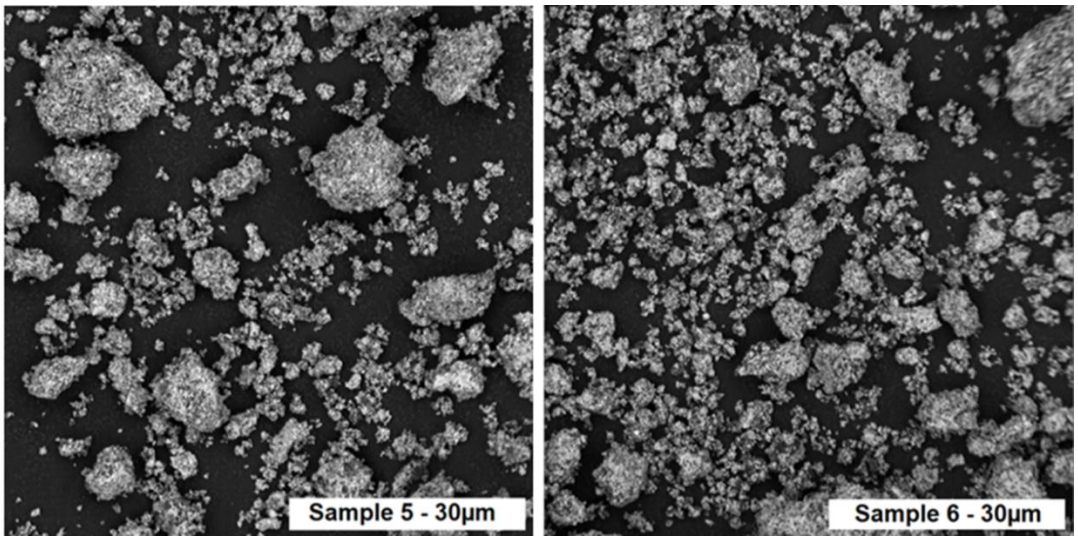

Figure 4.7 Backscattered electron images of samples 5 (30 wt. % Al, 20 wt. % I_2) and sample 6 (40 wt. % Al, 20 wt. % I_2).

Particle size distributions for samples 5 and 6 are shown in Figure 4.8. The mean particle sizes are 8.6 and 13.4 μm for samples 5 and sample 6, respectively. Sample 5 with greater boron content has finer particles. These powders are substantially finer than the previously prepared Al·B·I_2 material with the same 20 wt. % of iodine but only 11 wt. % of boron [90, 109].

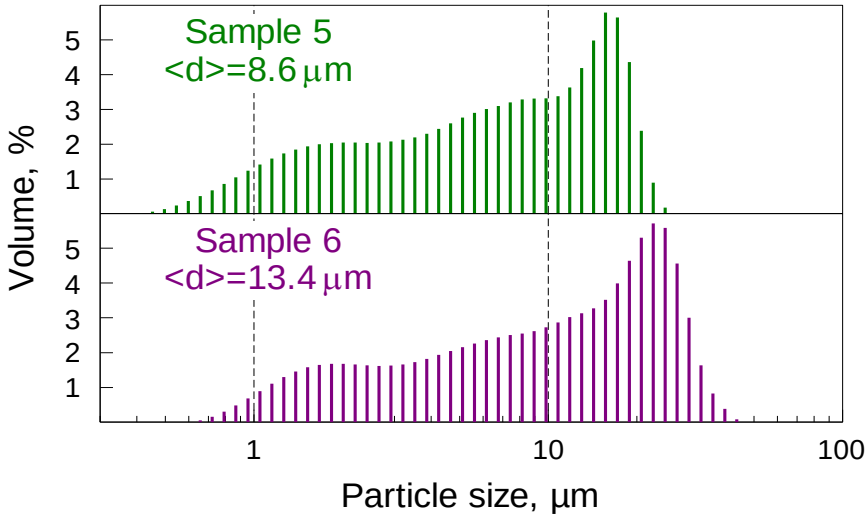

Figure 4.8 Particle size distributions for samples 5 and 6.

4.4.4 Material Structure and Composition

XRD patterns for freshly milled powders and powders quenched during heating are shown in Figure 4.9 for both samples 5 and 6. XRD patterns for as-prepared materials show peaks of aluminum and an increased background near 26° 2θ typical of the amorphous boron. As expected, aluminum peaks are stronger for sample 6, containing more aluminum.

Sample 5 (30 wt. % Al) was heated to and quenched at 770 and 1000 °C. Respective recovered samples show compositions of the material after stages III and IV of mass loss (cf. Figure 4.3). The sample quenched at 770 °C shows formation of AlB_2 as a main phase (see Figure 4.9a). Aluminum peaks disappear and the amorphous boron hump becomes much weaker. The sample quenched at 1000 °C shows formation of AlB_{12}.

Peaks of η-Al_2O_3 also appear although the experiments were performed in a flow of Ar. Peaks of $Al_{13}Fe_4$ are detected, which are likely caused by contamination of the prepared material by steel from the milling media.

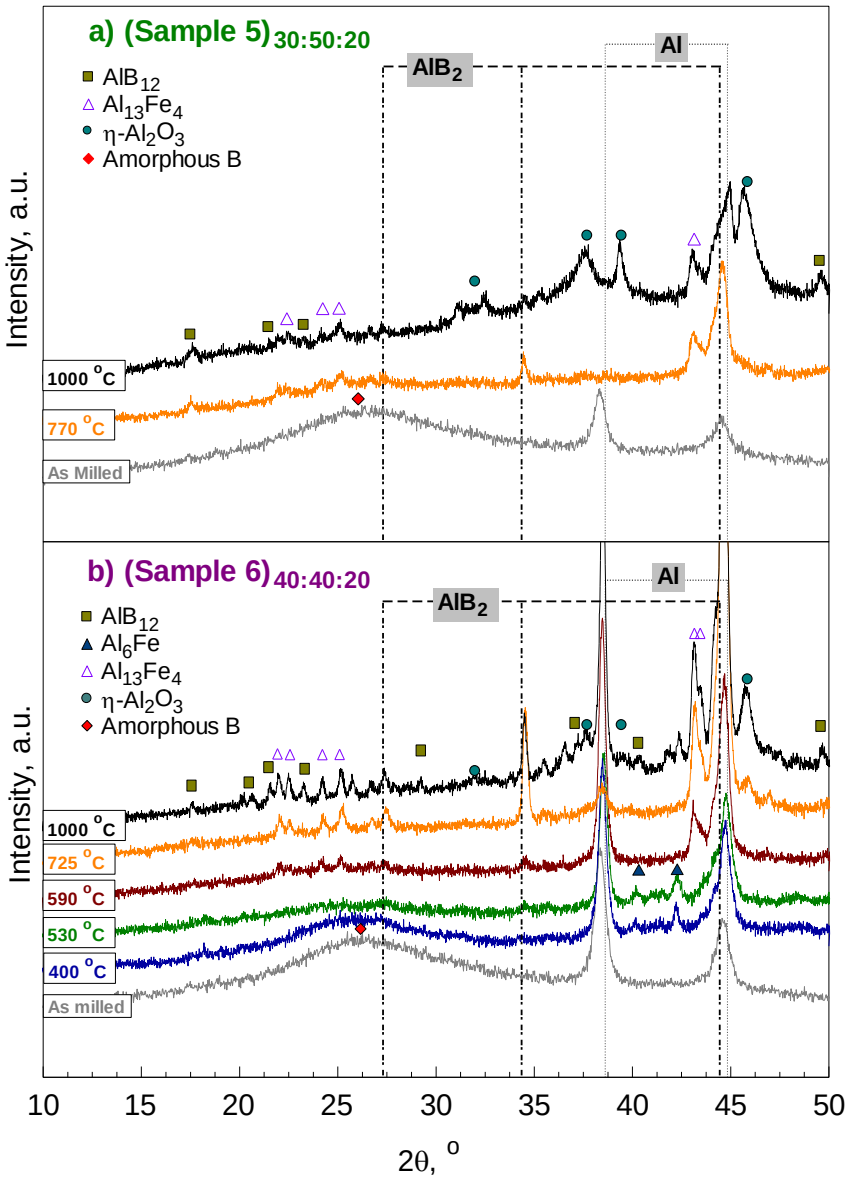

Figure 4.9 XRD patterns of freshly milled and quenched powders at various temperatures a) sample 5 (30 wt. % Al, 20 wt. % I_2) and b) sample 6 (40 wt. % Al, 20 wt. % I_2).

Sample 6 (40 wt. % Al) was heated to and quenched from multiple temperatures (Figure 4.9b). Samples quenched from 400, 530, 590, 725, and 1000 °C, represented

materials at the onset of stage II, after stage II, onset of stage III, after stage III, and after stage IV, respectively.

The sample quenched at 400 ºC shows a weaker hump of amorphous boron compared to the freshly prepared powder; it also shows an intermetallic Al_6Fe phase (contamination from steel milling media). The Al_6Fe pattern disappears above 530 °C and is replaced by $Al_{13}Fe_4$. Small peaks of intermetallic AlB_2 are first seen in the sample quenched at 530 °C; they increase gradually for the sample quenched at 590 °C. AlB_2 becomes a predominant phase for the sample quenched at 725 °C; its formation correlates with the strongest iodine release seen at stage III. Conversely, the peaks of aluminum almost disappear at this temperature. Sample 6 quenched at 1000 °C, showed formation of AlB_{12} and η-Al_2O_3, similarly to sample 5. In contrast to sample 5, the Al peaks remain visible for all quenched powders of sample 6.

4.5 Discussion

It is observed that the Al:B ratio affects the stability *S* of the prepared ternary $Al{\cdot}B{\cdot}I_2$ composite powders. The release of iodine detected at elevated temperatures can be interpreted assuming that in the as-prepared materials iodine is chemically bound to both, Al and B.

Different stages of mass loss are likely signifying formation of different iodine bearing compounds in the prepared powders.

Stage I mass loss, however, is not only caused by release of iodine. The TG traces of amorphous boron (not presented in this paper) and sample 1 suggest ~6% mass loss from release of water by hydrated boron oxides, which is observed to be important, especially

for the materials with low concentrations of aluminum. This reaction is weakly endothermic and can be described as:

$$B(OH)_3 \rightarrow 0.5\,B_2O_3 + 1.5\,H_2O\uparrow \quad \Delta H = 1540.9\,J/g\,B(OH)_3 \qquad \text{(R1)}$$

For materials with substantial concentrations of aluminum, hydrated boron oxides can be reduced to form pure boron; this exothermic redox reaction, shown below, can occur during milling or upon heating.

$$B(OH)_3 + Al \rightarrow Al(OH)_3 + B \qquad \Delta H = -2959.9\,J/g\,B(OH)_3 \qquad \text{(R2)}$$

It is likely that both reactions occur, resulting in a diminished low-temperature mass loss due to release of water for the materials containing aluminum.

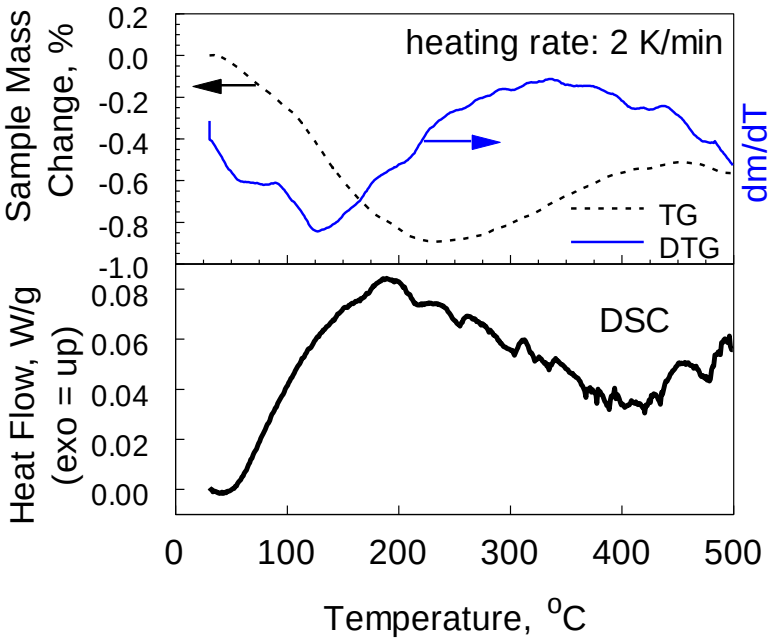

Figure 4.10 Details of the low-temperature reactions in sample 2 (10 wt. % Al, 10 wt. % I_2).

Separating the simultaneous release of water and iodine is difficult. As noted above, quantitative mass-spectrometric measurements of iodine release would be useful, but are cumbersome because iodine contaminates the instrument rapidly. An additional, low-temperature DSC scan in argon at 2 K/min for sample 2 (10 wt. % Al, 10 wt. % I_2) is

shown in Figure 4.10. There is a positive net heat release, indicative of the redox reaction. The endotherms, associated with release of water and iodine are likely masked by this stronger reaction. The TG trace of sample 2 with the lowest concentration of Al shows only 0.8 % of overall weight loss during stages I^a and I^b, suggesting release of only small amounts of water or iodine. Two closely spaced mass loss stages that can be distinguished in the DTG cannot be separated based on the measured DSC signal. For sample 2, the integral measured heat release for both sub-stages I^a and I^b is $\Delta H \approx 443$ J/g. The calculated net heat release assuming both sub-stages I^a and I^b are associated with release of water or iodine, yields 363 and 486 J/g, respectively. The measured value is bounded by the calculated values suggesting that the net heat release can be associated with both reactions; however, the extent of each reaction cannot be quantified.

The XRD results suggest that the most significant iodine release during stage II occurs as a consequence of the formation of new Al-bearing phases, and the concurrent destruction of the initial Al phase stabilizing iodine. In order to be released, iodine must be able to diffuse rapidly through the newly formed phases; there is presently no data on respective diffusion rates. First, the Fe contamination gives rise to the formation of Al_6Fe, which coincides with the onset of stage II. At higher temperatures AlB_2 forms, further consuming Al. Eventually the melting point of Al is reached, where the majority of the AlB_2 forms, and additional I_2 evolves. It is unclear whether the iodine released during formation of AlB_2 was bound to Al or B or to both materials, although the general temperature range of iodine release in this stage correlates with that observed for binary $Al{\cdot}I_2$ materials [50].

Stage IV was the most surprising and occurred only for materials which had Al:B mole ratio less than 0.4, indicating that some unreacted boron remained after the AlB_2 formation, which has a molar Al:B ratio of 0.5. Therefore, stage IV is assigned to release of iodine bound to boron. This high temperature mass loss stage was also observed for samples prepared in the absence of aluminum, supporting the above assignment. The mass loss was unambiguously associated with release of iodine based on EDX analysis on binary $B{\cdot}I_2$ material (sample 1). The EDX showed the presence of iodine in the sample quenched at 500 ºC, before stage IV, however, iodine was no longer present in the same binary material quenched at 1000 ºC, after stage IV. Because no unrecognized XRD peaks that could be assigned to metastable boron-iodine phases were detected for the quenched samples, it is possible that iodine does not form crystalline phases more stable than the solid solution in the amorphous boron, or that the iodine is stabilized at the surface of the relatively fine boron particles.

Amounts of iodine retained within the boron matrix can be estimated considering the mass loss observed during stage IV for all samples. For boron-rich materials, a total amount of unreacted boron after stage III, can be obtained assuming that all aluminum becomes part of the formed AlB_2, removing respective stoichiometric amount of boron from the material. The experimental values of the mass loss for stage IV and respective mass fraction of unreacted boron present after AlB_2 formation are shown in Table 4.2. The mass fraction of iodine retained in boron is also shown for each sample. This latter value varies in a relatively narrow range, remaining close to 10 – 11% for all samples prepared using low-purity, amorphous boron. It increases to about 13% for the higher purity boron. The difference is likely associated with the error made in the active boron content estimate

for the low-purity boron, which was relatively heavily oxidized. Thus, it can be suggested that boron can retain up to 13 wt. % of iodine until it is heated to nearly 900 ºC.

Table 4.2 Iodine Retained in Boron Metal Matrix

Sample ID	Mass Ratio Al:B:I_2	Free B after AlB_2 formation wt. %	Stage IV mass loss wt. %	I_2 in free B after AlB_2 formation wt. %
1	0:90:10	100.00	9.01	8.27
2	10:80:10	79.99	9.09	10.21
3A	10:70:20	77.48	7.32	8.63
3B	10:70:20	77.48	9.73	11.16
4	15:65:20	66.22	8.35	11.19
5	30:50:20	32.45	4.31	11.72
6	40:40:20	9.93	1.15	10.38
7	50:30:20	0.00	0.00	N/A
8	60:20:20	0.00	0.00	N/A
9	70:10:20	0.00	0.00	N/A
10	26:44:30	32.45	4.40	11.93
11*	0:90:10	100.00	7.67	7.12
12	30:50:20	32.45	4.95	13.24
13	40:40:20	9.93	1.50	13.12

*Stage IV is not completed at 1000 ºC

4.6 Conclusions

Metal-based materials containing iodine are of interest as reactive materials generating biocidal combustion products, which assist in rapid inactivation of harmful aerosolized microorganisms. In this work, ternary Al·B·I_2 materials with systematically varied Al:B ratios were prepared by mechanical milling. The materials were capable of retaining at least 20 wt. % of iodine, which was released upon heating in several stages. Low-temperature iodine release was relatively minor for the ternary materials. It overlapped with dehydration of $B(OH)_3$ accompanied by release of water. The most significant amounts of iodine were released in the 400 – 500 ºC temperature range, and during AlB_2 formation. Both AlB_2 formation and iodine release increased further by

melting of aluminum. For boron-rich samples with excess B after AlB_2 formation an additional, high-temperature iodine release stage was observed near 900 ºC. The results show that both boron and aluminum are capable of retaining substantial quantities of iodine stabilized in the metal matrix and released upon heating to temperatures much exceeding the iodine boiling point. The mechanism by which iodine is retained in boron and aluminum remains unclear.

CHAPTER 5

PREPARATION, IGNITION AND COMBUSTION OF Mg·S REACTIVE NANOCOMPOSITES

5.1 Abstract

Elemental magnesium and sulfur powders were ball milled to prepare a nanocomposite material, Mg·S. Ignition of the prepared powder was characterized using both a heated filament experiment and electric spark. Combustion of individual particles was studied by injecting the powder into a premixed hydrocarbon-air flame. Combustion of powder clouds was examined using a constant volume explosion chamber. Biocidal effect of the produced combustion products against aerosolized endospores of *Bacillus thuringiensis* (simulant of *Bacillus anthracis*) was quantified. The powders ignited at lower temperatures, compared to pure magnesium. Delayed ignition was observed for powders initiated by spark and for powder clouds ignited in a constant volume chamber by a heated wire. The delay is likely due to the formation of an evaporated sulfur cloud preceding ignition. The composite material burned faster than pure magnesium, which was shown by shorter measured burn times for individual particles, and by higher rates of pressure rise in the constant volume explosion experiments. The optical emission spectra produced by burning Mg·S nanocomposite powders exhibited an unusually strong emission at short wavelengths; additional spectroscopic studies of such flames are of interest. Combustion products generated by Mg·S composite powders effectively inactivated aerosolized spores; the effectiveness of inactivation was comparable to some previously examined formulations, including aluminum-based composite powders containing iodine.

5.2 Introduction

Mechanical milling has been recognized as a versatile and scalable technique used for preparation of a wide range of advanced materials [53, 54]. Among other materials, reactive powders of metal-based alloys [3-5, 9, 110] and composites [1, 2, 6-8, 16, 101, 111-114] were prepared for use as fuel additives in propellants, explosives, and pyrotechnics. Iodine-bearing metal fuels, including powders of $Al{\cdot}I_2$ [12, 16, 50], $Al{\cdot}CHI_3$ [101], $Al{\cdot}B{\cdot}I_2$ [111] and $Mg{\cdot}B{\cdot}I_2$ [115], were also prepared by mechanical milling. Such materials release biocidal species as combustion products and are of interest for advanced munitions designed to defeat biological weapons. A challenge is to stabilize a biocidal component (e.g., a volatile halogen, such as iodine) in the reactive material, which would allow for conventional storage, processing and handling of the material. At the same time, the combustion enthalpy and rate of reaction should remain high, while the biocidal species are released, preferably in the gas phase. Current research is focused to expand the range of novel materials capable of undergoing highly exothermic reactions and releasing biocidal products.

A recent study of nanocomposite thermite containing nano-$Al/K_2S_2O_8$ [116], suggested that combustion products containing sulfur, i.e., SO_2, could be of interest because of their biocidal properties. However, sulfur-containing reactive materials remain largely unexplored. Elemental sulfur is known to be moisture and air stable and capable of exothermic reactions with metals such as Zn, Zr, Hf, Ti, Fe, Mn, Mg, Si, and etc. [117-123]. Additionally, combustion of energetic composite containing porous silicon and elemental sulfur in oxidative environments was shown to form significant amount of gaseous products [124, 125], which are believed to be in the form of sulfur oxide species.

Therefore, sulfur-containing reactive materials capable of releasing large quantities of biocidal gases may be feasible.

In this study, reactive nanocomposites of magnesium with sulfur were prepared and characterized. This composition is selected based on a highly exothermic reaction between the components releasing 6,820 J/g and 12,812 J/cm^3 [126]. Powders with the stoichiometric magnesium over sulfur ratios, with 57 wt. % of sulfur were prepared by ball milling at room and liquid nitrogen temperatures starting with elemental powders. Their ignition kinetics and combustion dynamics in oxidizing environments were characterized. Biocidal properties of the combustion products of the prepared material against aerosolized endospores of *Bacillus thuringiensis* (simulant of *B. anthracis*, a causative agent of Anthrax) were investigated following the experimental protocols previously developed by this research team [13, 51, 90, 101, 127].

5.3 Experiment

5.3.1 Material Synthesis

Starting materials were elemental powders of magnesium, -325 mesh, 99.8% pure, purchased from Alfa Aesar and sulfur, -100 mesh, reagent grade, purchased from Sigma-Aldrich. Earlier studies report a mechanically triggered reaction in the metal-sulfur system to occur at very short milling times, before a well-mixed composite structure could be prepared [119, 122, 128, 129]. To prepare well mixed and unreacted composites, an exploratory study using two different mills and various milling conditions was conducted. Powders were milled at both cryogenic (77 K) and room temperatures. A freezer mill (SPEX 6850) with four 25 mL steel vials operated under liquid nitrogen was used for the

cryo-milling experiments. The milling tool was a 5.84-cm long steel rod with 9.525-mm diameter oscillating within the vial at a frequency of 15 Hz. Unfortunately, two milling experiments conducted with milling times of 100 and 150 min yielded powders that formed MgS, and thus not useful as reactive materials. No further cryomilling experiments were attempted in the present effort.

A shaker mill (SPEX Certiprep, 8000 series) with two 50 mL flat-ended steel vials cooled by room-temperature air jets was used for room-temperature milling. The milling vials were loaded and sealed inside an argon-filled glovebox. No process control agent was used. A 10-kΩ NTC thermistor (Model: MF52-103) with ceramic insulation was attached to the outside of one of the milling vials to monitor its temperature during milling. A mechanically activated reaction, detected by a temperature spike, occurred for several powders at different milling conditions, as shown in Table 5.1. Several powders were prepared by altering the milling media size (case-hardened carbon steel balls), ball-to-powder ratio (BPR) and mass of the material loaded to find the milling conditions yielding an unreacted composite material.

Table 5.1 Cryogenic and Room-Temperature (RT) Milling Parameters

Mill	Sample ID	Mass of material loaded (g)	BPR	Ball Size (mm)	Mg:S mole ratio	Milling time (min)	Reacted during milling
Freezer: Cryo-milling	1	2	--	--	1	150	Yes
	2	2	--	--	2	150	Yes
	3	2	--	--	1	100	Yes
Shaker: Room temp. milling	4	2	10	10	1	10	No
	5	5	10	10	1	<1	Yes
	6	5	5	5	1	22.5 – 28.5	Yes
	7	5	5	5	1	20	No

A list of all prepared powders is shown in Table 5.1 with their respective milling conditions. Only two samples, with IDs 4 and 7, produced composite powders rather than reacted MgS.

5.3.2 Material Characterization

Using a LEO 1530 Field Emission microscope, back-scattered scanning electron microscopy (SEM) images were acquired to characterize the powder morphologies and scale of mixing in the prepared powders. Particle size distributions (PSDs) for the prepared powders were measured in order to process particle combustion data following the methodology described elsewhere [103, 130, 131]. This methodology involves correlating the measured distributions of particle burn times and particle sizes with each other.

To obtain PSD of burning particles the powder was fed through the burner used for combustion measurements. The burner setup was described in detail elsewhere [103, 104, 130]; it is also summarized in Section 2.3 below. The powder was loaded into, and fed by, the screw feeder used by the burner. A gas flow carrying particles issued from the burner nozzle, although the flame was not ignited. The particles were captured electrophoretically using double-sided carbon tape attached to an SEM stub charged to 1 kV and placed above the burner. Individual particles as well as agglomerates were captured. Thus, possible agglomeration of the powder as a result of passing through the feeder and burner could be accounted for in the obtained size distributions. SEM images of the collected powder particles and agglomerates were processed using ImageJ 1.46r software [132] to obtain the PSDs. A brightness threshold was selected for each image to distinguish the background from particle, before allowing the built-in particle analyzer from ImageJ to process the particle sizes. Based on the observed particle sizes and resolution of the obtained SEM

images, particles with an area smaller than 1 μm^2 were discounted, as mostly representing image or substrate defects, rather than actual particles. The particle equivalent diameter was calculated using the area determined by ImageJ assuming spherical geometry. Additionally, PSDs were also measured by low-angle laser light scattering using a Beckman-Coulter LS230 Particle Counter, where agglomerates were removed by sonication during the measurement. Results from this measurement represent the true, non-agglomerated size distributions of the powder, while the PSDs determined from the SEM images by ImageJ represent the size distributions of particles and agglomerates fed into the flame.

X-ray diffraction (XRD) was used to determine phase compositions for as-milled powders and combustion products, using a PANalytical Empyrean diffractometer. The diffractometer was operated at 45 kV and 40 mA using unfiltered Cu K_α radiation (λ = 1.5438 Å).

5.3.3 Characterization of Ignition, Combustion and Biocidal Effectiveness

Ignition of the prepared powders was characterized in air using a heated filament experiment described in detail elsewhere [95, 96]. A hexane slurry with the powder was made to prepare a thin, 10-mm long coating on a 45-mm long, 0.5-mm diameter nickel-chromium alloy heating wire. The coated wire was heated by a DC current. Varied applied voltage and an adjustable resistor connected in series with the wire were used to vary the heating rates in a range of 10^3 to 10^5 K/s. The temperature of the filament was measured using a high-speed infrared pyrometer (DP1581 by Omega Engineering, Inc.) focused on an uncoated filament surface adjacent to the powder coating. The emission from the powder coating was visualized using a high speed video camera (MotionPro 500

by Redlake), operated at 500 fps. Prior to ignition, the coating surface was darker than that of the heated filament. The ignition instant was registered when the powder became brighter than the heated filament.

In a separate experiment, the ignition of the prepared powders was tested using an electro-static discharge (ESD). A setup based on a model 931 firing test system by Electro-Tech Systems, Inc., was used, which was described in detail elsewhere [114, 133]. The powder was placed inside a 0.5-mm deep, 6-mm diameter cavity of a grounded, custom-made polished brass sample holder. An even layer thickness was achieved by scraping away the excess of powder with a razor blade. A pin electrode was fixed ~ 0.2 mm above the surface of the powder. A selected capacitor was charged to a voltage in the range of 1 – 20 kV, before discharging through the pin electrode to the powder. All experiments were conducted inside a sealed test chamber with a volume of 624 cm^3. The ESD powder ignition was tested in different environments: air, argon, and helium at 1 atm, as well as in air at reduced pressures. All tests conducted in air at 1 atm used a 2000 pF capacitor. Different capacitors from 2000 to 20,000 pF were utilized for other environments. The powder ignited consistently only in air at 1 atm. The powder did not ignite when the chamber was filled with Ar or He. The powder could be ignited when a 20,000 pF capacitor was used at 0.098 atm (-27 in Hg) air; however, it could not be ignited if pressure was further reduced.

Optical emission produced by the ignited powder was recorded using a photomultiplier tube (PMT) filtered at a wavelength λ = 568 nm, placed 15 cm away from the sample. The chamber was also equipped with a Model 482A21 dynamic pressure transducer by Piezoelectronics to record the pressure as a function of time. The maximum

measured pressure and chamber volume were used to estimate the energy release during combustion, which was compared to the respective theoretical reaction enthalpy.

Aerosol combustion measurements were conducted using a constant volume explosion (CVE) experiment in air [2, 70]. Aerosol was ignited in a 9.2-L spherical vessel. The vessel was initially evacuated, and the aerosolized powder was introduced using an air blast delivered from a pressurized reservoir. The air blast raised the pressure in the vessel to approximately 1 atm before ignition. After a 0.3-s delay that was necessary to minimize turbulence, the aerosolized cloud was ignited by an electrically heated tungsten wire placed at the center of the vessel. The pressure inside the vessel was recorded as function of time using a PX2AN1XX500PSAAX pressure transducer by Honeywell. The ratio of the maximum pressure to the initial pressure, P_{max}/P_0, and the maximum rate of pressure rise, $(dP/\mathrm{d}t)_{max}$, were determined to characterize the energy released during the experiment and the rate of combustion, respectively. Assuming that the main combustion products were MgO, and SO_2, the experiments were conducted with a fuel-rich system at a constant powder load of 4.65 g of the Mg·S nanocomposites, corresponding to an equivalence ratio of about 1.57. Results obtained in this study can be directly compared to those reported previously for pure aluminum and Al·Mg alloy powders, which were evaluated using the same experimental set-up and powder mass loads [134, 135].

Particle combustion of Mg·S nanocomposites was studied by injecting the powder into an air-acetylene flame [103, 130, 131]. Powders burned in combustion products of acetylene mixing with surrounding air. This environment emulates those encountered by metal particles burning in an expanding fireball produced by explosives or in air-breathing propellants. Detailed descriptions of the pre-mixed air-acetylene laminar flame and the

experimental set-up including the particle feeder are available elsewhere [103, 104, 130]. Briefly, the powders were introduced into a premixed laminar flame using a custom screw feeder, where a thin layer of powder was deposited into threads of a stainless steel, 19-mm diameter screw with 629.9 threads per meter (16 threads per inch.) The screw placed inside a cylindrical enclosure was attached to a DC motor, turning it clock-wise. A nitrogen nozzle, connected with the enclosure was mechanically coupled with the screw and shifted along it as the screw rotated. A nitrogen jet directed across a thread of the screw removed deposited particles. The particle laden jet exited the screw enclosure and was fed into a thin tube placed axially in a burner tube feeding the premixed air/acetylene mixture. Particles entered the flame along its vertical axis.

Optical emission from the burning particles was recorded using an array of three filtered PMTs. In selected experiments, emission was also recorded using a 32-channel H7260 series linear array multianode PMT assembly by Hamamatsu. The PMT assembly was coupled with a spectrometer covering a wavelength range of 373.4 – 641.0 nm. The optical measurements were used to obtain both burn times and combustion temperatures of the ignited composite material particles and agglomerates.

Biocidal effectiveness of the generated combustion products was tested following the methods and protocols established earlier [13, 51, 90, 127]. Powder was fed into an air-acetylene flame at a rate of 0.9 – 1.2 g/min, using the same set-up as employed for particle combustion measurements discussed above. The burner was enclosed in a flow system enabling passage of a challenge bioaerosol above the flame. Vertical position of the burner was adjusted, so that the combustion products had different temperatures while being mixed with the bioaerosol. The challenge bioaerosol was generated by a Collison

nebulizer (BGI Inc.) operated at 6 L/min from a liquid suspension charged with viable spores of *Bacillus thuringiensis* serovar *kurstaki*, Btk. Freeze-dried Btk spores were acquired from Certis USA Inc., strain SA-11 (product # SA-11 SDTC; technical grade concentrate developed for US Army and Air Force). After exiting the nebulizer's nozzle, the bioaerosol was diluted with a 30 L/min HEPA-filtered dry air flow and charge-equilibrated with a 10-mCi ^{85}Kr charge equilibrator (model 3012, TSI Inc.). Combustion products and bioaerosol were mixed in the exposure chamber; an estimated exposure time of the bioaerosol to the combustion products was approximately 0.33 s. After passing through the chamber, the bioaerosol was collected on 25-mm sterile gelatin filter (SKC Inc.) for a culture-based analysis. As a result, an inactivation factor, IF [13, 51, 90, 127] , was determined by comparing the viable concentration of spores measured with and without exposure to combustion products of the tested nanocomposite.

5.4 Results and Discussion

5.4.1 Particle Shape, Size, and Morphology

SEM images of samples ID4 and ID7 (see Table 5.1), which did not form MgS during milling are shown in Figure 5.1. Powders consist of roughly equiaxial particles with broadly varied sizes. Individual composite particles in sample 7 appear to be more homogeneous and have smoother surfaces compared to sample 4, where the particles contain relatively coarse Mg flakes, with some flakes unattached to composite particles. The images are produced using backscattered electrons, which are sensitive to the phase contrast between elements containing different atomic masses. Therefore, sulfur should appear brighter than magnesium. Although the brightness differences are subtle, a close

examination of Figure 5.1B shows certain parts of the particle surfaces to be brighter, which may be indicative of sulfur coating. Generally, sample 7 appears to be the better mixed material, containing particles with lower porosity compared to sample 4. Hence, further experimental work in this study was conducted with sample 7.

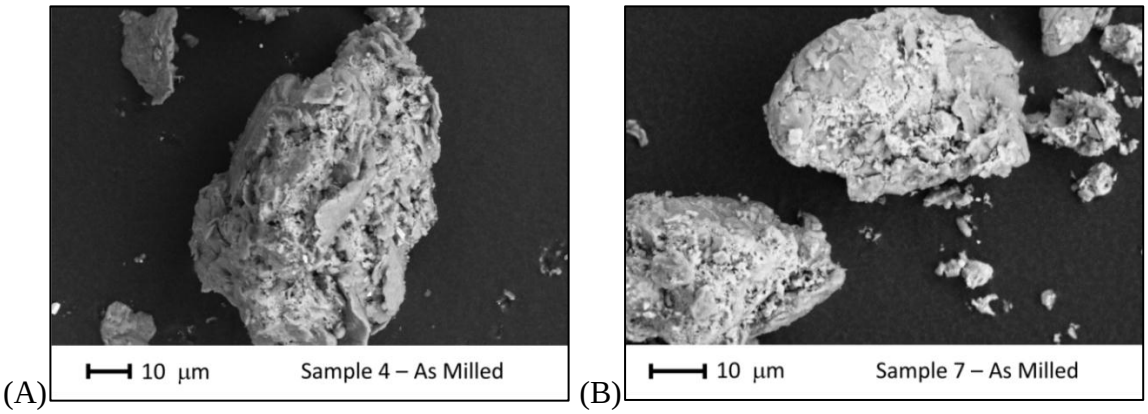

Figure 5.1 Backscattered electron images of samples 4 (A) and 7 (B).

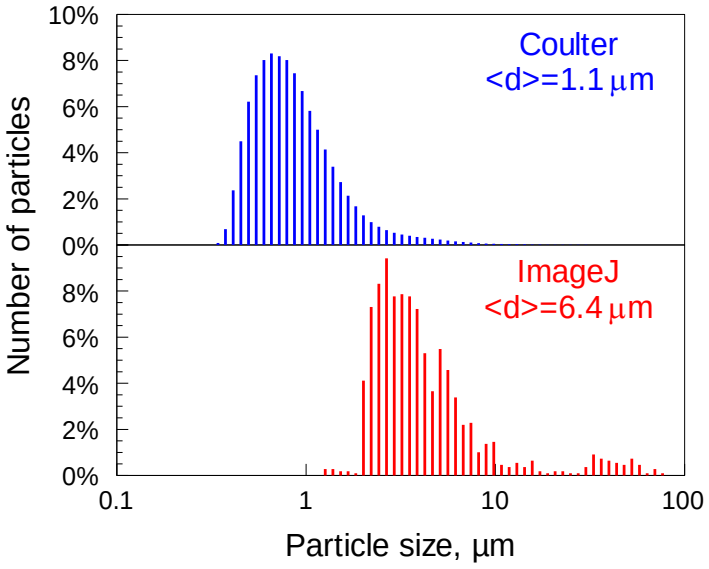

Figure 5.2 Particle size distribution for sample 7 acquired using the laser scattering with a Coulter particle analyzer and the ImageJ processing.

Particle size distribution for sample 7 obtained using the Coulter particle analyzer and by ImageJ processing are shown in Figure 5.2, where the mean particle sizes of a number-based distribution are 1.1 and 6.4 μm, respectively. It is not surprising that when

considering agglomerates for the PSDs in the ImageJ processing, the size distribution is shifted to the right compared to the PSDs obtained from Coulter analyzer, where agglomerates were removed. Additionally, when analyzing the PSDs from ImageJ, there are almost no particles with sizes below 2 μm, justifying the minimum threshold size of 1 μm selected for the image processing.

5.4.2 Material Stability and Phase Composition

The material stability of the Mg·S nanocomposites was tested by aging the material in ambient air for three weeks. XRD patterns for the freshly milled and aged powders are shown in Figure 5.3. No sign of significant aging was detected: for both fresh and aged powders, only crystalline peaks of pure magnesium and sulfur were observed. Additionally, XRD results confirmed that a substantial reaction during milling was, in fact, avoided.

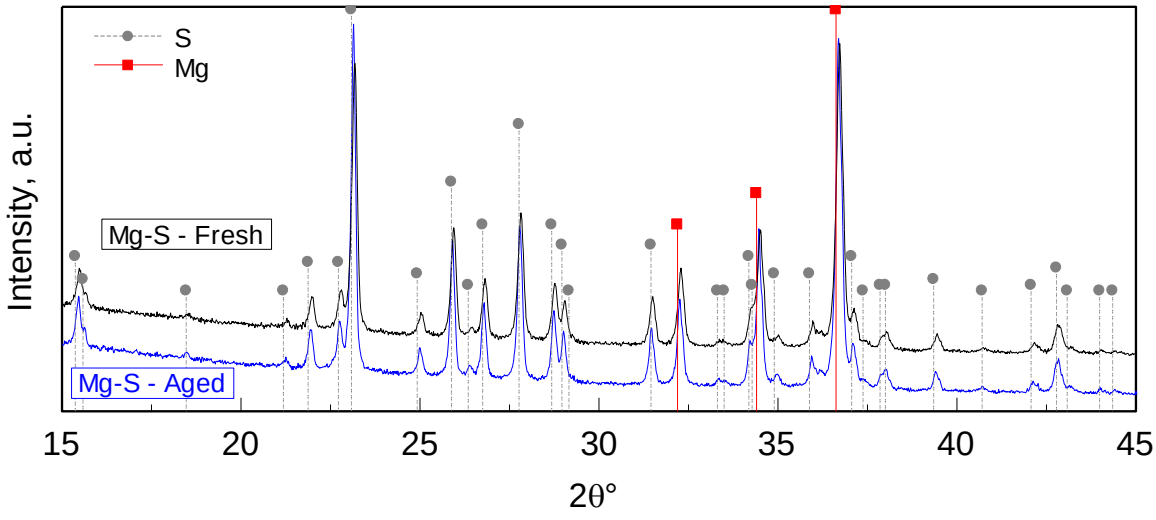

Figure 5.3 X-ray diffraction patterns of fresh and aged (3 weeks) powders of Mg·S nanocomposite material (sample 7).

5.4.3 Filament Ignition

Ignition temperatures measured for sample 7, both fresh and aged powders, are shown in Figure 5.4 as a function of heating rate. The data are scattered in a relatively narrow range of temperatures. For both fresh and aged materials, a weak increase in the ignition temperatures at greater heating rates is observed. This is in contrast to pure Mg powders [96], where the ignition temperature is a stronger function of the heating rate. Also, it should be noted that the Mg·S nanocomposites have lower ignition temperatures compared to pure Mg powders [96]. Interestingly, the ignition temperatures reported by [123] for Mg·S composites prepared using molten sulfur are comparable to the present measurements for the materials prepared by milling.

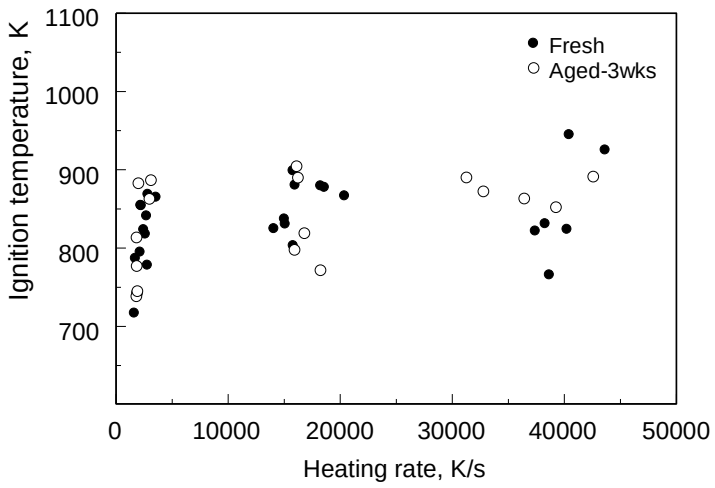

Figure 5.4 Ignition temperatures of sample 7 as a function of heating rate.

Individual frames collected from the high speed video imaging are shown in Figure 5.5. Images are turned 90°, so that the area above the heated wire is seen at the left part in each image. The first frame, taken 40 ms after the wire was heated, shows the initial emission from the igniting sample. This time can be considered the ignition delay at a heating rate of ~17,000 K/s. The frames at 42 and 46 ms show a growing flame produced

by ignition of an increasingly greater portion of the powder coated on the wire. In frame 46, some particles are seen to be ejected away from the filament, at estimated speeds of 1.6 to 2.7 m/s. At 50 ms and above, additional flame balls appear separately and away from the initial flame propagating from the wire. New flame balls may be caused by ignition of ejected composite particles in a cloud of evaporating sulfur. Such flame balls separated from the flame around the wire were not observed for pure magnesium or other metal powders ignited in the same experimental setup.

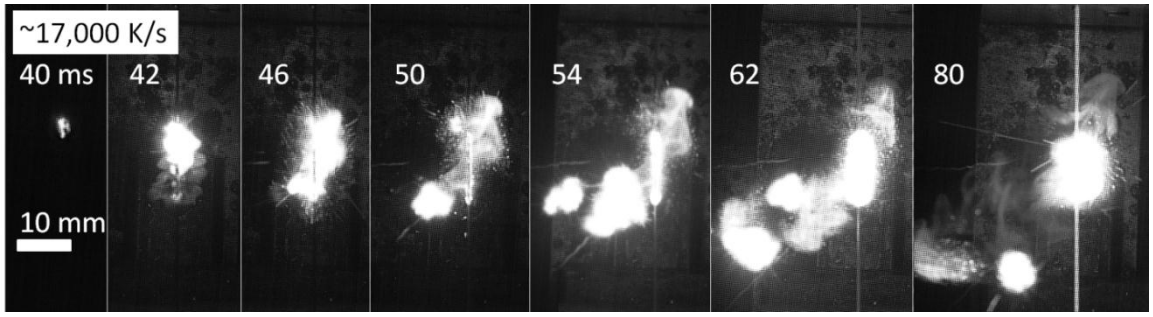

Figure 5.5 A sequence of images captured using a high speed video camera in the filament ignition experiments. The images are turned 90º, so that left = up. Frame rate is 500 fps. Individual frame exposure time is 2 ms.

5.4.4 Spark Ignition

In air, a minimum ESD voltage of 4 kV with a 2000 pF capacitor was necessary for ignition to occur consistently. Characteristic optical emission and pressure signals are presented in Figure 5.6. Emission pulses start 4 – 6 ms after the ESD, a longer ignition delay compared to pure magnesium powders [136] and to aluminum-based nanocomposite thermites [133]. The formation of an evaporating sulfur cloud is most likely the reason for the longer ignition delays. With an increase in the ESD voltage, the leading slope of the emission pulse does not shift significantly, while both amplitude and duration of the pulse increase. At 12 kV, an extended plateau follows the maximum emission intensity. Pressure traces are delayed compared to the emission signals. Considering the speed of sound and

chamber dimension, the sound wave can travel through the ESD chamber in approximately 1 ms, while shifts between the peaks of emission and pressure signals are of the order of tens of ms. Therefore, such shifts represent the actual time delay between the emission and pressure signals. Generally, pressure peaks when emission signal decays; the peak pressure times are indicative of the extinction or complete combustion of the ignited powder. Amplitudes of the pressure pulses increase substantially at greater ESD voltages. Note that vertical scales in Figure 5.6 are different for each voltage, so that the increase in the amplitude of both optical emission and pressure at higher voltages may not be immediately apparent.

Selected video frames of the combustion event captured at 500 fps for an ESD voltage of 12 kV are presented in Figure 5.7. The frame taken 4 ms after the spark, approximately when the onset of the emission pulse is registered, shows incandescent particles moving away from the region struck by the spark. The region near the spark is dark, while the incandescent particles are observed at a distances varied from 10 to 25 mm from the needle electrode, or from the location where the particles were directly heated by the spark. Based on that distance and the time the frame was taken, the velocities of the ejected particles are estimated to vary from 2.5 to 6.1 m/s. At 8 ms, the ignited particle cloud visible in the 4-ms frame is seen to move further up and produce a much brighter emission. Considering the displacement of the cloud, the speed of ignited particles can be estimated as 1.2 to 2.0 m/s. At the same time, it is apparent that particles continue being ejected from the sample holder and ignited by the heat produced by the burning cloud. Frames taken at longer times show slower moving burning particles involved with recirculating flow patterns. Similarly to filament ignition experiments, new individual

flame balls are observed at longer times, most probably caused by the ignition of the composite inside the evaporating sulfur cloud. It is seen that more powder is ejected from the sample holder and ignited, apparently explaining the nature of the observed emission plateau in Figure 5.6.

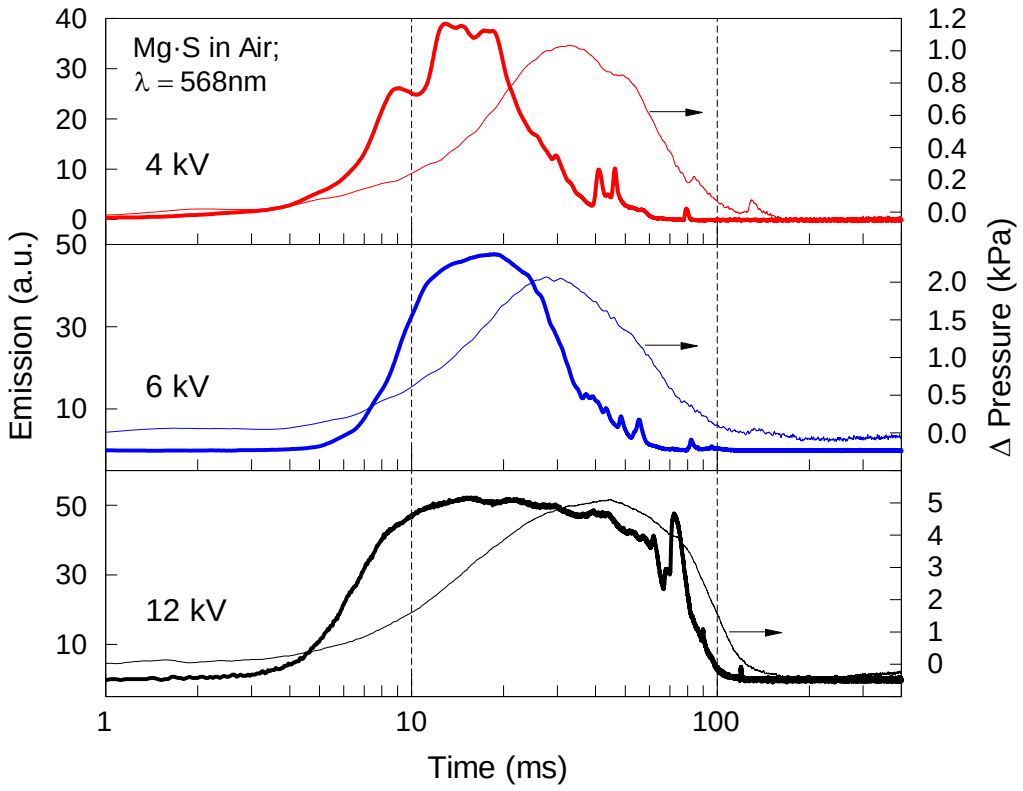

Figure 5.6 Emission trace filtered at 568 nm and pressure signal of the powder ignited in ambient air. Capacitor (2000 pF) was charged to 4, 6, and 12 kV for different experiments.

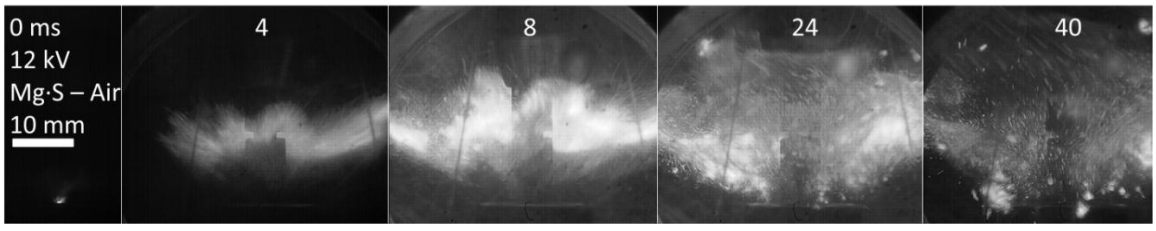

Figure 5.7 Images of the cloud combustion event in air initiated by ESD at 12 kV. Frame rate is 500 fps. Individual frame exposure time is 2 ms.

An example of the optical emission and pressure signals recorded for an experiment in low-pressure air is shown in Figure 5.8. A much stronger ESD was used to

ignite the powder. Respectively, a stronger and longer pressure pulse was recorded indicating a greater amount of the material ignited. Because ignition could not be achieved at lower pressures and in inert gases, presence of oxygen must have been critical for ignition of the prepared materials. The oxygen concentration inside the chamber at -27" Hg was more than sufficient to fully oxidize all the magnesium and sulfur ejected from the sample holder. Thermodynamic equilibrium calculations performed using NASA CEA code [99] at a constant volume configuration was selected to determine the final theoretical pressure for this experiment. Assuming that all of the air present inside the ESD chamber at -27" Hg (9.9 kPa) is allowed to react with the powder ejected from the sample holder, yields a theoretical ΔP of 44.2 kPa forming only MgO and SO_2 as the main product species. The combustion efficiency, ε, is calculated as a ratio of the experimental and theoretical values of ΔP, which produced $\varepsilon = 0.2$ for this case. In Figure 5.9, a set of CEA calculation results are shown where the volume fraction of air inside the chamber allowed to react with the ejected powder was varied while keeping the starting pressure of -27" Hg (9.9 kPa) constant by introducing additional inert N_2 gas into the starting reactants. The volume fraction is calculated relative to the reference volume representing the chamber filled with air at 1 atm. For clarity, an additional x-axis is shown with the amount of air reacting with the composites. The rationale behind this is that not the entire chamber volume participates in the reaction. The calculations therefore mimic a small cloud of variable, but a priori unknown volume reacting in a larger chamber filled with an effectively inert gas. Volume fraction of 0.1 in Figure 5.9 represents the calculation for a low-pressure chamber filled with air without any additional N_2 gas, for which the theoretical ΔP of 44.2 kPa was calculated. Additionally, the mole fraction of the formed magnesium sulfide, MgS, was

also tracked for each calculation and reported in Figure 5.9. The results show that the experimentally obtained pressure is clearly lower than the calculated one regardless whether the main reaction products are oxidized. Furthermore, the calculated pressure decreases drastically initially as the volume fraction of air is decreased until MgS formation becomes significant where theoretical ΔP plateaus. This suggests that the present measurement does not allow one to separate between MgS, MgO, or SO_2 formation in these experiments; rather a combination of these three species may form depending on the amount of air reacting with the composites.

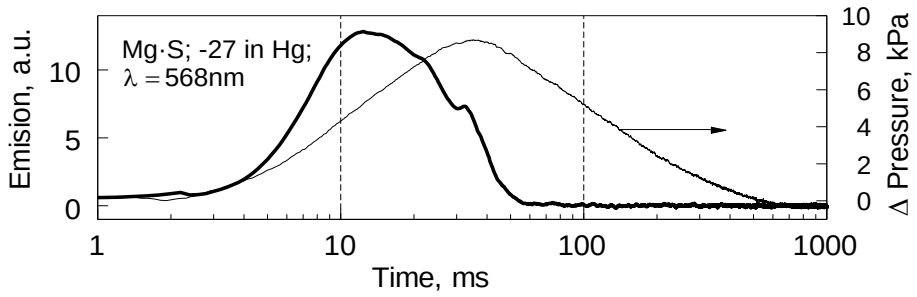

Figure 5.8 Emission trace filtered at 568 nm and pressure signal of the powder ignited at a low-pressure air (-27" Hg). Capacitor (20,000 pF) was charged to 20 kV.

Figure 5.10 demonstrates average values of the temporal characteristics of the optical emission traces obtained in experiments conducted in room air. Error bars represent standard deviations from repeat runs. The peak onset (t_{-10}) was defined as time from the ESD pulse initiation until the signal increased to 10% of its peak value. The peak width was taken at half maximum, between times t_{-50} and t_{+50}. In addition, peak position (t_{100}) is shown as well as the overall burn time (t_{+10}) identified when the signal decreased to 10% of its peak value. The peak onset shifts only slightly to lower times with an increased voltage. Both, the width of the peak and the burn time increase at higher voltages, are in qualitative agreement with the trend seen in Figure 5.6. This result is consistent with the

higher mass losses observed from the sample holder during experiments for higher voltages, shown in Table 5.2. It is clear that more powder ignited at higher voltages.

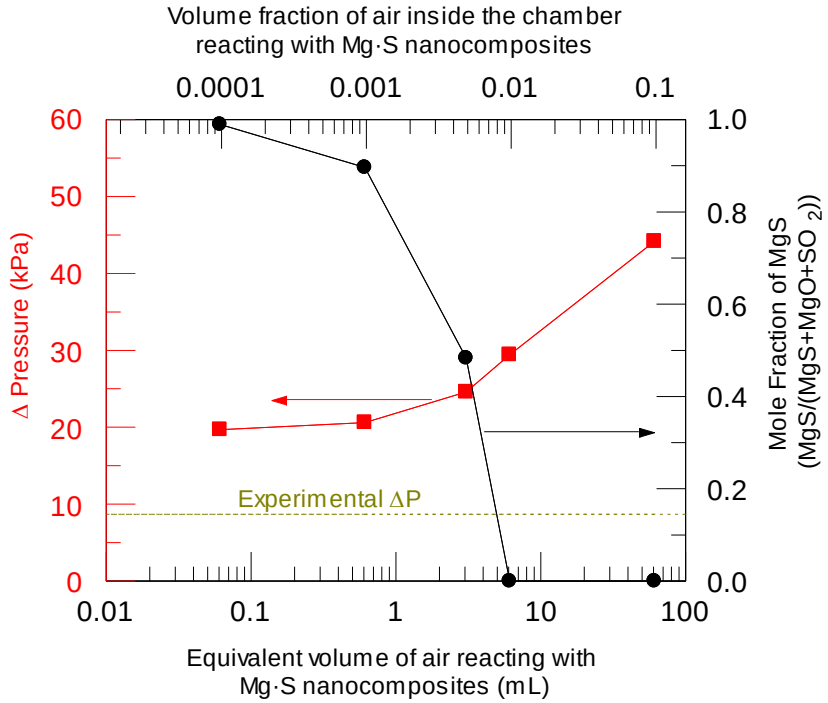

Figure 5.9 CEA pressures for various volume fractions of air inside the chamber which is allowed to react with Mg·S nanocomposite at a constant initial pressure of -27 in Hg (9.9 kPa). For clarity, an additional x-axis is shown with the amount of air reacting with the composites in mL. Constant starting pressure is achieved by replacing air with inert N_2 as an additional starting reactant in CEA. Mole fraction of the MgS species formation is also shown. The calculated pressures are about 2- to 5-fold greater than the experimental pressure.

Assuming that combustion adiabatically heats the gas in the entire chamber volume and causes respective pressure increase, we estimated the energy release based on the maximum pressures measured. Results are shown in Table 5.2. These are lower bound assessments for the heat release during spark ignition, neglecting any heat losses. Assuming that the reaction product was only condensed MgS, the theoretical energy release, $\Delta H_{calc.}$= 6.13 kJ/g based on the $\Delta_f H°_{(MgS)}$ values obtained from NIST Chemistry Webbook [107]. This energy release was reported to be 6.82 kJ/g by [126]. Similarly,

assuming that the reaction product was MgO and SO_2, the theoretical energy release, $\Delta H_{calc.}$= 15.92 kJ/g based on the $\Delta_f H°_{(MgO)}$ and $\Delta_f H°_{(SO_2)}$ values obtained from NIST Chemistry Webbook [107]. For higher discharge voltages, the estimate indicates that about 20% to 40% of the theoretical energy was released during the cloud combustion assuming MgO and SO_2 or only MgS was the product, respectively. This is a relatively high combustion efficiency, considering that the volume of the experimental chamber was substantially greater than the volume of the burning particle cloud, leading to substantial energy dissipation unaccounted for in the present estimate.

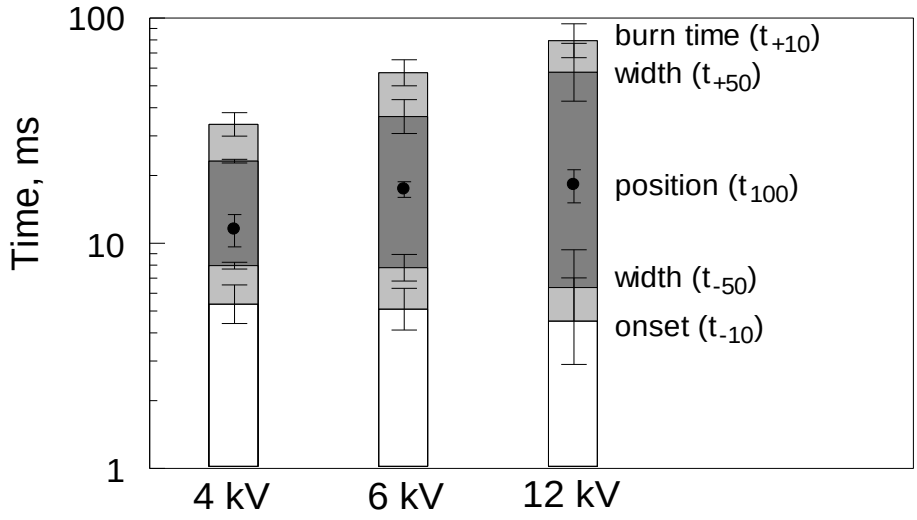

Figure 5.10 Temporal characteristics of the optical emission signals produced by the powders initiated by ESD at different voltages.

Table 5.2 Average Experimental Mass Loss from the Sample Holder and a Comparison of Theoretical and Experimental Energy Release for Experiments in Air

Voltage (kV)	Avg. experimental mass loss (mg)	$\Delta H_{exp.}$ (kJ/g)
4	0.70	1.32 ± 0.76
6	1.27	3.26 ± 1.29
12	3.37	2.60 ± 0.45

5.4.5 Aerosol Combustion

Figure 5.11 presents an example of characteristic pressure traces recorded in CVE experiments for sample 7. The initiation of the igniter corresponds to the time of zero. For comparison, CVE traces for pure Al [134] and for Al·Mg alloy [135] are shown. The experimental results obtained with the pure -325 mesh Mg powder are also shown in Figure 5.11. The ignition delay for Mg·S is substantially longer than for all other powders. This is qualitatively consistent with longer delays observed in the ESD ignition tests; likely due to the ignition occurring inside an evaporating sulfur cloud. The rate of pressure rise is higher than for the other tested powders. The value of $(P/P_0)_{max}$ is lower than those for Al and Al·Mg alloys, but higher than that for the coarser, pure Mg powder.

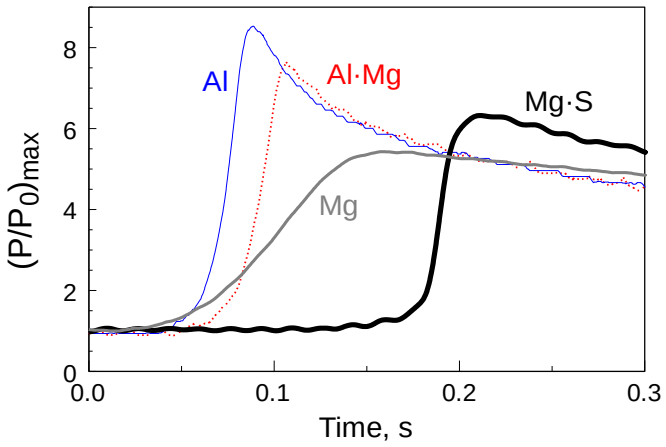

Figure 5.11 Characteristic pressure traces recorded in CVE experiments with the prepared Mg·S nanocomposite powders burning in air (sample 7) compared to similar traces for pure Al [134], Mg, and Al·Mg alloy [135].

When the vessel was opened after each experiment with Mg·S, gaseous products with a pungent odor escaped. Although, the gaseous products were not analyzed, this was the typical smell of sulfur oxide species in the form of SO and SO_2 [137]. The condensed combustion products were collected and analyzed using XRD. The results shown in Figure

5.12 indicated that both MgO and MgS were formed. Additionally, unreacted sulfur was also present.

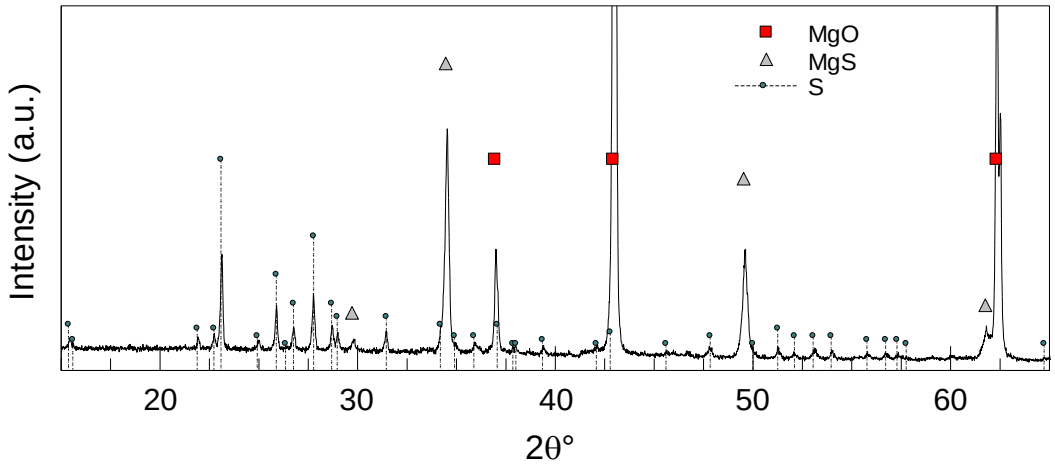

Figure 5.12 XRD patterns of combustion products collected from CVE experiments.

A summary of CVE results is given in Table 5.3 for the Mg·S composite and for pure Al, Mg and Al·Mg alloy powders. Both, average ratios of maximum explosion pressure, P_{max}, to the initial pressure, P_0, and average maximum rate of pressure rise, $(d(P/P_0)/dt)_{max}$, are shown as indicative of the energy release and rate of reaction, respectively. The average and standard deviation values were calculated from at least three repeated experiments.

A useful assessment of the combustion efficiency for different powders may be obtained comparing the experimentally determined pressure ratios, P_{max}/P_0 with those predicted by thermodynamic equilibrium calculations performed using NASA CEA code [99]. A constant volume configuration was selected in CEA. Three cases with different sets of reactants were considered. In one case, elemental Mg and S were mixed with air. In another, magnesium sulfide, MgS was mixed with air. Finally, in the third calculation elemental Mg and S were mixed with nitrogen. The experimental vessel volume and initial pressure were accounted for. For each case, calculations were carried out for different

powder mass loads, with the maximum representing the experimental mass powder load of 4.65 g. Results are shown in Figure 5.13. The powder masses lower than experimental were considered to account for imperfect aerosolization of the powder and possible deposition of the aerosolized powder on the chamber walls. Previous work suggests that the correction for the powder mass may be as large as 20% [100]. Labels in Figure 5.13 list the main combustion products predicted to form for each calculated case. The complete reaction in air predicts effectively no MgS in the products. The pressures are substantially greater than that observed in experiments, even if the mass of the powder is substantially reduced. For the cases considering MgS in air or Mg and S in nitrogen, the predicted pressures are closer to the experimentally obtained one. Because both MgO and MgS were detected in the products, the experimental situation was better represented by the latter two calculated cases.

Maximum pressures obtained in each calculation for the powder load of 4.65 g are shown in Table 5.3. In addition, Table 5.3 includes results of CEA calculations considering 4.65 g of other materials exposed to air, to provide appropriate comparison for the reference CVE experiments presented in Figure 5.11 and Table 5.3. The efficiency is calculated as a ratio of the experimental and theoretical values of $(P/P_0)_{max}$ for each material.

For all materials, the CEA-predicted pressures are higher than those experimentally determined. An anticipated reduction in the efficiency as a result of imperfect aerosolization was already discussed. In addition, the combustion efficiency is strongly affected by the particle sizes. This effect is likely responsible for the relatively low pressures and respective efficiencies observed for elemental Mg powder. It is instructive

to consider the effect of particle size on the combustion efficiency presented in Figure 5.14. For Al, Mg, and Mg·S, the efficiency drops linearly as a function of the particle size. The only outlier from the linear trend is the mechanically alloyed powder of Al·Mg, for which efficiency is greater, than is anticipated based on its particle size.

Table 5.3 CVE Experiment Results Compared to Other Fuels (Data Represent Average Values ± Standard Deviations)

Material	Volume-based avg. particle size (μm)	$(d(P/P_0)/dt)_{max}$ (s^{-1})	$(P/P_0)_{max}$ experim.	$(P/P_0)_{max}$ calculated by CEA	*Efficiency*
Mg·S	19.2	498 ± 125	6.4 ± 0.3	10.6	0.60
Al (H5) [134]	9.06	439 ± 105	8.5 ± 0.3	12.4	0.69
Mg (-325 mesh)	31.7	76 ± 42	5.7 ± 0.6	12.1	0.47
Al·Mg [135]	36.5	326 ± 53	7.6 ± 0.2	13.5	0.56

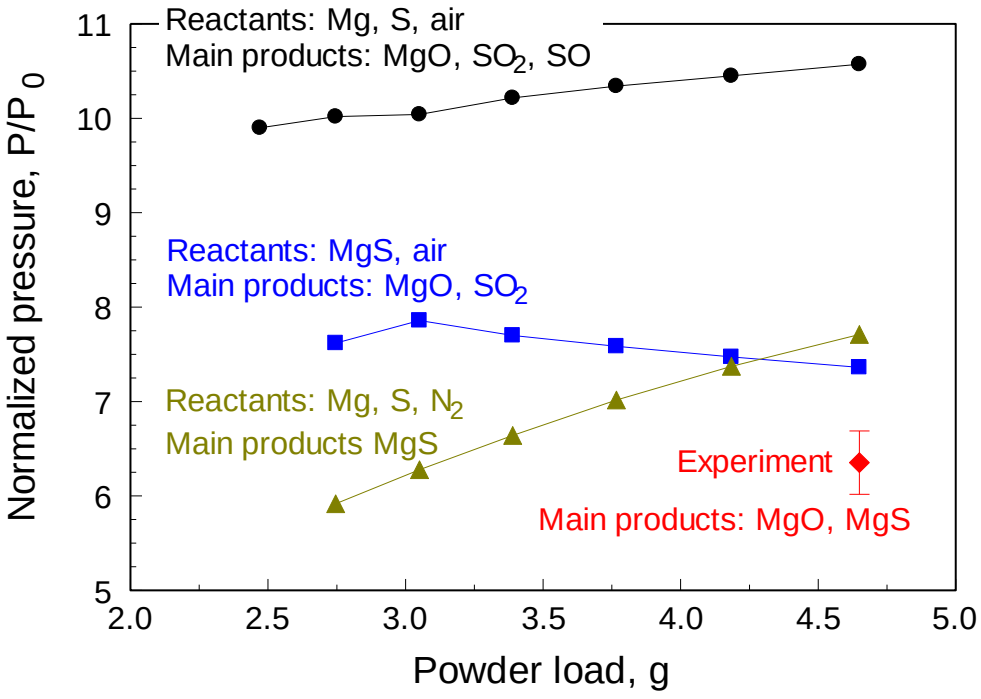

Figure 5.13 CEA pressure for three cases at various theoretical mass powder loads.

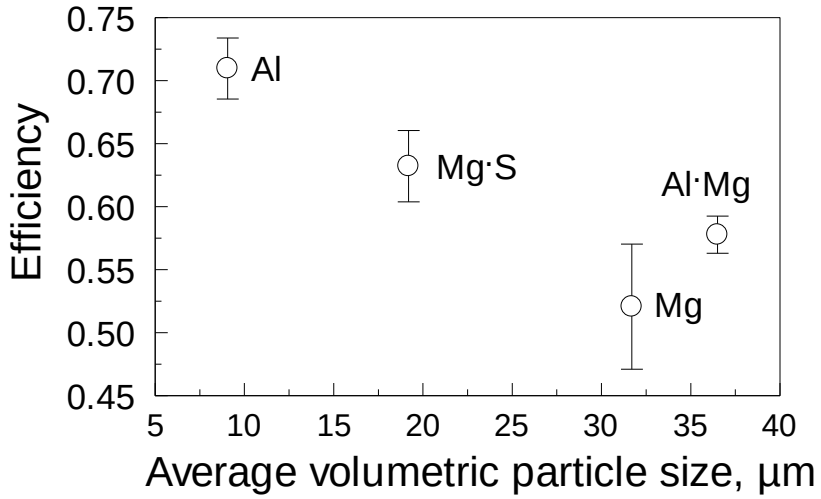

Figure 5.14 Efficiency of combustion in CVE experiments for powders of different materials as a function of their respective average volumetric particle sizes.

5.4.6 Particle Combustion in a Laminar Flame

Based on the emission pulses collected using the three filtered PMTs and processed using a technique described in [104], the distribution of the emission pulse durations representing burn times was correlated with the PSD. This allowed us to establish the relationship between the burn time and the particle size. Figure 5.15 demonstrates this relationship for the Mg·S nanocomposites as well as a pure Mg (from [104]). The results indicate that the particles of Mg·S nanocomposites have shorter burn times than the same size particles of the pure Mg, a characteristic often desired for reactive materials.

The optical emission from the 32-channel PMT for a selected particle burned inside the laminar flame with a burn time of ~2.2 ms is presented in

Figure 5.16A. The signals shown are subtracted from the background produced by the emission produced of the laminar acetylene-air flame. Additionally, the peak emission intensity (measured at 2.2 ms) is shown in

Figure 5.16B for all wavelengths. The intensity decreases for higher wavelengths; for a gray emitter this would indicate an unusually high combustion temperature (> 10,000K). The spectrum in

Figure 5.16B shows, therefore, that the emission produced by burning Mg·S composite cannot be interpreted as that produced by a gray emitter. Further spectroscopic studies of combustion of such materials are of interest.

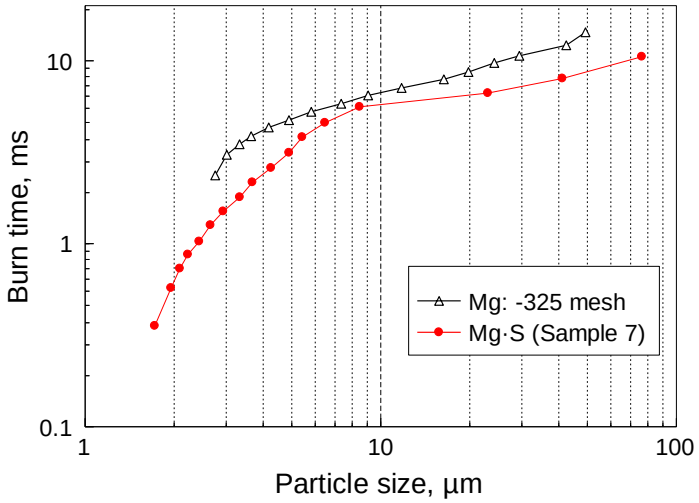

Figure 5.15 Combustion times of the Mg·S nanocomposites as a function of the particle size.

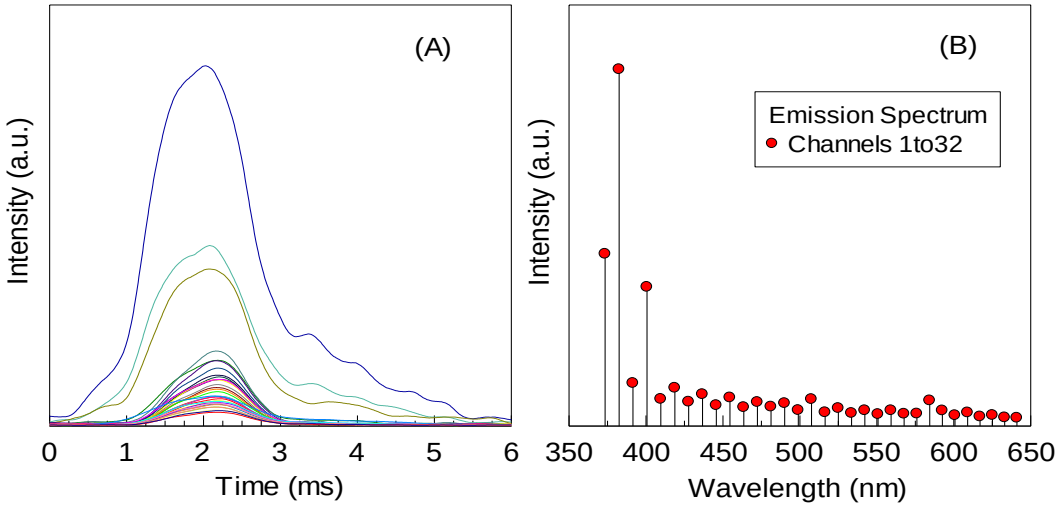

Figure 5.16 (A) Emission signals from 32 channel PMT for a single particle and (B) emission spectrum at the peak position of 2.2 ms.

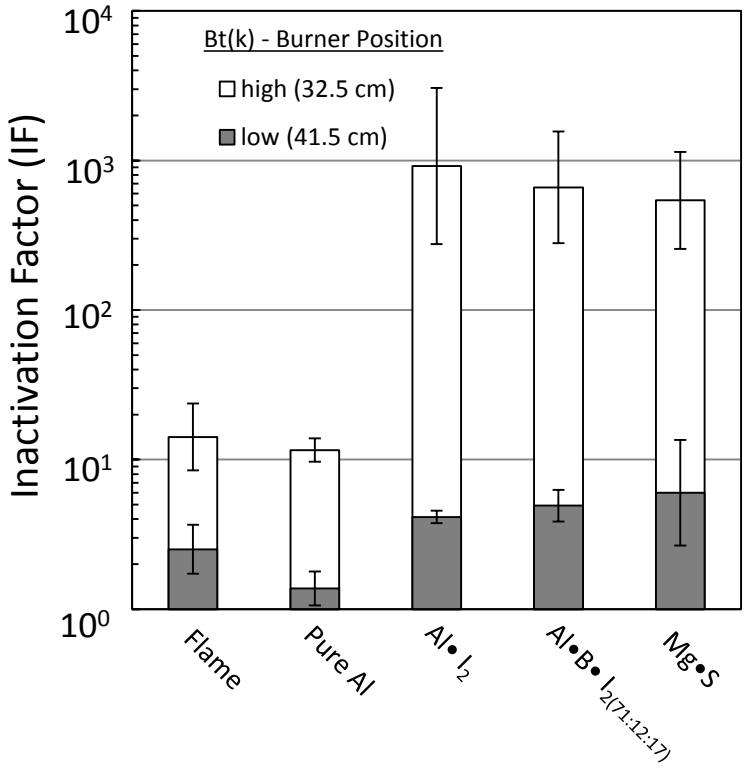

Figure 5.17 Average inactivation of aerosolized Btk spores with the Mg·S nanocomposites and other materials at two different burner positions. Exposure time is estimated to be 0.33 s. The geometric mean values and geometric standard deviations are reported.

5.4.7 Exposure of Microorganisms to Combustion Products

Inactivation of aerosolized Btk spores by combustion products of the Mg·S nanocomposite powder was observed for two selected burner positions. The weighted average temperature in the volume where the combustion products were mixed with endospores was approximately 170 and 260 ºC for the burner at low and high positions, respectively [90]. The exposure time of the bioaerosol to the combustion product was about 0.33 s. Figure 5.17 presents the IF values obtained for Mg·S. This figure also demonstrates the reference values previously reported for unseeded flame and flame seeded with pure Al powders along with IF values obtained for $Al{\cdot}I_2$ and $Al{\cdot}B{\cdot}I_2$ [90]. It was concluded that the

Mg·S nanocomposites prepared in the present study form combustion products capable of inactivating the challenge bioaerosol more effectively than unseeded hydrocarbon flame or the flame seeded with aluminum powder. The observed effect is statistically the same as for the iodine-containing materials, although mole fraction of sulfur is greater than that of iodine. Further comparison can be made with presented data in APPENDIX B as well.

5.5 Conclusions

Nanocomposite containing finely mixed magnesium and sulfur were prepared by arrested reactive milling. The powders were reactive and ignited at lower temperatures, compared to pure magnesium. Ignition of these materials occurred with substantial delays; a likely reason for such delays is formation of an evaporated sulfur cloud. The delayed ignition was observed for the powders initiated by spark and for the powder clouds ignited in a constant volume chamber by a heated wire. The powders burned faster than pure magnesium as evidenced by shorter measured burn times for individual particles, and higher rates of pressure rise in the constant volume explosion experiments. The optical emission spectra produced by burning Mg·S nanocomposite powders exhibited an unusually strong emission at short wavelengths; additional spectroscopic studies of such flames are of interest, which might establish utility of such composites in specialized pyrotechnic formulations. Combustion products generated by the Mg·S nanocomposite powders inactivated the aerosolized *Bacillus* spores much more efficiently than the combustion products originated by unseeded or aluminum-seeded flames. The efficiency of inactivation was approximately the same as that achieved by combustion of some aluminum-based composite powders containing iodine.

CHAPTER 6

COMBUSTION OF ENERGETIC POROUS SILICON COMPOSITES CONTAINING DIFFERENT OXIDIZERS

6.1 Abstract

We present a quantitative investigation of combustion of on-chip porous silicon (PS) energetic materials using oxidizers with improved moisture stability and/or minimized environmental impact compared to sodium perchlorate (NaClO4). Material properties of the PS films were characterized using gas adsorption porosimetry and profilometry to determine specific surface area, porosity and etch depth. PS energetic composites were formed using melt-penetrated or solution-deposited oxidizers into the pores. Combustion was characterized by high speed imaging and bomb calorimetry. The flame speeds quantified for PS/sulfur and PS/nitrate systems varied in the ranges of 2.9 – 3.7 $m \cdot s^{-1}$and 3.1 – 21 $m \cdot s^{-1}$, respectively. The experimental combustion enthalpies are reported for different oxidizer systems in both inert and oxidizing environments. For the PS/sulfur and the PS/nitrate systems, the experimental heats of combustion were comparable to those calculated for the thermodynamic equilibrium and taking into account an increased reactivity of PS due to the hydrogen terminated silicon surface.

6.2 Introduction

Observations of highly exothermic reactions between porous silicon (PS) and nitric acid [138] or liquid oxygen [139] in the early 1990's and the incorporation of solid oxidizers into PS pores reported in 2002 led to interest in PS composite energetic materials [17]. Initial demonstrations involved alcohol solutions facilitating transport of gadolinium nitrate and other similar oxidizers into the PS pores [17, 18]. That work was followed by

experimental surveys of several other oxidizer candidates by Clément et al. [19] and du Plessis [20, 21], including elemental sulfur which may be melt cast directly without a solvent.

One consistent result from the earlier studies is that sodium perchlorate ($NaClO_4$) performed very well in terms of the qualitative measures used, including optical emission and acoustic intensities. Our group [22-25] and others [26-29] have since carried out extensive studies of the PS/$NaClO_4$ system, quantitatively validating its performance observing highly tunable flame speeds from 1 $m \cdot s^{-1}$ [57] to over 3000 $m \cdot s^{-1}$ [58, 59], and heats of reaction of up to 22 kJ/g of PS [60]. The high performance of $NaClO_4$ is likely due in part to its high solubility in alcohols [28]; e.g., in methanol, where it exceeds 400 $g \cdot l^{-1}$ solvent at 25°C [61]. The high solubility increases oxidizer filling of the pores when the solvent evaporates [62]. Although the PS/$NaClO_4$ energetic materials perform well, the high solubility of $NaClO_4$ in both alcohols and water also correlates with its high hygroscopicity, making it difficult to use in many practical situations. Furthermore, perchlorates may present environmental and health hazards due to the long-term stability of the chlorate ion and its tendency to mimic iodide ions in biological processes [63, 64].

Therefore, in this paper we explore alternative oxidizers with potential benefits of increased moisture stability and/or perchlorate-free composition. Despite a recent study reporting interesting combustion of free standing PS films in air without the use of any additional oxidizers [140], we focus on combustion of substrate-integrated PS films with solid oxidizers including sulfur and several nitrates. A subset of these oxidizers has been qualitatively explored previously, including sulfur, calcium nitrate, and gadolinium nitrate [19-21]. This paper is the first report of quantitative measurements for flame speeds and

calorimetric combustion enthalpies using these oxidizers as well as magnesium and manganese nitrates with PS. Iodine containing oxidizers were also considered. We used thermodynamic calculations to establish a baseline for the combustion enthalpy measured. Comparisons of experiments and thermodynamic calculations suggested that combustion involved a significant amount of hydrogen, which was produced by the SiH_x passivating layer on the surface of PS; an artifact of the hydrofluoric acid etch [22, 139, 141].

6.3 Materials and Experimental Methods

6.3.1 Sample Fabrication

The authors would like to note that certain steps within the sample fabrication process can be hazardous without utilizing proper facilities, procedures, and equipment. In particular, the hydrofluoric acid (HF) used during the etch process must only be used under an appropriate fume hood designed for use with acids, and with the proper personal protective equipment.

The starting material for PS film fabrication was <100> oriented, double-side polished, boron doped, p-type silicon wafers of 525 μm thickness and 100 mm diameter with resistivity of 1-10 Ω·cm. The wafers were obtained from Rogue Valley Microdevices (Medford, OR) with a double sided 6000 Å silicon nitride (Si_3N_4) layer deposited using low stress, low pressure chemical vapor deposition (LPCVD). For etching, the silicon nitride layer was completely removed from the backside, attached to a platinum anode. A sputter deposited 1700 Å platinum layer acted as a cathode for the electrochemical etch.

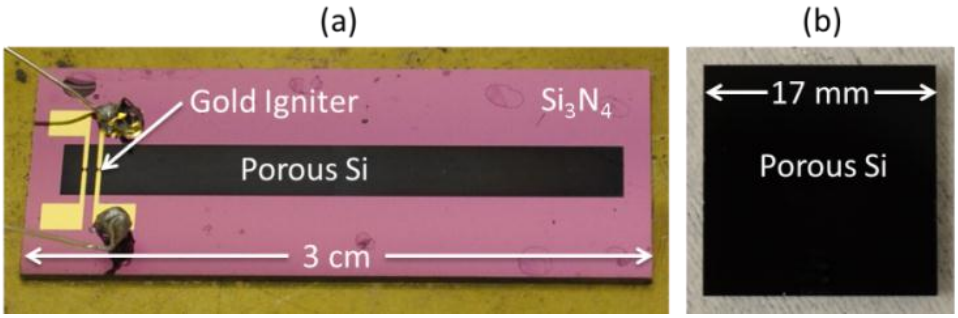

Figure 6.1 (A) PS strip (27 mm long x 3 mm wide) used for flame propagation measurements; (B) square PS chip (17 mm x 17 mm) used for bomb calorimetry measurements.

A detailed description for fabrication of the PS strips (27 mm long x 3 mm wide) shown in Figure 6.1(A) for flame propagation measurements is presented elsewhere [59, 60]. The etch solution consisted of hydrofluoric acid (HF, 49% in H_2O), ethanol (EtOH), and hydrogen peroxide (H_2O_2, 30% in H_2O) added at 2.4% of the HF-ethanol bath volume. The desired macro-structure of PS film was obtained by selectively removing the silicon nitride layer from the front side of the wafer with a photolithographic process to expose bare silicon. The HF:EtOH ratio of the etch solution was 3:1 for all PS strips. An etching time of 5 min was used for wafers with resistivities of 1-10 Ω·cm. Samples for bomb calorimetry shown in Figure 6.1(B) required a larger mass and therefore were different from those for flame speed analysis. These consisted of 1–10 Ω·cm wafers diced into 17 × 17 mm chips and etched in the HF:EtOH for 30 minutes. For these samples, a longer etch time was required due to a larger surface area ratio of front-side silicon to back-side platinum, which affects the etch current [142].

6.3.2 Porous Silicon Characterization

After the fabrication of PS films, material properties were characterized using gas adsorption porosimetry. The PS strip was cleaved and tested using a Micromeritcs Tristar

II 3020 surface area analyzer to determine the surface area, pore size, and pore volume. The system uses Brunauer-Emmett-Teller (BET) theory [143, 144] to determine surface area and Barrett-Joyner-Halenda (BJH) theory [143, 145] to determine pore size and pore volume. The mass of the PS was determined using a gravimetric technique, with mass recorded before and after the removal of PS via a reaction with sodium hydroxide (NaOH). Due to the destructive nature of this measurement, additional samples were prepared for every batch of etch solution for material characterization experiments. The mass for these samples varied from 1.6 – 1.8 mg for strips for the flame speed study and 9.1 – 18.3 mg for the chips for bomb calorimetry. We have previously showed [60] that the variation in material properties of samples from the same wafer is between 1% and 3%, and therefore the samples used for combustion were assumed to have the same material properties as samples from the same wafer that were used for material characterization.

Due to the variation in the mass from wafer to wafer, nitrogen adsorption porosimetry was conducted for each wafer used in this study to determine the PS material properties. Additionally, the porosity was determined using the following equation (6.1):

$$P\ (\%) = \frac{100v}{\left(v+\frac{1}{\rho}\right)} \tag{6.1}$$

where P is the porosity, v is specific volume of the pores found from porosimetry, and ρ is the bulk density of silicon (2.33 g·cm^{-3} [143]). The etch depth of PS strips was determined from profilometry using an Ambios Technology, Inc. XP-2 High Resolution Surface Profiler after the removal of PS with NaOH. The resolution of this device was 10 nm.

6.3.3 Pore Loading

The energetic composites were formulated by impregnating the PS film with various oxidizers. Previous efforts focused on characterizing PS with sodium perchlorate ($NaClO_4$), where a nearly saturated 3.2 M methanol solution of $NaClO_4$ was drop cast on top of the porous structure [59, 60, 142, 146]. The oxidizer was then allowed to seep into the pores and dry, resulting in an energetic system. Using the $NaClO_4$ system as a reference, the present study quantitatively investigates the reactivity of PS film with other viable oxidizers. The list of oxidizers is presented in Table 6.1 along with the pore loading technique used for each oxidizer. With various oxidizers, different pore loading techniques were necessary to achieve stable energetic composites. With the drop cast pore loading technique, different compatible solvents were used depending on the oxidizer. For sulfur, due to its low melting point, 119.6 ºC [147], and stability in the liquid state, melting sulfur powder on top of the PS strip (S_{melted}) was used as a pore loading technique. After melting, sulfur on top of the PS was cooled to room temperature.

All PS/oxidizer materials after pore loading became sensitive to ignition stimuli. Although we did not quantify the sensitivities, it should be noted that several samples ignited when being handled using non-grounded tools (i.e., metal tweezers). Electro-static sparks or friction likely caused ignition. PS based composites should be handled with extreme care after pore loading. Specifically, PS loaded with oxidizers, $NaClO_4$ and $Mn(NO_3)_2$, were observed to be most sensitive to handle. Samples with $Mg(NO_3)_2$, $Ca(NO_3)_2$ and sulfur were less sensitive.

For bomb calorimetry samples, the oxidizer content was measured for melted or drop cast cases. The average amount of sulfur melted on top of the PS chip was 0.077 ±

0.012 g. For nitrate-based oxidizers, 40 – 50 µL of solution was drop cast on top of the PS chip to fully cover the top surface of the chip and dried inside a nitrogen flowing dry-box for at least 30 minutes.

Table 6.1 Commercially available oxidizers used in this study

Chemical Name	Chemical Formula	Supplier	Purity	Pore Loading Technique
Sulfur, powder, -100 mesh	S	Sigma-Aldrich	Reagent grade	Melted on top of PS Drop cast CS_2 solution; 1.9M
Gadolinium nitrate hydrate	$Gd(NO_3)_3 \cdot xH_2O$ ($x \approx 6$)	Alfa Aesar	99.9%	Drop cast methanol solution; 0.8M & 2.7M
Magnesium nitrate hexahydrate	$Mg(NO_3)_2 \cdot 6H_2O$	Alfa Aesar	98%	Drop cast ethanol solution; 0.8M
Calcium nitrate tetrahydrate	$Ca(NO_3)_2 \cdot 4H_2O$	Alfa Aesar	99%	Drop cast ethanol solution; 1M
Manganese nitrate tetrahydrate	$Mn(NO_3)_2 \cdot 4H_2O$	Alfa Aesar	98%	Drop cast ethanol solution; 1M
Potassium periodate	KIO_4	Alfa Aesar	99%	Drop cast methanol solution; conc. <0.1M
Sodium metaperiodate	$NaIO_4$	Alfa Aesar	98%	Drop cast methanol solution; conc. <0.2M
Iodopentoxide	I_2O_5	Sigma-Aldrich	≥98%	Drop cast methanol solution; conc. <0.2M Drop cast acetone/ distilled water mixture solution; conc. <0.6M

Gravimetric measurements were conducted to estimate the oxidizer mass which fills the pores from drop casting sulfur and nitrates as described elsewhere [60]. In an attempt to account for excess dry oxidizer on the surface of each chip, surface oxidizer was removed from the insensitive (non- porous) Si_3N_4 regions on the top of the chip by a cotton swab, leaving excess oxidizer above the sensitive PS region. The removed oxidizer was weighed, and the surface area that was covered by it was measured. Assuming that the surface oxidizer above the active PS area, which was not wiped, was covered by the same mass per unit area of excess oxidizer, the mass of excess dry oxidizer above PS was estimated. By subtracting this estimate from the total amount of oxidizer left on the sample, the mass of oxidizer in the pores was calculated.

6.3.4 Characterization of Porous Silicon Energetic Composite

After oxidizing the PS strips, the ignition and combustion events were captured by a Photron FASTCAM SA5 high speed camera at 100,000 frames per second inside an enclosed optically transparent box. All experiments were conducted in a nitrogen flowing dry-box with at least three repeats, except one experiment performed in air. The high speed video was processed using open source software, Tracker Video Analysis and Modeling Tool, to track the flame front during combustion. The average flame speed was calculated for steady flame fronts using a linear fit of the distance traveled by the luminous flame front as a function of time. The standard deviation was calculated for all experiments with at least three or more flame speed measurements for all cases except for one. Flame speeds were successfully measured for energetic composites involving sulfur and nitrate-based oxidizers, but not for iodine-based oxidizers. All iodine-containing oxidizers had low solubility in the respective solvents, and the PS strips with iodine-based oxidizers did not self-propagate for the concentrations shown in Table 6.1. Because of their low reactivity, these materials were not characterized further.

Bomb calorimetry measurements were conducted with a Parr Semimicro Calorimeter (Parr 6725) and a Parr Calorimetric Thermometer (Parr 6772). The calibration of the calorimeter was completed using benzoic acid pellets. The constant volume specific heat capacity of the bomb calorimeter (C_v) was determined to be 2.1 ± 0.14 kJ m·s^{-1}. Using the PS chip (17 mm x 17 mm), the energetic composite was prepared with both sulfur and nitrate-based oxidizers for the bomb calorimetry measurement. The samples were placed inside the bomb cell pressurized to 2 atm with either dry nitrogen or oxygen. An electrically heated fuse wire was used to ignite the sample inside the sealed cell. The

consumed fuse wire length during each measurement was determined and the energy contribution from the burned fuse wire was subtracted from the total heat measured. The average combustion enthalpy and standard deviation after subtraction was calculated for all energetic composites. The measurement uncertainty also included the error associated with the calibrated C_v value of the calorimeter. For specific nitrates (containing Mg, Ca, or Mn), multiple experiments were not conducted in nitrogen. Therefore, error bars shown in the results are based only on the calibration error. Samples without multiple experimental runs were difficult to reproduce for a variety of reasons. For $Mn(NO_3)_2 \cdot 4H_2O$ samples, preparing and loading them inside the bomb cell was difficult due to their high sensitivity. Therefore, only one experiment was conducted in both nitrogen and oxygen. In the case of $Mg(NO_3)_2 \cdot 6H_2O$, and $Ca(NO_3)_2 \cdot 4H_2O$, a larger mass was required to register a successful signal in nitrogen, and therefore two 17 x 17 mm samples were placed in the calorimeter. These samples were less sensitive; however, extreme care was taken to load the bomb cell with two samples. Additionally, for the $S_{drop\ cast}$ sample, the fuse wire ignited the energetic composite but a signal was not registered under nitrogen environment even with the use of two PS chips. Although, sulfur containing samples were less sensitive than perchlorates and nitrates, they were still sensitive to handle. We did not attempt an experiment with more than two PS chips due to this reason for these samples.

6.4 Results and Discussion

6.4.1 Characteristics of PS

The gas adsorption porosimetry results for the PS strips for flame speed experiments are reported in Table 6.2. The pore size, pore volume, and surface area of these samples varied

in the range of 27.6 – 33.3 Å, 0.73 – 1.12 $cm^3 \cdot g^{-1}$, and 733 – 983 $m^2 \cdot g^{-1}$, respectively. The etch depth measured using profilometry (representing the maximum depth the oxidizer could penetrate) ranged from 24 to 26 μm. The porosity reported in Table 6.2 was calculated using equation (1) for all samples. PS chips for bomb calorimetry were also characterized using gas adsorption porosimetry, where pore size, pore volume, and surface area ranged from 32.4 – 34.0 Å, 0.81 – 1.08 $cm^3 \cdot g^{-1}$ and 647 - 911 $m^2 \cdot g^{-1}$, respectively.

In addition to porosity parameters, SiH_2 present on the surface of PS may have affected the combustion enthalpy significantly. It is well known that the etching of silicon with HF removes the native oxide layer and passivates the surface with a hydrogen terminated layer in the form of SiH_x (x = 1,2,3) [148, 149], where it can be assumed that the average x=2, as for SiH_2. Surface functionalization of PS and the presence of SiH_2 can affect combustion and, in particular, results of the bomb calorimetry measurements. Therefore, we estimated the mole ratio of silicon hydride relative to the bulk PS (bulk PS = porous silicon + hydrogen terminated surface), $n_{(SiH_2:PS)}$, using the following equation (6.2),

$$n_{(SiH_2:PS)} = \left(\frac{SA \cdot \rho_{atom}}{N_A}\right)\left(\frac{MW_{Si}}{1\ g\ of\ PS}\right) \tag{6.2}$$

where SA is the specific BET surface area (647 - 911 $m^2 \cdot g^{-1}$ of PS) for PS chip (17mm x 17mm bomb calorimetry samples), ρ_{atom} is the atom surface density (7.5×10^{18} atoms$\cdot m^{-2}$ of PS), N_A is the Avogadro constant, and MW_{Si} is the molecular weight of silicon. $n_{(SiH_2:PS)}$ was estimated to range from 0.23 to 0.32, due to the variation in surface area between wafers.

6.4.2 Pore Loading

The energetic composite can be further understood by determining the amount of oxidizer present inside the pores. To estimate this amount, a gravimetric technique presented in [60] for $NaClO_4$ was used for the drop cast pore loading of 1.8 M and 0.8 – 1 M concentrated sulfur and nitrate-based oxidizers, respectively. The measured oxidizer mass inside the pores ranged from 0.56 to 0.89 mg, depending on the drop cast oxidizer. The equivalence ratios derived from this measured mass, Φ_m, are reported in Table 6.3, and show the energetic systems to be fuel-rich. Additionally for drop cast samples, equivalence ratios, Φ_c, were calculated for samples with 70% porosity, assuming the concentrated solution initially occupies the entire porous volume, before the evaporation of the solvent. This calculation was expected to produce an upper bound for the amount of oxidizer deposited in the pores. For $NaClO_4$, the reported values of Φ_c and Φ_m are comparable to each other [60]. However, in this work, Φ_c was 1.5 – 3 times higher than Φ_m, indicating that the measured amount of oxidizer in the pores was larger than the calculated value. Although porosity values in Table 6.2 actually ranged from 63-72 %, Φ_c was still higher than Φ_m over this range for each sample. This apparently unrealistic result may be explained by different morphology of oxidizers deposited on top of the porous surface as compared to that of bulk Si. Therefore, it seems that the gravimetric technique using removal of oxidizer from insensitive surfaces of crystalline silicon is not well suited for drop cast sulfur and nitrate based oxidizers. A better estimate of mass inside the PS after pore loading remains to be the calculated Φ_c values presented in Table 6.3, and in any case it appears that very fuel-rich energetic composites were formed.

Since it was not possible to use the gravimetric technique for the S_{melted} case, the equivalence ratio as a function of porosity was calculated assuming that all the available volume inside the porous structure was occupied by sulfur, creating a fully dense system ($S_{fully\ dense}$). For example, a 70% porous system filled with sulfur (density of 2.069 $g \cdot cm^{-3}$ [147]) is expected to reach equivalence ratio of 1.1, near stoichiometric conditions (equivalence ratio of unity) as shown in Table 6.3.

6.4.3 Flame Propagation

6.4.3.1 PS/Sulfur. A built-in gold bridge wire [23, 58-60] was used to ignite the sample in nitrogen and simultaneously trigger the image capture process. Average measured flame speeds for different sets of samples are shown in Table 6.2. Samples with sulfur powder melted on top of the strip (S_{melted}) exhibited similar flame speeds as drop cast sulfur ($S_{drop\ cast}$) samples at 3 $m \cdot s^{-1}$. An additional flame speed experiment was repeated in air to ensure both the stability and reactivity of the S_{melted} system under ambient conditions. A comparable flame speed of 2.9 $m \cdot s^{-1}$ was observed in air; however, the flame appearance was very different from that in nitrogen. Figure 6.2(A) and Figure **6.2**(B) show the combustion events of Smelted tested in nitrogen and air, respectively. The flame in air flared much more aggressively and the combustion products emitted a higher intensity light compared to the flame in nitrogen for both S_{melted} and $S_{drop\ cast}$. We suspect a considerable secondary reaction in the presence of air occurred in the gas phase, which caused the intensified flame characteristics observed in air. The combustion products from the initial Si/S reaction are expected to further react in air to form various silicon and sulfur oxides. It is surprising that both S_{melted} and $S_{drop\ cast}$ with apparently different pore loading

and equivalence ratio as indicated in Table 6.3, showed comparable flame speeds that were much lower compared to the PS/$NaClO_4$ system [58-60]. It is also interesting that the violent gas phase reaction occurring in air did not alter the flame speed. Note that the pattern of the gas phase flame suggests a relatively low speed of gas motion and substantial effect of natural convection. Thus, produced gas species likely did not cause a local pressure increase or substantial convective heat transfer in the direction of flame propagation. Possibly, the flame speed in this case was controlled by heat transfer through a composite Si/S structure obtained in PS, although further work is desired to elucidate the flame propagation mechanism.

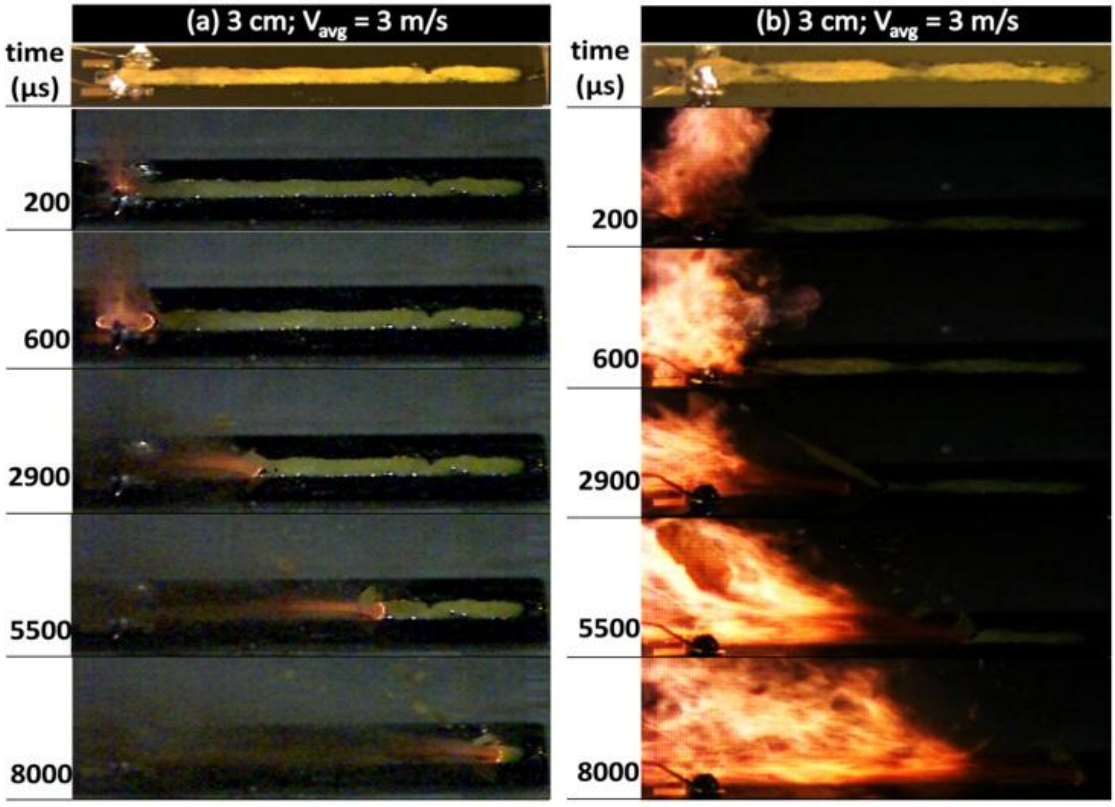

Figure 6.2 Combustion event of (A) Smelted tested in nitrogen and (B) Smelted tested in air.

Table 6.2 Material Properties of PS Strips for Flame Speed Characterization, Etched for 5 Minutes in 3:1 (HF:Et) Etch Solution; Flame Speed Measurements Using Various Oxidizers

Pore Loading Technique / Experimental Environment	Surface Area ($m^2 \cdot g^{-1}$)	Pore Volume ($cm^3 \cdot g^{-1}$)	Pore Size (Å)	Porosity (%)	Etch Depth (μm)	Flame Speed ($m \cdot s^{-1}$)
S_{melted} / Air	845	0.98	31.8	70	26	2.9
S_{melted} / N_2	808	0.73	27.6	63	24	3.0 ± 0.1
$S_{drop\ cast}$ / N_2	983	1.12	31.8	72	25	3.7 ± 0.1
2.7 M $Gd(NO_3)_{3\ drop\ cast}$ / N_2	845	0.98	31.8	70	26	3.1
0.8 M $Gd(NO_3)_{3\ drop\ cast}$ / N_2	845	0.98	31.8	70	26	10.1 ± 2.2
0.8 M $Mg(NO_3)_{2\ drop\ cast}$ / N_2	733	0.76	29.9	64	25	4.4 ± 1.4
1 M $Ca(NO_3)_{2\ drop\ cast}$ / N_2	777	0.76	28.9	64	25	9.8 ± 1.9
1 M $Mn(NO_3)_{2\ drop\ cast}$ / N_2	777	0.76	28.9	64	25	21.0 ± 7.0

Table 6.3 Gravimetrically Measured Amount of Oxidizer Inside the Pores Along with Measured and Calculated Equivalence Ratios

Pore Loading Assumption	Pore Loading Technique	Measured mass inside the pores (mg)	Eq. Ratio using measured mass (Φ_m)	Calculated Eq. Ratio using assumption (Φ_c)
70% porous sample fully dense with oxidizer	S_{melted}	--	--	1.1
1) 70% porous sample filled with oxidizer solution 2) only residual oxidizer after evaporation of solvent is expected to be loaded into the pores	$S_{drop\ cast}$	0.89	3.8	4.8
	0.8 M $Gd(NO_3)_{3\ drop\ cast}$	0.67	10.1	15.6
	0.8 M $Mg(NO_3)_{2\ drop\ cast}$	0.67	8.5	24.6
	1 M $Ca(NO_3)_{2\ drop\ cast}$	0.70	7.5	20.5
	1 M $Mn(NO_3)_{2\ drop\ cast}$	0.56	10.1	19.9

6.4.3.2 PS/Nitrates. The average flame speeds for PS/nitrate-based energetic composites are reported in Table 6.2, ranging from 4.4 – 21.0 $m \cdot s^{-1}$ for ≤ 1 M nitrate-based solution. In the case of $Gd(NO_3)_3$, a reduced flame speed was observed for a sample with a higher concentration obtained from a 2.7 M solution. We suspect that due to the higher viscosity solution, the pore loading was reduced, causing a decreased flame speed. When utilizing $Gd(NO_3)_3$ in solution, variation in oxidizer concentration produced visible differences in solution viscosity. The 2.7M solution created a thick layer of $Gd(NO_3)_3$ over the top of the PS film after drop casting and drying. This behavior was in contrast to the

energetic system involving sodium perchlorate [60], where a noticeable difference in viscosity was not seen for a nearly saturated 3.2 M solution of $NaClO_4$ compared to 0.8 M $NaClO_4$ solution. Additionally, the pore loading increased four times when drop casting higher concentrations of $NaClO_4$. We suspect that due to a higher viscosity solution in $Gd(NO_3)_3$, oxidizer penetration into the pores was limited, and likely hindered observed flame speeds.

Figure 6.3 shows combustion event snapshots for all nitrates used in this study. A self-propagating reaction was observed for these composites with flame speeds slightly greater than for the sulfur containing energetic composites. Qualitatively, greater amounts of ejected gas phase species observed in Figure 6.3 correlated with higher flame speeds in Table 6.2. This observation was supported by chemical equilibrium calculations performed with Cheetah 7.0 [150] under constant pressure for PS/sulfur, PS/$Ca(NO_3)_2$, and PS/$NaClO_4$. Other nitrates were not available in Cheetah 7.0. Results predicted that PS/$NaClO_4$ produces 25% more gaseous products than PS/$Ca(NO_3)_2$, and gas production from PS/$Ca(NO_3)_2$ was ~6x that of PS/sulfur. Note that based on the shape and structure of the luminous zones above the PS surface, it is apparent that the ejected gas species moved faster than those observed in Figure 6.2(B), for PS/sulfur combustion in air. Thus, it may be that the gas species released by decomposing nitrates accelerated convective heat transfer and thus caused greater flame speeds. Because all flame speeds observed in these experiments are much lower compared to PS/$NaClO_4$ system [58-60], the effect of convective heat transfer for nitrates appears weaker than for sodium perchlorate. This conclusion is consistent with a lower expected total gas release by the decomposing nitrates. Similarly, conductive heat transfer may increase in the PS/nitrates due to changes

in the combustion temperatures compared to PS/suflur. This could results in increasing flame speeds for PS/nitrates compared to PS/sulfur. Therefore, it is likely that both convective and conductive heat transfer mechanisms affect flame speeds for PS/nitrates. The dominating mechanism may be difficult to identify.

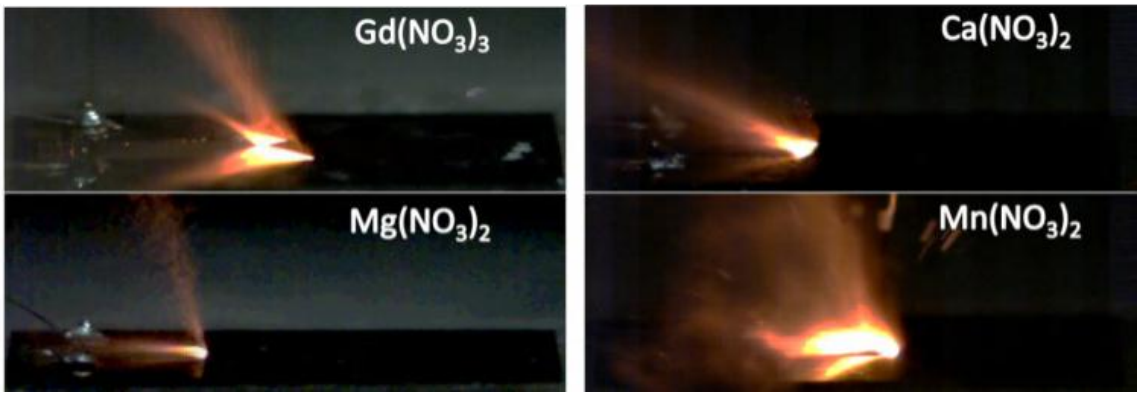

Figure 6.3 Combustion event snapshots of PS/nitrate systems during flame speed measurements.

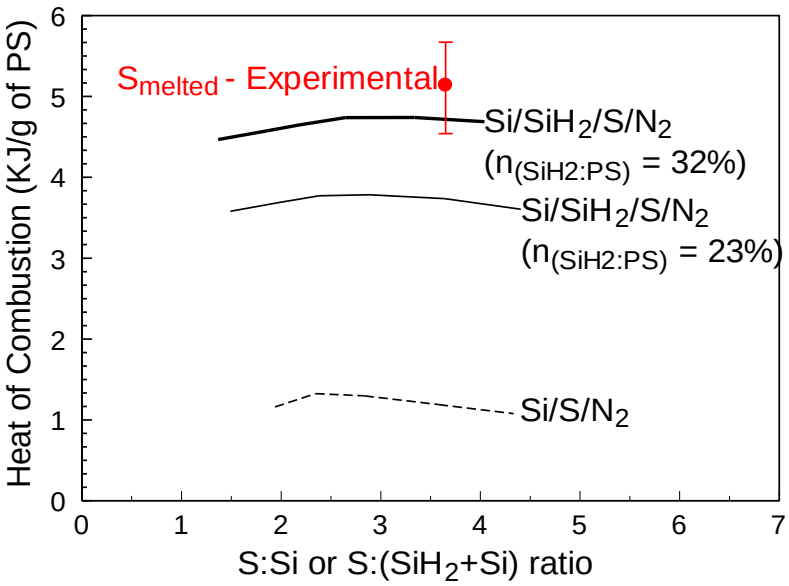

Figure 6.4 Combustion enthalpy for $Si/S/N_2$ and $SiH_2/Si/S/N_2$ system from CEA compared to bomb calorimetry experiment of S_{melted} in N_2.

6.4.4 Bomb Calorimetry

6.4.4.1 PS/Sulfur. Experimental results shown in Figure 6.4 are compared to calculations using NASA CEA thermodynamic equilibrium code [99] for the PS/sulfur combustion in nitrogen. A constant volume configuration was selected in CEA, where the calculations considered the experimental bomb cell volume and initial pressure. Using these parameters, the amount of nitrogen filling the bomb cell volume was calculated using ideal gas law. The initial amount of nitrogen which filled the bomb cell was kept constant for all experiments and for respective CEA calculations. Initially, a CEA calculation was performed with reactants involving $Si/S/N_2$ to compare with the experimental results. Additionally, two other calculations were performed using the reactants $SiH_2/Si/S/N_2$, accounting for possible functionalization of the PS surface as discussed in part 5.4.1. Because the heat of formation of functionalized PS is not well defined in the literature, the only available gas phase SiH_2 species from the CEA library was selected for calculations. Although the use of gas phase species may result in overestimation of the heat of combustion, the calculations will nevertheless provide insight into how functionalization affects combustion. For $SiH_2/Si/S/N_2$, the upper and lower range of $\boldsymbol{n_{(SiH_2:PS)}}$ obtained from equation (5.2) were used to calculate the combustion enthalpy. The mole ratios of S:Si and/or S:(Si+SiH_2) were varied in Figure 6.4 to account for the range between the sulfur limited case, $S_{\text{fully dense}}$ (mole ratio ≈ 1.40), and the excess sulfur case, S_{melted} (mole ratio ≈ 3.65). The calculations did not converge for the $Si/S/N_2$ at the lowest S:Si ratio, corresponding to its $S_{\text{fully dense}}$ case. Although the combustion enthalpies for the considered compositions ($Si/S/N_2$, and $SiH_2/Si/S/N_2$ with $\boldsymbol{n_{(SiH_2:PS)} = 0.23}$ and $\boldsymbol{n_{(SiH_2:PS)} = 0.32}$) show a maximum for each case, the variation in predicted reaction enthalpy was relatively

small. The maximum calculated combustion enthalpies for the compositions with S_{melted} were 1.2 kJ/g of PS for $Si/S/N_2$, 3.7 kJ/g of PS for $SiH_2/Si/S/N_2$ with $\boldsymbol{n_{(SiH_2:PS)} = 0.23}$ and 4.7 kJ/g of PS for $SiH_2/Si/S/N_2$ with $\boldsymbol{n_{(SiH_2:PS)} = 0.32}$. When comparing major product species predicted by CEA during combustion, silicon sulfide was the most dominant in all three cases. In the cases of $SiH_2/Si/S/N_2$, other major species such as H_2S and H_2 were present. The calculations did not predict significant amounts of silicon nitride species.

The experimental combustion enthalpy obtained from bomb calorimetry under nitrogen was 5.2 ± 0.6 kJ/g of PS. The error bar is based on standard deviation of both the error from multiple measurements as well as the error associated with the calibrated C_v value of the calorimeter. Note that the reported experimental value is normalized by the measured PS mass. The mass of the PS was determined using a gravimetric technique, with mass recorded before and after the removal of PS via a reaction with sodium hydroxide (NaOH). Since this was a destructive process, it was not possible to test the mass of the PS chips used in the actual bomb calorimeter measurements. Instead, the measured mass of one of the 17 mm x 17 mm PS chip from each wafer was assumed to be representative of every sample from that wafer, and was used to normalize the total heat release observed during the bomb calorimetry measurement conducted with samples from the same wafer. The error in defining the mass of PS used in the actual test was not quantified and not taken into account. Therefore, the error reported for the experimental values is under-estimated. Additionally, the bulk silicon and platinum were considered to be inert, while the total heat release was solely considered from the PS reaction. However, if even a small percentage of bulk silicon reacted with the oxidizer, the combustion

enthalpy per unit mass would decrease because of the additional higher density fuel. Even considering the above caveats, comparisons of CEA calculations and the experimental values suggest that the likely presence of SiH_2 species discussed in Section 6.4.1 led to a significant increase in the measured reaction enthalpy compared to that expected for PS with an unmodified surface. Indeed, only the combustion enthalpy calculated for the $^{0.32}SiH_2/Si/S/N_2$ system with the highest possible value of $n_{(SiH_2:PS)}$ was close to the experimental value.

6.4.4.2 PS/Nitrates. The combustion enthalpy of each energetic composite prepared using the nitrate-based oxidizer was tested inside the bomb calorimeter under a nitrogen environment. Comparisons of measurements with theoretical heats of combustion were of interest. The thermodynamic calculations for the PS/nitrates using NASA CEA code could not be conducted because the CEA library does not contain these chemicals. However, the enthalpies of formation for anhydrous form of nitrates and $NaClO_4$ were obtained from the literature [48] for all but $Gd(NO_3)_3$ to estimate the expected heat of reaction based on the following reactions (R1) and (R2). In reaction (R1), M represents the anions (Mg, Ca or Mn) and $\boldsymbol{n}$ represents the amount of hydrogen termination (23 – 32 % of SiH_2).

$$2.5n\ SiH_2 + 2.5(1-n)\ Si + M(NO_3)_2 \rightarrow 2.5\ SiO_2 + MO + 2.5n\ H_2 + N_2 \quad (R1)$$

$$n\ SiH_2 + (1-n)Si + (0.5 + 0.25n)NaClO_4 \rightarrow SiO_2 + (0.5 + 0.25n)NaCl + n\ H_2O \quad (R2)$$

According to the pore loading analysis conducted in Section 5.4.2, the composition of the reactive energetic composite depends on how the oxidizer is loaded into the pores of the PS film. For example, in the case of nitrates and $NaClO_4$, only about 20 - 30 wt. % of the oxidizer drop cast on the surface is expected to fill the pores, while the residual oxidizer sits on top of the chip [60]. This residual amount is not usually expected to participate in

the reaction due to a relatively long diffusion distance between the PS and residual oxidizer. However, this may not be the case for the combustion event taking place inside a pressurized constant volume cell in the bomb calorimeter, when the time of reaction could be extended. To evaluate the amount of oxidizer participating in the reaction with PS, the experimental results were compared with three calculations. For each calculation, a different oxidizer-limited assumption shown below was used to calculate the expected energy release for each system, while also including the SiH_2 terminated surface.

<u>oxidizer-limited assumptions</u>

(i) all of the drop cast oxidizer participated in the reaction with $n_{(SiH_2:PS)} = 0.32$

(ii) all of the drop cast oxidizer participated in the reaction with $n_{(SiH_2:PS)} = 0$

(iii) only the pore loaded oxidizer participated in the reaction with $n_{(SiH_2:PS)} = 0.32$

Results of these calculations are shown in Figure 6.5. The error bars include experimental error as well as calibration error. Only the experimental value for $Gd(NO_3)_3$ is shown because the heat of formation value for $Gd(NO_3)_3$ could not be obtained to calculate its combustion enthalpy. The measured energy release best correlates with the calculated heat of reaction for $Ca(NO_3)_2$, $Mn(NO_3)_2$ and $NaClO_4$ when considering an oxidizer limited case with all of the drop cast amount participating in reaction R1 and R2. Consistent with the result from the PS/sulfur system, it appears that the PS surface functionalization with SiH_2 had a substantial effect on the combustion enthalpy. In the case of $Mg(NO_3)_2$, the experimental value falls in between the assumptions ii and iii. This may be due to the fact that not all of the oxidizer reacted.

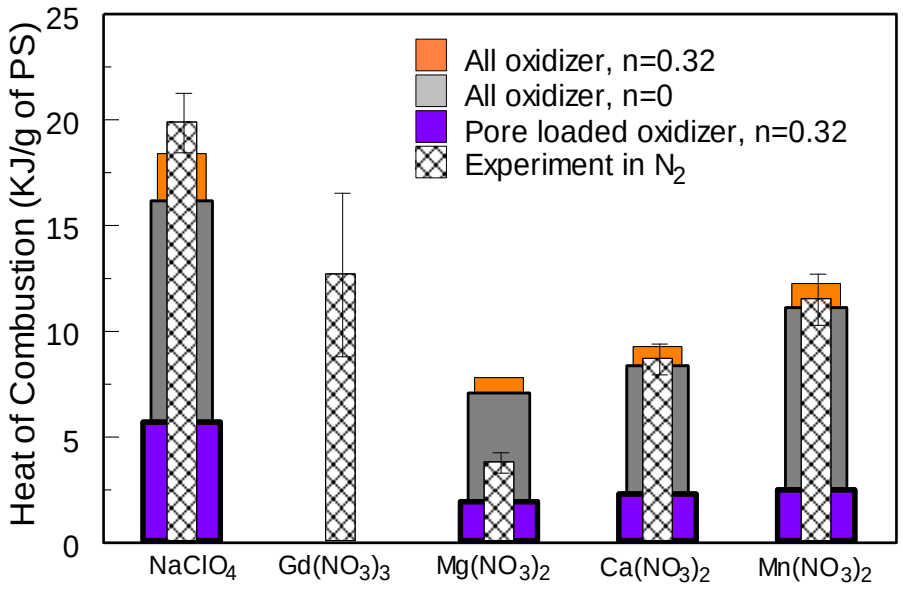

Figure 6.5 Experimental combustion enthalpy in nitro-gen for 3:1 etch solution ratio (HF:ethanol). The top of each bar color indicates the total heat calculated using each oxidizer-limited assumption.

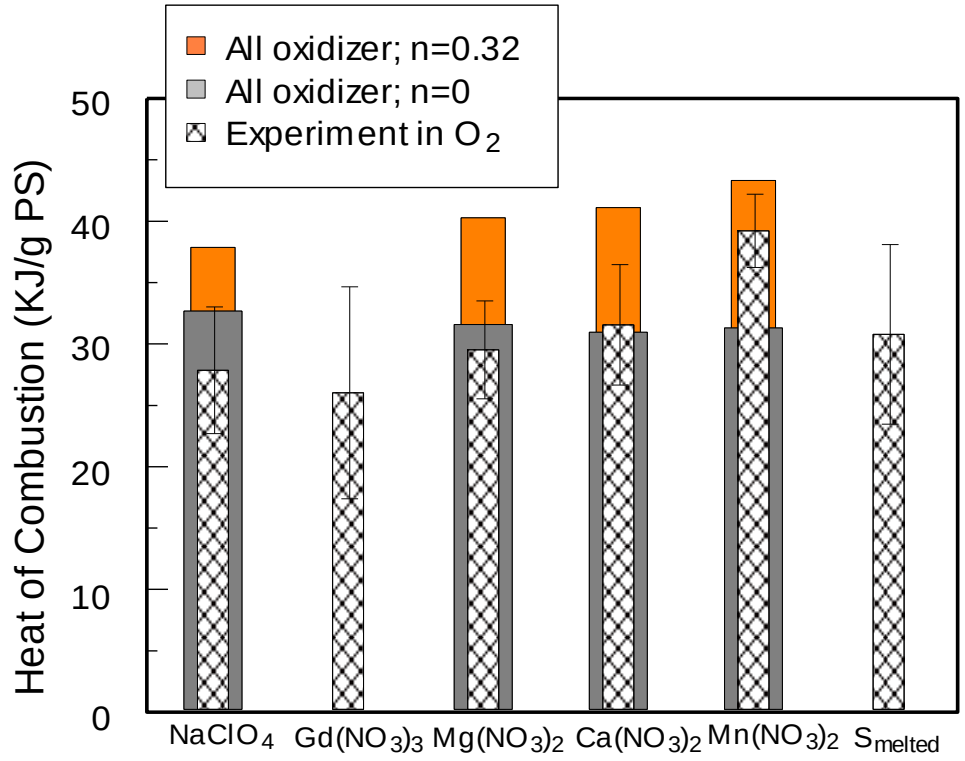

Figure 6.6 Experimental combustion enthalpy in oxygen for 3:1 etch solution ratio (HF:ethanol). The error bar includes experimental error as well as calibration error.

For all systems, the experimental enthalpies exceeded their calculated values obtained assuming that only the oxidizer within the pores was involved in the reaction with PS. This was a surprising result and suggests that in bomb calorimetry experiments, excess oxidizer on the sample surface contributes to its reaction — a concept that was previously neglected [60, 151]. The exact amount of oxidizer participating in the reaction with PS is still poorly defined, however. A gravimetric technique described in references [60, 151] is not sufficiently versatile to be used for all oxidizers. A better technique must be developed in the future to quantitatively correlate the amount of the pore loaded oxidizer with the heat release observed.

An additional experiment in oxygen was conducted for all composites and the results are shown in Figure 6.6. Consistently for all energetic systems, higher heat of combustion values were observed in oxygen compared to nitrogen, qualitatively confirming that fuel-rich PS energetic composites were, in fact, formed after loading the pores with the oxidizer. The combustion enthalpies calculated assuming that all of the drop cast oxidizer and excess oxygen are available to fully oxidize the PS correlated well with experimental results. Consistently with previous calculations, possible functionalization of the PS surface with SiH_2 affected the combustion enthalpy substantially. Calculations for PS/sulfur (not shown in Figure 6.6) predicted nearly complete oxidation of both Si and S. Resulting reaction enthalpy calculated from CEA exceeded substantially that observed in experiments, in which PS reacted with sulfur filled in pores, forming SiS_2 shielded from ambient oxygen by the excess layer of sulfur on the surface. The calculation were not performed for the case of $Gd(NO_3)_3$, due to the lack of heat of formation value for $Gd(NO_3)_3$. A direct comparison between Figure 6.5 and Figure 6.6 can be used to roughly

assess the amount of PS left unreacted in the experiments conducted in nitrogen. In the presence of oxygen, this unreacted PS appears to be fully oxidized, so that the measured enthalpies approach their respective theoretical limits.

6.5 Conclusions

Energetic composites using PS film with various oxidizers were prepared and their performance was analyzed quantitatively. In particular, moisture stable energetic composites were prepared using PS film and sulfur. PS/sulfur systems were similarly readily ignitable and combustible in both inert and oxidizing gases. Similar flame speeds around 3 $m \cdot s^{-1}$ were observed for the composites prepared using different pore loading techniques, S_{melted} and $S_{drop\ cast}$. The flame speed was also unaffected by the presence of an external oxidizing gas. The reaction heat was increased due to functionalization of PS surface with SiH_2, taking part in combustion. The PS/sulfur system is a potential alternative to $NaClO_4$ for applications requiring moisture stable and perchlorate-free energetic composites. The flame speed for PS/sulfur was much lower than for an earlier characterized PS/$NaClO_4$ system. A detailed study, outside the scope of present work, is needed to understand how more rapid combustion speeds might be achieved for PS/sulfur combustion.

Fuel-rich composites with minimal pore filling were also prepared with nitrate-based oxidizers. These energetic composites were ignited in nitrogen gas. The flame speeds for these oxidizers with PS were higher than for PS/sulfur, but still considerably lower than those for PS/$NaClO_4$. These oxidizers may be viable for applications requiring lower burn speeds and more controlled reactions. The combustion studies using the bomb calorimeter showed all systems have higher combustion enthalpies

in oxygen compared to nitrogen, confirming the starting composition to be fuel-rich. More interestingly, the thermodynamic estimates correlated better with experimental reaction enthalpies when the surface terminated hydrogen and excess oxidizer, in addition to the oxidizer loaded in the pores, were accounted for in the reaction. Determining the exact amount of the oxidizer reacting with PS remains a challenge.

CHAPTER 7

REACTIVE MATERIALS FOR EVAPORATING SAMARIUM

7.1 Abstract

Different reactive materials were prepared and evaluated as potential heaters to evaporate refractory and readily ionized samarium metal. Fully dense, nanocomposite powders of thermites and boride-forming compounds were prepared using arrested reactive milling. In some samples, samarium powder was blended with the nanocomposite powders; in other samples samarium was added using an additional short milling step. Powders were pressed in pellets and ignited at a low pressure. Flame propagation was monitored optically; combustion products were collected and analyzed. It was observed that nanocomposite 2B-Ti powder in which samarium was added via an additional milling step was most suitable for evaporating samarium, while preventing its reaction with other material components. Up to 30 wt. % of samarium could be added and most of it evaporated in the present experiments.

7.2 Introduction

Ejection of clouds of readily ionized metal atoms can be used to modify ionosphere to study and alter its properties important for transmission of optical and radio signals [30]. Clouds of lithium [31, 32], barium [33-35], and, most recently, samarium [36, 37] were explored. Some of the recent results were negatively affected by reduced efficiency of release and ionization of samarium [37]. It is possible that not the entire charge of samarium was evaporated; it is further possible that some of the metal was oxidized or chemically bound. Formation of a metal cloud in an upper atmosphere layer is not a trivial

task. It is particularly difficult when dealing with easy to ionize and thus fairly reactive metals, such as Li, Ba, or Sm. Using conventional propellants or explosives to generate metal clouds is problematic because of rapid reaction of evaporated metal with the simultaneously released combustion products to form i.e., samarium oxides or samarium borides. Here, an approach for generation of samarium clouds is explored using metal-based reactive materials producing high combustion temperatures and forming relatively stable, inert condensed products, which are unlikely to include Sm. Further, to minimize possible reaction of samarium with individual components of reactive materials, in this study, fully dense, micron-sized nanocomposite reactive material powders are prepared by arrested reactive milling (ARM) [1]. Conventional blending or mixing starting components with samarium to prepare reactive material is purposefully avoided in this study to diminish any reaction of samarium with other components of reactive materials. In ARM-prepared reactive materials, components capable of highly exothermic chemical reaction are mixed on the scale of 100 nm within each particle. Thus, such components ARM are much more likely to react with each other than with relatively coarse samarium particles, added later to the pre-milled nanocomposite powders using a distinct mixing step.

Review of the literature data suggested many potentially useful reactive materials, including composites forming borides, carbides, and sulfides, as well as thermite-like compositions undergoing redox reactions [126, 152-154], which are expected to generate the heat and temperature necessary to evaporate Sm. It was, however, difficult to determine in which systems, reactions of Sm with other components are least likely to occur. A preliminary survey aimed to select reactive systems for which high reaction rates

and temperatures were reported experimentally, enabled us to narrow down the compositions to be explored to 2B-Ti [1, 155, 156], 2B-Zr [157, 158], Ti-C [159-162], Mg-S [122], and a thermite system Al-MoO_3 with different fuel/oxidizer ratios [2, 99, 163, 164]. The above list of possible compositions is not exhaustive; however, it considers distinctly different types of reactive materials. Further work can consider other materials for each type of compositions, forming borides, carbides, sulfides, or oxides. This paper discusses experiments focused to determine which of the surveyed compositions is better suited to generate clouds of evaporated samarium.

7.3 Materials and Experimental Methods

7.3.1 Material Preparation

Several nanocomposite powders were prepared by ARM [1] starting from readily commercially available elemental metal, metalloid, or oxide powders. A list of the starting materials, their purity and the compositions of prepared nanocomposites are given in Table 7.1. ARM was used extensively to prepare variety of reactive materials in the past, e.g., [1, 2, 163-165]; here it was used to prepare 2B-Ti, 2B-Zr, Ti-C, Mg-S, and Al-MoO_3 nanocomposite powders. A shaker mill (SPEX Certiprep, 8000 series) with two 50 mL flat-ended steel vials cooled by room-temperature air jets was used to prepare all composites except for Mg-S. Case-hardened carbon steel balls 3/8”-diameter, were used as a milling media. Ball to powder mass ratio (BPR) was fixed at 10. During milling, about 2 – 5 mL of hexane was used as the process control agent (PCA). The milling vials were loaded and sealed inside an argon-filled glovebox. For Mg-S system, mechanically triggered reaction was reported to occur at very short milling times, before a well-mixed

composite structure was prepared [128, 129]. In an attempt to avoid premature reaction, a freezer mill (SPEX 6850) with four 25 mL steel vial operated at liquid nitrogen temperature was used. A 2.3" long steel rod with 3/8"-diameter oscillating within the vial at a frequency of 15 Hz was used as a milling tool. Powder load was 2 g. Unfortunately, two milling experiments conducted with milling times of 100 and 150 min yielded a powder that was reacted. Further attempts to prepare Mg-S composites were not made for this study.

Table 7.1 List of Elemental Powders Used to Prepare Nanocomposites

Chemical Name	Chemical Formula	Supplier	Purity	Nanocomposites
Titanium powder, -325 mesh (<44 μm)	Ti	Alfa Aesar	99%	2B-Ti, Ti-C
Amorphous boron powder, <1 μm	B	SB Boron	93-96%	2B-Ti, 2B-Zr
Carbon black powder, FE-603, 1-5 μm	C	Atlantic Equipment Engineers	99.9%	Ti-C
Zirconium powder, APS, 2-3 μm	Zr	Alfa Aesar	97.2%	2B-Zr, Zr-C
Magnesium powder, -325 mesh (<44 μm)	Mg	Alfa Aesar	99.8%	Mg-S
Sulfur, powder, -100 mesh (<149 μm)	S	Sigma-Aldrich	Reagent Grade	Mg-S
Aluminum powder, -325 mesh (<44 μm)	Al	Atlantic Equipment Engineers	99.5%	2Al-MoO_3, 4Al-MoO_3, 8Al-MoO_3
Molybdenum oxide, powder, -325mesh (<44 μm)	MoO_3	Alfa Aesar	99.95%	2Al-MoO_3, 4Al-MoO_3, 8Al-MoO_3

Preliminary material assessments described briefly in Section 3.1 were used to downselect 2B-Ti and Al-MoO_3 as the most promising reactive materials for evaporation of Sm. However, in the case of 2B-Ti, the heats of formation of TiB_2 and commonly found SmB_6 are comparable to each other [166]. Additionally, other samarium borides (i.e., Sm_2B_5, SmB_2, SmB_4, SmB_{66}) are reported in the literature [167-169], suggesting possible reactions of boron with Sm instead of Ti. Similarly, in the case of Al-MoO_3, formation of samarium oxide (Sm_2O_3) is thermodynamically favored due to its higher heat of formation

values compared to aluminum oxide (Al_2O_3) [166]. It was therefore desired to maximize the reaction rates between components of the heat-generating reactive material, to reduce the likelihood of added Sm particles to participate in the reaction. Reaction rates of 2B-Ti and Al-MoO_3 are directly correlated with surface area of the reactive interface between B and Ti and Al and MoO_3, respectively. Therefore, ARM was used to prepare fully dense nanocomposites, in which reactive components fully contact each other and mixed on the scale of ca. 100 nm. material assessments described below showed that 2B-Ti and Al-MoO_3 were the most promising reactive materials for evaporation of Sm.

Table 7.2 Test Mixtures Based on 2B-Ti and Al-MoO_3 Nanocomposites

Sample ID	Reactive mixture base	Evaporating metal		Mixing conditions		
		Type	Mass fraction (%)	Reactive base	Evaporating metal	*M_p/M_i(%)
1	2B-Ti	--	0	ARM – 3hrs	--	N/A
2	2B-Ti	--	0	Blend – 6min	--	N/A
3	2B-Ti	Cu	56	ARM – 3hrs	Blend – 6min	No data
4	2B-Ti	Cu	47	ARM – 3hrs	Blend – 6min	No data
5	2B-Ti	Cu	45	ARM – 3hrs	Blend – 6min	No data
6	2B-Ti	Sm	47	ARM – 3hrs	Blend – 6min	1.017
7	2B-Ti	Sm	46	ARM – 3hrs	Blend – 6min	No data
8	2B-Ti	Sm	44	ARM – 3hrs	Blend – 6min	No data
9	2B-Ti	Sm	40	ARM – 3hrs	Blend – 6min	No data
10	2B-Ti	Sm	47	ARM – 3hrs	ARM – 15 min	0.944
11	2B-Ti	Sm	47	ARM – 3hrs	ARM – 30 min	0.866 ± 0.01
12	2B-Ti	Sm	40	ARM – 3hrs	ARM – 30 min	0.863 ± 0.02
13	2B-Ti	Sm	40	ARM – 3hrs	ARM – 60 min	0.925
14	2B-Ti	Sm	30	ARM – 3hrs	ARM – 30 min	0.717 ± 0.02
15	2Al-MoO_3	--	0	ARM – 30 min	--	N/A
16	4Al-MoO_3	--	0	ARM – 25 min	--	N/A
17	8Al-MoO_3	--	0	ARM – 60 min	--	N/A
18	2Al-MoO_3	Cu	60	ARM – 30 min	Blend – 6min	No data
19	2Al-MoO_3	Cu	50	ARM – 30 min	Blend – 6min	No data
20	8Al-MoO_3	Cu	50	ARM – 60 min	Blend – 6min	No data
21	2Al-MoO_3	Sm	60	ARM – 30 min	ARM – 30 min	1.011
22	2Al-MoO_3	Sm	50	ARM – 30 min	ARM – 30 min	0.887
23	4Al-MoO_3	Sm	50	ARM – 25 min	ARM – 30 min	0.989
24	4Al-MoO_3	Sm	40	ARM – 25 min	ARM – 30 min	0.975
25	4Al-MoO_3	Sm	30	ARM – 25 min	ARM – 30 min	0.949

*M_p = mass of the combustion products; M_i = mass of the initial sample

Using 2B-Ti and Al-MoO_3 nanocomposites, several test mixtures were prepared by blending or milling with a surrogate material, elemental copper powder, -325 mesh, 99% pure, from Alfa Aesar, or directly with samarium powder, <250 micron, REacton®, 99.9% (REO), from Alfa Aesar. All test mixtures prepared using 2B-Ti and Al-MoO_3 nanocomposites are listed in Table 7.2.

To blend an additional metal powder (Cu or Sm) with the prepared nanocomposite reactive material powders, both powders were placed inside 50 mL glass vials and rotated at 130 rpm for 6 minutes. To distribute the metal more homogeneously, an additional milling step was used for some samples; the same shaker mill used to prepare initial nanocomposite powders was exploited. The powders were wet milled using 2 – 5 mL of hexane. Detailed preparation conditions used for different test mixtures are presented in Table 7.2.

7.3.2 Characterization Techniques and Instrumentation

Back-scattered scanning electron microscopy (SEM) images were used to characterize the powder morphologies and scale of mixing in the prepared powders. Condensed combustion products collected after experiments were also examined using SEM. A PANalytical Empyrean diffractometer was used for X- ray diffraction (XRD) to determine phase compositions of combustion products. The XRD powder diffractometer was operated at 45 kV and 40 mA using unfiltered Cu Kα radiation (λ = 1.5438 Å).

All combustion experiments were conducted inside a chamber constructed based on a HPS® NW 50 ISO-KF vacuum tee with a 2.06”-diameter. A sketch of the experimental set-up is shown in Figure 7.1. The bottom flange of the chamber contained electrical feedthroughs to power an igniter, a tungsten wire. The top flange included a port

connected to a vacuum pump. Experiments were performed at a negative pressure of -27 in Hg. The side flange of the chamber was used to mount a Lexan® window. The experiments were observed and recorded through the window using a high-speed video camera at 100 – 200 frames per second.

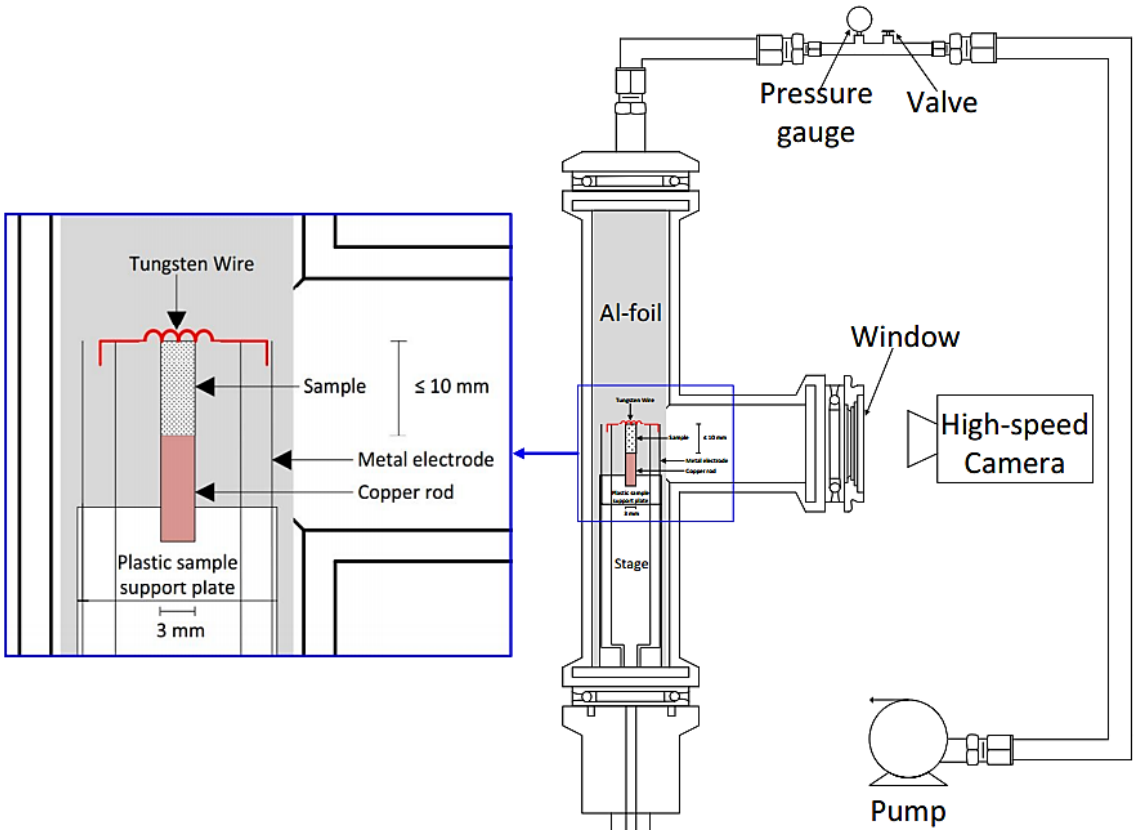

Figure 7.1 Experimental setup.

A cylindrical sample was mounted on a 3.2 mm-diameter copper rod. A short paper tube (≤3-mm in height) was used to hold the pellet on top of the rod. The rod was inserted into a hole in a plastic support plate shown in the zoomed inset in. Two metal electrodes were positioned on either side of the sample. The electrodes were connected to an electrically heated tungsten wire (0.2-mm diameter).

Preliminary combustion experiments were conducted in air with powders loosely packed in a 3.2 mm-diameter, ≤ 10 mm height paper tube. These tests were used to identify more reactive heat source materials to be used in experiments in vacuum. The loosely packed powder samples did not burn well in vacuum, however. Combustion experiments in vacuum, aimed to imitate conditions in the upper atmosphere, were conducted using 3.2 mm-diameter pellets pressed out of the prepared powders. The pellet heights varied from 3.2 to 8.0 mm. Both pellets and powder filled paper tubes were placed on the copper rod support and ignited at the top end. The flame propagated downward.

The pellets were prepared with a Carver automatic pellet press using a uniaxial die at a nominal force of 1000 – 1500 lbs. Some of the materials did not press well and prepared pellets could crack or contain fractures. In particular, for 2B-Ti/Sm blends, most of the pellets had hairline fractures after their recovery from the pressing die. The fractures were likely formed due to the particle size differences and poor mixing between 2B-Ti nanocomposites and Sm. Despite minor defects, these samples were useful for the ignition and combustion tests.

The combustion products were collected two different ways. The vaporized combustion products were collected by lining the sample support plate and vacuum chamber walls with aluminum foil. Most of the vaporized products deposited on the foil. The foil was replaced between each experiment. In addition to the vapor deposits on the foil, larger fragments of solid combustion products left over from the burning pellet or powder tube were collected for further characterization. In addition to XRD and SEM, weight of these collected fragments was measured.

7.4 Results and Discussion

7.4.1 Preliminary Assessment of Reactivity for the Prepared Materials

Prepared 2B-Ti, 2B-Zr, Ti-C, and Al-MoO3 nanocomposite powders were ignited initially in vacuum using both loose powder cylinders and pellets. 2B-Ti and Al-MoO3 nanocomposites readily ignited; while ignition was not consistently achieved for other compositions. In addition, preparing pellets of Ti-C proved to be difficult; the powder did not consolidate using the presently available press and die set. Therefore, 2B-Zr, and Ti-C, materials were not considered for further combustion tests. Since, the preparation of Mg-S composite was unsuccessful; this material was also not considered for further testing.

7.4.2 Particle Size, Morphology and Scale of Mixing

Back-scattered scanning electron microscopy (SEM) images of the prepared mixtures of 2B-Ti nanocomposites and Sm are shown in Figure 7.2. In these materials, Sm was milled with the nanocomposite powders and milling times were 15 and 30 minutes for the samples shown in the left and right panels of Figure 7.2, respectively. Longer milling caused reduction in particle sizes. Because back-scattered electrons are sensitive to the phase contrast between elements with different atomic weights, samarium inclusions and particles appear the brightest, followed by titanium and boron.

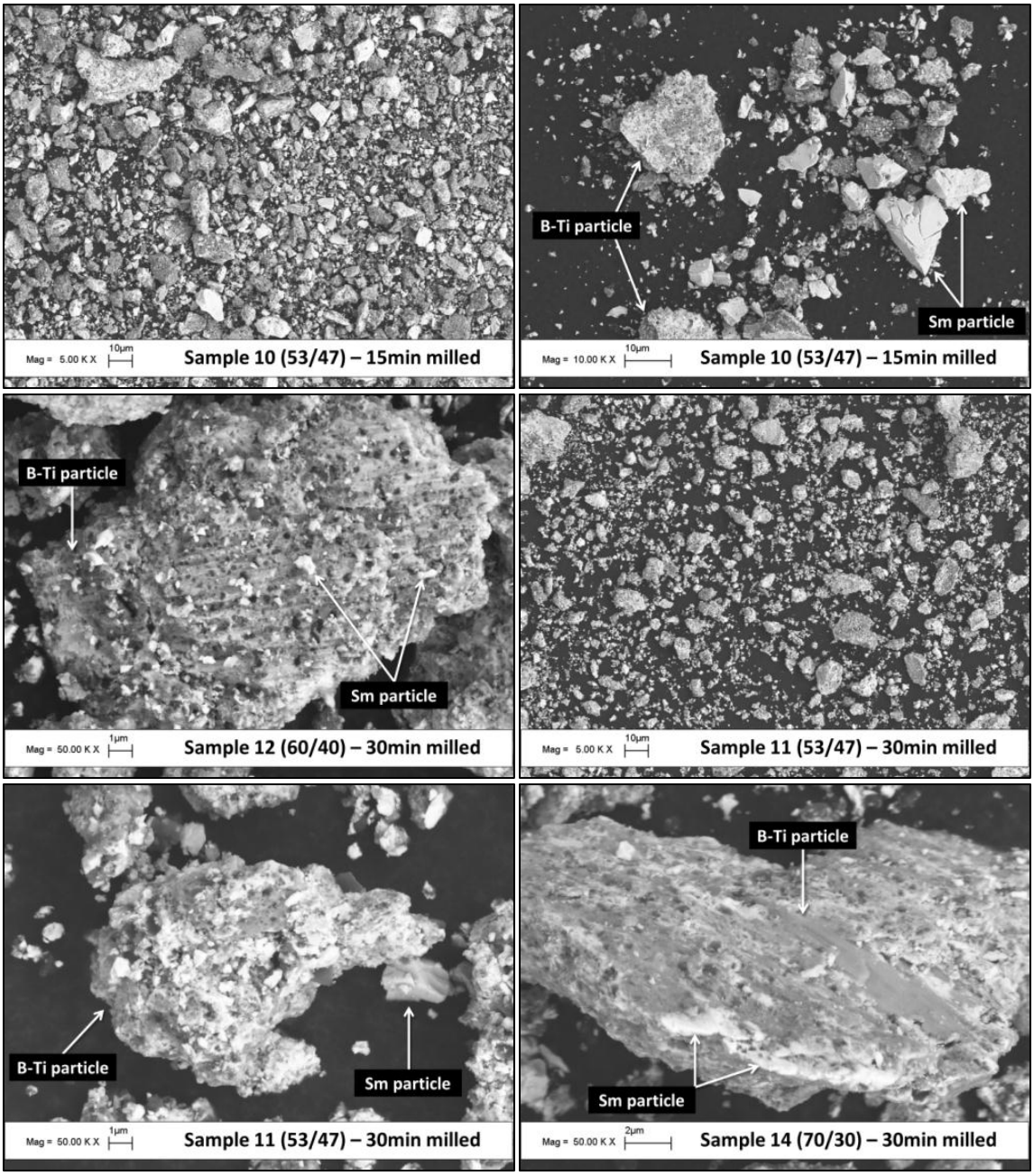

Figure 7.2 Back-scattered SEM images of as milled samples 10 – 12, and sample 14.

In SEM images, Sm appears to have a smoother surface than 2B-Ti nanocomposites. For the sample milled for 15 min, relatively coarse unattached Sm particles are observed. However, no such particles could be found in the 30-min milled sample. Most of Sm is finely dispersed and attached to the surface of 2B-Ti composite

particles. It appears to be more spread and better adhered to the 2B-Ti composite surface for the 30-min milled sample. No formation of 3-dimensional ternary composite particles could be detected.

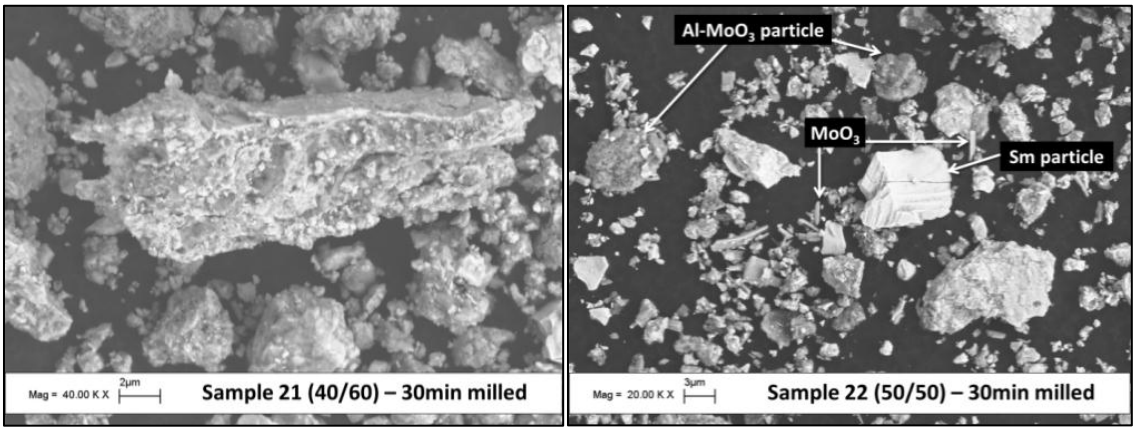

Figure 7.3 Back-scattered SEM images of as milled sample 21 and sample 22.

Similarly in Figure 7.3, the SEM images of the prepared mixtures containing Al-MoO_3 nanocomposite and Sm are shown. The surface of Sm is smoother than that of the Al-MoO_3 nanocomposites. We observe fine particles of Sm attached to the surface of the Al-MoO_3 nanocomposites. Additionally, some unattached MoO_3 is also present, which can be identified by characteristic elongated crystallite shapes. It suggests that the mixing between Al and MoO_3 was not fully optimized while the nanocomposite material was prepared.

7.4.3 Combustion Experiments

7.4.3.1 Preliminary Combustion Experiments in Air. In preliminary experiments, behavior of ARM-prepared 2B-Ti nanocomposite powders ignited in air was compared to that of 2B-Ti powder blends with the identical phase compositions. Only the ARM-prepared 2B-Ti nanocomposite ignited and burned in a self-sustaining fashion. The

blend of 2B-Ti (sample 2, cf. Table 7.2) did not ignite in either powder or pelletized forms. Therefore, all other experiments were conducted using mixtures prepared from the ARM-prepared 2B-Ti nanocomposite powder. An example of self-propagating combustion for a sample placed as a loose powder in a paper tube is shown in Figure 7.4 for sample 4 (containing 47% of Cu as a surrogate for Sm). In this and following several figures, the image on the left shows configuration of the sample being tested. The sample is placed on top of the copper rod (cf. Figure 7.1). Tungsten ignition wire is touching the top of the sample. The following images are frames of the video shot at 200 fps, with the lens aperture closed to avoid saturation. Time zero is selected as the frame before the first sign of the sample ignition was seen on the videos. The labels in subsequent frames show time after time zero in ms. In Figure 7.4, in several initial frames following ignition of the sample (images at 10, 45, and 100 ms), hot particles are ejected upwards. As the combustion wave propagates through the sample, the products formed on top prevent or limit the upwards particle ejection and consequently, particles are ejected from the sides of the paper tube (image at 535 ms).

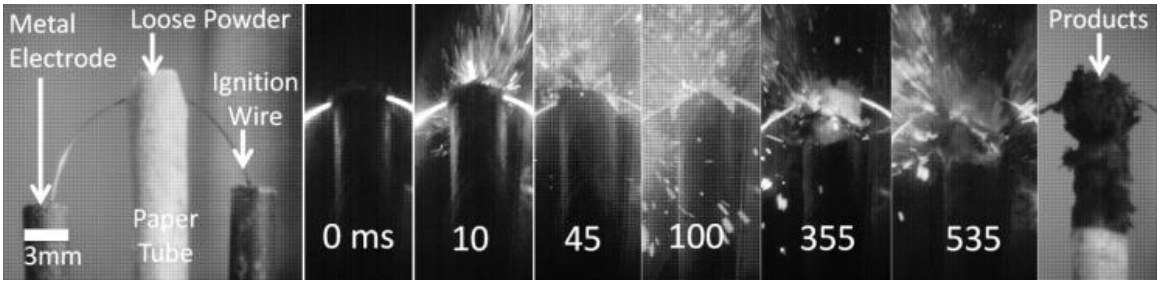

Figure 7.4 A sequence of video frames illustrating combustion of sample 4 (47% Cu) in air. The time between 2nd frame and other frames shown are in milliseconds. Image of the combustion product is also shown.

7.4.3.2 Combustion Experiments in Vacuum. As noted above, copper was used as a surrogate material for initial experiments to understand the effectiveness of milled 2B-Ti

and Al-MoO_3 nanocomposites to vaporize a high boiling point metal. Similar to samarium, copper has a high boiling point of 2,562 °C and vaporization of Cu can be easily detected by examining deposits on the foil lined around the burning sample. Unlike samarium, however, copper is not reactive. It also has a very high thermal conductivity, enhancing heat propagation in the mixed sample and minimizing temperature gradients even if the powder is not homogeneously mixed with the nanocomposite material.

In contrast to experiments in air, self-propagating flame was not observed for loosely packed powders in vacuum. Particles on top of the paper tube, which were in direct contact with the tungsten wire, ignited and were ejected up from the sample. Particles further below in the sample were not effectively heated and did not ignite. Heat transfer was improved in pressed pellets, which were, therefore, more suitable for experiments in vacuum.

All of the samples shown in Table 7.2 were ignited in the vacuum chamber. Qualitatively three different modes of combustion were observed, in which the flame propagated as follows:

(i) without significant particle ejection,

(ii) accompanied by ejection of large fragments comparable to the size of the pellet, and

(iii) accompanied by ejection of fine fragments, which were smaller than the pellet size.

Each combustion regime is described below. Note that in some cases, it was difficult to clearly distinguish between regimes I and II or between regimes II and III.

(i) Propagation without significant particle ejection

This combustion regime was observed for samples 6, 10, and 11. In all these samples, 47 wt. % of samarium was added to the milled 2B-Ti composite. All of these samples completely self-propagated without any significant observed particle ejection from the burning pellet. An illustration of this combustion regime is shown in Figure 7.5 for sample 11. The bottom of the pellet is wrapped into a paper tube, attached to the copper rod under the sample. The paper tube prevented the pellet from shifting upon its ignition. The burning pellet is observed to expand somewhat, pushing the ignition wire up as the flame propagates down through the pellet. It was observed that the flame propagation was faster for test mixtures, for which Sm was milled in compared to the ARM-prepared 2B-Ti nanocomposite blended with Sm. Few particle streaks were observed for the milled test mixtures. We suspect that in regime (i), the fast flame propagation and particle streaks observed for the milled 2B-Ti/Sm mixtures were due to both reduction in particle size and enhanced mixing achieved by mechanical milling. The weight measurement of the collected condensed products (cf. Table 7.2 – samples 6, 10, and 11) showed no weight loss for sample 6 with blended Sm. A small weight increase observed could be associated with a fragment of the heating wire welded into the sample products. The weight loss was detected for samples 10 and 11, increasing for longer milling times. However, the weight loss remained much smaller than the mass fraction of Sm in the sample.

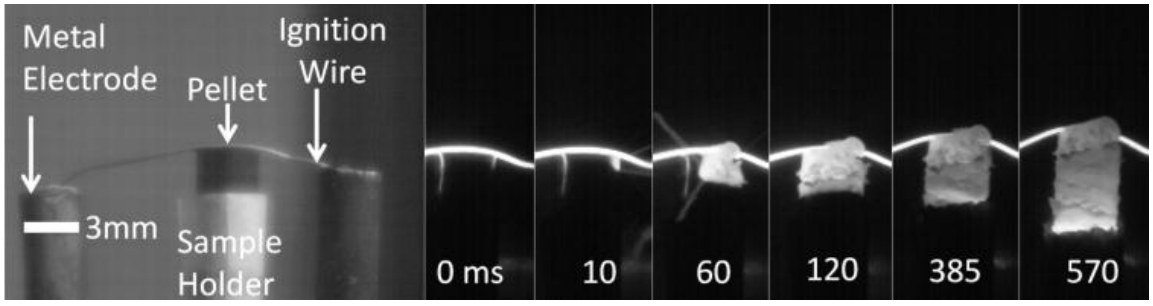

Figure 7.5 A sequence of video frames illustrating combustion of sample 11 (47% Sm) in vacuum.

(ii) Propagation with ejection of large fragments comparable to the size of the pellet

Combustion regime II and intermediate behavior between regimes ii and iii were observed for many samples listed in Table 7.2. For samples 5, 7 – 9, 18, 19, 21, 23, and 24, when the pellet ignited, combustion started with streaks of fine particles ejected up from the surface. This was followed by formation and break-up of larger fragments. The fragments could also be ejected up and often fell down soon after their ejection. In most cases, ejection of a large fragment disrupted the flame propagation. In some cases, it was possible to re-ignite the quenched pellet by additional heating achieved by increasing the voltage across the tungsten wire. This resulted in further ejection of particles/fragments or the entire burning pellet lifting off. An illustration of this combustion regime is shown in Figure 7.6 for sample 18, where initial frames show ejection of multiple fine particle; frames taken at longer times show larger fragments breaking-off and quenching the reaction. The image on the right hand side (at 75 ms) shows a large cylindrical fragment turned 90º while falling down after being ejected from the burning pellet.

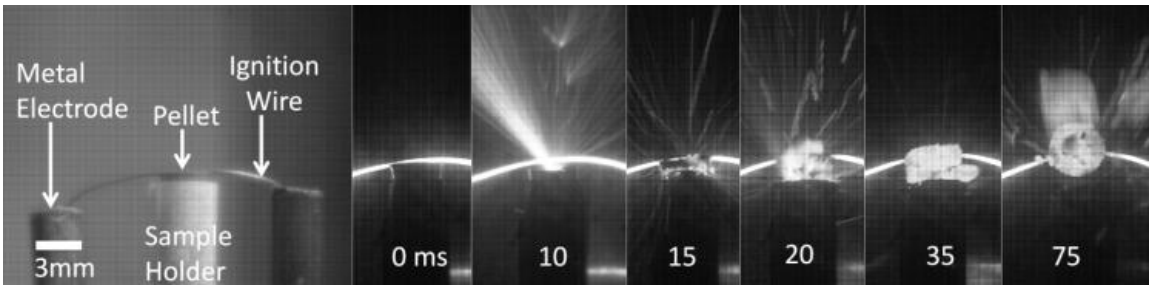

Figure 7.6 A sequence of video frames illustrating combustion of sample 18 (60% Cu) in vacuum.

It is interesting to note that none of the pellets prepared using milled 2B-Ti/Sm showed this combustion behavior. In contrast, most of the pellets containing 2Al-MoO_3 and 4Al-MoO_3 burned in this regime. A transition from regime (ii) to regime (iii) occurred

when the mass ratio of Sm decreased to 50 and 30 wt. % for samples containing 2Al-MoO_3/Sm and 4Al-MoO_3/Sm, respectively.

(iii) Propagation with ejection of fine fragments

Burning particles that were much finer than the pellet were ejected as the combustion propagated downward through the pressed samples. Samples 3, 4, 12 – 14, 20, 22, 25 showed this behavior. In all cases, ejection removed substantial fraction of material from the burning pellets. Figure 7.7 shows an illustration of this combustion regime for sample 14. A qualitative trend was observed for the pellets of milled 2B-Ti/Sm, where increasing milling time and reducing the Sm mass increased the ejection rate of fine particles. This combustion regime is most desired for Sm evaporation based on the measured mass of the remaining coarse condensed combustion products. It is likely that Sm effectively evaporates both from the burning pellet and from the ejected fine fragments.

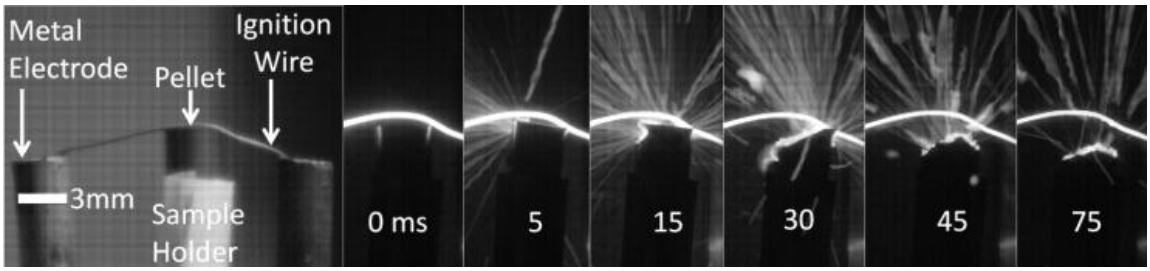

Figure 7.7 A sequence of video frames illustrating combustion of sample 14 (30% Sm) in vacuum.

After conducting a set of experiments in air and vacuum; a portion of the prepared powder was stored in air for 2 months to analyze the effect of aging on its combustion. Combustion experiments in air and vacuum were repeated, where the aged material ignited and combusted similarly to that of the freshly prepared material. Additionally, from the mass balance analysis, comparable masses were measured from the condensed combustion

products of the aged materials to that of fresh, indicating that similar amount of Sm evaporates from the aged material during combustion.

7.4.3.3 Mass Balance. In order to optimize the milling conditions and the compositions capable of vaporizing the most amount of Sm, mass measurements of the remaining condensed products were taken into account. After pelletizing samples 10 – 14 and 21 – 25, prepared using milled 2B-Ti/Sm and milled Al-MoO3/Sm, the pellet masses were measured before igniting them inside the vacuum chamber. Similarly, after each combustion experiment, the products were collected and weighed to obtain the final mass (Mf) of the products. All results are given in Table 7.2. For some cases, unexpectedly, the mass of the products slightly exceeded the mass of the original sample. It is possible that the additional mass in the products was caused by carbonaceous products of combustion of the paper cylinder used to position the pellets and by fragments of embedded tungsten wire used for ignition.

Assuming the difference between the initial and final mass, ($M_i - M_f$), represented the amount of Sm evaporated from the pellet, the percentage of Sm vaporized during the combustion event was calculated and shown in Figure 7.8a. In the case of milled 2B-Ti/Sm, comparison between three milling times suggests that 15 min and 60 min used to mill Sm were inferior to 30 min for Sm evaporation. For all samples prepared with the 30 min milling time, a trend was observed where the percentage of evaporated Sm increased as the Sm content in the starting mixture was reduced. As an aside observation, bronze colored deposits were clearly seen on the aluminum foil surrounding the sample area.

In the case of milled Al-MoO_3/Sm, two different base reactive materials, 2Al-MoO_3 and 4Al-MoO_3, were tested. Again, the mass of the pellet recorded before and after combustion was used to determine the amount of Sm evaporated during combustion. Results are illustrated in Figure 7.8b for samples 21 – 25. Similarly to 2B-Ti/Sm system, as the amount of Sm in the initial mixture was decreased, the Sm vaporization amount increased. However, the total amounts of evaporated Sm were significantly lower for mixtures prepared with Al-MoO_3 compared to 2B-Ti. Although combustion events recorded using the high-speed camera show some particle streaks for the Al-MoO_3 based samples, the amounts of material deposited on the aluminum foil were qualitatively smaller compared to those with 2B-Ti – based pellets.

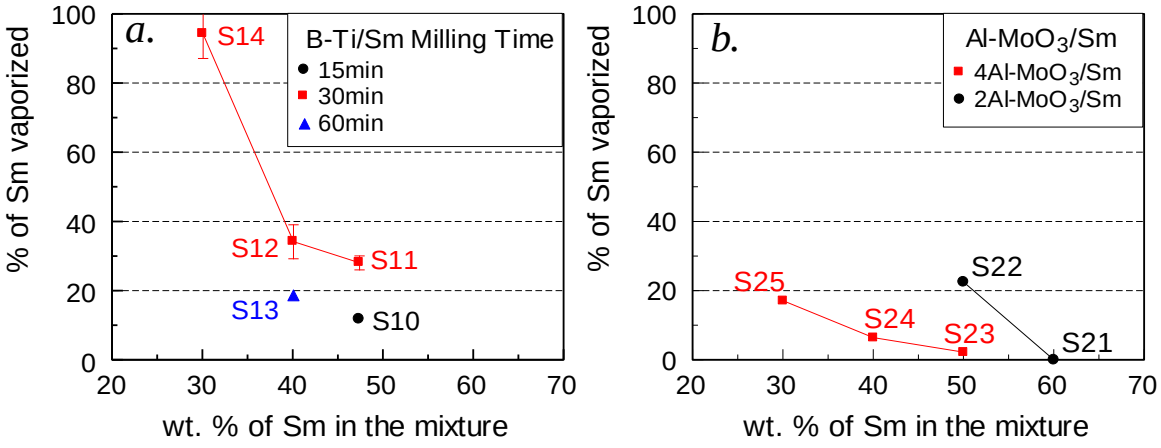

Figure 7.8 The percentage of Sm vaporized as a function of initial Sm mass load in the starting mixture. Experiments were repeated at least 3 times and error was determined for 30 min milled sample.

7.4.3.4 Flame Speed. Recorded videos were used to measure the flame speed for the burning pellets. Results are shown in Figure 7.9, with the focus on a trend produced by samples 11, 12, and 14. The flame speed becomes lower for the materials with more Sm added. This is in qualitative agreement with the trend shown in Figure 7.8.

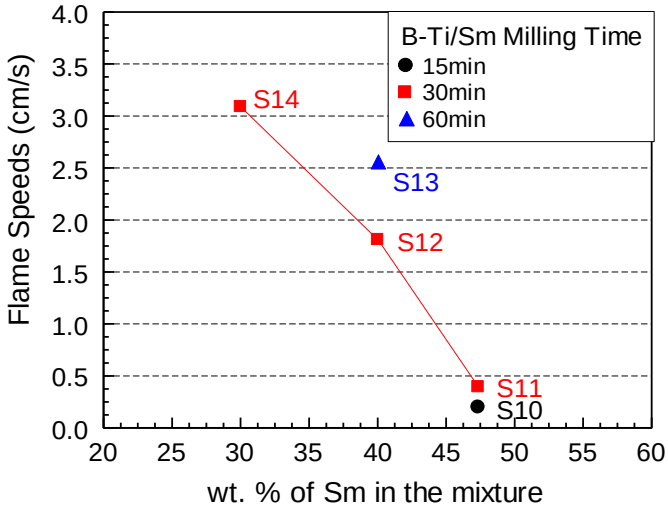

Figure 7.9 Flame propagation velocity for 2Bi-Ti/Sm milled samples.

7.4.4 Combustion Products

Optical microscopy images of the combustion deposits collected using aluminum foil are shown in Figure 7.10. Qualitative comparisons showed that the surrogate Cu metal produced more visible deposits on the foil compared to Sm. Comparing the reactive base nanocomposite 2B-Ti to Al-MoO_3 it was observed that substantially more Sm was deposited on the aluminum foil in combustion experiments with test mixtures containing 2B-Ti nanocomposite. This result was consistent with the low percentage of Sm vaporization calculated using the mass balance analysis in Section 7.4.3.3.

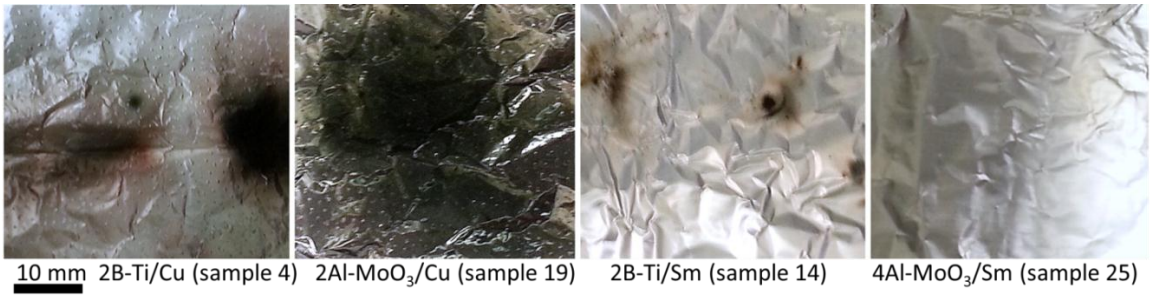

Figure 7.10 Vaporized combustion products collected on the aluminum foil. Optical microscopy images.

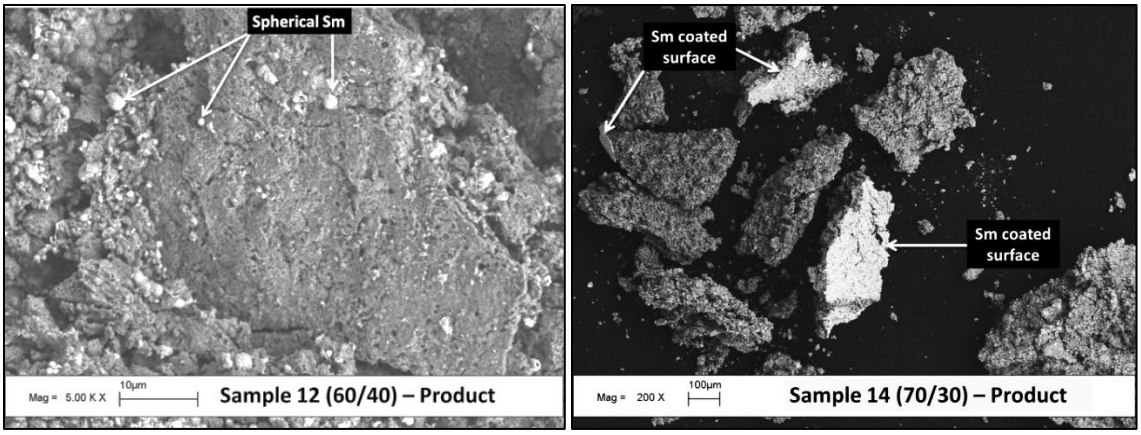

Figure 7.11 Back-scattered SEM images of combustion products of milled 2B-Ti/Sm (sample 12 and sample 14).

In Figure 7.11, SEM images of the solid combustion products collected are shown for the milled 2B-Ti/Sm system. A morphological change to the milled 2B-Ti nanocomposite was observed when comparing the combustion products to the starting powder shown in Figure 7.2. A porous structure was formed during the combustion, indicating that samarium was vaporized and ejected out of the pellet.

Both fine spherical Sm particles and Sm surface coatings on larger particles are seen in Figure 7.11. Presence of Sm detected in Figure 7.11 based on the image brightness was supported by more detailed Energy-dispersive x-ray spectra (EDX) obtained using SEM. This morphology of the products suggests that Sm was molten; but not all of it evaporated leaving spherical particles in the material. Part of the evaporated Sm could condense on top of the cooled burned out pellet fragments, forming the surface coating. Further EDX characterization qualitatively indicated significantly lower concentrations of Sm present for sample 14 compared to other samples; note that this was the same sample, for which the highest percentage of Sm evaporation was expected based on the mass measurements discussed in Section 7.4.3.3.

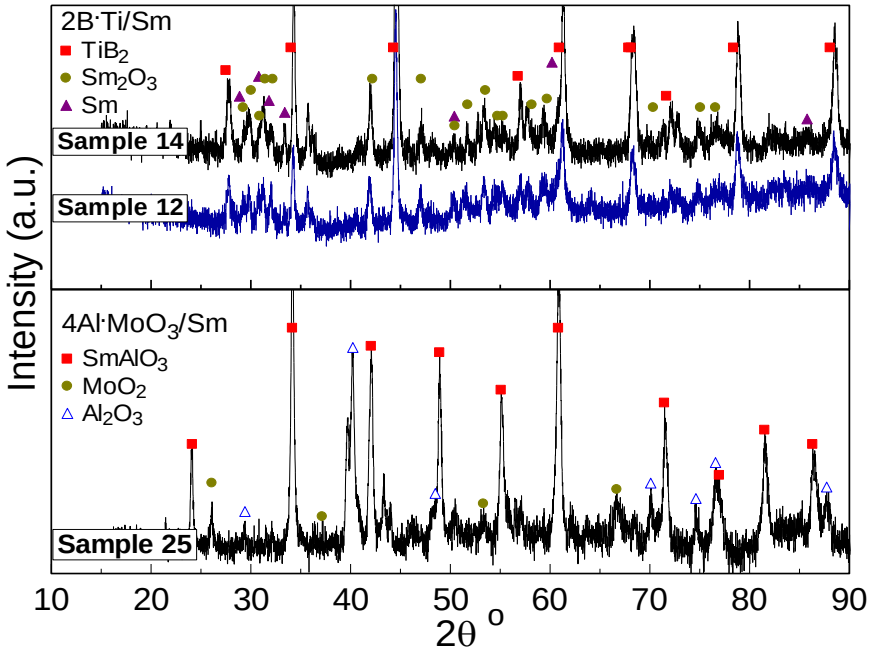

Figure 7.12 XRD analysis conducted on the combustion products of milled 2B-Ti/Sm (samples 12, and 14) and milled 4Al-MoO_3/Sm (sample 25).

The results of the XRD analysis conducted on the combustion products from milled 2B-Ti/Sm and 4Al-MoO_3/Sm are shown in Figure 7.12. In the 2B-Ti/Sm system, majority of the products composed of TiB_2 with small amounts of Sm_2O_3 and elemental Sm. No sign of reaction products between Sm and B was detected in the XRD analysis, confirming that ARM technique to prepare the 2B-Ti nanocomposite does, in fact, inhibit the reactions between Sm and B or Ti. However, for 4Al-MoO_3/Sm system, the major combustion product was ternary oxide $SmAlO_3$. This result indicates that Sm oxidation minimized its evaporation. This makes the present thermite system not viable for Sm evaporation. These results are consistent with the low percentage of Sm vaporization calculated from the mass balance analysis for Al-MoO_3/Sm pellets. Furthermore, they support the qualitative observations showing very small amount of deposits present on aluminum foil lining the chamber walls after respective combustion experiments.

7.5 Conclusions

Nanocomposite 2B-Ti material prepared by ARM is a viable heating material for Sm evaporation. In the present experiments, mixing Sm with the ARM-prepared powder was most effective when 30 wt. % of Sm was added using an additional 30-min milling step. For that material, nearly all samarium evaporated during combustion, as confirmed by change in weight of the combusted sample and analysis of the condensed combustion products. No reaction products of Sm with either B or Ti were detected in the collected condensate.

CHAPTER 8

ENERGY STORAGE MATERIALS WITH OXIDE-ENCAPSULATED INCLUSIONS OF LOW-MELTING POINT METAL

8.1 Abstract

A composite energy storage material with inclusions of a low-melting point metal encapsulated in protective metal oxide shells is prepared and characterized. A reactive nanocomposite thermite prepared using arrested reactive milling, is used as a precursor for preparation of the energy storage material. This precursor material is a composite with a metal matrix and metal oxide inclusions capable of a redox reaction. The metal oxide is selected to yield an easy to melt metal upon completion of the redox reaction. The precursor material is heated slowly to a temperature not to exceed the melting point of the metal matrix and kept at an elevated temperature to initiate and complete the redox reaction. The product of this redox reaction is a composite material comprising inclusions of an easy to melt metal encapsulated with an oxide produced by the redox reaction. In this study, Al/Bi_2O_3 nanocomposite thermites were prepared as precursors for energy storage materials with Al matrix and Bi inclusions encapsulated with Al_2O_3. Thermal and mechanical properties of the prepared material were compared to those of reference binary Al/Bi and ternary Al/Bi/Al_2O_3 materials. The material containing encapsulated Bi inclusions was shown to be capable of storing energy by melting and solidifying Bi inclusions repeatedly. The inclusions did not drift inside the material upon heating; prepared composite structure remained largely intact upon thermal cycling. Conversely, the structure of reference composite materials with similar bulk compositions but without encapsulated Bi inclusions was not preserved upon thermal cycling. Molten Bi tended to separate from Al and form interconnected coarse network of inclusions. Upon cycling, Bi

accumulated on surface of the material. Difference in mobility between encapsulated and non-encapsulated Bi inclusions caused dramatic differences in the mechanical properties of the resulting composites. Materials with encapsulated Bi inclusions were much stronger and capable of retaining their structure and strength despite thermal cycling expected for useful energy storage materials.

8.2 Introduction

Metal based energy storage materials (ESM) have advantages of high thermal conductivity, potentially high strength, and others [65]. The main issue is that the metal that melts upon heating (and thus serves as an energy storage medium) needs to be contained in order for the material to be used in repetitive heating cycles. Containment of liquid metals is difficult; often bulk containers are used [66], which limit significantly the types of structures that can be manufactured using the ESM. Using couples of metals that do not form intermetallics, such as Ag/Bi was reported recently [67]; however, such systems are limited and even if no intermetallics are formed, inclusions of an easily melting metal (Bi) are expected to migrate and coalesce after thermal cycling.

Composite materials can be readily prepared, in which a low-melting point metal is dispersed in a metal or ceramic matrix with a higher melting point. However, without encapsulation of the low-melting point metal inclusions, the material becomes structurally weak when the low-melting metal is liquid, and therefore deteriorates rapidly. Repeated heating may additionally cause formation of alloys and other compounds, altering the melting point of inclusions and thus affecting their energy storage capacity. Further, repeated melting may cause redistribution of non-encapsulated material within the structure, causing loss of uniformity. Finally, the strength of the composite material

containing low-melting point inclusions would be reduced dramatically when the inclusions melt. The above negative effects can be circumvented if inclusions of the low-melting point material are encapsulated in a matrix that is thermally stable and mechanically sound.

In the structures described here, the energy storing medium (an easy to melt metal or alloy) is enclosed in nano-scale inclusions or layers surrounded by protective metal oxide. Such structures are stable in time and are not destroyed by repeated melting and solidification of the encapsulated inclusions.

8.3 Technical Approach

The ESM is made using a precursor material, a nanocomposite thermite powder prepared by arrested reactive milling [1]. Alternatively, it may be a nanocomposite layered structure prepared by vacuum deposition. The preparation of the energy storage material by milling and its structure are illustrated schematically in Figure 8.1. Starting materials for the milling are regular powders, one of which is a metal, such as aluminum, and another is a readily reducible metal oxide. For ESM, the reduced oxide should yield an easily melting metal; examples include oxides of bismuth, indium, tin, and others. After milling, a fully dense composite is prepared with the metal matrix and oxide inclusions. Typically, the dimensions of inclusions are close to 100 nm [170]. Using a highly heat conductive aluminum as the metal matrix ensures the capability to reduce nearly all metal oxides. Other metal fuels that can be used with many oxides include magnesium, zirconium, and titanium. Different metal/oxide combinations can be used to prepare the ESM capable of storing energy at different temperatures and having tunable thermal conductivity and heat capacity.

To prepare the energy storage material, the nanocomposite material prepared by milling is heated up slowly so that the redox reaction between the metal matrix and oxide inclusions occurs. The heating should be well controlled so that the reaction occurs heterogeneously and the structure of the composite material is retained. For example, maintaining the temperature below the melting point of the metal matrix will help stabilize the structure. As a result of the redox reaction, each oxide inclusion is reduced to its respective metal surrounded by a layer of the product oxide. For the example of aluminum matrix and bismuth oxide inclusions, the product will be bismuth metal inclusions encapsulated in aluminum oxide. The encapsulated bismuth inclusions will be inside a metal matrix for fuel rich compositions. For compositions close to stoichiometry, the matrix will be primarily made of the formed oxide. For tin oxide inclusions in aluminum matrix, the product will be tin inclusions encapsulated in aluminum oxide. Once produced, such encapsulated metal inclusions can be heated above the melting point of the encapsulated metal, e.g., Bi. The metal will remain within the protective oxide shell (e.g., Al_2O_3 shell) and will be capable of melting and solidifying repeatedly, without changing the overall material structure or morphology. The continuity and structure of the matrix will be unaffected by melting of encapsulated inclusions. Thus, the desired energy storage material is produced.

Properties of the nanocomposite energy storage material derived from energetic nanocomposites can be adjusted by changing the original metal/oxide ratio: compositions closer to the stoichiometry of the redox reaction will produce more metal (e.g., Bi), as well as more product oxide (e.g., alumina). The resulting energy storage material has therefore a higher energy storage capacity, and it is mechanically stronger. Its bulk thermal

conductivity will be lower, however. More metal-rich energetic composites will result in energy storage materials with less product metal (lower energy storage capacity), less product oxide (lower mechanical strength), and more residual metal (higher thermal conductivity). This gives the opportunity to tailor the material to specific applications.

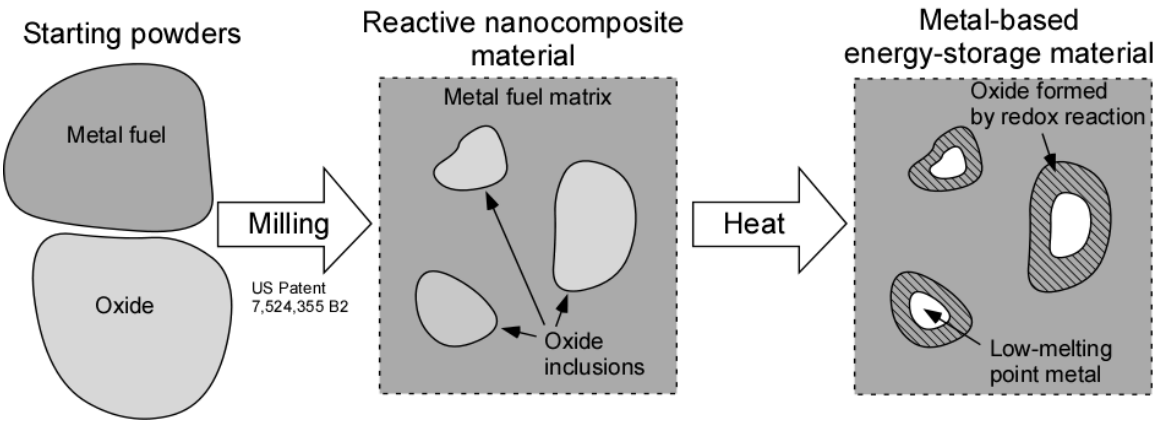

Figure 8.1 Schematic diagram showing preparation of the metal-based energy storage material and its structure.

8.4 Experimental and Instrumentation Techniques

8.4.1 Material Synthesis

Bismuth inclusions serve as melting energy-storing medium in the materials described here. Selecting bismuth is justified by earlier studies of ESM [67, 68]. Starting materials used to prepare fuel rich Al/Bi_2O_3 nanocomposite were elemental aluminum powder, -325 mesh (<45 μm), 99.5% pure, from Atlantic Equipment Engineers and fine powder of bismuth oxide, 99% pure, from Skylighter, Inc. The powders were mixed to produce two different compositions, with 6 and 12 moles of Al per mole of Bi_2O_3, designated respectively as $6Al/Bi_2O_3$ and $12Al/Bi_2O_3$. The blended powders were ball-milled under inert argon gas environment using a shaker mill (SPEX Certiprep, 8000 series) with two 50 mL flat-ended steel vials cooled by room-temperature air jets. Case-hardened carbon steel

balls 3/8”-diameter, were used as a milling media. Ball to powder mass ratio (BPR) was fixed at 10. During milling, 3 mL of hexane was used as the process control agent (PCA). Milling time was set to 45 min.

Nanocomposite powders, consisting of fully dense individual particles obtained by ball milling [53, 171], were used to prepare two types of ESM samples. For thermal analysis, the powders were pressed into 1/8-inch diameter pellets with a uniaxial die at a force of 1000 lbs using a Carver automatic pellet press in room air. Although not quantified, pervious experience shows negligible amount of air may have been trapped inside during pelletizing at these conditions [172]. The pellets were heated in a furnace of a thermal analyzer (Netzsch STA409 PG) in argon to obtain bismuth inclusions encapsulated in aluminum oxide. The pellets were heated to 550 °C and 300 °C and were held at the maximum temperature for 6 and 64 hrs, respectively. For mechanical testing, ¼-inch pellets were prepared using the same pellet press and annealed at 300 °C for 5 days using an Omegalux LMF-3550 box furnace under inert argon gas environment. Any air trapped within the pellet at the particle-particle interfaces, may react with the Al-rich surface of the particle to form Al_2O_3 during annealing under inert argon gas environment. However, this should only add additional barrier to prevent molten Bi migration and should not be in contact with the reduced Bi during the redox reaction, which occur inside the particle. From previous experience [172], pelletizing conditions described above, may only lead to 10 to 20% of porosity, which should not cause any differences to the finally formed ESM structure.

For comparison, two additional composites were prepared. One reference material was used to observe the effect of encapsulation of Bi inclusions on its re-melting as a result

of cycled heating. It consisted of a binary composite of Al and Bi with 6.5 moles of Al per mole of Bi: 6.5Al/Bi. It was also used to compare mechanical properties of different materials. The second material was used as a more appropriate reference for mechanical properties of the prepared material and included Al_2O_3 as well, which could cause dispersion strengthening. It consisted of a ternary Al, Al_2O_3 and Bi composite, with mole composition of $4Al/Al_2O_3/2Bi$. The specific compositions 6.5Al/Bi and $4Al/Al_2O_3/2Bi$ were selected to fix the bismuth volume fraction of the Al/Bi and $Al/Al_2O_3/Bi$ composites to mimic the expected bismuth volume fraction in the encapsulated ESM produced using $12Al/Bi_2O_3$ and $6Al/Bi_2O_3$ nanocomposite powders, respectively. Both reference composites were prepared using the same elemental aluminum as used to prepare Al/Bi_2O_3 nanocomposite powders, elemental bismuth powder, 99.5% pure, - 325 mesh from Alfa Aesar, and α-aluminum oxide nano powder, 99.85% pure, APS 150 nm, from Inframat Advanced Materials. The blended Al/Bi, and $Al/Bi/Al_2O_3$ powders used for different reference materials were ball milled using the same conditions as described above. The milling times were 45 minutes for $4Al/Al_2O_3/2Bi$, and 60 minutes for 6.5Al/Bi. Pellets with diameters 1/8 and 1/4-inch were pressed for thermal analysis and mechanical tests, respectively.

8.4.2 Characterization Techniques

The particle and inclusion sizes, shapes, and morphology of both, as-prepared and reacted materials were characterized using back-scattered scanning electron microscopy (SEM) using a LEO 1530 Field Emission microscope. Since backscattered electrons are sensitive to the phase contrast between elements with different atomic weights, bismuth appears brighter than aluminum in the images.

Thermal stability and temperature-dependent phase changes were analyzed using differential scanning calorimetry (DSC). A Netzsch Simultaneous Thermal Analyzer STA409 PG with a DSC sample carrier and corundum sample crucibles was used to conduct the experiments in ultra-high purity argon (50 mL/min) environment at a heating rate of 10 °C/min.

The thermal stability and latent heat storage of the reacted materials (PCM) were analyzed in the DSC by cycling the annealed samples between 50 °C and 300 °C for 5 times. The thermal energy storage due to the melting of Bi, and the onset temperature of the melting peak was obtained for each cycle.

Using an Instron 5567 universal testing system equipped with a furnace, two different types of mechanical testing were conducted on the consolidated pellets. First, stress-strain curves were recorded at constant temperatures of 250 °C and 300 °C, selected to be respectively below and above the Bi melting point. These isothermal tests were performed for the annealed 12Al/Bi_2O_3 and 6.5Al/Bi pellets. A compressive stress-strain curve and strength at 5 % strain as function of temperature were obtained. In addition, creep tests at a constant load of 3kN were performed where the temperature was scanned from 200 to 300 °C. The strain as function of temperature was recorded; the test was performed for annealed 6Al/Bi_2O_3 and 4Al/Al_2O_3/2Bi. The temperature was scanned by changing the furnace setpoint, which resulted in a nonlinear heating profile. The actual sample temperature was estimated from baseline creep tests, assuming initial and final stable states represent the respective temperature setpoints.

8.5 Results and Discussion

8.5.1 Preparation of Composite with Encapsulated Bismuth Inclusions

DSC traces for 1/8-inch diameter pellets of milled 12Al/Bi_2O_3, and 6.5Al/Bi composites are shown in Figure 8.2. The samples were heated at 10 ºC/min to 550 °C, well above the melting point of pure bismuth. For 12Al/Bi_2O_3 pellet, the DSC signal shows a broad exothermic peak overlapping with a weak endothermic peak near the melting point of pure bismuth metal. The exothermic reaction indicates reduction of Bi_2O_3 and oxidation of Al. By the time the Bi melting point is reached, a small amount of Bi has formed, causing a small endothermic peak overlapping with the broader exothermic peak. In contrast, as expected for the 6.5Al/Bi pellet, the DSC signal shows only an endothermic peak, indicating melting of Bi.

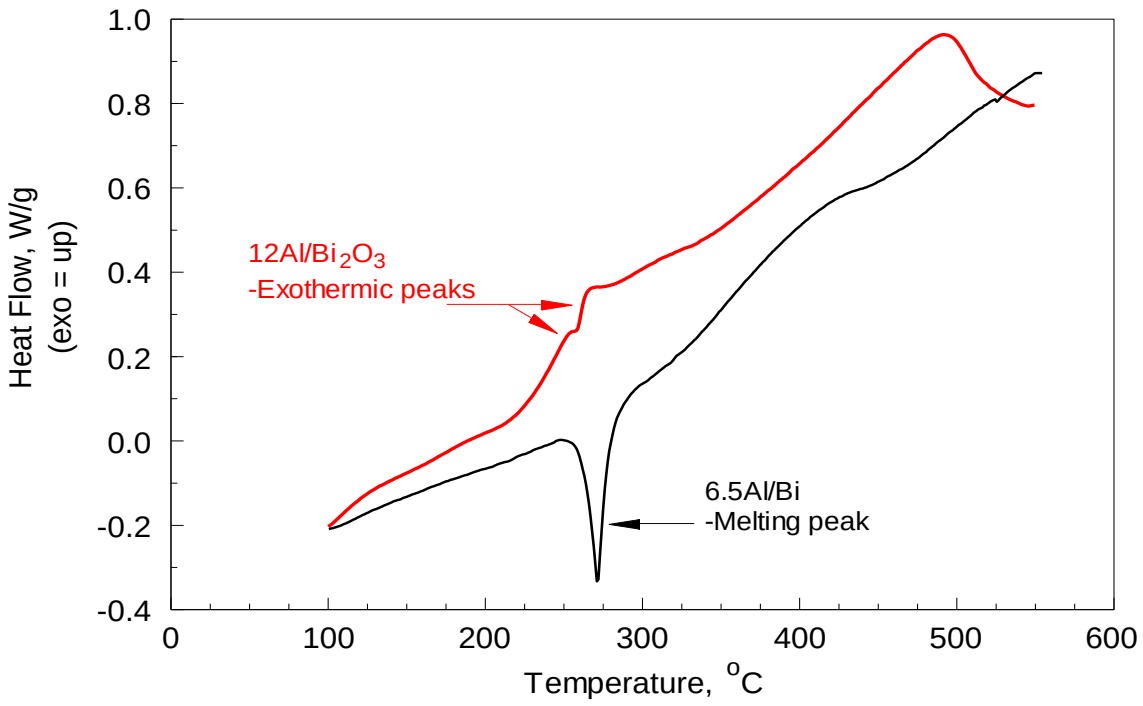

Figure 8.2 DSC signal of 12Al/Bi_2O_3 nanocomposite and 6.5Al/Bi metal-metal composite heated to 550 °C at 10ºC/min.

Backscattered electron SEM images of cross-sectioned pellets for as-milled and annealed 12Al/Bi_2O_3 and 6.5Al/Bi materials are shown in Figure 8.3. Annealed materials were heated to 300 ºC, held at that temperature for 64 hours, and then cycled between 200 and 300 ºC for five times.

For as-milled 12Al/Bi_2O_3, light-colored micron- and nano-sized inclusions of Bi_2O_3 are embedded into a dark-grey Al matrix. After the material is annealed, it is observed that fine light-colored inclusions remain uniformly distributed in the material. Their dimensions remain close to those of the original Bi_2O_3 inclusions. The boundaries and shapes of inclusions change, but no coalescence or migration of inclusions within the sample are detected. The inclusions formed after annealing are mostly composed of Bi. Encapsulating Al_2O_3 cannot be distinguished from the Al matrix. Only amorphous Al_2O_3 is expected to form in samples exposed to 300 ºC and 550 ºC [173]. Such Al_2O_3 layers are nonporous, when formed in absence of an alumina-dissolving solvent [174] and thus should prevent migration of the Bi inclusions.

For as-milled 6.5Al/Bi, the structure is very homogeneous and only nano-scaled inclusions of Bi are observed. After annealing, however, the structure changes substantially. Bismuth is redistributed to form a relatively coarse, interconnected web-like structure. Further, bismuth migrates to the surface of the sample pellet, forming a Bi-rich layer. This behavior is consistent with phase separation occurring in similar alloys upon heating [175]. The phase separation is due to a combination of the Marangoni and Stokes motions. No such redistribution was detected for the material prepared using 12Al/Bi_2O_3 nanocomposite as precursor and producing encapsulated nano-sized Bi inclusions. It is expected that after continuing thermal cycling, the 6.5Al/Bi metal-metal composite will

become mechanically weaker as more and more bismuth metal will concentrate at the outside of the pellet. The composite structure would further coarsen limiting practical usefulness of such material as ESM.

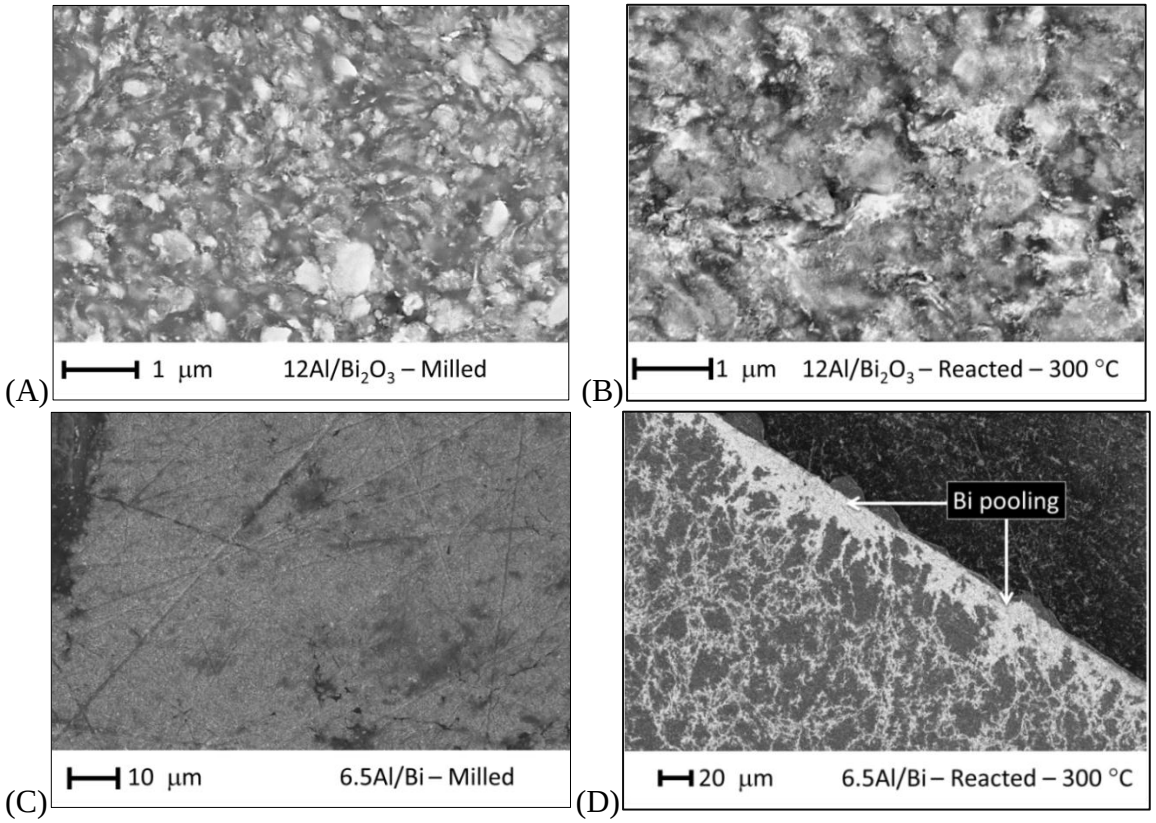

Figure 8.3 Backscattered electron cross-sectional SEM image of (A) $12Al/Bi_2O_3$ metal-metal oxide nanocomposite as milled (B) $12Al/Bi_2O_3$ pellet annealed at 300 °C and held at isothermal for 64 h before cycled for 5 times (C) 6.5Al/Bi metal-metal composite as milled (D) 6.5Al/Bi pellet annealed at 300 °C and held at isothermal for 64 h before cycled for 5 times and evidence of Bi metal pooling to the outer surface is observed.

8.5.2 Energy Storage Performance

DSC traces for both ESM prepared using $12Al/Bi_2O_3$ and for reference 6.5Al/Bi samples are shown in Figure 8.4. For each material, two samples were used in experiments: annealed at 550 and 300 °C for 6 and 64 hrs, respectively. For clarity, the traces for materials annealed at different temperatures are shifted vertically relative to each other. For both $12Al/Bi_2O_3$, and 6.5Al/Bi, an endothermic peak is observed near the pure Bi

melting point. The peak onset temperatures and respective integrated heat effects are listed in Table 8.1. In addition, the heat effects estimated based on the total available amount of Bi for each material are shown.

The peaks occur at a slightly lower temperature, are slightly broader and less deep for the ESM prepared using $12Al/Bi_2O_3$. For this material, the peak comprises two closely overlapping endothermic events, particularly well seen for the sample annealed at 300 ºC. The double peak may indicate dissolution of very small amount of aluminum in bismuth. The Bi-rich part of the Al-Bi phase diagram is not well quantified and the eutectic composition contains more than 99 at-% of Bi [176]. Eutectic melting occurs at 270 ºC, very close to the melting point of pure Bi, 271.442 ºC. If the amount of dissolved Al is less than that of the eutectic composition, the melting peak is expected to split into two closely located peaks, similar to what is observed in Figure 8.4(A). However, if the amount of dissolved Al exceeds that of the eutectic composition, only the eutectic melting peak should be detectable in the present experiments. The liquidus line for the remaining, Al-rich solution will be at a much higher temperature, which was not reached in the present DSC tests. Because of the dissolved aluminum, the enthalpy of melting may exceed the melting enthalpy of pure Bi, as observed in Figure 8.4(B).

The melting peak onset temperatures are slightly lower for the ESM with encapsulated Bi inclusions compared to those for the binary Al/Bi material. It likely is associated with reduced dimensions of the Bi inclusions, so that the effect of melting point depression for nano-sized bismuth domains becomes noticeable [67, 68].

The enthalpy of melting is consistently greater for the samples annealed at a higher temperature for both ESM with encapsulated Bi inclusions and for the reference material.

For the ESM prepared using a nanocomposite thermite, the effect is most likely caused by a more complete reduction of Bi_2O_3 at elevated temperatures. Conversely, for the reference metal-metal composite, the effect is likely caused by a more significant dissolution of aluminum in the molten bismuth upon its heating to higher temperatures.

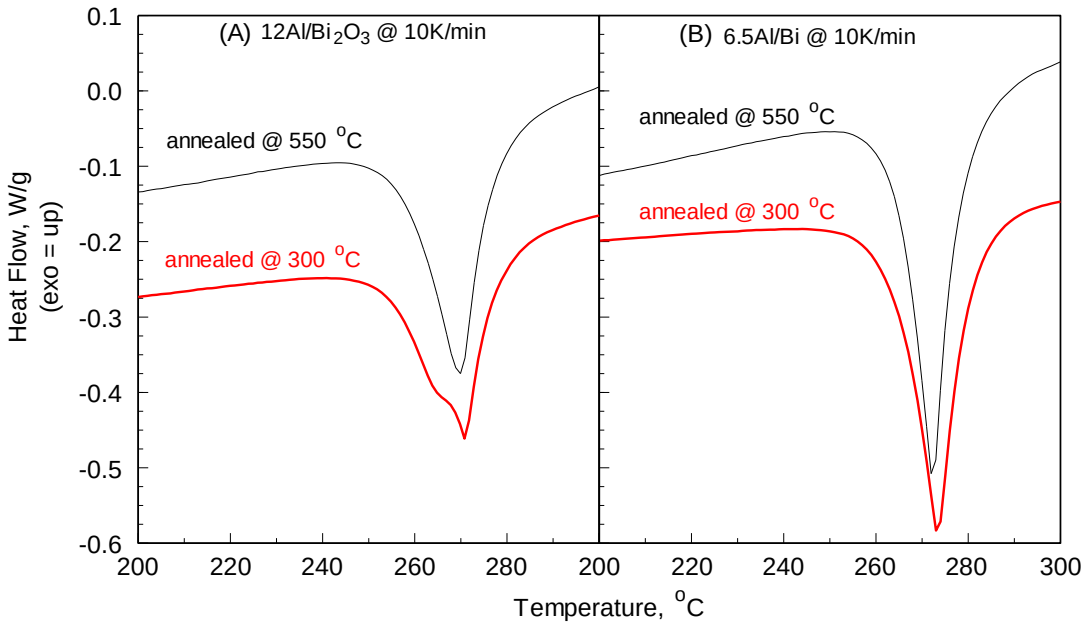

Figure 8.4 DSC signal of $12Al/Bi_2O_3$ nanocomposite and 6.5Al/Bi metal-metal composite annealed at 550 °C and 300 °C for 6 hrs and 64 hrs, respectively, and heated a second time to 300 °C.

Table 8.1 Peak Onset Temperature and Energy Stored for the Prepared Materials. For the Measurements, Annealed Samples were Cooled to 50 °C and Re-heated to 300 °C, Above the Melting Point of Bi

Material	Annealing conditions	Peak onset, °C	Energy Stored, J/g	
			Actual	Expected
$12Al/Bi_2O_3$	550 °C for 6 hrs	256.9	26.40	27.5
	300 °C for 64 hrs	253.4	22.39	27.5
6.5Al/Bi	550 °C for 6 hrs	264.4	31.74	28.3
	300 °C for 64 hrs	264.2	29.40	28.3

8.5.3 Mechanical Testing

Traces of stress as a function of strain for the isothermal mechanical loading tests are shown in Figure 8.5 for annealed 12Al/Bi_2O_3 and 6.5Al/Bi samples. Compressive stress-strain curves were recorded at 250 °C and 300 °C, below and above the Bi melting point of 271.442 °C, respectively. Both materials deform elastically initially, until the yield strength is reached, after which plastic deformation starts. The ESM with encapsulated Bi inclusions prepared using a nanocomposite thermite is generally stronger than the metal composite. Both materials show a reduction in yield strength above the Bi melting point. At 5 % strain, the softening of the encapsulated composite amounts to a 15.6 % reduction in strength, while the strength of the metal composite decreases by 31.3 %. This suggests that the encapsulation of Bi in the molten state results in a material that is mechanically more sound, and less likely to deteriorate at prolonged or repeated exposure to temperatures above the melting point.

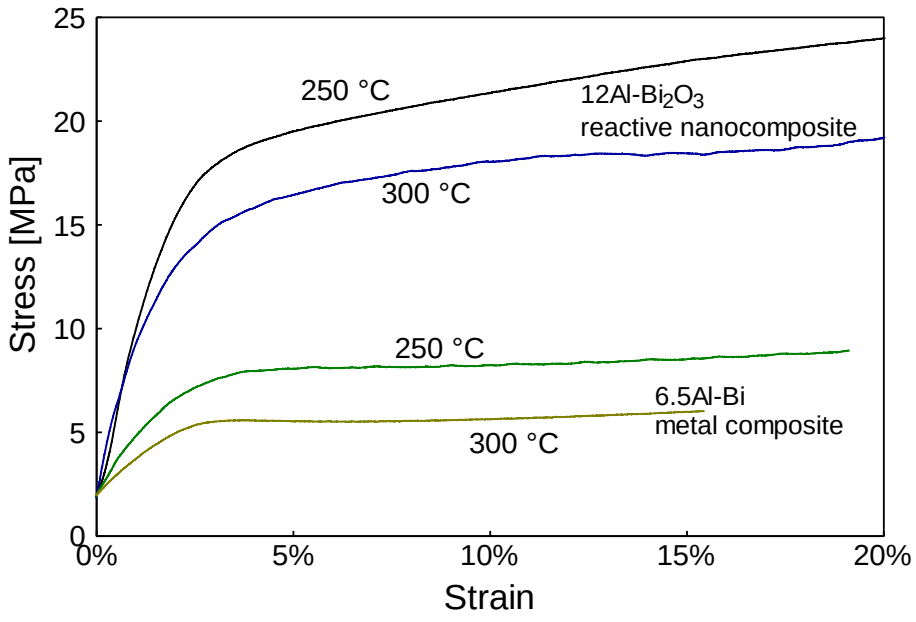

Figure 8.5 Stress-strain curves of 1/4-inch pellets of a 12Al/Bi_2O_3 metal-metal oxide nanocomposite, and a 6.5Al/Bi metal-metal composite.

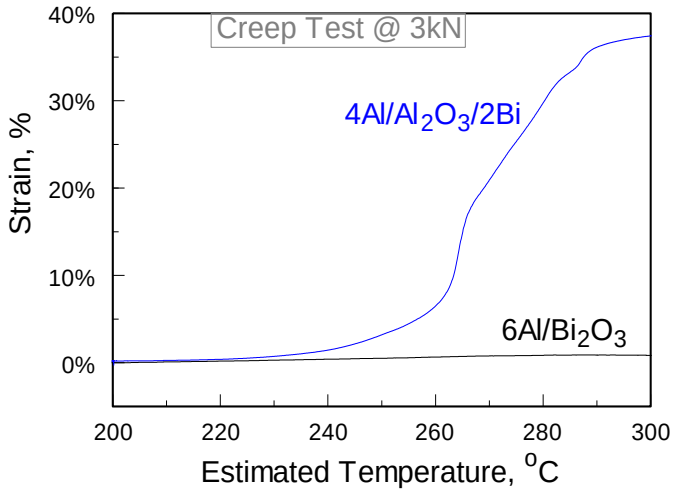

Figure 8.6 Creep Test of $6Al/Bi_2O_3$ and $4Al/Al_2O_3/2Bi$.

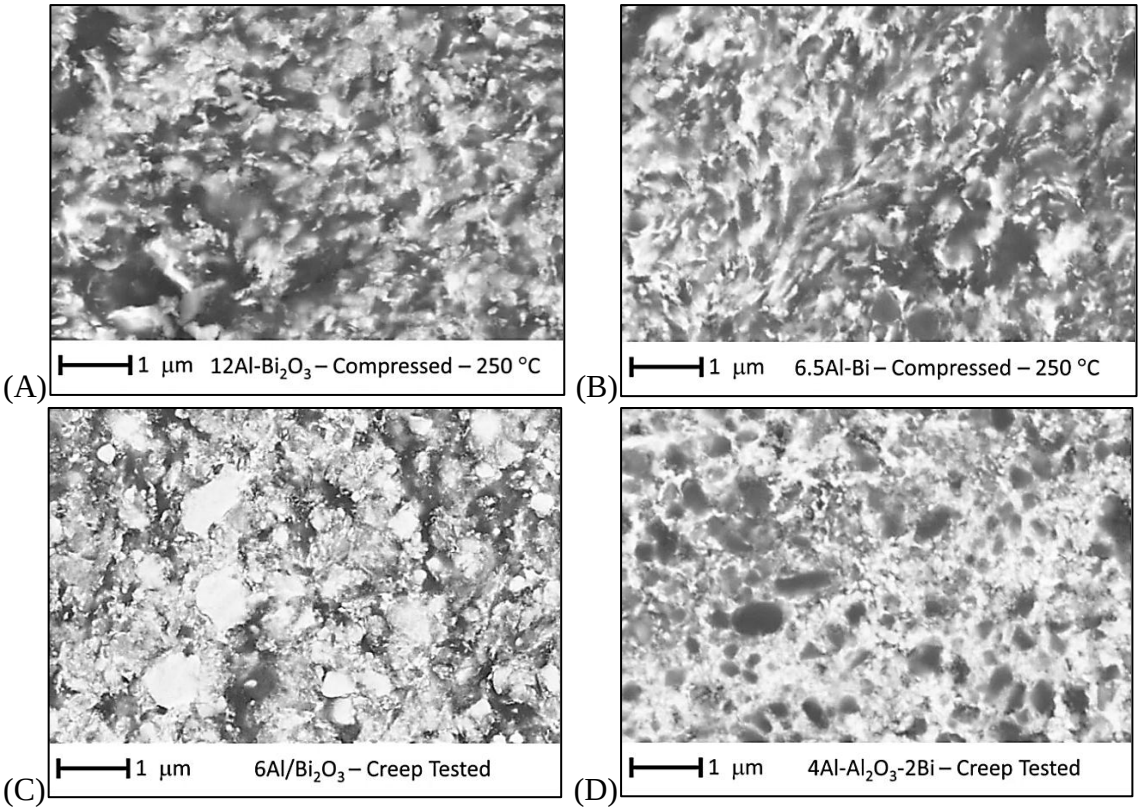

Figure 8.7 Backscattered electron cross-sectional SEM image of samples annealed at 300 °C for 5 days before compression and creep tested using Instron (A) $12Al/Bi_2O_3$ metal-metal oxide nanocomposite compression tested at 250 °C (B) 6.5Al/Bi metal-metal composite compression tested at 250 °C (C) $6Al/Bi_2O_3$ metal-metal oxide nanocomposite creep tested from 200 – 300 °C at 3 kN. (D) $4Al/Al_2O_3/2Bi$ creep tested from 200 – 300 °C at 3kN.

Strain measured in creep tests, when the samples were loaded with a constant force of 3 kN and heated up to 300 ºC is shown in Figure 8.6. The results are shown for the ESM prepared using nanocomposite thermite $6Al/Bi_2O_3$ and for reference ternary composite material $4Al/Al_2O_3/2Bi$ annealed preliminarily at 300 ºC for 120 hrs. It is observed that the reference ternary material begins deforming at about 230 ºC as the Bi component starts to soften. Near the melting point of Bi, dramatic deformation occurs. Conversely, the ESM containing encapsulated Bi inclusions does not show an appreciable deformation in the entire temperature range considered.

SEM images of mechanically tested samples are shown in Figure 8.7 for the encapsulated materials prepared from $12Al/Bi_2O_3$ and $6Al/Bi_2O_3$ and the non-encapsulated materials, 6.5Al/Bi and $4Al/Al_2O_3/2Bi$. For both materials containing encapsulated Bi shown in Figure 8.7(A) and Figure 8.7(C), the bright Bi inclusions appear to be roughly equiaxial and uniformly dispersed in the darker Al-rich matrix. As in Figure 8.3, it is difficult to detect Al_2O_3. For the material with greater Bi concentration (Figure 8.7(C)), the Bi inclusions are greater in size and occupy a greater fraction of the material's volume. For both materials containing non-encapsulated Bi, bright Bi inclusions form interconnected networks. It is interesting to compare structures shown in Figure 8.7(C) and Figure 8.7(D), which have similar concentrations of Al, Bi, and Al_2O_3. Clear morphological differences between the two materials are observed. In Figure 8.7(D), crystalline Al_2O_3 particles are visible. Such particles are well separated from one another and are surrounded by interconnected Bi metal matrix. In contrast, the Al_2O_3 is hard to detect in Figure 8.7(C); however, multiple separated Bi inclusions are observed instead. Most of the Bi inclusions

have well-defined boundaries surrounded by a darker phase, which is expected to be Al_2O_3 and Al.

8.6 Conclusions

Energy storage materials containing inclusions of an easy-to melt metal, Bi, encapsulated with protective Al_2O_3 in an aluminum matrix were prepared using nanocomposite Al/Bi_2O_3 thermite as a precursor material. The precursor material was slowly annealed to reduce Bi_2O_3 and form encapsulated Bi inclusions. The material is shown to be capable of storing energy by melting and solidifying Bi inclusions. The inclusions do not drift inside the material upon heating; prepared composite structure remains largely intact upon thermal cycling. Conversely, the structure of reference composite materials with similar bulk compositions but without encapsulated Bi inclusions is not preserved upon thermal cycling. Molten Bi tends to separate from Al and form interconnected coarse network of inclusions. Upon cycling, Bi accumulates on surface of the material. Difference in mobility between encapsulated and non-encapsulated Bi inclusions causes dramatic differences in the mechanical properties of the resulting composites. Materials with encapsulated Bi inclusions are much stronger and capable of retaining their structure and strength despite thermal cycling expected for useful energy storage materials.

CHAPTER 9

BIMETAL Al-Ni NANO-POWDERS FOR ADVANCED ENERGETICS

9.1 Abstract

Four bimetal Al-Ni nano-powders with compositions varied from 5 to 45 at. % of nickel were synthesized by explosion of electrically heated twisted pure metal wires in argon. The nano-powders were characterized using electron microscopy, x-ray diffraction, and thermal analysis. In addition, ignition experiments were performed using an electrically heated filament and electrostatic discharge to initiate the reaction. The results were compared to those for pure nano-aluminum powder (n-Al) prepared using the same wire explosion technique. The nano-powders with high nickel concentrations contain fully reacted intermetallic phases, which are difficult to oxidize making them unattractive for energetic formulations. Nano-powders with lower nickel concentrations do not contain significant amounts of the intermetallic phases. No intermetallics could be detected in the powder with 5 at. % Ni, which oxidized qualitatively similar to n-Al. The overall mass gain during oxidation for the bimetal powder was nearly identical to that of n-Al, indicating the same heat release anticipated from their combustion. Oxidation kinetics assessed for this material accounting directly for the measured particle size distribution was compared to that of n-Al. The bimetal powder oxidized slower than n-Al, indicating its greater stability during handling and storage. The bimetal powder was less ESD-ignition sensitive than n-Al, but generated a stronger emission signal when ignited. Therefore, the bimetal powder with 5 at. % Ni is an attractive replacement of n-Al for advanced energetics with lower ESD sensitivity, better stability, and improved combustion performance.

9.2 Introduction

Aluminum powders are the most common metal fuel additives to propellants, explosives and pyrotechnics due to the high energy density [177-179]. There is significant interest in aluminum nano-powders (n-Al), which can be readily manufactured using electrically exploded wires, a technique developed in recent decades [72-74]. Such nano-powders react faster than conventional micron-sized aluminum powders, due to a large available surface area [75-77]. Availability of n-Al stimulated development of many novel nano-energetic systems, including nano-thermites and intermetallics [69, 71, 180]. Significant improvements in reaction rates, correlated directly with the increased available reactive surface, observed for nano-energetic materials are unfortunately accompanied with their increased ignition sensitivity to electrostatic discharge (ESD) and other ignition stimuli [78, 79]. Additionally, aging causing deterioration of reactive properties has been a concern for nano-energetic materials and n-Al, in particular [80, 81].

Commonly, metal nano-powders and associated nano-energetic materials may be desensitized using less reactive non-metal additives [38, 39]. For example, carbon nanotubes were used to desensitize Al-CuO nano-thermites; however, they had adverse effects on combustion rates and overall energy density [40]. Similarly, organic coatings applied to n-Al substantially reduce its energy density [41, 42]. Preserving both energy density and high reactive surface while reducing the sensitivity remains a main challenge in developing nano-energetic materials.

The approach explored here involves aluminum-based bimetal nanoparticles. In particular, aluminum-nickel (Al-Ni) nano-powders are considered. Formation of intermetallic Al-Ni alloys is well-known to occur through exothermic reactions [181-184],

which could be boosting ignition and ensuing metal oxidation. It is also expected that the oxides produced at elevated temperatures in the bimetal Al-Ni system may be less protective than pure Al_2O_3; thus the heterogeneous reactions controlling ignition may be accelerated. At the same time, the presence of Ni may reduce the sensitivity of respective nanoparticles to oxidation at low temperatures.

9.3 Technical Approach

Four bimetal spherical nano-powders are prepared with different aluminum to nickel ratios. Each powder is characterized to assess its phase composition, reactions occurring upon heating, and ignition temperature. A composition with the most attractive properties is identified, for which additional measurements are performed. In particular, oxidation kinetics is characterized following a recently developed experimental methodology enabling one to explicitly account for oxidation of particles of different sizes [83, 185, 186]. Results are used to predict the aging behavior of the bimetallic powder; they are also compared directly with similar results for n-Al. Finally, electrostatic ignition experiments are performed for both the bimetal nano-powder and pure n-Al.

9.4 Materials and Experimental Methods

9.4.1 Materials

A technique used to prepare spherical aluminum nano-powders (n-Al) in argon by electro-exploded wires was recently adapted to prepare bimetal nano-powders [187-189]. Instead of a single wire, two pure metal wires are twisted together and heated by a high current pulse. The evaporated metal condenses forming composite bimetal nanoparticles.

Spherical Al-Ni nano-powders with various compositions were prepared, as listed in Table 9.1. The powders were passivated at room temperature for 72 hours at a reduced oxygen pressure.

Table 9.1 Al-Ni Nano-powders Prepared with Their Sample IDs

Sample IDs	Composition (atomic %)
Al95-Ni05	95% Al : 5% Ni
Al90-Ni10	90% Al : 10% Ni
Al80-Ni20	80% Al : 20% Ni
Al55-Ni45	55% Al : 45% Ni

9.4.2 Characterization

The prepared nano-particles were examined using a JEOL JEM-100 CXII transmission electron microscope (TEM) and a LEO 1530 Field Emission back-scattered scanning electron microscope (SEM). The TEM images were processed to obtain particle size distributions for selected powders. A PANalytical Empyrean diffractometer was used for X-ray diffraction (XRD) to determine phase compositions of the prepared materials. The XRD powder diffractometer was operated at 45 kV and 40 mA using unfiltered Cu Kα radiation (λ = 1.5438 Å). A Netzsch Simultaneous Thermal Analyzer STA409 PG with corundum sample crucibles was used to conduct the differential scanning calorimetry (DSC) measurements in ultra-high purity argon (50 mL/min) at a heating rate of 20 K/min. Thermo-gravimetric (TG) experiments combined with DSC were conducted in an argon/oxygen gas mixture at 20 K/min for all powders. In addition, a set of TG measurements was performed for a selected nano-powder oxidized at heating rates varied from 5 to 20 K/min using a TA Instruments TA Q5000-IR.

Ignition of the nano-powders was characterized in air using a heated filament experiment described in detail elsewhere [96, 190]. A hexane slurry with the powder was

made to prepare a thin, 10-mm long coating on a 45-mm long, 0.5-mm diameter nickel-chromium alloy heating wire. A DC current was used to heat the coated wire. Varied applied voltage and an adjustable resistor connected in series with the wire were used to vary the heating rates in a range of 10^3 - 10^5 K/s. Using a high-speed infrared pyrometer (DP1581 by Omega Engineering, Inc.) focused on an uncoated filament surface adjacent to the powder coating, the temperature of the filament was measured. Powder emission was visualized using a high speed video camera (MotionPro 500 by Redlake), operated at 500 fps. The ignition instant was registered when the powder became brighter than the heated filament.

In a separate ignition experiment, selected nano-powders were ignited using an ESD to identity the minimum ignition threshold and compared it with that of n-Al. A setup based on a model 931 firing test system by Electro-Tech Systems, Inc., was used, which was described in detail elsewhere [114, 133]. The powder was placed inside a 0.5-mm deep, 3-mm diameter cavity of a grounded, custom-made polished aluminum sample holder. An even layer thickness was achieved by scraping away the excess of powder with a razor blade. A pin electrode was fixed ~ 0.2 mm above the surface of the powder. A 2000 pF capacitor was charged to a voltage in the range of 2 – 7 kV, before discharging through the pin electrode to the nano-powders. All experiments were performed in air at 1 atm. Optical emission produced by the ignited powder was recorded using a photomultiplier tube (PMT) filtered at a wavelength λ = 568 nm, placed 17 cm away from the sample. In selected experiments, optical emission was recorded using a 32-channel H7260 series linear array multianode PMT by Hamamatsu with a spectrometer covering a wavelength range of 373.4 – 641.0 nm (see APPENDIX C).

9.5 Results and Discussion

9.5.1 Characteristics of Bimetal Nano-powders with Different Compositions

Both TEM and SEM images of the prepared nano-powders show that all powders are mostly spherical without significant phase contrast between aluminum and nickel. A TEM image of Al95-Ni05 nano-powder is presented in Figure 9.1 as an example. Most of the particle images have uniform brightness, suggesting that aluminum and nickel are mixed homogenously. In some particles, however, dark inclusions are observed indicative of nickel-rich phases. Few particles have dark shells, suggesting nickel-rich surface layers. However, such particles with pronounced heterogeneities are relatively rare.

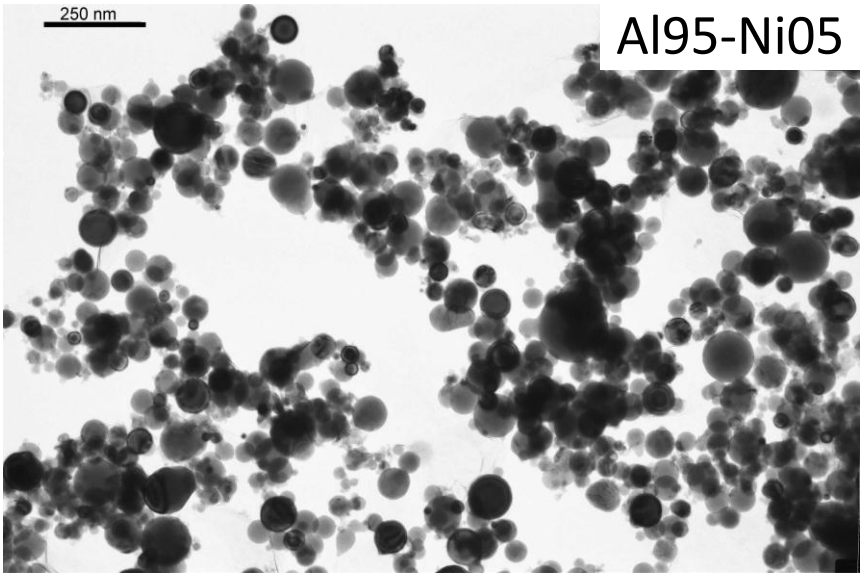

Figure 9.1 TEM image of Al95-Ni05 nano-powder.

A particle size distribution for the powder shown in Figure 9.1 was obtained from processing multiple TEM images; the result is shown in Figure 9.2. In addition, a size distribution for a reference pure n-Al sample is shown. The same wire explosion apparatus

was used to prepare both n-Al and bimetal Al-Ni powders. Typically, Al-Ni powders are finer than n-Al, which is observed in Figure 9.2 for the example shown.

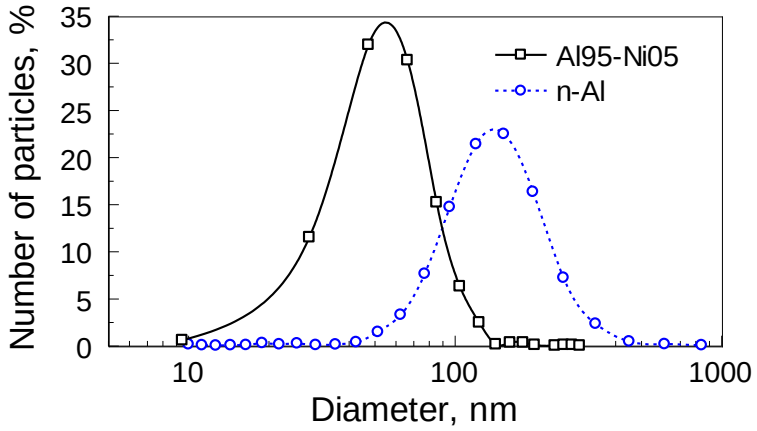

Figure 9.2 Particle size distributions of Al95-Ni05 and n-Al obtained from processing TEM images.

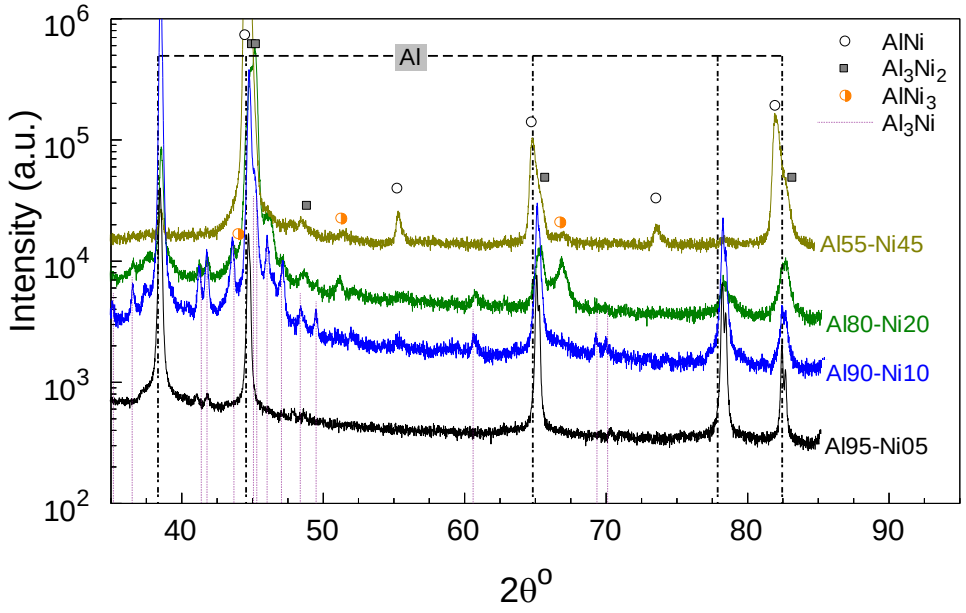

Figure 9.3 XRD patterns for all as-prepared Al-Ni nano-powders.

XRD patterns for all nano-powders are shown in Figure 9.3. For the most nickel-rich material Al55-Ni45, aluminum peaks are not observed; instead AlNi intermetallic alloy dominates the recorded XRD pattern. Smaller peaks of other alloys,

including $AlNi_3$ and Al_3Ni_2 are also observed. Thus aluminum and nickel are fully reacted for this material, making it less interesting for applications in energetic systems. For Al80-Ni20, pure Al peaks are significant along with peaks produced by intermetallics Al_3Ni_2 and $AlNi_3$. In addition, weak peaks of Al_3Ni appear. Peaks of Al_3Ni become much stronger and comparable to the peaks of Al for Al90-Ni10. The least reacted sample is Al95-Ni05, for which the XRD pattern shows peaks of Al with only minor indication of Al_3Ni.

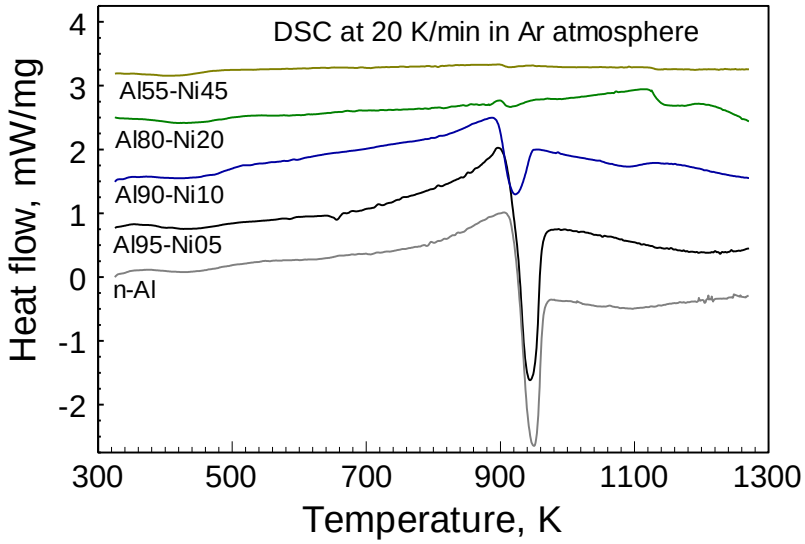

Figure 9.4 DSC of Al-Ni and n-Al powders obtained in a flow of argon at the heating rate of 20 K/min.

The results of the DSC experiment conducted in argon are shown in Figure 9.4 for all Al-Ni nano-powders and compared to n-Al. All samples, except Al55-Ni45, show a weak exothermic peak followed by a strong endotherm near pure aluminum melting point. Both peaks become stronger for samples with smaller concentrations of Ni. The exothermic peak was caused by the sample reacting with residual or trace oxygen remaining in the furnace that was being flushed with argon. This peak could be reduced by multiple repeated evacuations and refills of the furnace with argon prior to the experiment.

It suggests that the samples with less Ni are oxidizing more readily. The melting occurs at the same temperature as for the bulk aluminum, and thus the melting point is not apparently affected by the particle sizes. In qualitative agreement with the observed XRD patterns, the endothermic Al melting peaks are diminished as the concentration of Al is decreased. For example, for Al55-Ni45, no Al melting peak is observed, consistently with its respective XRD pattern only showing intermetallic alloys and no aluminum in that material. Conversely, aluminum melting peak for Al95-Ni05 is identical to that observed for pure n-Al.

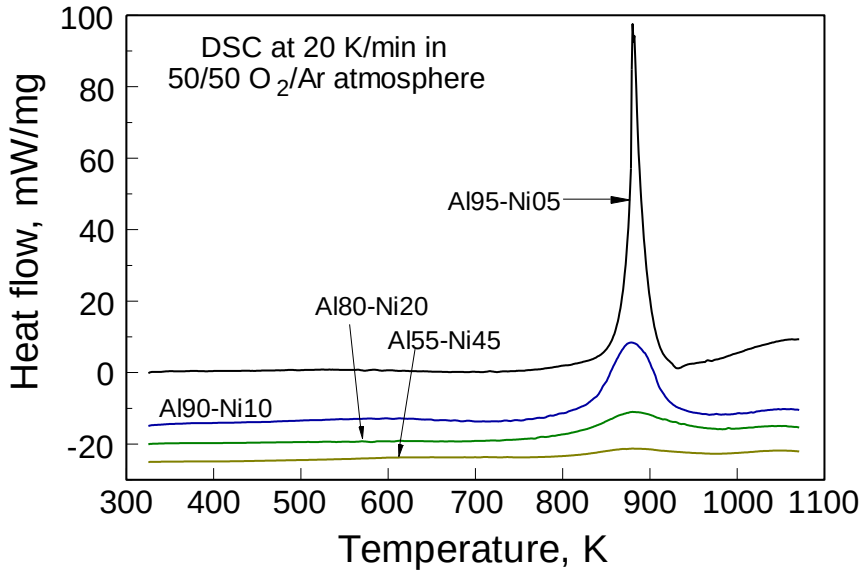

Figure 9.5 DSC of Al-Ni nano-powders conducted in an argon/oxygen mixture at 20 K/min.

Results of simultaneous DSC and TG measurements conducted in an argon/oxygen mixture are shown in Figure 9.5 and Figure 9.6, respectively. The experiment conducted at the same conditions with a similar starting mass load of n-Al resulted in its ignition. DSC and TG signals for all nano-powders show an exothermic peak and a respective sample mass gain prior to the Al melting point, similar to the first pronounced oxidation step for aluminum caused by transformation of the amorphous oxide into a γ-Al_2O_3 crystalline

polymorph [191-194]. Nano-powders with lower concentrations of nickel show sharper exothermic peaks and higher percentages of relative mass gain. The shape of the DSC peak for Al95-Ni05 suggests that this material nearly ignited at about 880 K. These results suggest that materials with lowest concentrations of nickel, such as Al95-Ni05, are most interesting as potential replacements of pure n-Al in energetic formulations. On the other hand, aluminum appears to be fully passivated in materials containing primarily intermetallic alloys; the lack of its oxidation upon heating in thermo-analytical experiments suggests that a poor combustion performance is also expected.

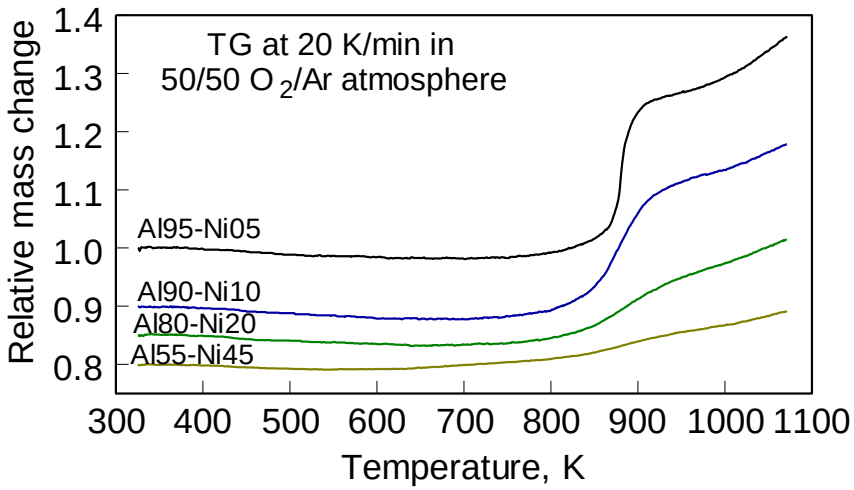

Figure 9.6 TG of Al-Ni nano-powders conducted in an argon/oxygen mixture at 20 K/min.

Results of the heated filament experiments for all bimetal nano-powders are shown in Figure 9.7. Ignition temperatures are plotted as a function of the heating rate. Each point represents at least five individual tests performed at the nominally the same heating rate. All powders ignite in vicinity of the aluminum melting point. For all nano-powders except Al55-Ni45, containing mostly AlNi (cf. Figure 9.3), the ignition temperatures do not change at different heating rates. This suggests that the aluminum melting is an ignition trigger. It is likely that the first oxidation step begins for all powders below the

aluminum melting point; however, it may be incomplete by the time the powder is heated to the aluminum melting point when the heating rates are much higher than in TG experiments. When aluminum melts, particle surface morphology is changed, and a reactive fresh surface is likely produced further accelerating oxidation and causing ignition of the nanoparticles. For Al55-Ni45, the ignition temperature increases at greater heating rates, suggesting a different ignition mechanism compared to other powders. Indeed, this material does not contain pure aluminum and thus no changes in particle morphology is expected at the aluminum melting point, unlike for other Al-Ni nano-powders.

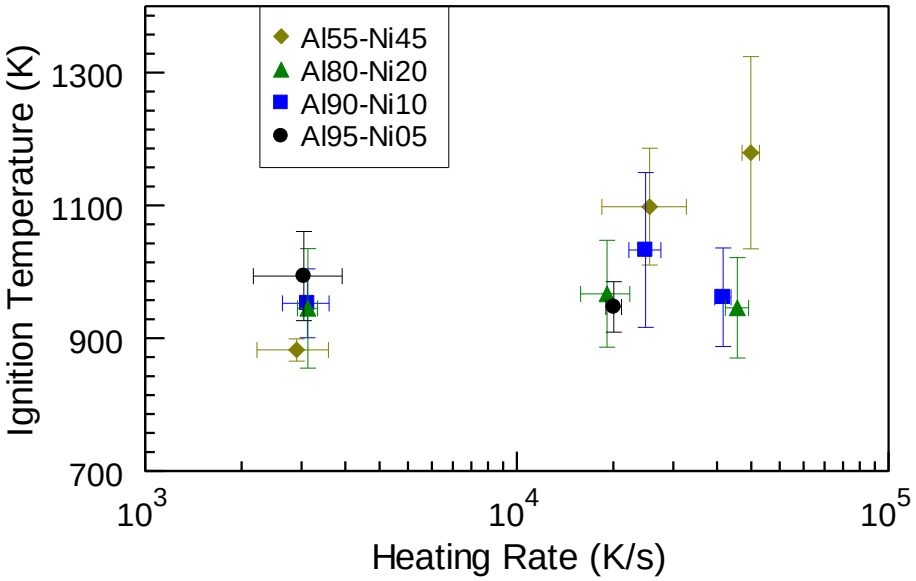

Figure 9.7 Ignition temperatures of Al-Ni nano-powders as function of heating rate.

9.5.2 Oxidation of Al95Ni05

Results of DSC and TG measurements with different prepared Al-Ni nano-powders suggested that the material with the lowest concentration of Ni, Al95-Ni05 is most attractive as a potential replacement of n-Al. Thus, more detailed measurements were performed to characterize reactivity and sensitivity for this material. A set of TG measurements performed for Al95-Ni05 in pure oxygen at different heating rates is

presented in Figure 9.8. In addition, a similar measurement for n-Al at one of the heating rates is shown for comparison. A cursory inspection of data shown in Figure 9.8 suggests that the oxidation of n-Al occurs very similarly to that of Al95-Ni05. Comparing directly the TG traces recorded at 5 K/min for both materials, one observes that the first oxidation step for Al95-Ni05 nano-powder occurs at a slightly lower temperature than for n-Al. Qualitatively, this observation can be interpreted considering that Al95-Ni05 is substantially finer than n-Al (cf. Figure 9.2). The overall mass change of Al95-Ni05 is similar to that of n-Al, suggesting that the amount of reactive aluminum is similar to each other in both materials.

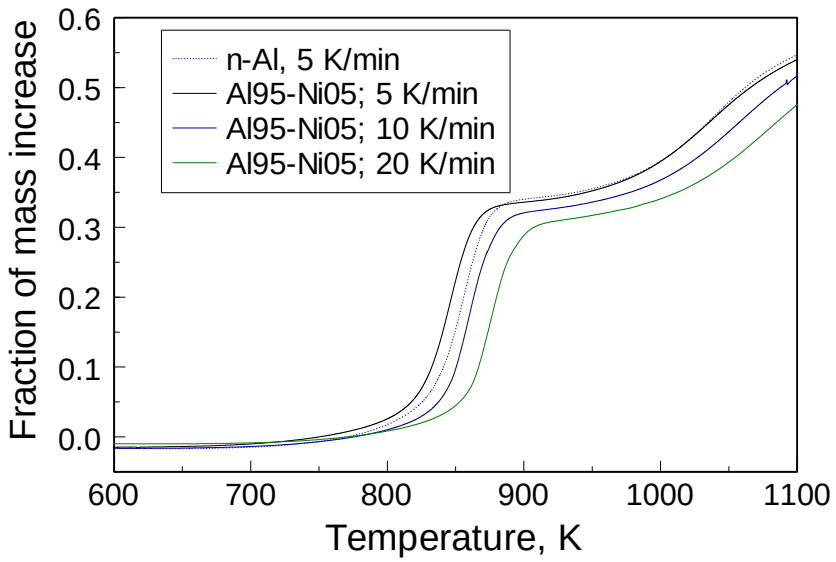

Figure 9.8 TG of Al-Ni and n-Al powders in oxygen-argon flow at various heating rates.

9.5.3 TG Data Processing

Results of the TG experiments were processed considering a specific oxidation model in order to account explicitly for the effect of particle size distribution [83]. The model is illustrated in Figure 9.9. As the metal is consumed, a void grows inside the particle core.

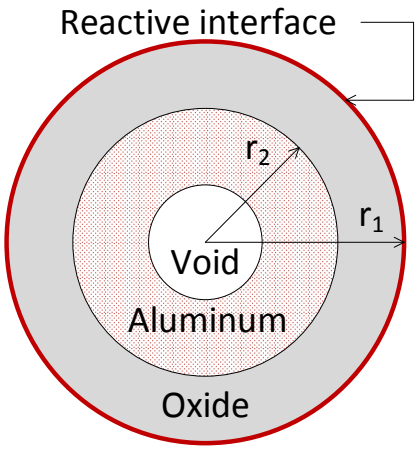

Figure 9.9 Schematic diagram of the particle geometry used for the oxidation model.

The weight gain measured in a TG experiment is split among powder particle size bins:

$$\frac{dM}{dt} = \sum_i \frac{dm_i}{dt} = \sum_i A_i j_i \tag{9.1}$$

where M is the total powder mass, t is time, m is the mass of particles in an individual particle size bin, A is the area of the reactive interface, and j is mass flux of the slowest-diffusing species. Index i numbers particle size bins. Following earlier work on aluminum oxidation [83, 186], the outward diffusion of aluminum is assumed to limit the rate of reaction, so that the reaction interface is located outside of the growing oxide shell, at $r=r_1$, as shown in. The presence of nickel was neglected for the purpose of the present analysis, considering its relatively low concentration and considering that the TG curves for the bimetal Al95-Ni05 are very similar to those of n-Al (cf. Figure 9.8). The change in the reactive surface area for each size bin, $A_i = 4N_i\pi r_{1,i}^2$, is determined accounting for number of particles in each bin, N_i, and radius of the respective reactive interface, $r_{1,i}$. Based on the solution of diffusion equation for a spherical particle with a growing oxide shell, the flux depends on the radii r_1 and r_2 as:

$$j_{r=r1} = \frac{r_2}{r_1}\frac{\rho D}{r_2 - r_1} \tag{9.2}$$

where D is diffusion coefficient, and ρ is density. Outer and inner radii of the oxide shell are labeled as r_1 and r_2, respectively (see Figure 9.9). Index i marking an individual size bin is removed for brevity in equation (9.2). Thus, the measured mass uptake is distributed proportionally to the function $A_i \cdot \frac{r_2}{r_1}\frac{1}{r_2 - r_1} \sim \frac{r_2 r_1}{r_2 - r_1}$ accounting for the effect of particle geometry on the mass flux. The density affects the thickness of the growing oxide layer; it is assumed to increase in a stepwise fashion when a polymorphic transition between amorphous and γ-Al_2O_3 occurs. For simplicity, this transition is assumed to occur at a fixed temperature, although a more accurate model would need to account for the effect of both temperature and thickness of the oxide shell [195-197]. Thermal expansion was accounted for both metal core (assuming it behaves as the pure aluminum) and the oxide.

TG traces representing oxidation of particles of each given size bin obtained for different heating rates are processed using a model-free isoconversion technique [198, 199] to obtain activation energy as a function of the reaction progress. Once the activation energies are obtained, the reaction model represented by Figure 9.9 is considered to identify the pre-exponent and thus to fully quantify the rate of oxidation.

9.5.4 Oxidation Mechanism and Kinetics

Results shown in Figure 9.8, processed as described above can be recast in terms of the thickness of the oxide shell grown on particles of different sizes as a function of temperature. This is illustrated for several particle sizes in Figure 9.10. All particles are assumed to have the same initial oxide layer (2.5-nm thick), and smaller particles are fully oxidized first. For the smallest, 9-nm, particle size, the complete oxidation is predicted at

about 770 K, which is close to the assumed temperature of the polymorphic phase change in alumina. This phase change accounts for a sudden reduction in the oxide thickness observed around 770 K for all particles. Larger size particles are fully oxidized at increasingly higher temperatures. For the oxidizing particles, the thickness of the growing oxide shell is a weak function of the particle size, with larger particles predicted to have slightly thicker oxide shells.

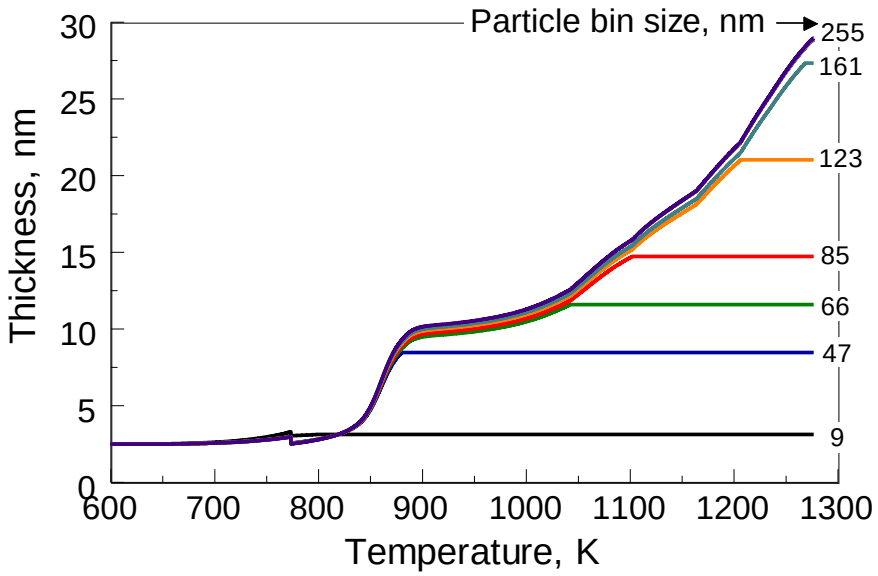

Figure 9.10 Thickness of the oxide layer grown on particles of different sizes as a function of temperature for Al95-Ni05 heated in oxygen-argon flow at 10 K/min. Particle bin size represents the initial particle diameter.

Data shown in Figure 9.10 are useful to compare oxidation rates for different materials. Instead of considering the TG-measured overall mass increase for the whole powder, as shown in Figure 9.8, which is affected by the initial particle size distribution, oxidation rates of different materials are compared directly considering the thickness of the oxide shell grown on particles of the same sizes heated following the same program. Such a comparison for Al95-Ni05 and n-Al is presented in Figure 9.11. Results are shown for two representative size bins, one is close to 120 and the other, to 255 nm for both powders.

It is observed that particles of n-Al oxidize faster, growing thicker shells than the same size particles of Al95-Ni05 while being heated at the same rate to the same temperature. This result could not have been obtained examining direct measurements, shown in Figure 9.8; it emerges only after the present processing accounting for the measured particle size distributions is applied. It is clear from Figure 9.11 that Al95-Ni05 is substantially more stable than n-Al, and thus is expected to age slower and ignite at a higher temperature than n-Al. Considering only a minor reduction in the total reaction enthalpy of Al95-Ni05 compared to n-Al, this bimetal material may be an attractive replacement of n-Al in the applications requiring a reduced ignition sensitivity and greater stability of the energetic formulation.

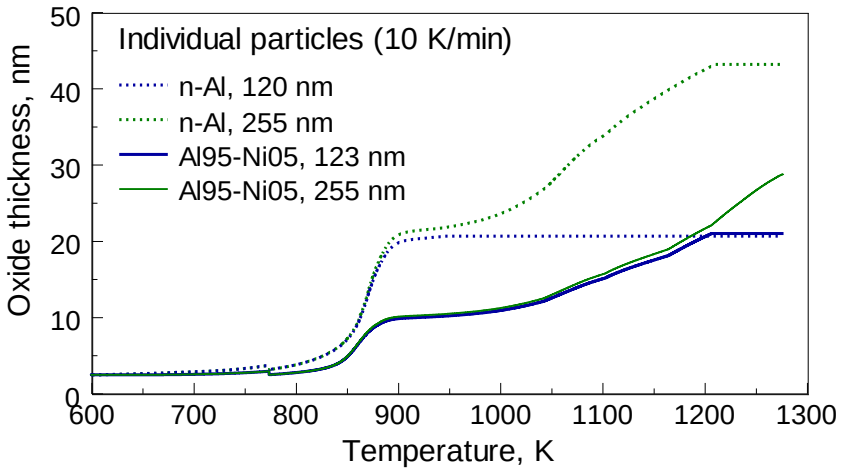

Figure 9.11 Comparison of the oxide thickness for the close particle sizes for n-Al and Al95-Ni05 as a function of temperature. The results obtained by splitting the respective measured TG traces among different powder size bins and accounting for the oxidation model illustrated in Figure 9.9.

The thickness of the grown oxide layer is a convenient indicator of the oxidation reaction progress. TG traces for individual particle size bins recast in terms of the oxide thickness, as shown in Figure 9.10 and Figure 9.11, and obtained from experiments performed at different heating rates were used to calculate the activation energy using a

model-free isoconversion processing method [199]. This processing was performed for different particle size bins for both n-Al and Al95-Ni05, yielding self-consistent descriptions for the apparent activation energy as a function of the oxide thickness for both materials. Results of this analysis are presented in Figure 9.12. Shown are the apparent activation energies obtained for particles with sizes equal to the surface averages for each powder. The activation energies as functions of the oxide thickness for other particle sizes overlapped with the present curves nearly perfectly for both materials.

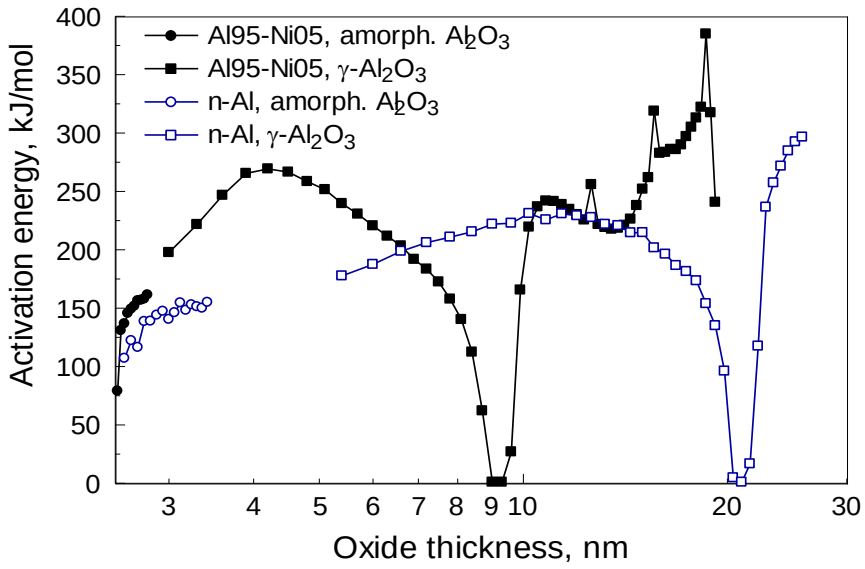

Figure 9.12 Apparent activation energies as a function of the oxide thickness characterizing growth of both amorphous and γ-Al_2O_3 polymorphs for n-Al and Al95-Ni05.

The processing was conducted separately for the apparent activation energies describing growth of amorphous alumina below 770 K, and growth of γ-Al_2O_3 with a higher density at higher temperatures. Thus, two separate reaction progress functions were used, i.e., thicknesses of each of the alumina polymorphs. For each calculation, an initial thickness registered for all three heating rate measurements was treated as the starting value, corresponding to zero reaction progress. This treatment was straightforward for the

growth of amorphous oxide, which was always assumed to have the same "natural" thickness of 2.5 nm. However, when the assumed phase change temperature of 770 K was reached, different oxide thicknesses were grown at different heating rates. The processing for γ-Al_2O_3 started from its thickness observed for the lowest heating rate – and thus also registered for all three heating rates, but at slightly higher temperatures, which explains a range of oxide thicknesses near the phase change in Figure 9.12, for which no activation energy was obtained.

Qualitatively, the trends describing changes of the apparent activation energy as a function of the oxide thickness are similar for both Al95-Ni05 and n-Al. A rapid increase in the activation energy occurs at the beginning of oxidation. This increase was proposed to be caused by healing of imperfections and defects existing in the natural amorphous alumina, as its thickness is increasing [84]. The rate of this increase is reduced before γ-Al_2O_3 begins to form. The activation energy continues to increase for γ-Al_2O_3; eventually, a peak in the activation energy is reached. After the peak, a relatively rapid decrease in the apparent activation energy is observed down to unrealistically low values. Finally, another increase in the apparent activation energy occurs at still greater thicknesses. For both materials, a rapid reduction in the apparent activation energy occurs when the temperature is close to the melting point of aluminum. The decrease in the apparent activation energy is most likely associated with a substantial change in the morphology of the reaction interface, e.g., formation of cracks in the oxide shell, coalescence/sintering of different particles, leakage of molten aluminum, etc. These phenomena cannot be described in terms of the oxidation model considered here (cf. Figure 9.9). Therefore, any useful interpretation of the results presented in Figure 9.12

should be limited to the initial changes in the apparent activation energy. It is suggested that the initial growth of the apparent activation energy up to its peak value may represent the actual heterogeneous oxidation occurring following a scenario shown in Figure 9.9. This initial reaction is important to quantify because it most likely determines how the material ignites and how its aging occurs before substantial fraction of the material have been oxidized. Comparison of the trends shown in Figure 9.12 shows that the apparent activation energy of oxidation is generally higher for Al95-Ni05 than it is for n-Al. This result is consistent with the observed greater stability of Al95-Ni05 compared to n-Al. A higher activation energy (and thus a greater stability) for Al95-Ni05 is most likely associated with the modified properties of the growing oxide scale. Although the structure of the growing oxide remains generally unchanged, based on the same observed sequence of the oxidation steps as observed for pure aluminum, its diffusion resistance is increased as a result of its doping with the oxidized nickel.

9.5.5 Preliminary Analysis of Aging of Al95-Ni05 and n-Al

Activation energies obtained from the model-free isoconversion processing are inserted in the explicit oxidation model represented in Figure 9.9, where the diffusion coefficient D is described using an Arrhenius expression. The pre-exponent for the diffusion coefficient is then adjusted to describe the actual oxidation kinetics; thus, the pre-exponent is specified as a function of the oxide thickness, similar to that for the apparent activation energies. The obtained complete description of the reaction kinetics is then used to predict aging of n-Al and Al95-Ni05 powders. For a specific example, aging for both powders was considered upon their exposure to an oxygen-containing environment at 30 °C. For simplicity, calculations for each powder considered a spherical 100-nm diameter particle.

The predicted reduction in the radius of the metal core as a function of exposure time is shown in Figure 9.13. As expected, n-Al is aging substantially faster than Al95-Ni05. Note that the present data and estimates were made for oxidation in dry environments, where both aluminum-based powders are quite stable. A lower overall stability is anticipated for humid environments, for which improvements in the powder stability offered by the bi-metal Al95-Ni05 could be more tangible.

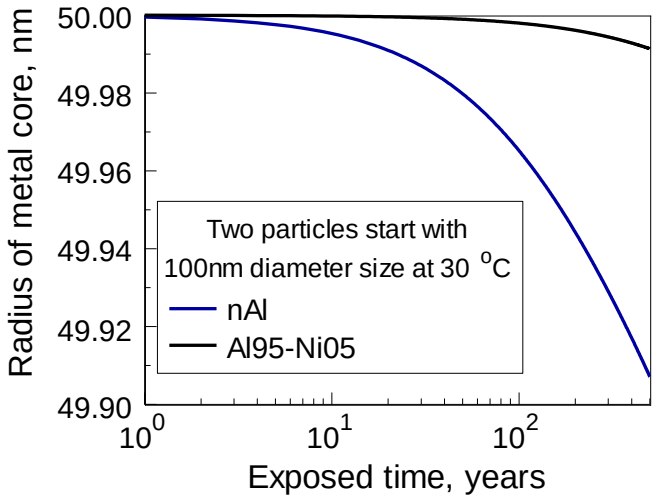

Figure 9.13 Aging of 100-nm diameter particles of n-Al and Al95-Ni05 exposed to a dry oxidizing environment at 30 °C in terms of reduction in the radius of their respective metal cores.

9.5.6 Ignition of Nano-powders Al95-Ni05 and n-Al by ESD

The experiments were conducted in air with a 2000 pF capacitor allowed to characterize the minimum ignition threshold of both Al95-Ni05 and n-Al. It was noted that at voltages below 4 kV, some of the Al95-Ni05 powder remained in the sample holder after the spark discharge. All n-Al was always ejected, however. Characteristic optical emission signals produced by the ignited powders are shown in Figure 9.14. The peak structure typically includes a relatively weak prompt ignition event, with characteristic times of about 2 – 4

ms, and a stronger delayed ignition, occurring typically after 10 ms. The prompt ignition peak is not discernable for all recorded traces; its timing is comparable to that observed in experiments with individual aluminum nanoparticles [200, 201]. Thus, the initial weak peak likely represents particles directly ignited by ESD. The stronger, delayed peak occurring at 15 – 60 ms may be associated with ignition of an aerosolized powder cloud. It is stronger for n-Al at lower ESD voltages, as expected based on the larger amount of powder ejected from the sample holder. However, in contrast, the peak emission at ESD voltages greater than 5 kV, is consistently stronger for Al95-Ni05.

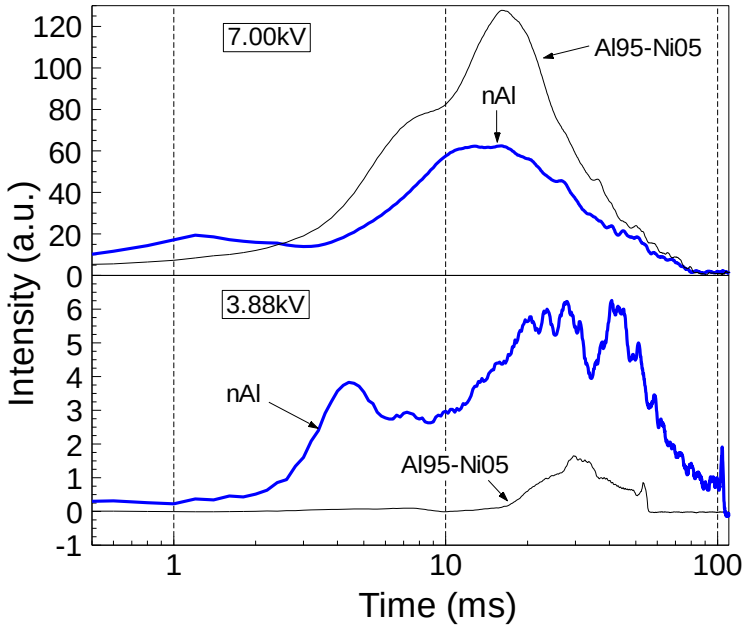

Figure 9.14 Emission trace of Al95-Ni05 and n-Al powders filtered at 568 nm and ignited in ambient air. Capacitor (2000 pF) was charged to 7.00 and 3.88 kV for different experiments.

As ESD voltage was decreased to identify the minimum ignition energy, at which no emission pulse could be detected. Results of these experiments are shown in Figure 9.15. The trends implied by the peak emission plotted as a function of the ESD energy indicates that about 2 times more energy is required to ignite Al95-Ni05 compared to n-Al.

Therefore, the bimetal powder is substantially less ESD-sensitive than n-Al. This result is consistent with the analysis of oxidation of these materials, presented in Figure 9.11 and Figure 9.12.

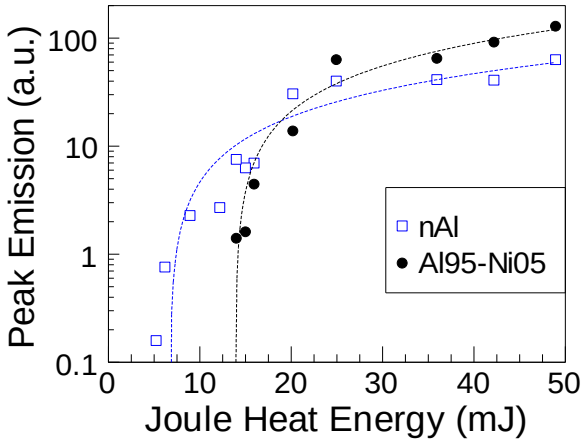

Figure 9.15 Peak emissions from ESD experiments conducted in air as a function of the ESD energy produced by the capacitor (2000 pF) which was charged to 2 – 7 kV.

Optical emission from a 32-channel PMT (see APPENDIX C) was used to identify the combustion temperature for experiments at ESD voltage of 7 kV. The intensities were initially fit to a gray emitter, resulting in the unusually high combustion temperatures of 4150 K for both n-Al and Al95-Ni05. The highest temperature was observed near the peak of the emission signal for both powders. When the emissivity was assumed to change as a function of the wavelength as $\varepsilon \sim \lambda^{-1.2}$, following recent work [202], the peak combustion temperature was reduced to about 3500 K for both materials (see APPENDIX C).

9.6 Conclusions

Bimetal Ni-Al nano-powders with different compositions were synthesized by explosion of twisted pure metal wires. The nano-powders prepared with high nickel concentrations contain fully reacted intermetallic phases. Such intermetallics are difficult to oxidize making them unattractive for energetic formulations. Nano-powders with lower nickel

concentrations do not contain significant amounts of the intermetallic phases. In particular, no intermetallics could be detected in the powder with 5 at. % Ni, which oxidized qualitatively very similarly to n-Al. The overall mass gain during oxidation for the bi-metal powder was nearly identical to that of n-Al, indicating the same heat release anticipated from their combustion. Oxidation kinetics assessed for this material accounting directly for the measured particle size distribution was compared to that for n-Al. Qualitatively, oxidation for both materials included the same stepwise accelerations in the reaction rates at increased temperatures, attributed earlier to polymorphic phase changes in the growing alumina scale. Therefore, it was concluded that oxide scales formed on oxidizing bimetal particles were structurally similar to those growing on pure aluminum. It was observed that the bimetal powder is oxidizing slower than n-Al, leading to its greater stability during handling and storage. The difference in the oxidation kinetics was attributed to doping the growing aluminum oxide scale with the oxidized nickel. A quantitative description of the oxidation kinetics, including apparent activation energy and pre-exponent for the diffusion coefficient controlling the oxidation rate was obtained. The model was used to predict how the bimetal nanoparticles age when exposed to an oxidizing environment; it was observed that they age slower than n-Al. It was further observed that the bi-metal powder is less ESD-ignition sensitive than n-Al. While the combustion temperatures for both materials are similar to each other and close to 3500 K, a stronger emission signal is produced by the bimetal powder than by n-Al when similar masses of powders are ignited by high energy sparks. Therefore, the bimetal powder with 5 at. % Ni is an attractive replacement of n-Al for advanced energetics, combining a lower ESD sensitivity and better stability with the same or even improved energetic performance.

CHAPTER 10

CONCLUSIONS AND FUTURE WORK

10.1 Conclusions

Several preparation techniques are successfully applied to prepare novel nanomaterials for energetics and energy applications. Mechanical milling has been a versatile technique used to prepare most of the nanomaterials discussed in this work. Additional preparation techniques such as electrochemical etching for on-chip energetics and electro-exploded wires for bimetal nano-powders are also presented.

As presented in Chapters 2 – 4, aluminum-based composites containing halogens are prepared using cryo and room-temperature milling techniques. It is shown that cryomilling is a necessity for powders containing aluminum as fuel and volatile additives including iodoform or metal halides ($NbCl_5$ and TiI_4). Milling at liquid nitrogen temperature is more effective in stabilizing such additives into aluminum matrix compared to room temperature milling. Specifically for metal halides, the material is further coated using Teflon® to improve material stability. In Chapter 4, a systematic study on several ternary $Al{\cdot}B{\cdot}I_2$ composites is presented. In these composites, the presence of boron allows to stabilize high concentrations (20 wt. %) of volatile iodine into boron and aluminum matrix using mechanical milling at room temperatures.

TG measurements in argon environment are used to quantify the material stability of each composite (see also APPENDIX A), where the most stable composites of $Al{\cdot}CHI_3$, $Al{\cdot}TiI_4$, $Al{\cdot}NbCl_5$, and $Al{\cdot}B{\cdot}I_2$ showed stabilities of 83%, 68%, 94%, 96%, respectively. Ignition temperatures characterized using a heated filament experiment show that all

Al-based and B-based composites have lower ignition temperatures than the pure Al or pure B. The lowest ignition temperatures are seen for $Al{\cdot}CHI_3$ composites. Furthermore, in single particle combustion experiments, all composites have longer burn times than pure Al.

Additionally, in Chapter 5, the preparation of Mg·S nanocomposite using mechanical milling at room temperature with substantially increased amount of sulfur is discussed. Mg·S nanocomposite ignited at lower temperatures and burned faster than pure magnesium. Ignition initiated by spark during ESD experiment and by a heated wire for aerosol combustion experiment, occurred with substantial delays; a likely reason is the formation of an evaporated sulfur cloud. The nanomaterials discussed in Chapters 2 – 5 are capable of inactivating the challenge bioaerosol more effectively than pure metal powders. Because mole fraction of chlorine and sulfur is greater than of iodine, the observed effect is statistically the best for $Al{\cdot}B{\cdot}I_2$ (see APPENDIX B) compared to $Al{\cdot}CHI_3$, $Al{\cdot}NbCl_5$, and Mg·S, indicating that the iodine-containing composites are the most effective for biological weapon defeat applications.

As presented in Chapter 6, PS film prepared using electrochemical etching is impregnated with sulfur and different nitrate oxidizers to prepare on-chip energetic composites. In particular, perchlorate-free and moisture stable PS/sulfur composites are readily ignitable and combustible in both inert and oxidizing environments, where flame speeds around 3 $m{\cdot}s^{-1}$ remained unaffected by the presence of different external environments. Furthermore, the heat of reaction was increased due to functionalization of PS surface with SiH_2, taking part in combustion. Fuel-rich PS/nitrate composites with minimal pore filling are easily ignited under inert environment. The flame speeds and

combustion enthalpies are quantified and compared to PS/$NaClO_4$ composites. These composites are viable for applications requiring perchlorate-free on-chip energetics with lower burn speeds and more controlled reactions. The thermodynamic estimates correlated better with experimental combustion enthalpies when the surface terminated hydrogen and excess oxidizer, in addition to the oxidizer loaded in the pores, were accounted for in the reaction.

In Chapter 7, nanocomposite 2B-Ti material prepared by ARM is shown to be a viable heating material for Sm evaporation. During experiments, the composition containing mixture of 30 wt. % of Sm with the ARM-prepared powder is most effective in Sm evaporation when 30 wt. % of Sm was added using an additional 30-min milling step. Al-MoO_3 nanocomposite is not a viable heating material due to the undesired reactions between Sm and combustion products to form the ternary oxide, $SmAlO_3$ and minimizing Sm evaporation. In contrast, no reaction products of Sm with either B or Ti were detected in the collected condensate.

In Chapter 8, ESM prepared using nanocomposite Al/Bi_2O_3 thermite as a precursor material and slowly annealing it to reduce Bi_2O_3 to form Bi inclusions, encapsulated with protective Al_2O_3 in an aluminum matrix is discussed with the goal of making a material capable of storing energy by melting and solidifying Bi inclusions. Upon thermal cycling, the inclusions do not drift inside the material and composite structure remains intact. In contrast, reference composite materials containing similar bulk compositions but without encapsulated Bi inclusions show that molten Bi tends to separate from Al and form interconnected coarse network of Bi metal; further cycling accumulates Bi on surface of the material. Dramatic differences in the mechanical properties of the encapsulated and

non-encapsulated composites are observed, where the Bi encapsulation results in a much stronger and mechanically sound structure useful for allowing repeated cycles of energy storage.

In Chapter 9, bimetal Al-Ni nano-powders with different compositions are synthesized by explosion of twisted pure metal wires. Nano-powders with 5 at. % Ni do not contain significant amounts of the intermetallic phases and oxidizes similarly to n-Al, indicating the same heat release during combustion. Oxidation kinetics assessed for this material accounting directly for the measured particle size distribution was compared to that for n-Al. Qualitatively, oxidation for both materials included the same stepwise accelerations in the reaction rates at increased temperatures; therefore, growing alumina scales formed on oxidizing bimetal particles were structurally similar to those growing on pure aluminum. The bimetal powder oxidizes slower than n-Al due to the presence of doped nickel oxide in the growing alumina, which results in greater stability during handling and storage. Oxidation model developed was used to predict that the bimetal nano-powder age slower than n-Al due to their difference in oxidation kinetics. Furthermore, the bimetal nano-powder is less ESD-ignition sensitive than n-Al with similar combustion temperatures of 3500 K. Hence, Al-Ni bimetal nano-powder with 5 at. % Ni could be an attractive replacement of n-Al for advanced energetics, when lower ESD sensitivity is desired and/or when the powder needs to be handled and stored while being exposed to oxidizing environments.

10.2 Future Work

This work with composites prepared for bioagent defeat applications showed that both aluminum and boron are capable of retaining substantial quantities of iodine stabilized in the metal matrix and released upon heating to temperatures much exceeding the iodine boiling point. X-ray diffraction used to analyze different phases was ineffective in clarifying how iodine was retained in aluminum and boron. However, it is interesting what those metal-iodine phases are. Other characterization techniques using TEM or XPS may provide spatially resolved phase compositions to better understand the retention mechanism. Composites containing greater mole fractions of biocidal content, e.g., chlorine and sulfur, are statistically less effective in inactivating the bioaerosol than iodine containing Al·B·I_2 composite. Additional studies addressing combustion of such halogen- or other biocidal agent containing materials using time-resolved optical spectroscopy can identify the combustion products generated from each composite to establish which products are most important for the spore inactivation. The same optical measurements would also be useful to further optimize the reactive materials in the practical agent defeat energetic formulations. This work showed that 20 wt. % iodine is the maximum amount which can be stabilized into aluminum and boron metal fuel matrices. Thus, new formulations with iodine-containing oxidizers, e.g., $Ca(IO_3)_2$, will be needed to be combined with metal-based fuels to further improve upon the inactivation effectiveness.

Varying HF:ethanol ratios of the electrochemical etching solution can be used to alter the material properties, i.e., porosity and surface area, of the PS film. An in-depth analysis by varying material properties may be used to achieve faster burn rates for PS/sulfur and PS/nitrate systems.

Feasibility of preparing metal-based energy storage material is only shown using Al/Bi_2O_3 at operating temperature around 270 °C. Further development using metals including Ga, Sn, In, and Zn will cover melting points from 30 – 420 °C for new metal-based nano-encapsulated ESMs to expand the range of operating temperatures.

Preliminary aging study for n-Al and Al95-Ni05 was conducted in oxygen/argon mixture. It is further beneficial to study the oxidation and aging processes of these powders in humid environments.

APPENDIX A

STABILITY OF HALOGEN CONTAINING COMPOSITES

A relative measure of material stability, *S*, introduced for $Al{\cdot}I_2$ composite[12] was used to compare the stability of halogen containing composites prepared using various milling techniques. The parameter *S* was defined as the percentage of weight loss at temperatures exceeding 400 °C (673 K). In Figure A.1, the stability of all composites are presented, where $Al{\cdot}B{\cdot}I_{2(40:40:20)}$ composite is seen to be the most stable. Additionally, the substantial increase due to Teflon® coating and glove box (GB) aging is also observed.

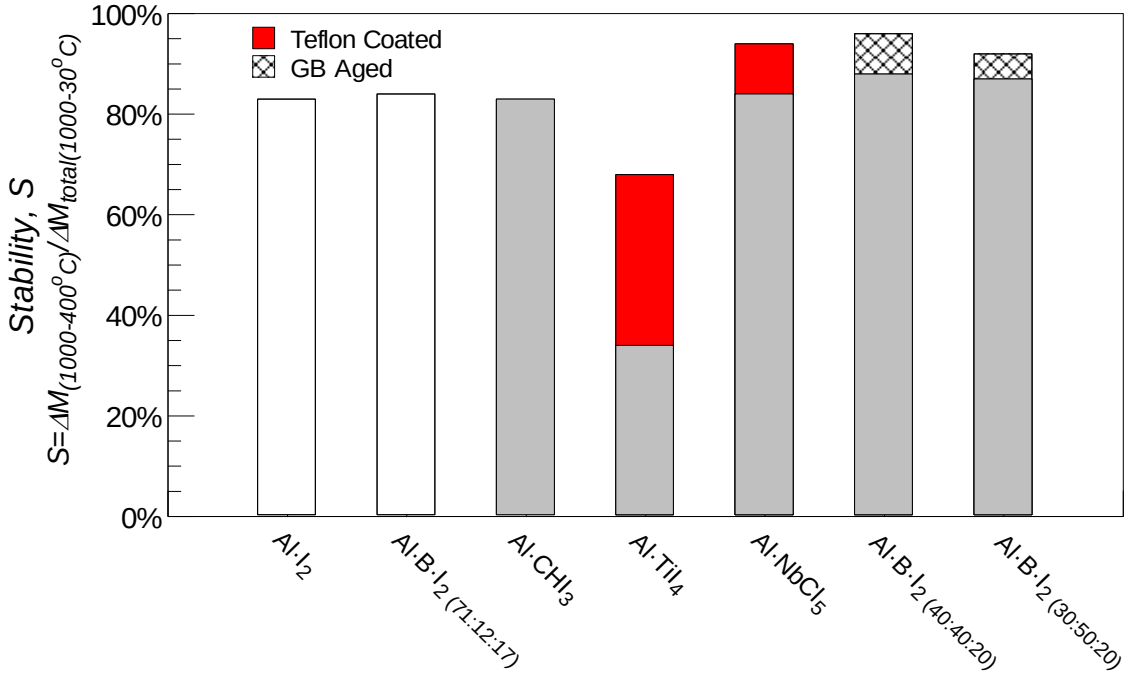

Figure A.1 Stability of halogen containing composites prepared via mechanical milling.

APPENDIX B

INACTIVATION OF BIOAEROSOL SPORES

Inactivation of aerosolized Bt(k) spores and BG spores without crystals by combustion products of prepared composites were observed. The exposure time of the bioaerosol to the combustion product was about 0.33 s. Figure B.1 and Figure B.2 presents the inactivation factor (IF) values obtained for Bt(k) spores and BG spores, respectively. Al·B·$I_{2(40:40:20)}$ composite show significant inactivation effectiveness towards Bt(k) spores compared to other composites. Additionally, all composites show relatively strong inactivation towards BG spores as well. These experiments were conducted in collaboration with Prof. Sergey Grinshpun's group at University of Cincinnati.

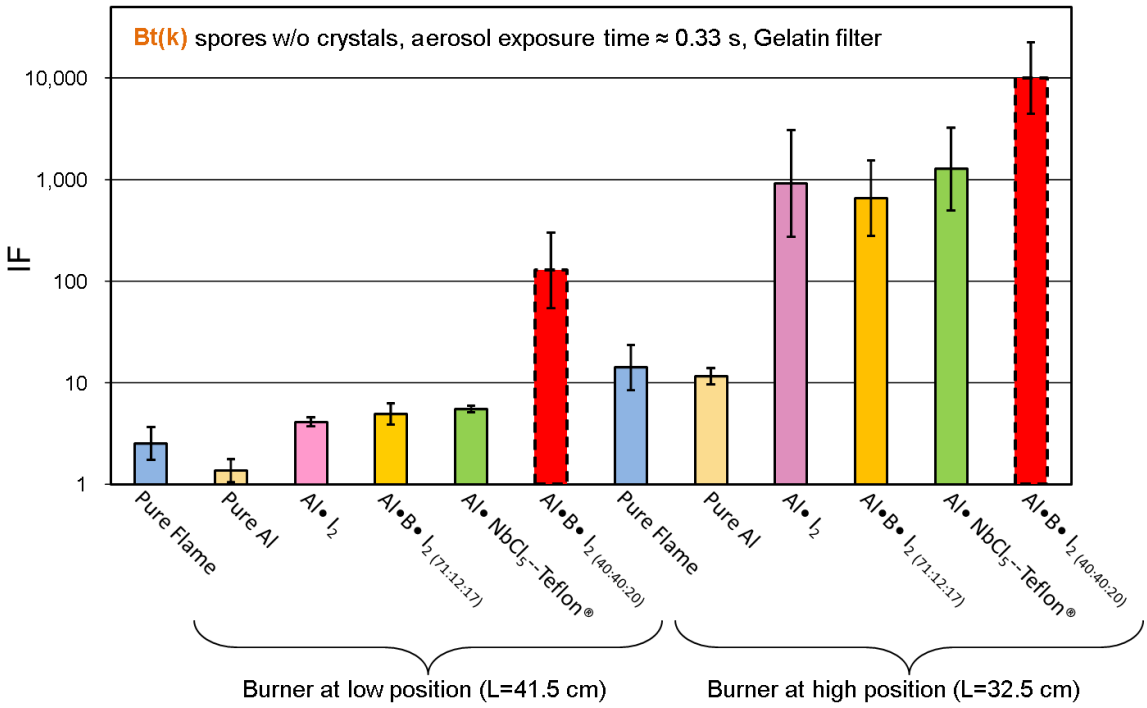

Figure B.1 Average inactivation of aerosolized Bt(k) spores with the combustion products of prepared composites at two different burner positions.

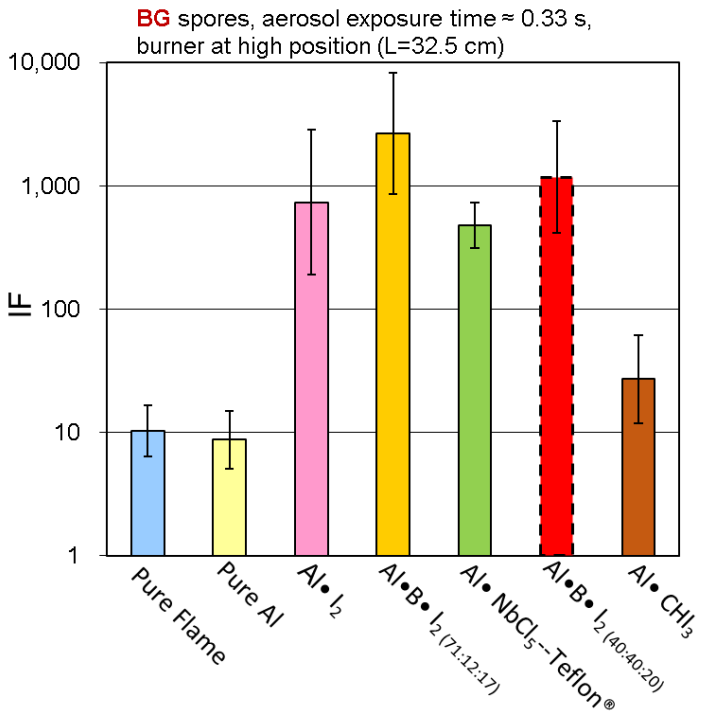

Figure B.2 Average inactivation of aerosolized BG spores with the combustion products of prepared composites at high burner position.

APPENDIX C

COMBUSTION TEMPERATURE MEASUREMENT

Optical emission from the combustion event at ESD voltage of 7 kV was recorded using a 32-channel PMT to obtain combustion temperatures for both n-Al and Al95-Ni05. In Figure C.1, an example of the collected emission spectra is shown for Al95-Ni05. The intensities fit to a grey emitter indicated unusually high combustion temperatures of 4150 K for both powders. Therefore, a power-law dependence, $\varepsilon \sim \lambda^{-1.2}$, suggested for emissivity as function of wavelength in recent work [202], was assumed. The combustion temperatures of both powders are shown in Figure C.2, along with an emission trace. Highest combustion temperature of about 3500 K occurs at the peak emission for both powders.

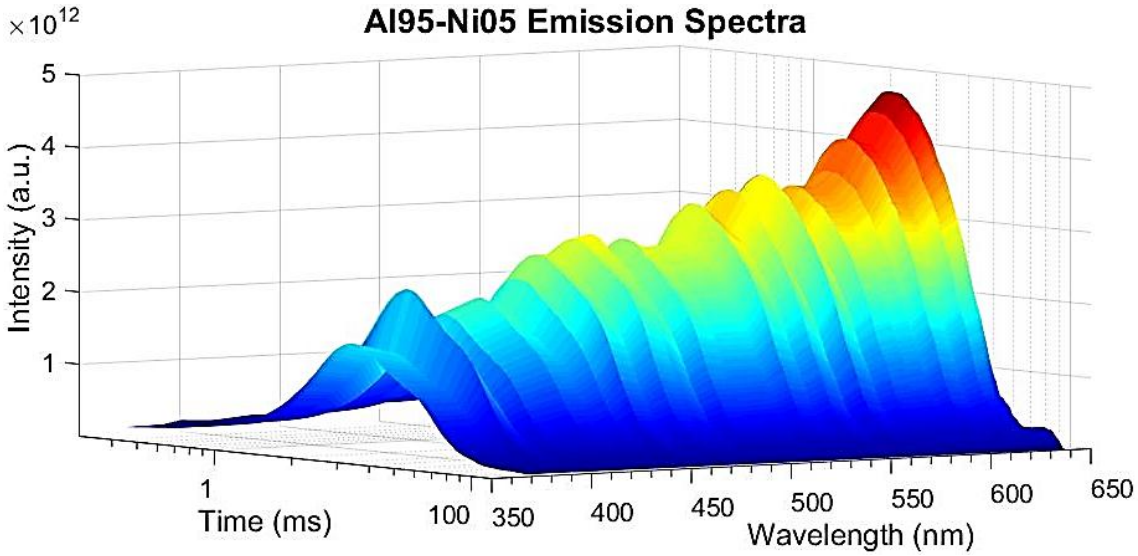

Figure C.1 Emission spectra of Al95-Ni05 recorded using 32-channel PMT.

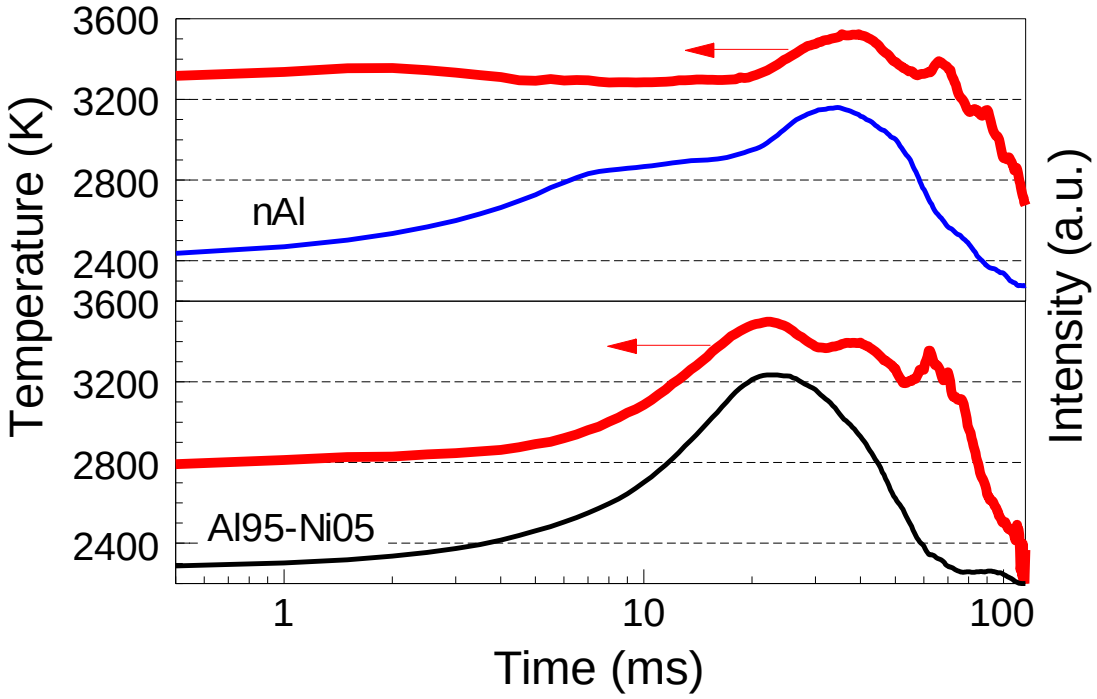

Figure C.2 Combustion temperatures of n-Al and Al95-Ni05.

REFERENCES

[1] E.L. Dreizin, M. Schoenitz, Nano-composite energetic powders prepared by arrested reactive milling, US Patent 7,524,355 New Jersey Institute Of Technology, Newark, NJ, USA, 2009.

[2] S.M. Umbrajkar, S. Seshadri, M. Schoenitz, V.K. Hoffmann, E.L. Dreizin, Aluminum-rich Al-MoO3 nanocomposite powders prepared by arrested reactive milling, J. Propul. Power 24 (2008) 192-198.

[3] M. Schoenitz, E.L. Dreizin, Structure and properties of Al-Mg mechanical alloys, Journal of Materials Research 18 (2003) 1827-1836.

[4] M. Schoenitz, E. Dreizin, Oxidation processes and phase changes in metastable Al-Mg alloys, Journal of Propulsion and Power 20 (2004) 1064-1068.

[5] Y.L. Shoshin, E.L. Dreizin, Particle combustion rates for mechanically alloyed Al-Ti and aluminum powders burning in air, Combustion and Flame 145 (2006) 714-722.

[6] A.S. Rogachev, A.S. Mukasyan, Combustion of heterogeneous nanostructural systems (review), Combustion, Explosion and Shock Waves 46 (2010) 243-266.

[7] M.A. Korchagin, B.B. Bokhonov, Combustion of mechanically activated 3Ti + 2BN mixtures, Combustion, Explosion and Shock Waves 46 (2010) 170-177.

[8] A.N. Sterletskii, A.Y. Dolgoborodov, I.V. Kolbanev, M.N. Makhov, S.F. Lomaeva, A.B. Borunova, V.E. Fortov, Structure of mechanically activated high-energy Al + polytetrafluoroethylene nanocomposites, Colloid Journal 71 (2009) 852-860.

[9] R.H. Chen, C. Suryanarayana, M. Chaos, Combustion characteristics of mechanically alloyed ultrafine-grained Al-Mg powders, Adv. Eng. Mater. 8 (2006) 563-567.

[10] K.T. Sullivan, C. Wu, N.W. Piekiel, K. Gaskell, M.R. Zachariah, Synthesis and reactivity of nano-Ag2O as an oxidizer for energetic systems yielding antimicrobial products, Combustion and Flame 160 (2013) 438-446.

[11] C.E. Johnson, K.T. Higa, Iodine-rich biocidal reactive materials, MRS Online Proc. Libr. 1521 (2013).

[12] S. Zhang, C. Badiola, M. Schoenitz, E.L. Dreizin, Oxidation, ignition, and combustion of Al·I2 composite powders, Combustion and Flame 159 (2012) 1980-1986.

[13] S.A. Grinshpun, A. Adhikari, M. Yermakov, T. Reponen, E. Dreizin, M. Schoenitz, V. Hoffmann, S. Zhang, Inactivation of aerosolized Bacillus atrophaeus (BG) endospores and MS2 viruses by combustion of reactive materials, Environmental Science and Technology 46 (2012) 7334-7341.

[14] K.T. Sullivan, N.W. Piekiel, S. Chowdhury, C. Wu, M.R. Zachariah, C.E. Johnson, Ignition and combustion characteristics of nanoscale Al/AgIO3: A potential energetic biocidal system, Combustion Science and Technology 183 (2011) 285-302.

[15] C. Farley, M. Pantoya, Reaction kinetics of nanometric aluminum and iodine pentoxide, Journal of Thermal Analysis and Calorimetry 102 (2010) 609-613.

[16] S. Zhang, M. Schoenitz, E.L. Dreizin, Mechanically alloyed Al-I composite materials, Journal of Physics and Chemistry of Solids 71 (2010) 1213-1220.

[17] F.V. Mikulec, J.D. Kirtland, M.J. Sailor, Explosive nanocrystalline porous silicon and its use in atomic emission spectroscopy, Advanced Materials 14 (2002) 38-41.

[18] S.K. Lazarouk, A.V. Dolbik, P.V. Jaguiro, V.A. Labunov, V.E. Borisenko, Fast exothermic processes in porous silicon, Semiconductors 39 (2005) 881-883.

[19] D. Clément, J. Diener, E. Gross, N. Künzner, V.Y. Timoshenko, D. Kovalev, Highly explosive nanosilicon-based composite materials, Physica Status Solidi A: Applications and Materials Science 202 (2005) 1357-1364.

[20] M.D. Plessis, Nanoporous silicon explosive devices, Materials Science and Engineering B: Solid state Meterials for Advanced Technology 147 (2008) 226-229.

[21] M.D. Plessis, Properties of porous silicon nano-explosive devices, Sensors and Actuators, A: Physical 135 (2007) 666-674.

[22] C.R. Becker, L.J. Currano, W.A. Churaman, C.R. Stoldt, Thermal analysis of the exothermic reaction between galvanic porous silicon and sodium perchlorate, ACS Applied Materials and Interfaces 2 (2010) 2998-3003.

[23] W. Churaman, L. Currano, C. Becker, Initiation and reaction tuning of nanoporous energetic silicon, Journal of Physics and Chemistry of Solids 71 (2010) 69-74.

[24] L.J. Currano, W.A. Churaman, Energetic nanoporous silicon devices, Journal of Microelectromechanical Systems 18 (2009) 799-807.

[25] W. Churaman, L. Currano, A.K. Singh, U.S. Rai, M. Dubey, P. Amirtharaj, P.C. Ray, Understanding the high energetic behavior of nano-energetic porous silicon, Chemical Physics Letters 464 (2008) 198-201.

[26] V.S. Parimi, S.A. Tadigadapa, R.A. Yetter, Control of nanoenergetics through organized microstructures, Journal of Micromechanics and Microengineering 22 (2012).

[27] S. Wang, R. Shen, Y. Ye, Y. Hu, An investigation into the fabrication and combustion performance of porous silicon nanoenergetic array chips, Nanotechnology 23 (2012).

[28] E.C. Koch, D. Clément, Special materials in pyrotechnics: VI. Silicon - An old fuel with new perspectives, Propellants, Explosives, Pyrotechnics 32 (2007) 205-212.

[29] D. Clément, D. Kovalev, Nanosilicon-based explosives, in: L. Pavesi, R. Turan (Eds.) Silicon Nanocrystals: Fundamentals, Synthesis and Applications, Weinheim, Germany: Wiley-VCH Verlang GmbH & Co. KGaA, 2010, pp. 537-554.

[30] R.W. Schunk, T.Z. Ma, Field-aligned expansion of plasma clouds in the ionosphere, Adv. Space. Res. 15 (1995) 107-110.

[31] J. Uemoto, T. Ono, T. Yamada, T. Suzuki, M.Y. Yamamoto, S. Watanabe, A. Kumamoto, M. Iizima, Impact of lithium releases on ionospheric electron density observed by impedance probe during WIND campaign, Earth Planets Space 62 (2010) 589-597.

[32] T.Z. Ma, R.W. Schunk, A two-dimensional model of plasma expansion in the ionosphere, Planet. Space Sci. 38 (1990) 723-741.

[33] Y.Y. Ruzhin, A.K. Depueva, L. Palasio, Acoustic Gravity Wave (AGW) generation during the barium injection experiments, COSPAR Colloquia Series, 1998, pp. 111-114.

[34] L. Xie, L. Li, J. Wang, R. Tao, Determining wind field and electric field by a barium release experiment in the ionosphere, Sci. China Ser. D 58 (2015) 1210-1215.

[35] N.I. Izhovkina, Interaction between plasma structures in an unstable ionospheric plasma, Geomag. Aeron. 53 (2013) 345-353.

[36] S.G. Ard, J.J. Melko, N.S. Shuman, A. Viggiano, Reactions of Sm, Sm+, and SmO+ in the atmosphere: Temperature dependent kinetics, American Chemical Society (2014).

[37] N. Jackson-Booth, P. Cannon, M. Angling, R. Caton, K. Groves, T. Pedersen, R. Parris, Y.J. Su, Preliminary HF results from the Metal Oxide Space Cloud (MOSC) experiment, 31th URSI General Assembly and Scientific Symposium, IEEE, 2014, pp. 1-4.

[38] E.S. Collins, B.R. Skelton, M.L. Pantoya, F. Irin, M.J. Green, M.A. Daniels, Ignition sensitivity and electrical conductivity of an aluminum fluoropolymer reactive material with carbon nanofillers, Combust. Flame 162 (2015) 1417-1421.

[39] K.H. Poper, E.S. Collins, M.L. Pantoya, M.A. Daniels, Controlling the electrostatic discharge ignition sensitivity of composite energetic materials using carbon nanotube additives, Journal of Electrostatics 72 (2014) 428-432.

[40] R. Steelman, B. Clark, M.L. Pantoya, R.J. Heaps, M.A. Daniels, Desensitizing nano powders to electrostatic discharge ignition, Journal of Electrostatics 76 (2015) 102-107.

[41] S.W. Chung, E.A. Guliants, C.E. Bunker, D.W. Hammerstroem, Y. Deng, M.A. Burgers, P.A. Jelliss, S.W. Buckner, Capping and passivation of aluminum nanoparticles using alkyl-substituted epoxides, Langmuir 25 (2009) 8883-8887.

[42] W.K. Lewis, A.T. Rosenberger, J.R. Gord, C.A. Crouse, B.A. Harruff, K.A.S. Fernando, M.J. Smith, D.K. Phelps, J.E. Spowart, E.A. Guliants, C.E. Bunker, Multispectroscopic (FTIR, XPS, and TOFMS−TPD) investigation of the core−shell bonding in sonochemically prepared aluminum nanoparticles capped with oleic acid, The Journal of Physical Chemistry C 114 (2010) 6377-6380.

[43] G. Ma, D. Zhuang, H. Dai, P. Wang, Controlled hydrogen generation by reaction of aluminum with water, Progress in Chemistry 24 (2012) 650-658.

[44] H.W. Wang, H.W. Chung, H.T. Teng, G. Cao, Generation of hydrogen from aluminum and water - Effect of metal oxide nanocrystals and water quality, International Journal of Hydrogen Energy 36 (2011) 15136-15144.

[45] P. Dupiano, D. Stamatis, E.L. Dreizin, Hydrogen production by reacting water with mechanically milled composite aluminum-metal oxide powders, International Journal of Hydrogen Energy 36 (2011) 4781-4791.

[46] F. Franzoni, M. Milani, L. Montorsi, V. Golovitchev, Combined hydrogen production and power generation from aluminum combustion with water: Analysis of the concept, International Journal of Hydrogen Energy 35 (2010) 1548-1559.

[47] F. Franzoni, S. Mercati, M. Milani, L. Montorsi, Operating maps of a combined hydrogen production and power generation system based on aluminum combustion with water, International Journal of Hydrogen Energy 36 (2011) 2803-2816.

[48] O.C. Eneh, Biological weapons-agents for life and environmental destruction, Research Journal of Environmental Toxicology 6 (2012) 65-87.

[49] R.W. Nelson, Nuclear bunker busters, mini-nukes, and the US nuclear stockpile, Physics Today 56 (2003) 32-37.

[50] S. Zhang, M. Schoenitz, E.L. Dreizin, Iodine release, oxidation, and ignition of mechanically alloyed Al-I composites, Journal of Physical Chemistry C 114 (2010) 19653-19659.

[51] S.A. Grinshpun, C. Li, A. Adhikari, M. Yermakov, T. Reponen, M. Schoenitz, E. Dreizin, V. Hoffmann, M. Trunov, Method for studying survival of airborne viable microorganisms in combustion environments: Development and evaluation, Aerosol and Air Quality Research 10 (2010) 414-424.

[52] K.O. Christe, R. Haiges, Iodine fluoride, oxofluoride and oxide chemistry, ACS 21st Winter Fluorine Conference, 2013.

[53] C. Suryanarayana, Mechanical alloying and milling, Progress in Materials Science 46 (2001) 1-184.

[54] B.S. Murty, S. Ranganathan, Novel materials synthesis by mechanical alloying/milling, International Materials Reviews 43 (1998) 101-141.

[55] D.M. Badgujar, M.B. Talawar, S.N. Asthana, P.P. Mahulikar, Advances in science and technology of modern energetic materials: An overview, Journal of Hazardous Materials 151 (2008) 289-305.

[56] J.P. Agrawal, Some new high energy materials and their formulations for specialized applications, Propellants, Explosives, Pyrotechnics 30 (2005) 316-328.

[57] A. Plummer, V. Kuznetsov, T. Joyner, J. Shapter, N.H. Voelcker, The burning rate of energetic films of nanostructured porous silicon, Small 7 (2011) 3392-3398.

[58] N.W. Piekiel, C.J. Morris, L.J. Currano, D.M. Lunking, B. Isaacson, W.A. Churaman, Enhancement of on-chip combustion via nanoporous silicon microchannels, Combustion and Flame 161 (2014) 1417-1424.

[59] C.R. Becker, S. Apperson, C.J. Morris, S. Gangopadhyay, L.J. Currano, W.A. Churaman, C.R. Stoldt, Galvanic porous silicon composites for high-velocity nanoenergetics, Nano Letters 11 (2011) 803-807.

[60] N.W. Piekiel, C.J. Morris, W.A. Churaman, M.E. Cunningham, D.M. Lunking, L.J. Currano, Combustion and material characterization of highly tunable on-chip energetic porous silicon, Propellants, Explosives, Pyrotechnics 40 (2015) 16-26.

[61] H.H. Willard, G. Frederick Smith, The perchlorates of the alkali and alkaline earth metals and ammonium. Their solubility in water and other solvents, Journal of the American Chemical Society 45 (1923) 286-297.

[62] M. D. Plessis, A decade of porous silicon as nano-explosive material, Propellants, Explosives, Pyrotechnics 39 (2014) 348-364.

[63] K. Sellers, K. Weeks, W.R. Alsop, S.R. Clough, M. Hoyt, B. Pugh, J. Robb, Perchlorate: Environmental problems and solutions, Boca Raton, FL: CRC/Taylor & Francis, 2006.

[64] J.A. Conkling, C. Mocella, Chemistry of pyrotechnics: Basic principles and theory, New York, NY: CRC/Taylor & Francis, 1985.

[65] H. Ge, H. Li, S. Mei, J. Liu, Low melting point liquid metal as a new class of phase change material: An emerging frontier in energy area, Renewable Sustainable Energy Rev. 21 (2013) 331-346.

[66] A.J. Spero, F.S. Wyle, Design of high energy density thermal storage device, US Patent 20110308762A1, Thermal Storage Systems, USA, 2011.

[67] M. Liu, Y. Ma, H. Wu, R.Y. Wang, Metal matrix-metal nanoparticle composites with tunable melting temperature and high thermal conductivity for phase-change thermal storage, ACS Nano 9 (2015) 1341-1351.

[68] M. Liu, R.Y. Wang, Phase change nanocomposites with tunable melting temperature and thermal energy storage density, Nanoscale 5 (2013) 7234-7237.

[69] R.A. Yetter, G.A. Risha, S.F. Son, Metal particle combustion and nanotechnology, Proceedings of the Combustion Institute 32 II (2009) 1819-1838.

[70] D. Stamatis, Z. Jiang, V.K. Hoffmann, M. Schoenitz, E.L. Dreizin, Fully dense, aluminum-rich Al-CuO nanocomposite powders for energetic formulations, Combustion Science and Technology 181 (2009) 97-116.

[71] A. Gromov, L.T. DeLuca, A.P. Il'in, U. Teipel, A. Petrova, D. Prokopiev, Nanometals in energetic systems: achievements and future, Int. J. Energ. Mater. Chem. Propul. 13 (2014) 399-419.

[72] F. Tepper, Electro-explosion of wire produces nanosize metals, Metal Powder Report 53 (1998) 31-33.

[73] F. Tepper, Metallic nanopowders produced by the electro-exploding wire process, International Journal of Powder Metallurgy 35 (1999) 39-44.

[74] W. Jiang, K. Yatsui, Pulsed wire discharge for nanosize powder synthesis, IEEE Trans. Plasma Sci. 26 (1998) 1498-1501.

[75] P. Brousseau, C.J. Anderson, Nanometric aluminum in explosives, Propellants, Explosives, Pyrotechnics 27 (2002) 300-306.

[76] A. Pivkina, P. Ulyanova, Y. Frolov, S. Zavyalov, J. Schoonman, Nanomaterials for Heterogeneous Combustion, Propellants, Explosives, Pyrotechnics 29 (2004) 39-49.

[77] L.T. De Luca, L. Galfetti, F. Severini, L. Meda, G. Marra, A.B. Vorozhtsov, V.S. Sedoi, V.A. Babuk, Burning of nano-aluminized composite rocket propellants, Combustion, Explosion and Shock Waves 41 (2005) 680-692.

[78] C. Weir, M.L. Pantoya, M.A. Daniels, The role of aluminum particle size in electrostatic ignition sensitivity of composite energetic materials, Combust. Flame 160 (2013) 2279-2281.

[79] A. Azhagurajan, N. Selvakumar, M. Mohammed Yasin, Minimum ignition energy for micro and nano flash powders, Process Safety Progress 31 (2012) 19-23.

[80] Q.S.M. Kwok, C. Badeen, K. Armstrong, R. Turcotte, D.E.G. Jones, V.Y. Gertsman, Hazard characterization of uncoated and coated aluminium nanopowder compositions, Journal of Propulsion and Power 23 (2007) 659-668.

[81] O.B. Nazarenko, Y.A. Amelkovich, A.I. Sechin, Characterization of aluminum nanopowders after long-term storage, Appl. Surf. Sci. 321 (2014) 475-480.

[82] M.V. Coulet, B. Rufino, P.H. Esposito, T. Neisius, O. Isnard, R. Denoyel, Oxidation mechanism of aluminum nanopowders, Journal of Physical Chemistry C 119 (2015) 25063-25070.

[83] S. Zhang, E.L. Dreizin, Reaction interface for heterogeneous oxidation of aluminum powders, Journal of Physical Chemistry C 117 (2013) 14025-14031.

[84] H. Nie, M. Schoenitz, E.L. Dreizin, Initial stages of oxidation of aluminum powder in oxygen, International Journal of Thermal Analysis and Calorimetry, in press (2016).

[85] G. Jian, S. Chowdhury, J. Feng, M.R. Zachariah, Thermite reaction based on nano-Al and iodine pentoxide: Ignition and combustion characterization, AIChE Annual Meeting, Conference Proceedings, 2012.

[86] K.O. Christe, R. Haiges, W.W. Wilson, High-oxidation state iodine oxides and their application as highenergy-density-materials (HEDM), Halchem V, Sardinia (2010).

[87] Z. Doorenbos, J. Puszynski, D. Kapoor, The effect of particle morphology on the combustion properties of MIC materials, AIChE Annual Meeting, Conference Proceedings, 2009.

[88] C.J. Bulian, J.A. Puszynski, J.J. Swiatkiewicz, Tunability of nanoenergetic materials, AIChE Annual Meeting, Conference Proceedings, 2008.

[89] E.L. Dreizin, C. Badiola, S. Zhang, Y. Aly, Particle combustion dynamics of metal-based reactive materials, International Journal of Energetic Materials and Chemical Propulsion 10 (2011) 297-319.

[90] Y. Aly, S. Zhang, M. Schoenitz, V.K. Hoffmann, E.L. Dreizin, M. Yermakov, R. Indugula, S.A. Grinshpun, Iodine-containing aluminum-based fuels for inactivation of bioaerosols, Combustion and Flame 161 (2014) 303-310.

[91] S.A. Grinshpun, A. Adhikari, M. Yermakov, T. Reponen, E. Dreizin, M. Schoenitz, V. Hoffmann, Neutralization of viable aerosolized microorganisms due to exposure to combustion of reactive materials, European Aerosol Conference, 2012.

[92] L.J. Gillespie, L.H.D. Fraser, The normal vapor pressure of crystalline iodine, Journal of the American Chemical Society 58 (1936) 2260-2263.

[93] H. Shemer, N. Narkis, Sonochemical removal of trihalomethanes from aqueous solutions, Ultrasonics Sonochemistry 12 (2005) 495-499.

[94] D.M. Bieliński, L. Ślusarski, P. Głąb, Modification of rubber by iodoform, Journal of Applied Polymer Science 105 (2007) 177-189.

[95] Y.L. Shoshin, M.A. Trunov, X. Zhu, M. Schoenitz, E.L. Dreizin, Ignition of aluminum-rich Al-Ti mechanical alloys in air, Combustion and Flame 144 (2006) 688-697.

[96] T.S. Ward, M.A. Trunov, M. Schoenitz, E.L. Dreizin, Experimental methodology and heat transfer model for identification of ignition kinetics of powdered fuels, International Journal of Heat and Mass Transfer 49 (2006) 4943-4954.

[97] M.J. Starink, The determination of activation energy from linear heating rate experiments: A comparison of the accuracy of isoconversion methods, Thermochimica Acta 404 (2003) 163-176.

[98] P.R. Santhanam, V.K. Hoffmann, M.A. Trunov, E.L. Dreizin, Characteristics of aluminum combustion obtained from constant-volume explosion experiments, Combustion Science and Technology 182 (2010) 904-921.

[99] B.J. McBride, S. Gordon, Computer Program for Calculation of Complex Chemical Equilibrium Compositions and Applications II. Users Manual and Program Description, NASA RP 1311, 1996.

[100] B.Z. Eapen, V.K. Hoffmann, M. Schoenitz, E.L. Dreizin, Combustion of aerosolized spherical aluminum powders and flakes in air, Combustion Science and Technology 176 (2004) 1055-1069.

[101] A. Abraham, S. Zhang, Y. Aly, M. Schoenitz, E.L. Dreizin, Aluminum-iodoform composite reactive material, Advanced Engineering Materials 16 (2014) 909-917.

[102] A. Corcoran, S. Mercati, H. Nie, M. Milani, L. Montorsi, E.L. Dreizin, Combustion of fine aluminum and magnesium powders in water, Combustion and Flame 160 (2013) 155-160.

[103] A.L. Corcoran, S. Wang, Y. Aly, E.L. Dreizin, Combustion of mechanically alloyed Al·Mg powders in products of a hydrocarbon flame, Combustion Science and Technology 187 (2015) 807-825.

[104] S. Wang, A.L. Corcoran, E.L. Dreizin, Combustion of magnesium powders in products of an air/acetylene flame, Combustion and Flame 162 (2015) 1316-1325.

[105] S. Zhang, M. Schoenitz, E.L. Dreizin, Oxidation, ignition and combustion of Al-hydrocarbon composite reactive powders, International Journal of Energetic Materials and Chemical Propulsion 11 (2012) 353-373.

[106] E. Wiberg, N. Wiberg, A.F. Holleman, Inorganic chemistry, San Diego, CA: Berlin: Academic Press, W. de Gruyter, 2001.

[107] M.W. Chase, NIST-JANAF themochemical tables, fourth edition., J. Phys. Chem. Ref. Data, Monograph 9 (1998) 1-1951.

[108] A.F. Armington, G.F. Dillon, R.F. Mitchell, The preparation of high-purity boron via the iodide, Defense Technical Information Center (1964).

[109] E.L. Dreizin, C. Badiola, S. Zhang, Y. Aly, Particle combustion dyanmics of metal-based reactive materials, International Journal of Energetic Materials and Chemical Propulsion 10 (2011) 22.

[110] Y. Aly, V.K. Hoffman, M. Schoenitz, E.L. Dreizin, Preparation, ignition, and combustion of mechanically alloyed Al-Mg powders with customized particle sizes, Materials Research Society Symposium Proceedings, (2013), pp. 43-48.

[111] A. Abraham, J. Obamedo, M. Schoenitz, E.L. Dreizin, Effect of composition on properties of reactive Al·B·I2 powders prepared by mechanical milling, Journal of Physics and Chemistry of Solids 83 (2015) 1-7.

[112] D. Stamatis, X. Jiang, E. Beloni, E.L. Dreizin, Aluminum burn rate modifiers based on reactive nanocomposite powders, AIChE Annual Meeting, Conference Proceedings, 2008.

[113] R.A. Williams, M. Schoenitz, A. Ermoline, E.L. Dreizin, On gas release by thermally-initiated fully-dense 2Al·3CuO nanocomposite powder, International Journal of Energetic Materials and Chemical Propulsion 11 (2012) 275-292.

[114] R.A. Williams, E. Beloni, E.L. Dreizin, Ignition of metal powder layers of different thickness by electrostatic discharge, Journal of Propulsion and Power 28 (2012) 132-139.

[115] S. Wang, A.L. Corcoran, V. Leybova, E.L. Dreizin, Metal-based iodine bearing materials prepared by mechanical milling, MRS Online Proceedings Library 1758 (2015).

[116] W. Zhou, J.B. DeLisio, X. Li, L. Liu, M.R. Zachariah, Persulfate salt as an oxidizer for biocidal energetic nano-thermites, Journal of Materials Chemistry A 3 (2015) 11838-11846.

[117] V.K. Garg, L. Takacs, Studies of combustion mechanochemical reactions in off-stoichiometric powder mixtures of Fe1-xS1+x, Materials Science 38 (2002) 846-852.

[118] L. Takacs, Self-sustaining metal-sulfur reactions induced by ball milling, Journal of Materials Synthesis and Processing 8 (2000) 181-188.

[119] L. Takacs, Multiple combustion induced by ball milling, Applied Physics Letters 69 (1996) 436-438.

[120] V.S. Trofimov, E.V. Petrov, On detonation in Zn-S blends, Int. J Self-Propag. High-Temp. Synth. 23 (2014) 187-191.

[121] S. Goroshin, J.H.S. Lee, D.L. Frost, Combustion synthesis of ZnS in microgravity, Symposium (International) on Combustion 25 (1994) 1651-1657.

[122] L. Takacs, Ball milling-induced combustion in powder mixtures containing titanium, zirconium, or hafnium, Journal of Solid State Chemistry 125 (1996) 75-84.

[123] S. Goroshin, A. Miera, D.L. Frost, J.H.S. Lee, Metal-sulfur combustion, Symposium (International) on Combustion 26 (1996) 1883-1889.

[124] A. Abraham, N.W. Piekiel, C.R. Knick, C.J. Morris, E. Dreizin, Quantification of oxidizer systems for porous silicon combustion, MRS Online Proceedings Library 1758 (2015).

[125] A. Abraham, N.W. Piekiel, C.J. Morris, E.L. Dreizin, Combustion of energetic porous silicon composites containing different oxidizers, Propellants, Explosives, Pyrotechnics 41 (2016) 179-188.

[126] S.H. Fischer, M.C. Grubelich, Theoretical energy release of thermites, intermetallics, and combustible metals, Other Information: Supercedes report DE98005512; PBD: Jun 1998; PBD: 1 Jun 1998, 1998.

[127] S.A. Grinshpun, A. Adhikari, C. Li, T. Reponen, M. Yermakov, M. Schoenitz, E. Dreizin, M. Trunov, S. Mohan, Thermal inactivation of airborne viable Bacillus subtilis spores by short-term exposure in axially heated air flow, Journal of Aerosol Science 41 (2010) 352-363.

[128] L. Takacs, M.A. Susol, Combustive mechanochemical reactions in off-stoichiometric powder mixtures, Mater. Sci. Forum 225-227 (1996) 559-562.

[129] L. Takacs, Self-sustaining reactions induced by ball milling, Prog. Mater. Sci. 47 (2002) 355-414.

[130] A.L. Corcoran, S. Mercati, H. Nie, M. Milani, L. Montorsi, E.L. Dreizin, Combustion of fine aluminum and magnesium powders in water, Combustion and Flame 160 (2013) 2242-2250.

[131] A.L. Corcoran, S. Wang, Y. Aly, E.L. Dreizin, Combustion of mechanically alloyed Al·Mg powders in products of a hydrocarbon flame, Combustion Science and Technology 187 (2015) 807-825.

[132] W.S. Rasband, ImageJ, U. S. National Institutes of Health, Bethesda, Maryland, USA, 1997-2015.

[133] R.A. Williams, J.V. Patel, E.L. Dreizin, Ignition of fully dense nanocomposite thermite powders by an electric spark, Journal of Propulsion and Power 30 (2014) 765-774.

[134] Y. Aly, M. Schoenitz, E.L. Dreizin, Ignition and combustion of mechanically alloyed Al-Mg powders with customized particle sizes, Combustion and Flame 160 (2013) 835-842.

[135] Y. Aly, E.L. Dreizin, Ignition and combustion of Al·Mg alloy powders prepared by different techniques, Combustion and Flame 162 (2015) 1440-1447.

[136] E. Beloni, E.L. Dreizin, Experimental study of ignition of magnesium powder by electrostatic discharge, Combust. Flame 156 (2009) 1386-1395.

[137] T. Sandstrom, B. Kolmodin-Hedman, N. Stjernberg, M.C. Andersson, G. Lofvenius, Challenge test for sulfur dioxide - symptom and lung function measurements, Scandinavian Journal of Work, Environment and Health 14 (1988) 77-79.

[138] P. McCord, S.L. Yau, A.J. Bard, Chemiluminescence of anodized and etched silicon: Evidence for a luminescent siloxene-like layer on porous silicon, Science 257 (1992) 68-69.

[139] D. Kovalev, V.Y. Timoshenko, N. Künzner, E. Gross, F. Koch, Strong explosive interaction of hydrogenated porous silicon with oxygen at cryogenic temperatures, Physical Review Letters 87 (2001) 683011-683014.

[140] Y. Ohkura, J.M. Weisse, L. Cai, X. Zheng, Flash ignition of freestanding porous silicon films: Effects of film thickness and porosity, Nano Letters 13 (2013) 5528-5533.

[141] A. Loni, L.T. Canham, Exothermic phenomena and hazardous gas release during thermal oxidation of mesoporous silicon powders, Journal of Applied Physics 113 (2013).

[142] N.W. Piekiel, W.A. Churaman, C.J. Morris, L.J. Currano, Combustion and material characterization of porous silicon nanoenergetics, Proceedings of the IEEE International Conference on Micro Electro Mechanical Systems (MEMS), 2013, pp. 449-452.

[143] M. Ruike, M. Houzouji, A. Motohashi, N. Murase, A. Kinoshita, K. Kaneko, Pore structure of porous silicon formed on a lightly doped crystal silicon, Langmuir 12 (1996) 4828-4831.

[144] S. Brunauer, P.H. Emmett, E. Teller, Adsorption of gases in multimolecular layers, Journal of the American Chemical Society 60 (1938) 309-319.

[145] E.P. Barrett, L.G. Joyner, P.P. Halenda, The determination of pore volume and area distributions in porous substances. I. Computations from nitrogen isotherms, Journal of the American Chemical Society 73 (1951) 373-380.

[146] N.W. Piekiel, W.A. Churaman, D.M. Lunking, B. Isaacson, C.J. Morris, Characterization of patterened galvanic porous silicon for on-chip combustion, 52nd AIAA Aerospace Sciences Meeting - AIAA Science and Technology Forum and Exposition, SciTech, 2014.

[147] B. Meyer, Elemental sulfur, Chemical Reviews 76 (1976) 367-388.

[148] A. Grosman, C. Ortega, Chemical composition of 'fresh' porous silicon, in: L. Canham (Ed.) Properties of Porous Silicon, Boca Raton, FL: CRC/Taylor & Francis, 1997, pp. 145-153.

[149] R.B. Heimann, M.B. Ives, N.S. McIntyre, The effect of deposition mechanism on the composition of surface films on silicon, Thin Solid Films 112 (1984) 329-348.

[150] S. Bastea, L.E. Fried, K.R. Glaesemann, W.M. Howard, I.-F.W. Kuo, P.C. Souers, P.A. Vitello, Cheetah 7.0, Lawrence Livermore National Laboratory, 2012.

[151] V.S. Parimi, A. Bermúdez Lozda, S.A. Tadigadapa, R.A. Yetter, Reactive wave propagation in energetic porous silicon composites, Combustion and Flame 161 (2014) 2991-2999.

[152] M. Comet, V. Pichot, B. Siegert, F. Schnell, F. Ciszek, D. Spitzer, Phosphorus-based nanothermites: A new generation of energetic materials, J. Phys. Chem. Solids 71 (2010) 64-68.

[153] J.A. Puszynski, L.J. Groven, Formation of nanosized aluminum and its applications in condensed phase reactions, in: C. Altavilla, E. Ciliberto (Eds.) Inorganic Nanoparticles: Synthesis, Applications, and Perspectives, Boca Raton, FL: CRC/Taylor & Francis, 2011, pp. 133-157.

[154] R. Thiruvengadathan, A. Bezmelnitsyn, S. Apperson, C. Staley, P. Redner, W. Balas, S. Nicolich, D. Kapoor, K. Gangopadhyay, S. Gangopadhyay, Combustion characteristics of novel hybrid nanoenergetic formulations, Combust. Flame 158 (2011) 964-978.

[155] J.B. Holt, D.D. Kingman, G.M. Bianchini, Kinetics of the combustion synthesis of TiB2, Mater. Sci. Eng. 71 (1985) 321-327.

[156] T. Kottke, L.J. Kecskes, A. Niiler, Control of TiB2 SHS reactions by inert dilutions and mechanical constraint, AIChE Journal 36 (1990) 1581-1584.

[157] Z. Fang, H. Wang, Z. Fu, Preparation of ZrB2 ceramics powder in Zr-B system by self-propagating high-temperature synthesis, Kuei Suan Jen Hsueh Pao/ Journal of the Chinese Ceramic Society 32 (2004) 1016-1018.

[158] H.E. Çamurlu, F. Maglia, Preparation of nano-size ZrB2 powder by self-propagating high-temperature synthesis, J. Eur. Ceram. Soc. 29 (2009) 1501-1506.

[159] A. Saidi, A. Chrysanthou, J.V. Wood, J.L.F. Kellie, Characteristics of the combustion synthesis of TiC and Fe-TiC composites, Journal of Materials Science 29 (1994) 4993-4998.

[160] S.D. Dunmead, D.W. Readey, C.E. Semler, J. Birch Holt, Kinetics of combustion synthesis in the Ti-C and Ti-C-Ni systems, J Am. Ceram. Soc. 72 (1989) 2318-2324.

[161] J.B. Holt, Z.A. Munir, Combustion synthesis of titanium carbide: Theory and experiment, Journal of Materials Science 21 (1986) 251-259.

[162] H.H. Nersisyan, J.H. Lee, C.W. Won, Self-propagating high-temperature synthesis of nano-sized titanium carbide powder, J. Mater. Res. 17 (2002) 2859-2864.

[163] D. Stamatis, E.L. Dreizin, K. Higa, Thermal initiation of Al-MoO3 nanocomposite materials prepared by different methods, J. Propul. Power 27 (2011) 1079-1087.

[164] D. Stamatis, E.L. Dreizin, Thermal initiation of consolidated nanocomposite thermites, Combust. Flame 158 (2011) 1631-1637.

[165] R.A. Williams, J.V. Patel, A. Ermoline, M. Schoenitz, E.L. Dreizin, Correlation of optical emission and pressure generated upon ignition of fully-dense nanocomposite thermite powders, Combust. Flame 160 (2013) 734-741.

[166] C.L. Yaws, Yaws' Handbook of Thermodynamic Properties for Hydrocarbons and Chemicals, Knovel, 2009.

[167] G.D. Sturgeon, H.A. Eick, Samarium Borides. The Tetraboride-Hexaboride Conversion1, J. Phys. Chem. 69 (1965) 3705-3708.

[168] G.I. Solovyev, K.E. Spear, Phase Behavior in the Sm-B System, J Am. Ceram. Soc. 55 (1972) 475-479.

[169] S.V. Meschel, O.J. Kleppa, Thermochemistry of alloys of transition metals and lanthanide metals with some IIIB and IVB elements in the periodic table, J. Alloy. Compd. 321 (2001) 183-200.

[170] R.A. Williams, M. Schoenitz, E.L. Dreizin, Validation of the thermal oxidation model for Al/CuO nanocomposite powder, Combustion Science and Technology 186 (2014) 47-67.

[171] M. Schoenitz, T.S. Ward, E.L. Dreizin, Fully dense nano-composite energetic powders prepared by arrested reactive milling, Proceedings of the Combustion Institute 30 (2005) 2071-2078.

[172] D. Stamatis, X. Zhu, M. Schoenitz, E.L. Dreizin, P. Redner, Consolidation and mechanical properties of reactive nanocomposite powders, Powder Technology 208 (2011) 637-642.

[173] A.L. Dragoo, J.J. Diamond, Transitions in vapor-deposited alumina from 300° to 1200°C, Journal of the American Ceramic Society 50 (1967) 568-574.

[174] I. Levin, D. Brandon, Metastable alumina polymorphs: Crystal structures and transition sequences, Journal of the American Ceramic Society 81 (1998) 1995-2012.

[175] R. Dai, S. Zhang, X. Guo, J. Li, Formation of core-type microstructure in Al–Bi monotectic alloys, Materials Letters 65 (2011) 322-325.

[176] H. Okamoto, Supplemental literature review of binary phase diagrams: Al-Bi, Al-Dy, Al-Gd, Al-Tb, C-Mn, Co-Ga, Cr-Hf, Cr-Na, Er-H, Er-Zr, H-Zr, and Ni-Pb, J. Phase Equilib. Diffus. 35 (2014) 343-354.

[177] L. Meda, G. Marra, L. Galfetti, F. Severini, L. De Luca, Nano-aluminum as energetic material for rocket propellants, Materials Science and Engineering C 27 (2007) 1393-1396.

[178] K.T. Higa, Energetic nanocomposite lead-free electric primers, Journal of Propulsion and Power 23 (2007) 722-727.

[179] A.N. Pivkina, Y.V. Frolov, D.A. Ivanov, Nanosized components of energetic systems: Structure, thermal behavior, and combustion, Combustion, Explosion and Shock Waves 43 (2007) 51-55.

[180] E.L. Dreizin, Metal-based reactive nanomaterials, Progress in Energy and Combustion Science 35 (2009) 141-167.

[181] M.C. Dumez, R.M. Marin-Ayral, J.C. Tédenac, The role of experimental parameters in combustion synthesis of NiAl under high gas pressure, Journal of Alloys and Compounds 268 (1998) 141-151.

[182] J.P. Lebrat, A. Varma, Self-propagating high-temperature synthesis of Ni3Al, Combustion Science and Technology 88 (1993) 211-222.

[183] L. Plazanet, F. Nardou, Reaction process during relative sintering of NiAl, Journal of Materials Science 33 (1998) 2129-2136.

[184] P. Swaminathan, M.D. Grapes, K. Woll, S.C. Barron, D.A. Lavan, T.P. Weihs, Studying exothermic reactions in the Ni-Al system at rapid heating rates using a nanocalorimeter, Journal of Applied Physics 113 (2013).

[185] H. Nie, M. Schoenitz, E.L. Dreizin, Oxidation of magnesium: implication for aging and ignition, The Journal of Physical Chemistry C, in press (2016).

[186] H. Nie, M. Schoenitz, E.L. Dreizin, Initial stages of oxidation of aluminum powder in oxygen Journal of Thermal Analysis and Calorimetry, under review (2016).

[187] F. Noor, A. Vorozhtsov, M. Lerner, E.P. Bandarra Filho, D. Wen, Thermal-chemical characteristics of Al-Cu alloy nanoparticles, Journal of Physical Chemistry C 119 (2015) 14001-14009.

[188] F. Noor, A. Vorozhtsov, M. Lerner, D. Wen, Exothermic characteristics of aluminum based nanomaterials, Powder Technology 282 (2015) 19-24.

[189] A. Vorozhtsov, M. Lerner, N. Radkevich, S. Bondarchuk, D. Wen, Production and characterization of Al-Cu and Al-Ni nanoparticles, MRS Online Proceedings Library 1758 (2015) 44-55.

[190] S. Mohan, Y.L. Shoshin, E.L. Dreizin, Ignition of aerosolized reactive particles at high heating rates, MRS Online Proceedings Library 896 (2006) 165-170.

[191] M. Schoenitz, B. Patel, O. Agboh, E.L. Dreizin, Oxidation of aluminum powders at high heating rates, Thermochimica Acta 507-508 (2010) 115-122.

[192] M.A. Trunov, M. Schoenitz, X. Zhu, E.L. Dreizin, Effect of polymorphic phase transformations in Al2O3 film on oxidation kinetics of aluminum powders, Combust. Flame 140 (2005) 310-318.

[193] M.A. Trunov, S.M. Umbrajkar, M. Schoenitz, J.T. Mang, E.L. Dreizin, Oxidation and melting of aluminum nanopowders, Journal of Physical Chemistry B 110 (2006) 13094-13099.

[194] X. Zhu, M. Schoenitz, E.L. Dreizin, Oxidation of aluminum particles in mixed CO2/H2O atmospheres, Journal of Physical Chemistry C 114 (2010) 18925-18930.

[195] L.P.H. Jeurgens, W.G. Sloof, F.D. Tichelaar, E.J. Mittemeijer, Growth kinetics and mechanisms of aluminum-oxide films formed by thermal oxidation of aluminum, Journal of Applied Physics 92 (2002) 1649.

[196] L.P.H. Jeurgens, W.G. Sloof, F.D. Tichelaar, E.J. Mittemeijer, Structure and morphology of aluminium-oxide films formed by thermal oxidation of aluminium, Thin Solid Films 418 (2002) 89-101.

[197] F. Reichel, L.P.H. Jeurgens, G. Richter, E.J. Mittemeijer, Amorphous versus crystalline state for ultrathin Al2O3 overgrowths on Al substrates, J. Appl. Phys. 103 (2008).

[198] S. Vyazovkin, Model-free kinetics: Staying free of multiplying entities without necessity, Journal of Thermal Analysis and Calorimetry 83 (2006) 45-51.

[199] S. Vyazovkin, Modification of the integral isoconversional method to account for variation in the activation energy, Journal of Computational Chemistry 22 (2001) 178-183.

[200] C. Kong, Q. Yao, D. Yu, S. Li, Combustion characteristics of well-dispersed aluminum nanoparticle streams in post flame environment, Proceedings of the Combustion Institute 35 (2015) 2479-2486.

[201] R.J. Jacob, B. Wei, M.R. Zachariah, Quantifying the enhanced combustion characteristics of electrospray assembled aluminum mesoparticles, Combustion and Flame (2015).

[202] P. Lynch, H. Krier, N. Glumac, Emissivity of aluminum-oxide particle clouds: Application to pyrometry of explosive fireballs, Journal of Thermophysics and Heat Transfer 24 (2010) 301-308.